Investigations of open-shell open-shell interactions: NO-O_2 and NO_2-O_2 complexes

A thesis submitted for the degree of Doctor of Philosophy at the University of Oxford

by

Tony George Starkey
The Queen's College

Trinity Term - 2007

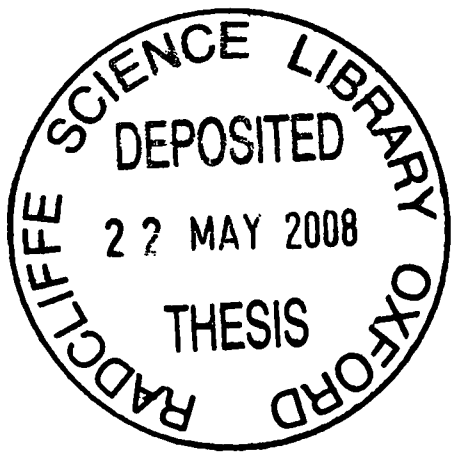

Abstract

Investigations of open-shell open-shell interactions:

NO-O_2 and NO_2-O_2 complexes

A thesis submitted for the degree of Doctor of Philosophy at the University of Oxford

Tony George Starkey, The Queen's College, Trinity Term - 2007

This thesis details research undertaken in the investigation of the open-shell open-shell Van der Waals complexes between nitric oxide (NO) and oxygen (O_2) and between nitrogen dioxide (NO_2) and oxygen (O_2).

The Fourier transform microwave spectroscopy technique was used during the experimental work. Spectra were recorded for a mixture of NO and O_2 over the frequency range 7.0 to 18.2 GHz. Detailed *ab initio* calculations have been performed on the potential energy surface of both NO-O_2 and NO_2-O_2 using Multi-reference Rayleigh Schrödinger Second Order Perturbation Theory. These calculations were performed for the four distinct states of NO-O_2, $^2A''$, $^4A''$, $^2A'$ and $^4A'$, and for the two distinct states of NO_2-O_2, ^2A and ^4A. Predicted rotational spectra have been generated by modelling the systems with a rigid-rotor Hamiltonians. The effective Hamiltonians included the rotational Hamiltonian, $\hat{\mathscr{H}}_{rot}$, fine structure terms and hyperfine structure terms. It was not possible, for rationalizable reasons, to fit the predicted spectra for NO-O_2 to the experimental observations.

Experimental details, calculation methods and rotational theory are discussed in the main body of the thesis. Predicted spectra, relevant calculations and other data is presented in the appendices.

Acknowledgments

Initially I would like to thank Prof Brian Howard for his original ideas, ongoing theoretical and practical assistance and his good humour even when the whole world seemed against us. Thanks are also due to the workshops in the Physical and Theoretical Chemistry Laboratories for the hardware which was used during the research.

Specific thanks are required to the other members of the research group, namely Christian Hill, Pete Hume, Richard Minton, Mark Snow, Bin Ouyang, Peter Dunbar, George Economides, Leon Harrington and Rebecca Swarbrick. Many days of trial, error and confusion was saved by brief discussions with the group.

Invaluable assistance was offered in the preparation of the thesis from Dr A J Starkey. Not only in the form of proof reading, but also providing clarity to the expression of ideas.

"Friends applaud, the comedy is finished."

Ludwig van Beethoven,
March 26, 1827

Contents

List of Figures

Chapter 1

Introduction

"The days just prior to marriage are like

a snappy introduction to a tedious book"

Wilson Mizner

Overview

One of the current important areas of interest within physical chemistry is the study of the weak attractive and repulsive forces that are present between all atoms and molecules. Despite the fact that these forces represent only about 1% of the strength of a standard covalent bond, they are responsible for many of the phenomena observed in the physical world. If these forces are balanced correctly it is possible to form bound states, complexes, which can be studied experimentally. Most of the weakly bound systems that have been studied to date are either composed entirely of closed-shell species, or one closed shell and one open-shell species. Closed-shell means that all of the electrons within the molecule are paired within molecular orbitals, whereas open-shell means that at least one electron is not paired. The preference in research for closed-shell species results from the inherent simplifications that they provide over their open-

shell cousins. However, there are many potentially interesting open-shell open-shell complexes.

Open-shell species are commonly referred to as radicals and are often reactive. Most atoms, molecular fragments and excited molecules are open-shell species. Open-shell species are present in biological systems, the atmosphere and inter-stellar gases. One could initially anticipate that open-shell open-shell complexes would not form, as by their very nature one could expect the formation of a strong chemical bond, rather than a weak intermolecular interaction. However, there are several examples of stable radicals, including O_2 and NO, which do not illustrate any inherent tendency to dimerise. The interaction of these radicals could be expected to be follow that of Van der Waals systems, since H_2 in a triplet state illustrates Van der Waals behaviour.

Within the study of Van der Waals complexes, there is less literature of complexes containing open-shell moieties than of closed-shell moieties and even fewer of open-shell open-shell complexes. This is a result not only of the experimental difficulty of recording spectra of these reactive species in the gas phase, but also the complexity of the spectra obtained and the complications encountered in their interpretation. Details on how to interpret the rotational spectra of open-shell systems are given in chapter 5.

Of the, roughly 1,000, Van der Waals complexes that have been studied experimentally, only sixty are open-shell closed-shell and only five are stable open-shell open-shell [1].

Before discussing species-specific points, several general issues are discussed in this chapter. Firstly, intermolecular forces and complexes are considered, detailing not only their general features, but also the additional complications caused by open-shell species. Secondly, details are given on general experimental techniques used to study intermolecular complexes. The final two sections give a brief overview of computational calculation methods currently in use and the various theoretical models used to represent complexes. Full details of the experimental

techniques, calculations and rotational theory are given in the following chapters.

1.1 Intermolecular Forces

1.1.1 Mechanisms of Molecular Interaction

Weak attractive and repulsive forces between molecules are responsible for numerous physical phenomena. Such phenomena include the formation of liquids and solids, deviation from 'perfect' gases, the adsorption of gases onto solid surfaces, mediation of chemical reactions and the energy transfer during molecular collisions. The mechanisms which cause these interactions can be divided into four main categories:

1. Electrostatic Forces

   All of the interactions that are observed between molecules are a direct or indirect result of the electrostatic interaction of the individual charged particles, the electrons and the nuclei protons. It is these electrostatic forces that lead to the formation of the molecules in the first place. However, when classifying the interactions of molecules into the four categories listed here, the electrostatic forces refer to the interaction of the unperturbed charge distributions of the atoms or molecules in question. The force is the sum of the Coulombic interactions of all the charges on the first atom or molecule with those on the second at the relevant separation and orientation.

   To be significant, these electrostatic forces require specific functional groups to be present in the interacting systems. A typical functional group could be an OH group forming a hydrogen bond to a lone pair on an electronegative atom. These particular forces are the most powerful of the intermolecular forces and can represent 2-8% [2] of the strength of a standard covalent bond. The interaction arises from two or more permanent dipole, or higher, moments. The strength of the interaction is dependent on the separation of

the dipoles, or higher moments, and their relative orientation. The energy of dipole-dipole interactions drops as r^{-3} [3], where r represents the intermolecular distance. The r dependence is greater for higher multipole interactions [4], and is clearly dependent on mutual orientation. Electrostatic interactions of polar molecules are typically of the order of 300-1,500 cm^{-1} [2].

2. Induction Forces

   These forces result from a permanent dipole, or higher, moment on one of the participants inducing a dipole in the second participant. The disturbance of the charge distribution of the latter results in an attractive force. This is distinct from the permanent dipole-dipole interactions detailed above. The energy drops off more rapidly than for electrostatic interactions, with an r^{-6} [5] dependence. These forces can exist between atoms and dipolar molecules, which cannot exhibit the electrostatic forces detailed above. Induction force are typically of the order of 100 cm^{-1} [6].

3. Dispersion Forces

   These forces are present between all atoms and molecules and are not dependent on the presence of any specific functional groups. These forces are the most important interaction for non-polar molecules. The forces arise from the interaction of instantaneous dipoles in the atoms or molecules. Since the electrons associated with a nuclei are in continuous motion there is a transitory dipole moment in all systems. These transitory dipoles induce reactionary dipoles in secondary atoms or molecules, which result in attractive forces. For these dispersion forces, the energy drops with an r^{-6} [3] dependence. Dispersion force are typically of the order of 100 cm^{-1} [4].

4. Repulsive Forces

   At short intermolecular distances the electron clouds of the atoms or molecules overlap. This overlapping results in a repulsive electrostatic force, predominantly explained by the Pauli exclusion principle. The repulsion, in addition to the attractions, can be anisotropic,

due to the physical shape of the molecules and hence their electron clouds. The repulsive interaction increases exponentially as the intermolecular distance decreases [6].

The combined effect of the interactions is illustrated in figure 1.1, showing the change in potential energy as a function of deviation from the equilibrium intermolecular distance. A stable complex will form if the forces provide a potential well of sufficient depth to support bound vibrational levels.

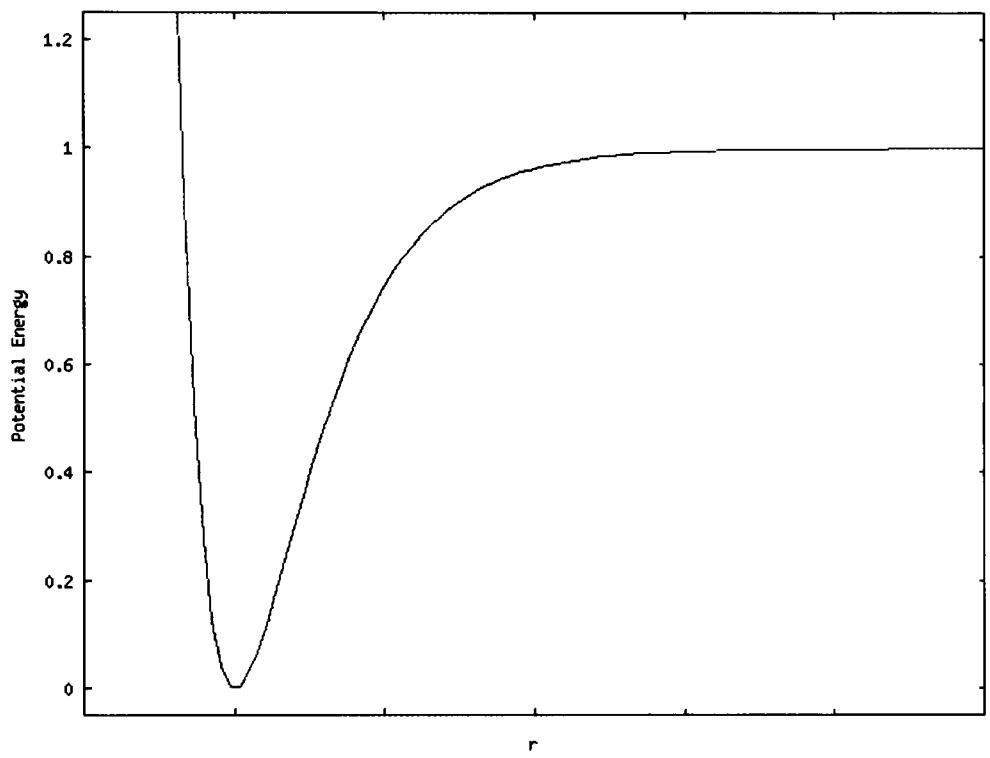

Figure 1.1: Typical Potential Energy Well. Intermolecular separation given by r

One such potentially stable complex is nitric oxide - oxygen, NO-O_2, which is believed to form an open-shell open-shell complex with a weak interaction, rather than a strong chemical bond. Weak intermolecular interactions are observed for several nitrogen containing species, including NO_2-O_2. The complex NO-O_2 is a possible intermediate in the oxidation reaction of NO to NO_2

$$2NO + O_2 \rightarrow 2NO_2$$

This third order chemical reaction has a negative activation energy, which suggests that the reaction may proceed by an intermediate complex. Conventionally the intermediate complex is thought to be $(NO)_2$, but NO-O_2 has been proposed as an alternative [7]

$$2NO+O_2 \rightarrow (NO)_2+O_2 \rightarrow 2NO_2$$

or

$$2NO+O_2 \rightarrow NO+NO\text{-}O_2 \rightarrow 2NO_2$$

Studying NO oxidation is important as it can improve understanding of the distribution and conversions of nitrogen oxides in the atmosphere. These contribute to the production of tropospheric ozone, which is itself a toxic secondary air pollutant. Thus, in addition to the development of fundamental understanding of open-shell open-shell interactions, the study of the complex NO-O_2, and NO_2-O_2, may provide useful information for atmospheric chemists.

The open-shell open-shell Van der Waals complexes NO-O_2 and NO_2-O_2 are the species investigated in this thesis.

1.1.2 Geometry

During the formation of an intermolecular complex, or even in the approach of two molecules, there can be a significant change in the geometry of the moieties. These geometric changes may be seen in the rotational constants determined from experimental observations. The moiety bond lengths and bond angles which account for the rotational constants can be determined by *ab initio* calculations, see section 1.3.

As an example consider the complex of trifluoroacetic acid, F_3C-COOH, and water [8]. Using high quality *ab initio* calculations (MP2/6-311++G(2df,2pd)), see chapter 3, it can be seen that there are changes in the geometry of both H_2O and the acid on complex formation. The H_2O bond lengths remain unchanged at 0.96 Å on complex formation, but the bond angle

increases from 104.1° to 106.0°. For the acid, the OH bond length increases from 0.97 Å to 0.99 Å , and the C-OH bond angle increases from 107.1° to 107.7°.

1.1.3 Examples

One of the first Van der Waals complexes to be studied by high resolution spectroscopy was argon-hydrogen chloride, Ar-HCl [9]. The original structure determination was conducted by S. E. Novick et al. in 1973. This system was the test ground for many of the ideas about Van der Waals complexes. The early studies were at microwave and radio frequencies and were conducted with a molecular beam system. For Ar-HCl, the observed intermolecular distance is approximately 4.0Å and the average angle the HCl makes to the intermolecular axis of centres of mass is approximately 41.5 degrees, see figure 1.2.

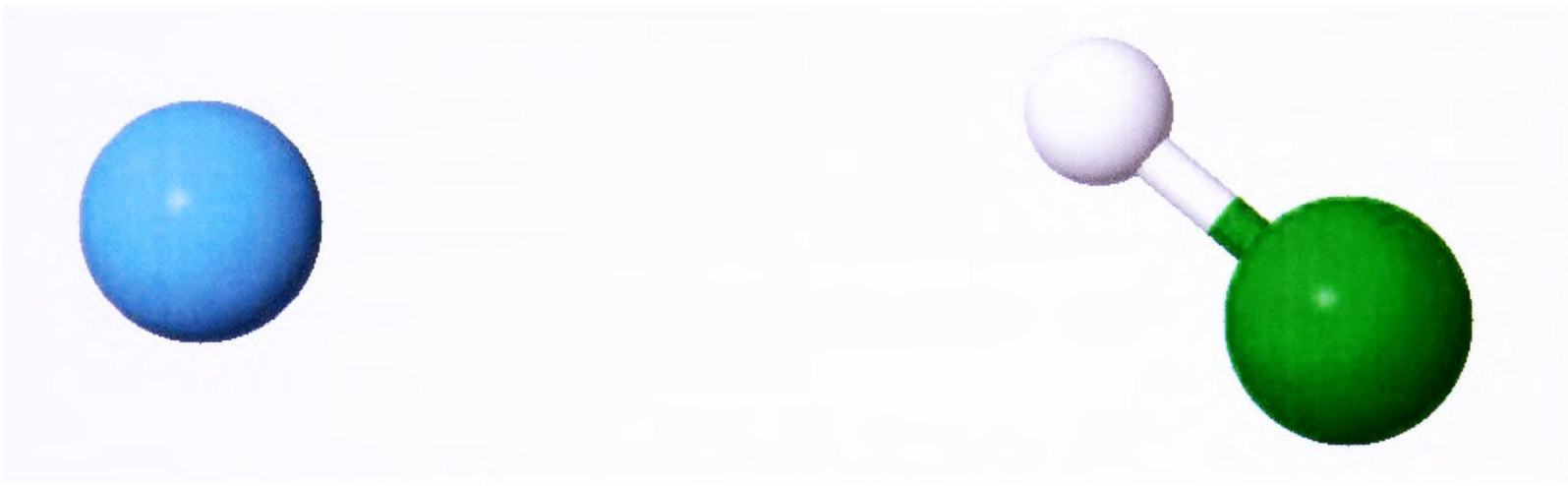

Figure 1.2: Van der Waals complex of Ar-HCl

Simple alcohols, such as butan-2-ol [10], have also been studied in Van der Waals complexes. These systems form chiral complexes, where the main interaction results from a hydrogen bond from the OH on one of the moieties to the OH on the second. Other alcohols have been studied by the Howard group [11] with the aim of extending current understanding to biologically relevant systems.

Numerous open-shell closed-shell complexes formed with the stable radicals NO [12-17], NO_2

[18-21] and O_2 [22], [23], and open-shell open-shell and open-shell closed-shell complexes of the unstable radical OH [24], have been studied with various spectroscopic techniques. This work not only extends our fundamental understanding of open-shell complexes, but may also provide useful material for atmospheric modellers. The resolution of the spectra for these species has increased with improvements in experimental techniques, as have the sophistication of the theoretical models used to fit the spectra once rough assignments have been made.

Previous work conducted on species related to NO-O_2 and NO_2-O_2 provides a context for the work of this thesis. Some of the earliest work on NO containing complexes was conducted in by J. Bonamy et al. in 1981 [12] where linewidths of NO vibration-rotation transitions were investigated in the presence of Ar. At this point there were no anisotropic potentials available for Ar-NO leading to rough approximations been used to model the system. In 1986 P. D. A. Mills et al. [13], [14] provided the first high resolution microwave spectra for Ar-NO and also provided a new Hamiltonian to assign their observations. The types of Hamiltonians used to fit open-shell spectra are discussed in section 1.4. Subsequent work on Ar-NO has extended the experimental techniques used to study the complex [15], [25]. The knowledge gained in the investigations of Ar-NO has been applied to NO-HF [16], [17]. A similar Hamiltonian, to that used for Ar-NO, has been used in the modelling of microwave spectrum of NO-HF. However, due to the presence of the hydrogen and fluorine, the hyperfine theory is much more complex for NO-HF.

The early research into Van der Waals complexes containing NO_2 also involved investigation of Rg-NO_2 species. The first high resolution spectra of an Rg-NO_2 was recorded in the microwave region in 1994 by R. J. Low et al. [18], [19]. Here the rare gas was argon, and the work built on the previous experience the group had with Ar-NO. In the initial work only four rotational transitions were assigned and several of the rotational parameters were taken from geometrically similar complexes. However, subsequent investigations assigned ten rotational

transitions allowing not only for a determination of all relevant rotational parameters, but also an assignment based on a dynamic model of the potential, see section 1.4. Xe-NO_2 [20] and Kr-NO_2 [21] have been investigated in the microwave region with similar techniques.

Investigations into complexes containing O_2 have been conducted in both open-shell closed-shell and open-shell open-shell complexes. H. Qian et al. published two papers in 1997 [22], [23] investigating the microwave spectra of the open-shell closed-shell species O_2-N_2O. The work assigned sixty four transitions and illustrated several different fits for the rotational parameters. In 2005 K. Suma et al. presented an assigned spectrum of O_2-OH [24]. That work closely parallels that for NO-O_2 which is electronically similar to O_2-OH. The publication by K. Suma et al. provided an insight to the problems encountered when one tries to calculate the potential of these open-shell open-shell species, see section 1.3.

As with all scientific investigations the level of theory and experimental techniques used to probe the system in question have been refined over the years. As the level of experimental resolution increases a more sophisticated theoretical understanding is required, and vice versa. The literature, which covers the investigation of numerous other Van der Waals complexes, illustrates the relationship between the standards of theory and experiment.

1.2 Experimental Techniques

To experimentally probe the structure of Van der Waals complexes, spectroscopy is the technique of choice due to the level of detail it provides. High resolution microwave and infrared (IR) spectra have proved the most productive in the study of weakly bound complexes. Routinely collected spectra of complexes are of rotational, vibrational or electronic excitation, which correspond, respectively, to microwave, IR and UV-Visible frequencies.

There is a wide range of techniques used to collect spectra across the various frequency

ranges. The exact techniques used in this study of NO-O_2 are detailed in chapter 2. Detailed description of some of the alternative techniques currently used are given in the literature [26].

The overall electro-magnetic spectrum can be divided into various regions, each with its own experimental techniques:

1. UV-Visible Spectroscopy

   The UV-Visible region is defined to roughly cover the frequency range from 3×10^{14} to 3×10^{16} Hz, which corresponds to a range of 10^4 to 10^6 cm^{-1}. Excitation in this energy range involves the excitation of valence electrons leading to a moving of electronic charge within the molecules.

   Techniques used in this region of the electro-magnetic spectrum include Laser-Induced Fluorescence (LIF), Resonant Multiphoton Ionization (REMPI) and Zero Energy Kinetic Energy Spectroscopy (ZEKE). LIF and REMPI have been used in the study of Ar-NO [25] and Ar-OH [27]. Given the high energies involved in the transitions observed with these techniques they are often of a low resolution. However, recent REMPI studies of relevant species have achieved resolution comparable with that of rotational spectra. A typical resolution is of the order of 0.1 cm^{-1} [26].

2. IR Spectroscopy

   The IR region covers, approximately, 3×10^{12} to 3×10^{14} Hz, or 100 to 10^4 cm^{-1}. Within this range the energy of excitation leads to a change in the physical configuration of the molecule, a vibration. This vibration can be a stretch, compression or flex of inter-atomic bonds. Of course, these configuration changes will be accompanied by rotational transitions. The change in the molecule's geometry during the vibration leads to an alternating electric dipole which interacts with the electrical component of the electromagnetic radiation.

High resolution IR spectra can be recorded by using an IR diode laser as the excitation source. These solid state, narrowly tunable sources can provide rotational resolution down to approximately 0.001 cm^{-1} [26].

3. Microwave Spectroscopy

   The Microwave region covers, approximately, 3×10^9 to 3×10^{12} Hz, or 0.1 to 100 cm^{-1}. This spectral region is sometimes sub-divided into a lower frequency microwave region and a higher frequency millimetre wave region. Excitation at these energy levels corresponds to pure rotational excitation. As with IR spectroscopy, the change in the system orientation leads to a changing electrical or magnetic dipole moment, which interacts respectively with the electrical or magnetic component of the electromagnetic radiation. The rotational excitation leads to a rotational spectrum.

   Spectra within this region have the narrowest linewidth, and are therefore of the highest resolution. The observed transition linewidth is dependent on collision broadening, Doppler broadening, pressure broadening, power saturation broadening and the Heisenberg uncertainty principle. A typical linewidth is of the order of 10^{-7} cm^{-1} [26], but this is highly dependent on pressure.

   There are a range of techniques that cover the microwave region, including Molecular Beam Electric Resonance Spectroscopy (MBERS) and Fourier Transform Microwave Spectroscopy (FTMS). MBERS have been used in the study of Ar-NO [14] where detailed rotational information was obtained. FTMS is the experimental technique used in this study, and is explained in depth in chapter 2. FTMS has been used extensively in the study of Ar-NO_2 [18], [19], NO-HF [16] and Ar-OH [28]. All of these studies have provided high resolution spectra. In overview, with FTMS, the sample under goes a supersonic expansion into a resonance chamber, a microwave pulse is then injected which rotationally

excites the molecules and complexes, the coherent emission is detected, mixed down to a radio frequency and digitally sampled by a computer. The FTMS technique typically covers the frequency range of 3×10^9 to 4×10^{10} Hz.

1.3 *Ab initio* Calculations

With the development of powerful computers, it has become possible to use numerical techniques to solve the time independent Schrödinger's equation for a collection of fixed nuclei [2]

$$\hat{\mathscr{H}}\Psi = E\Psi \tag{1.1}$$

Numerical calculations based solely on this equation are known as *ab initio* calculations. There are various techniques available for the solution of Schrödinger's equation for electrons, all with advantages and disadvantages. These techniques are outlined in chapter 3.

For Van der Waals complexes, these *ab initio* calculations allow, in theory, determination of the geometry and binding energy of the complex. This means that it is not only possible to tell if the complex is likely to form, but also to evaluate the rotational constants, A, B and C, without conducting any experiments. Significant time can be saved by avoiding futile experimental work in the study of unbound systems.

Ab initio calculations for closed-shell closed-shell Van der Waals complexes are normally computationally relatively stable, but complications are encountered with open-shell open-shell systems [24]. The reasons for these difficulties are discussed in chapters 3 and 6, but are generally related to single-reference calculations being unable to properly represent the complex's wavefunction in the ground state.

1.4 Theoretical Models

As an initial approximation, the spectrum of a Van der Waals complex can be modelled as a rigid rotor. The Hamiltonian is constructed with rotational constants A, B and C. This model can usually give fitted spectra that are within a few MHz of experimental results, assuming that the system is closed shell. For an open-shell system the spectra is much more complex for the reasons outlined in chapters 4 and 5.

The earliest high resolution spectra of open-shell closed-shell species related to NO-O_2 [12], [13] were modelled with rigid rotors. The reasons for this potentially simplistic choice of model is that to model a complex containing an open-shell moiety one has to take into account several additional terms, beyond the rotational Hamiltonian, to represent the coupling of the various angular momentum.

It is possible to refine the rigid rotor model by taking into account centrifugal distortion. These distortions become significant if there is mixing of vibrationally excited states into the ground state wavefunction. This mixing can be accounted for with a single parameter (several parameters are used in the case of an asymmetric rotor), which is dependent on the J level of the rotation. These semi-rigid models can give fitted rotational spectra that are accurate to a few kHz, for closed-shell molecules or complexes.

Semi-rigid models are the most commonly used models for open-shell closed-shell [22], [23] and open-shell open-shell [24] complexes as they can provide an accuracy of fitting to a few kHz. However, these fits will be based on the refinement of initial rough assignments made without any centrifugal distortion parameters.

Semi-rigid models provide information about the Potential Energy Surface (PES) of the system. The distortion parameters indicate the magnitude of the vibrational force constants

within the PES. However, the PES is a multi-dimensional representation of the potential energy, with one dimension for each internal degree of freedom. Given that there are only five distortion constants at the first-order, the level of information that can be obtained from them regarding the PES is severely limited. Whereas if the PES is known, independently, it can provide not only the values of the distortion constants, but also vast amounts of other data.

For the case of the three body reaction

$$\mathbf{AB + C \rightarrow A + BC}$$

an example PES, with the A-B and B-C separations as plotted variables and a fixed angle of interaction, can be seen in figure 1.3.

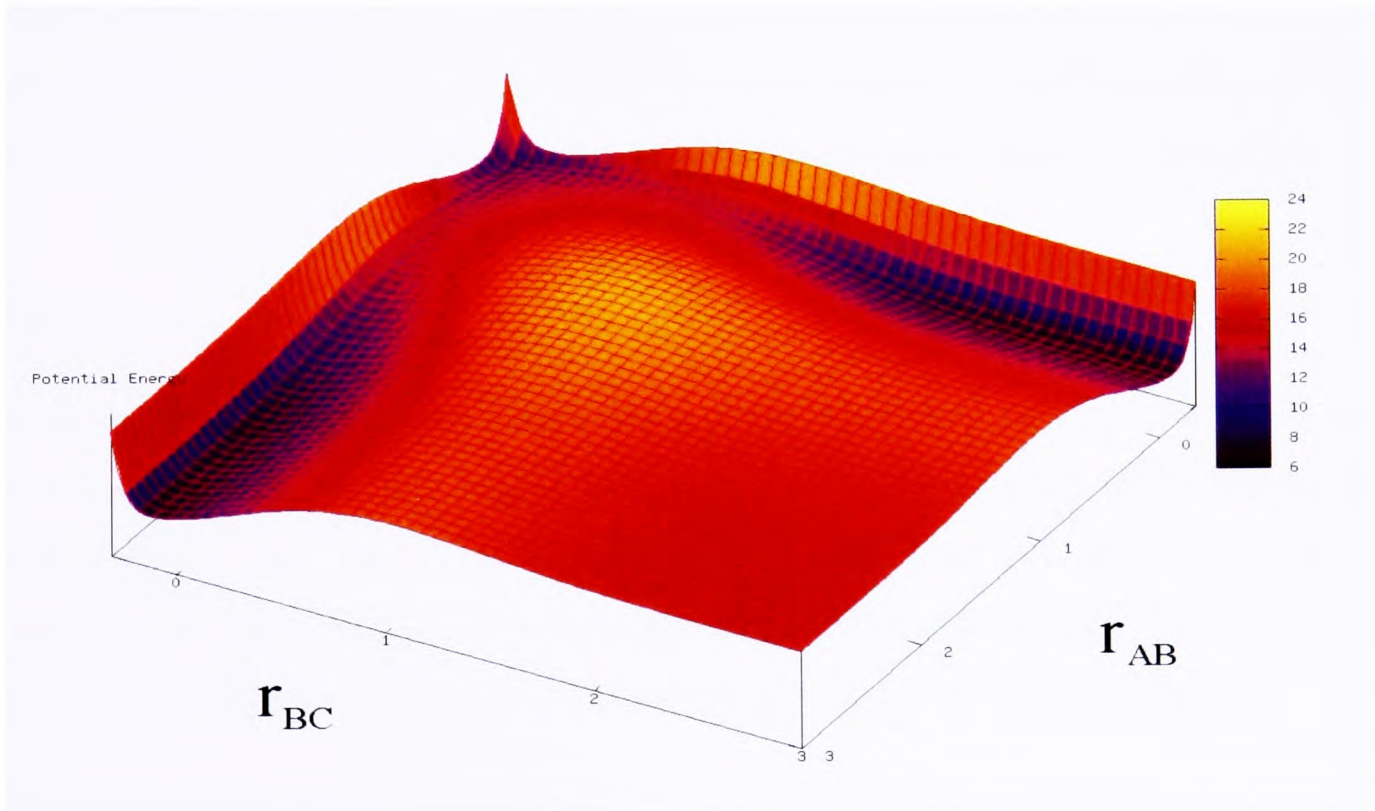

Figure 1.3: Two Dimensional Potential Energy Surface for a three-body reaction

Further improvements in the model can be made by incorporating the internal dynamics of the complexes. This level of modelling, which is typically used on open-shell systems, can

improve the accuracy of predictions to a few hundred kHz for open-shell molecules or complexes.

The Howard research group has used such dynamic modelling in the study of a number of complexes, such as Ar-NO_2 [19], [29]. In that case the Hamiltonian was defined as

$$\hat{\mathscr{H}} = \frac{\hbar}{2\mu}\left(-R^{-1}\frac{\partial^2}{\partial R^2}R + \frac{(\hat{J}-\hat{j})^2}{R^2}\right) + \hat{\mathscr{H}}_{mon} + V(R,\theta,\chi) \tag{1.2}$$

where μ is the reduced mass, $\hat{J}$ is the total angular momentum, $\hat{j}$ is the angular momentum of NO_2, $\hat{\mathscr{H}}_{mon}$ is the Hamiltonian for NO_2 and $V(R,\theta,\chi)$ is the vibrationally averaged intermolecular potential.

This technique can be used to match the observed intermolecular potential, $V(R,\theta,\chi)$, by adjusting the parameters to fit the predictions more accurately to the observations. Correct initial assignment of the observations is required before dynamical fitting can be applied.

Summary

In summary, there are four main classifications of interaction that can, if correctly balanced, lead to the formation of intermolecular complexes. Further, the moieties can be distinct from the uncomplexed forms due to geometry changes on complex formation. With regards to NO-O_2 and NO_2-O_2, which are both open-shell open-shell species, additional features beyond those of closed-shell complexes are important in the interpretation of the recorded spectra.

There are various frequency ranges and techniques available to study a complex, the choice of which depends on the specific properties of the complex been studied.

It is possible to use computer based calculations to predict that a complex is likely to form,

and so reduce the risk of conducting futile experiments. The selection of a numerical technique is dependent on the type of system in question and the amount of computer time available.

There are several levels of theory which can be used to analyse the observed spectra. The selection of theoretical method is dependent on the required accuracy of the predictions and the level of understanding sought.

The choices made in this study are fully documented in the following chapters of this thesis.

References

[1] S. Novick *BIBLIOGRAPHY OF ROTATIONAL SPECTRA OF WEAKLY BOUND COMPLEXES.* http://www.wesleyan.edu/chem/faculty/novick/vdw.html (accessed March 2007)

[2] F. Jensen *Introduction to Computational Chemistry.* John Wiley & Sons (2002)

[3] P. W. Atkins *Molecular Quantum Mechanics.* Oxford University Press (1997)

[4] B. J. Howard *The Structure and Dynamics of Van der Waals Molecules.* Iberdrola Lectures, Consejo Superior de Investigaciones Cientificas (CSIC), Madrid (2001)

[5] A. J. Stone *The Theory of Intermolecular Forces.* Clarendon Press, Oxford (1996)

[6] P. W. Atkins *Physical Chemistry.* Oxford University Press (1994)

[7] H. Tsukahara, T. Ishida and M. Mayumi, Nitric Oxide **3**, 191 (1999)

[8] B. Ouyang, T. G. Starkey and B. J. Howard, *High-resolution microwave spectroscopy study of ring-structured trifluoroacetic acid and water complexes.* Manuscript submitted for publication.

[9] S. E. Novick, P. Davies, S. J. Harris and W. Klemperer, J. Chem. Phys. **59**, 2273 (1973)

[10] A. K. King *A High resolution, Microwave Spectroscopic study of the Conformations and Clusters of Butan-2-ol.* D.Phil Thesis, Oxford University (2002)

[11] M. S. Snow *Spectroscopic Investigation of Chiral and Induced Chiral Interactions.* D.Phil Thesis, Oxford University (2006)

[12] J. Bonamy, A. Khayar and D. Robert, Chem. Phys. Lett. **83**, 539 (1981)

[13] P. D. A. Mills, C. M. Western and B. J. Howard, J. Phys. Chem. **90**, 3331 (1986)

[14] P. D. A. Mills, C. M. Western and B. J. Howard, J. Phys. Chem. **90**, 4961 (1986)

[15] H. Meyer, J. Chem. Phys. **107**, 7732 (1997)

[16] C. R. Dennis, C. J. Whitham, R. J. Low and B. J. Howard, Chem. Phys. Lett. **282**, 421 (1998)

[17] C. R. Dennis, C. J. Whitham, and B. J. Howard, J. Chem. Phys. **115**, 1355 (2001)

[18] R. J. Low, C. J. Whitham, T. D. Varberg and B. J. Howard, Chem. Phys. Lett. **222**, 443 (1994)

[19] R. J. Low, M. D. Brookes, C. J. Whitham and B. J. Howard, J. Chem. Phys. **105**, 6756 (1996)

[20] C. J. Whitham, R. J. Low and B. J. Howard, Chem. Phys. Lett. **286**, 408 (1998)

[21] S. Blanco, C. J. Whitham, H. Qian and B. J. Howard, Phys. Chem. Chem. Phys. **3**, 3895 (2001)

[22] H. Qian, S. J. Low, D. Seccombe and B. J. Howard, J. Chem. Phys. **107**, 7651 (1997)

[23] H. Qian, D. Seccombe and B. J. Howard, J. Chem. Phys. **107**, 7658 (1997)

[24] K. Suma, Y. Sumiyoshi and Y. Endo, Science **308**, 1885 (2005)

[25] Y. Kim, K. Patton, J. Fleniken and H. Meyer, Chem. Phys. Lett. **318**, 522 (1999)

[26] J. M. Hollas *High Resolution Spectroscopy.* John Wiley & Sons (1998) D.Phil Thesis, Oxford University (1995)

[27] M. T. Berry, M.R. Brustein, J. R. Adamo and M. I. Lester, J. Phys. Chem. **92**, 5551 (1988)

[28] Y. Ohshima, M. Iida and Y. Endo, J. Chem. Phys. **95**, 7001 (1991)

[29] R. J. Low *High Resolution Spectroscopy of Weakly Bound Molecular Complexes*

Chapter 2

Experimental

"Our view ... is that it is an essential characteristic of experimentation that is carried out with limited resources and an essential part of the subject of experimental design to ascertain how these should be best applied or, in particular, to which causes of disturbance care should be given, and which ought to be deliberately ignored."

Sir Ronald A Fisher

Introduction

Spectroscopy is the study of the interaction of electro-magnetic radiation with matter. The task in spectroscopy is to subject the matter to the radiation and record any resulting radiation emissions or absorptions. The experimental setup used during the research of this thesis studies this interaction within the microwave region of the electro-magnetic spectrum.

All the experimental work was conducted on a pulsed-nozzle Fourier Transform Microwave Spectrometer (FTMS). The apparatus is based on the Balle and Flygare [1] set up and has been used previously by the Howard group, and others, to successfully record high resolution microwave spectra for numerous gaseous systems [2], [3].

The use of FTMS has superseded the original technique of Molecular Beam Electric Resonance Spectrometer (MBERS) [4]. The MBERS technique has been used to record the rotational spectra of the Van der Waals complexes of Ar-NO and Ne-NO [5]. MBERS has the advantage of being able to work over a wider range of frequencies than FTMS and has a comparable linewidth.

A diagrammatic overview of the apparatus is given in figure 2.1. In overview the experiment is conducted within a near-confocal resonant cavity, a Fabry-Perot Cavity, held within a vacuum chamber. Confocal implies that the two mirrors have the same foci. The sample is introduced to this chamber via a supersonic expansion from a pulse nozzle mounted in one of the cavity mirrors. Microwave radiation is subsequently pulsed into the cavity via an antenna located on the second cavity mirror. The microwave radiation starts to form a standing wave which can rotationally excite the sample. Once the microwave pulse has finished, the radiation is allowed to ring-down. The sample, if excited, will spontaneously emit, giving a Free Induction Decay. This Free Induction Decay is detected by the same antenna, and once converted from the time domain to the frequency domain with the use of a Fourier Transformation, gives the observed spectrum.

The set up has been described previously by other members of the group [6], [7], but additional features have been added regularly. The details of the particular FTMS used during the experimental work are provided in the following chapter.

This chapter discusses the physical apparatus, the expansion of the gaseous samples into the

cavity, signal production and processing, experimental controls and the miscellaneous apparatus used.

2.1 Microwave Apparatus

The microwave system used in a FTMS is composed of two parts; the Fabry-Perot Cavity which is in resonance with the radiation and the external circuit which provides and controls the radiation source and detects any emitted radiation. These components are discussed separately below.

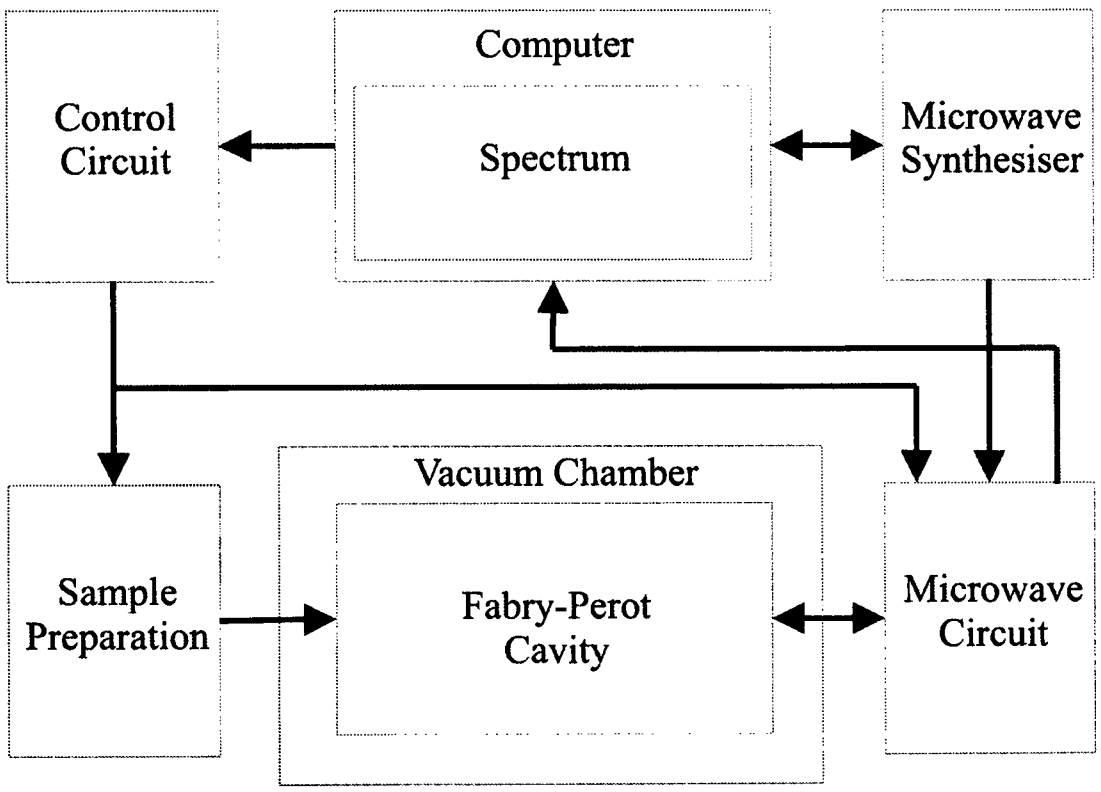

Figure 2.1: Schematic of Spectrometer

2.1.1 Fabry-Perot Cavity

The Fabry-Perot cavity is an essential component of a practical experimental set up, even though it is possible in theory to conduct microwave spectroscopy without a cavity. The cavity consists of two spherically machined mirrors held in a near-confocal arrangement. This arrangement allows for the concentration of the microwave power within a well defined region inside the vacuum chamber. In addition to uses within FTMS, these cavities have been used extensively in studies with masers [8]. The cavity the mirrors were constructed from aluminium and machined to a focal length of 50 cm. An overview of the cavity can be seen in figure 2.2.

The sample is introduced via the gas nozzle mounted on the first mirror. The microwaves are introduced by the antenna in the second mirror. The microwaves generate a standing wave along the intermirror axis with a physical beam waist. This radiation interacts with the sample in the transition region and subsequently leads to a spectrum.

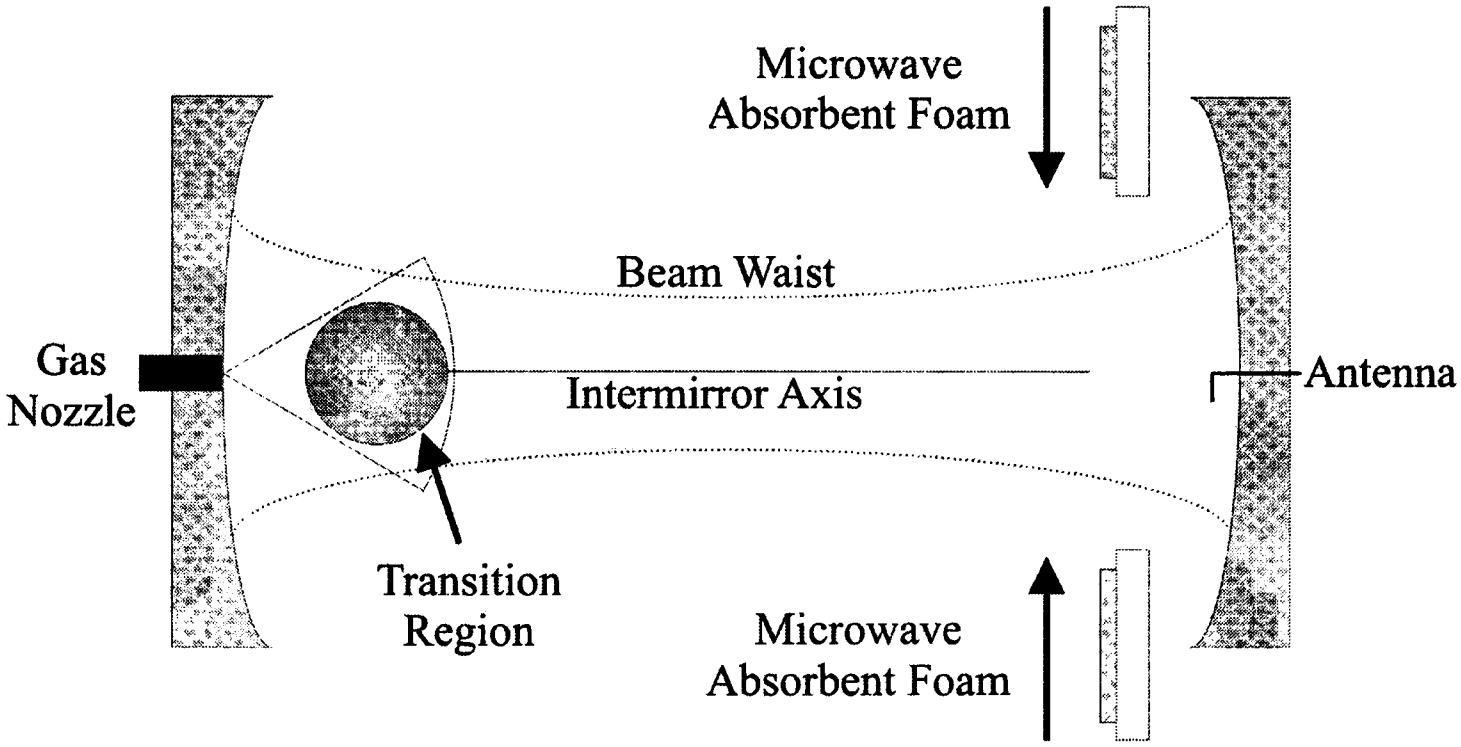

Figure 2.2: Fabry-Perot Cavity

Mode Structure

Within the cavity the microwaves, emitted from an antenna, can set up a standing wave if the correct conditions are achieved. The cavity allows a long path length for the radiation within a fixed physical size. The gas sample can be transversed numerous times by the radiation, allowing greater absorption and hence a stronger emitted signal. Standing wave resonance is achieved if the round trip of the radiation gives a phase delay which is a multiple of 2π. The cavity modes generated by this resonance are of two types, transverse and axial, which are respectively normal to and along the intermirror axis. The transverse modes are labelled TEM_{ml}, where TEM stands for Transverse Electric and Magnetic and m and l are integers to specify the order of the mode. Examples of the first few TEM modes can be seen in figure 2.3. The TEM modes represent the radiation in two-dimensions perpendicular to the intermirror axis, but in the case of standing waves the dimension along the intermirror axis is of importance. This third dimension is represented by q, the number of half wavelengths between the cavity mirrors, see equation 2.1.

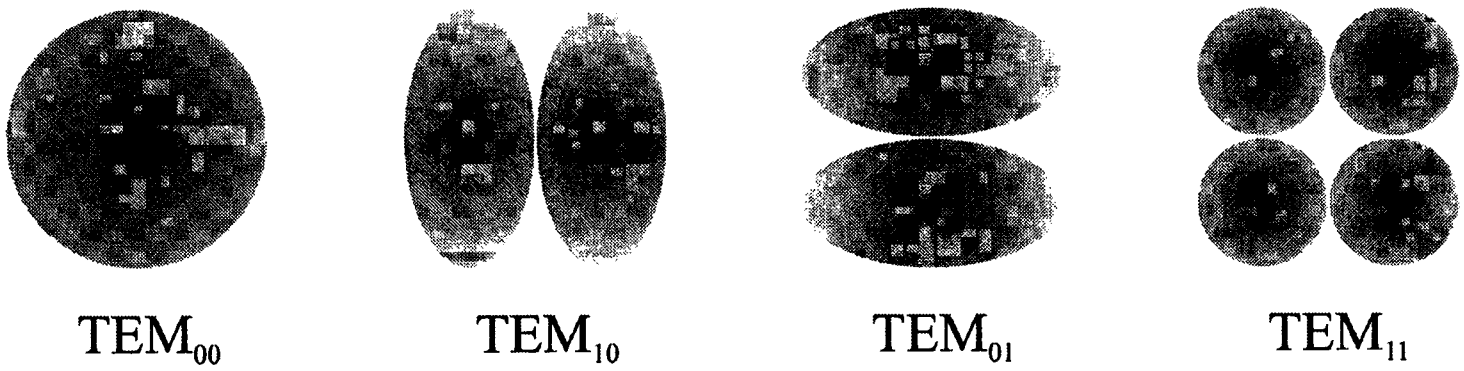

Figure 2.3: Transverse Electric and Magnetic Modes

The different modes arise as a result of the different ways in which a wave can travel between the two cavity mirrors and still constructively interfere. It is possible that the wave can travel in a zig-zag manner and still be reinforced. The integers m and l correspond to the number of vertical and horizontal nodal planes within the mode. For spectroscopy the preferred mode is TEM_{00}, which has a gaussian intensity distribution around the intermirror axis. Other TEM modes are suppressed with the variable attenuators of absorbent foam, which absorb the mi-

crowaves, see figure 2.2. The reason for this preference is that the sample will be located about the intermirror axis, due to the arrangement of the chamber inlet. Thus TEM_{00} will give the greatest degree of spatial overlap of the microwaves and the sample.

The resonant frequencies that are supported by the cavity are given by

$$\upsilon_0 = \frac{c}{2d}\left(q + \frac{1}{\pi}(m+n+1)\arccos\left(1-\frac{d}{R}\right)\right) \tag{2.1}$$

where R is the radius of curvature of the mirrors, d is the mirrors separation and q is the number of half wavelengths between the cavity mirrors. In the case of a confocal arrangement, when R is equal to d, equation 2.1 is simplified to

$$\upsilon_0 = \frac{c}{2d}\left(q + \frac{1}{2}(m+n+1)\right) \tag{2.2}$$

These equations give a set of modes with well defined frequencies. An illustration of the possible modes in a near-confocal cavity is given in figure 2.4.

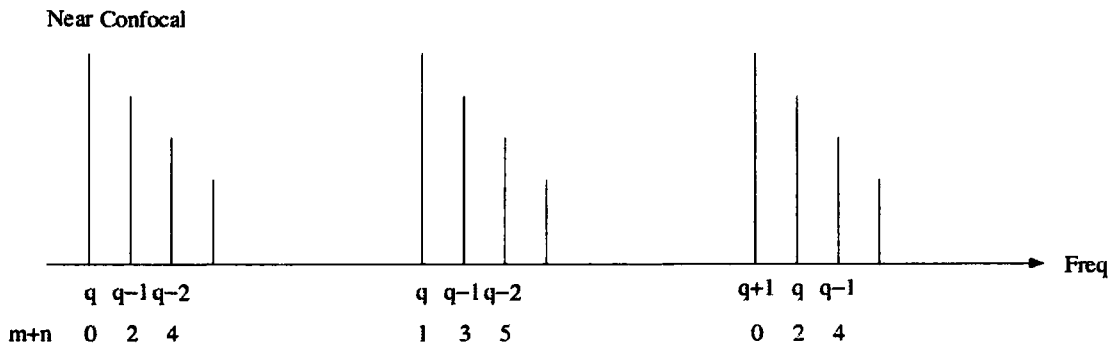

Figure 2.4: Resonant frequencies in a Fabry-Perot cavity for a near-confocal, R $< d$ arrangement

The cavity used for this thesis has $R = 50$ cm and $d \approx 60$ cm, which has supported frequencies given by

$$\upsilon_0 = \frac{3 \times 10^{10}}{120} (q + 0.564(m + n + 1)) \tag{2.3}$$

The supported modes are separated by approximately 250 MHz

$$\upsilon_0(q = x) - \upsilon_0(q = x - 1) = \frac{3 \times 10^{10}}{120} = 250 \text{ MHz} \tag{2.4}$$

Cavity Energy Storage

Within the cavity power is stored for a finite time represented by the cavity ring-down time, τ_c. This is defined as

$$\tau_c = \frac{E_s}{E_l} \tag{2.5}$$

where E_s is the energy stored within the cavity and E_l is the energy lost from the cavity per unit time. The cavity ring-down time is typically of the order of 300 ns, which is much more rapid than the Free Induction Decay (FID) of the samples which is typically of the order of 50 μs. This mis-match in the duration of the cavity ring-down and the FID means that it is possible to excite the sample, allow the ring-down of the exciting microwave radiation to completely decay and still have an observable emission signal from the FID of the sample.

The quality factor, the Q-factor, can be used to describe the calibre of the cavity resonance. This factor measures the energy stored in the cavity, and is related to the cavity ring-down time and cavity bandwidth by

$$Q = 2\pi\upsilon\tau_c = \frac{\upsilon}{\Delta\upsilon} \tag{2.6}$$

where υ is the microwave frequency and $\Delta\upsilon$ is cavity bandwidth measured as Full-Width at Half-Height (FWHH).

A typical value of Q is 5×10^4. This value can be reduced by deliberate attenuation of the microwaves using microwave absorbent foam. The value of Q depends on several factors including the reflectivity of the mirrors used inside the cavity. A large Q value indicates how the presence of cavity increases the amount of power to which the sample is subjected [9]. It would have been possible to conduct experimental research for this thesis without the use of a Fabry-Perot cavity, but the observed signal strengths would have been reduced by several orders of magnitude.

Energy is lost from the cavity as a result of four main mechanisms:

1. Diffractive Loss

   The propagating waves within the cavity may be too large for the diameter of the cavity mirrors. If this is the case, then energy will overflow around the edge of the mirrors. The size of the modes increases as they become of higher order and more diffuse [9]. As the frequency of the modes increase they become more compact, and their beam waist is reduced, see figure 2.2. This means for high frequency and low order modes this mechanism of energy loss is minimised. This therefore favours the use of TEM_{00}.

2. Imperfect Mirrors

   The mirrors used were constructed of machined aluminium. These are highly reflective in the microwave region, but their reflectivity is still less than the ideal 100%. The reflectivity decreases with increasing frequency [10], but in comparison with other loss mechanisms,

this does not lead to a significant energy loss.

3. Coupling of radiation out by the antenna

   The antenna acts in a symmetric manner. This means that radiation will be able to couple out of the cavity as easily as it can couple into the cavity and so energy can be lost via the antenna itself. This effect, unfortunately, cannot be minimised without degrading signal collection.

4. Deliberate attenuation

   At high frequencies, the Q-factor is often too large for FTMS to be conducted, as the cavity ring-down time becomes too long and the "active" frequency of the spectrometer, the cavity bandwidth, is reduced. This means that the resonance is deliberately attenuated to shorten the ring-down of the cavity and to limit the beam width. This control is achieved with variable attenuators, see figure 2.2, which can be adjusted from outside the vacuum chamber allowing for dynamic adjustment of the Q-factor during a data-collection run. This external control provides a valuable tool to control the width of the resonance of the spectrometer at different frequencies. It reduces the duration required to optimise the machinery for each run.

2.1.2 Microwave Circuit

The microwave circuit provides microwaves to the chamber via the antenna in short pulses. The pulse width is typically set to 1 μs. The species signal, the emission from the sample species, is detected via the same antenna. The signal is amplified, frequency mixed down to a recordable frequency, and then recorded by a rapid Analogue to Digital (A-D) converter within the controlling PC.

Antenna Design

The antenna used to couple the power in and out of the chamber is illustrated in figure 2.5.

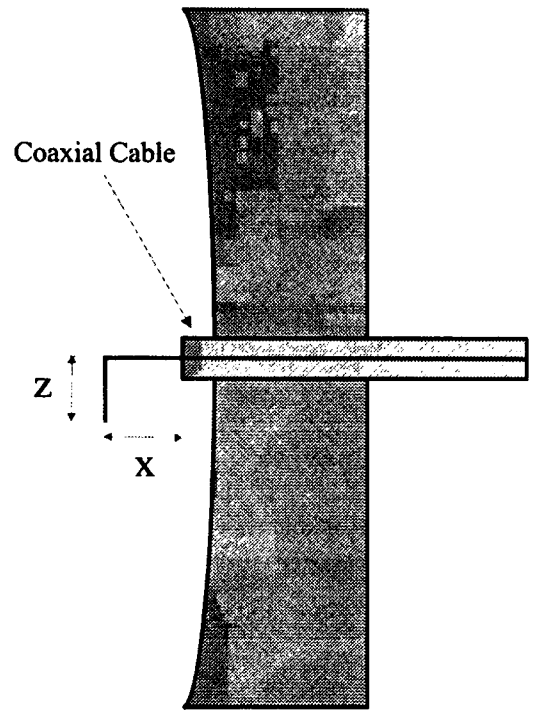

Figure 2.5: Antenna

The antenna is formed from a coaxial cable, cut to the central conductor which is then bent through 90 degrees. This design allows easy optimisation of coupling radiation to the cavity.

To determine the ideal values for the parameters x and z in figure 2.5, the antenna can be modelled as a Linear Antenna using standard theory [11]. Consider the antenna illustrated in figure 2.6 where $I(z)$ is the current distribution along the antenna element and l is the length of the antenna.

It is not possible to model radiation intensity, $U(\theta, \phi)$, of the linear antenna with the Hertzian dipole, unless the antenna is electrically short, when $l << \lambda$. This means that the radiation intensity has to be solved for directly. By careful application of the standard theory,

it can be shown that for a centrally driven dipole antenna the radiation intensity is given by [11]

$$U(\theta, \phi) = \frac{\eta k^2}{32\pi^2} |F_z(\theta)|^2 \sin^2 \theta \tag{2.7}$$

where η is the intrinsic impedance of the medium, $k = 2\pi/\lambda$ and $F_z(\theta)$ is the radiation vector defined as

$$F_z(\theta) = \int_{-l/2}^{l/2} I(z) e^{ikz\cos\theta} dz \tag{2.8}$$

As can be seen from equation 2.7, the radiation pattern is independent of the azimuthal angle ϕ and tends to concentrated at $\theta = 90.0°$. As the length of the antenna increases from 0.5λ to 1.25λ the radiation pattern concentrates at the plane of $\theta = 90.0°$. If the length of the antenna is increased beyond 1.25λ, the radiation pattern becomes multi-lobed, with the

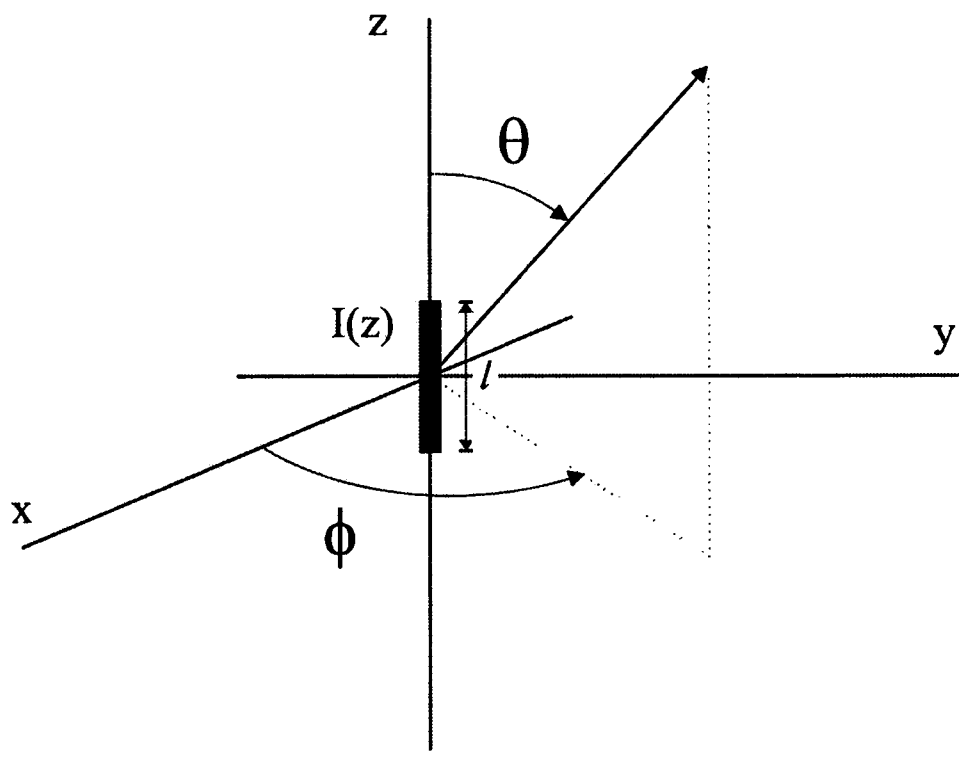

Figure 2.6: Linear Antenna - Length l

maximum at $\theta \neq 90.0°$.

Experimentally, in the ideal situation the radiation would concentrate about $\theta = 90.0°$. The actual antenna used is constructed from a co-axial central conductor, see figure 2.5. This means that in the above calculations where the ideal dipole antenna has a length of 0.5 to 1.25 λ, the corresponding length for the co-axial central conductor would be 0.25 to 0.63 λ [12]. This means that the length of the antenna used, z, should be set between 0.25 and 0.63 λ. The microwaves used in the experimentation ranged from 7 to 18 GHz, which correspond to a length for z of 2.7 to 1.1 cm. This lead to z typically been set to 1.0 cm, since most of the work was conducted at higher rather than lower frequencies.

To determine the value of x, one has to consider the interaction of radiation both emitted from the antenna and reflected from the mirror through which the antenna is mounted. To form a standing wave inside the cavity, these two waves need to interfere constructively. If the waves were to interfere destructively, then the standing waves, which are the TEM, would not form. For constructive interference the phase shift between the interfering waves needs to be $2n\pi$ for an integer n. Given that there is a phase shift of π on an external reflection, which is the case for the vacuum/aluminium mirror interface, the relationship of x to λ is given by

$$\begin{aligned} 2x &= \lambda\left(n+\frac{1}{2}\right) \\ x &= \frac{\lambda}{2}\left(n+\frac{1}{2}\right) \end{aligned} \tag{2.9}$$

This means x should set to either $\lambda/4$, $3\lambda/4$, etc. Experimentally x was typically set to 0.5 cm.

The Circuit

The microwave circuit used in the experimental collection has evolved within the group over several years. The developments have all aimed at increasing the signal to noise (S/N) ratio which can be recorded for any specific transition. The basic circuit can be seen in figure 2.7.

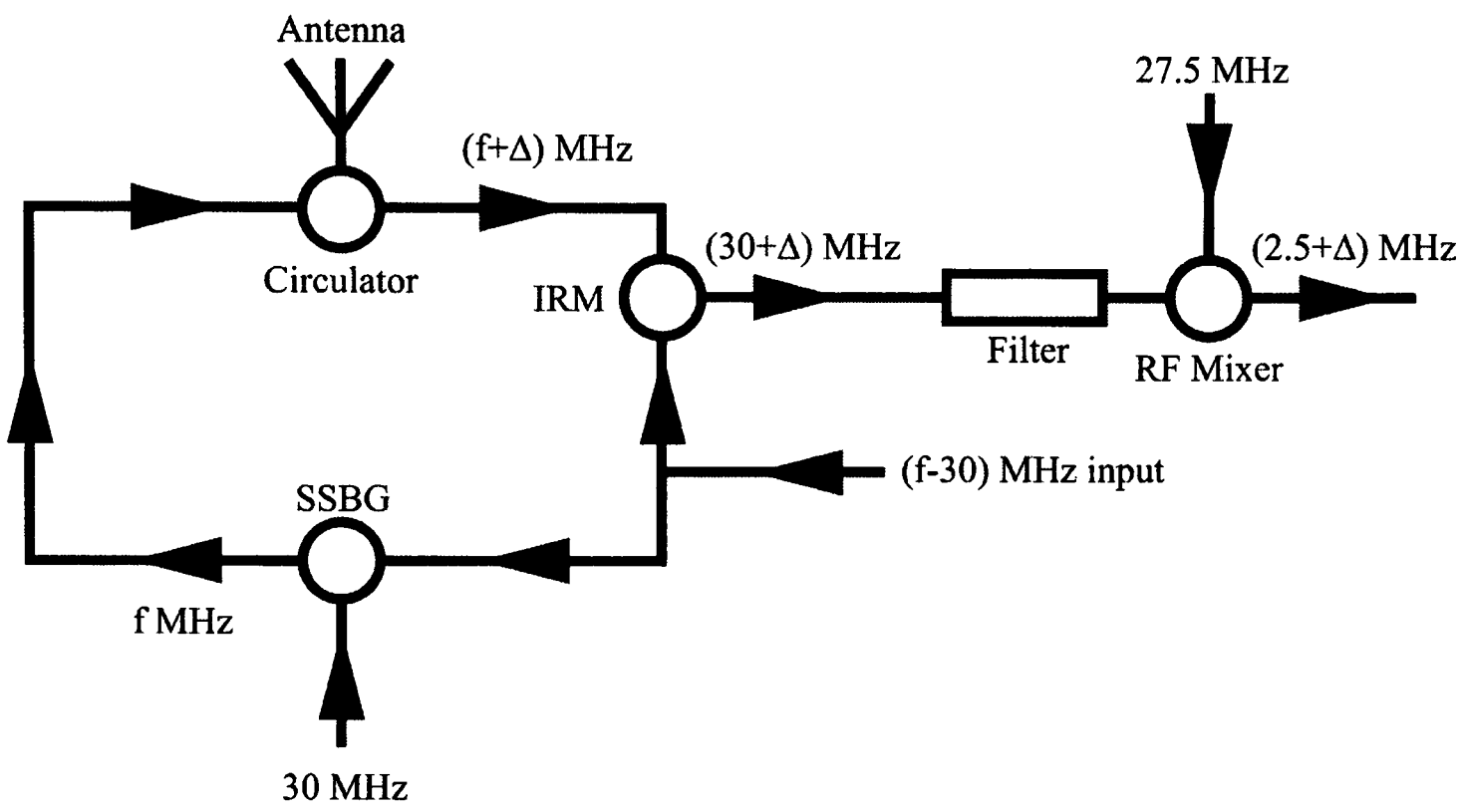

Figure 2.7: Schematic of Microwave Circuit. SSBG = Single Side-Band Generator, IRM = Image Rejection Mixer, RF = Radio Frequency

As can be followed in the schematic, the circuit starts with a short pulse (1 μs) of phase-locked, single frequency microwave radiation. The microwave radiation is generated by a tunable microwave synthesiser. The frequency of this radiation is set to $f - 30$ MHz, where f MHz is the frequency used in the actual experiment. The initial radiation is then mixed up with a source of 30 MHz to f MHz at the Single Side-Band Generator (SSBG) and transmitted into the chamber via the antenna. A SSBG mixes the two frequencies, one of microwave frequency and one of radio frequency, to give mainly a microwave frequency. The suppression of the difference, $f - 60$ MHz, is achieved by use of relative phase delays. The radiation within the chamber

pulse-broadens so that the species within the chamber will experience a range of frequencies of about a MHz. As the sample is exposed to a range of frequencies around f, it can absorb and subsequently emit at a frequency $f + \Delta$ MHz. Any species signal within the cavity which is present after the cavity ring-down has completed, is collected by the antenna and mixed down to be collected by the computer A-D converter. This mixing down process is done in two stages. Initially the FID is mixed with the original $f - 30$ MHz pulse at the Image Rejection Mixer (IRM) to give a resultant of $30 + \Delta$ MHz. An IRM mixes two microwave frequencies to give a radio frequency, favouring one combination over the other. The $30 + \Delta$ MHz signal is then filtered and amplified, and mixed with a 27.5 MHz pulse, to give $2.5 + \Delta$ MHz, which can be directly sampled by the computer A-D converter.

To observe the species signal one requires the S/N ratio to be as high as possible. The strength of the actual signal is determined the by the species present and the specific transition observed, see chapters 6 and 7. Thus, to improve the S/N ratio within the microwave circuit the level of the noise within the collection process must be reduced as far as possible. The level of noise is reduced in several ways. Firstly, the cavity provides the initial stage of filtering, by resonating with the frequencies within the supported modes and reducing noise from other frequencies. Secondly, the use of the IRM to mix the frequencies reduces the noise levels by favouring only one of the possible combinations, and eliminating possible contamination. Thirdly, in the collection process the 30 MHz filter only allows the passage of a narrow collection of frequencies around 30 MHz, again reducing noise from outlying signals. Finally, the final mixing to $2.5 + \Delta$ MHz, rather than just Δ MHz is to reduce thermal noise which tends to dominate at low frequencies. Also, since the centre is at 2.5 MHz, it is possible to determine the sign of the Δ MHz signal and hence not superimpose the noise at -Δ MHz onto the signal at Δ MHz.

The actual circuit used for the data collection of this thesis included several switches used to isolate the detection side of the circuit during the input period, a power amplifier and a

variable attenuator on the input side to vary the power input to the chamber. The full circuit can be seen in figure 2.8.

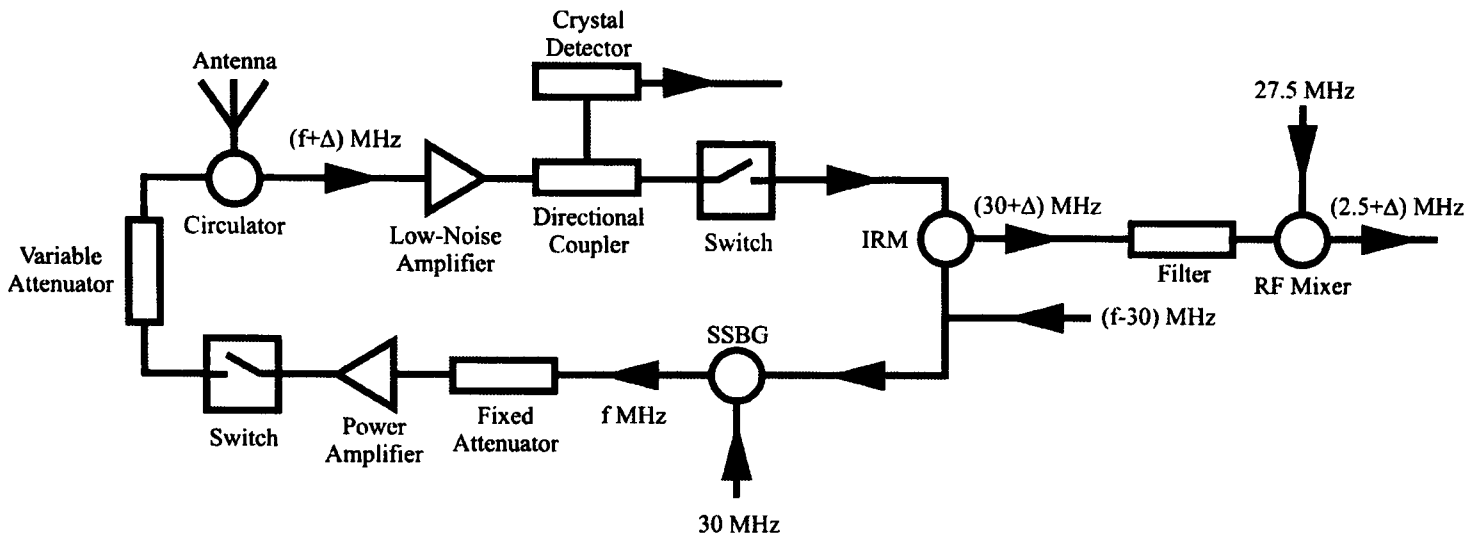

Figure 2.8: Full Microwave Circuit

2.2 Supersonic Jet

The study of weakly bond complexes has been made a practical pursuit by the development in the 1960s of the supersonic expansion technique. In this, the gas is expanded from a high pressure region, to a low pressure region, via a small aperture. The expansion leads to a narrowing of the distribution of velocities, a precipitous drop in temperature and a virtually collision free environment. The expanding gas becomes "trapped" in a thermal non-equilibrium state, by the lack of molecular collisions, with a high concentration of complexes due to the low temperature. The duration of the actual microwave experiment is typically 1 ms, which can be timed to occur while the density of the expanding gas is sufficiently high to allow for a strong species signal.

To allow independent control of sample density and of pre-expansion pressure a rare gas is used into which the sample gas is seeded. The use of a rare gas also contributes to the cooling of the sample, see section 2.2.1

2.2.1 Expansion

The supersonic expansion of gases has been studied extensively in the arena of aerospace propulsion, but for spectroscopy the approach is still largely empirical. During the experimental research of this thesis, the conditions in the expansion proved to be critical to the collection of relevant data. The conditions required for usable data collection are discussed below.

To cause the expansion, high pressure gas, typically 1.0 to 1.5 bar, is passed through a narrow aperture, typically 0.5 mm in diameter to a low pressure region, typically 1.0×10^{-5} mbar. For the expansion to be adiabatic, converting the random thermal motion of the high pressure gas into a directed mass flow with a narrow distribution of velocities, the aperture must be constructed such that

$$\lambda << d \tag{2.10}$$

where λ is the mean free path of the gas upstream of the aperture and d is the diameter of the aperture. If this inequality applies, then there will be a high number of collisions within the aperture. The value of λ is given by

$$\lambda = \frac{kT}{\sqrt{2}\sigma P_{ext}} \tag{2.11}$$

where k is the Boltzmann constant, σ is the collisional cross-section and P_{ext} is the pressure external to the cavity, the stagnation pressure.

The velocity distribution of the gas within the stagnation region conforms to a Maxwell distribution

$$f(\nu) = 4\pi \left(\frac{m}{2\pi kT}\right)^{\frac{3}{2}} \nu^2 exp\left(-\frac{m\nu^2}{2kT}\right) \tag{2.12}$$

which yields a mean speed of

$$\bar{\nu} = \left(\frac{8kT}{\pi m}\right)^{\frac{1}{2}} \tag{2.13}$$

In both equations 2.12 and 2.13 m is the mass of the gas molecule. A typical distribution of gas velocities against probability density is shown for both a high pressure gas and a supersonic expansion in figure 2.9. As can be seen in diagrammatic form in figure 2.9, the speed distribution for the supersonic expansion is considerably narrower than that of the same gas under thermal equilibrium.

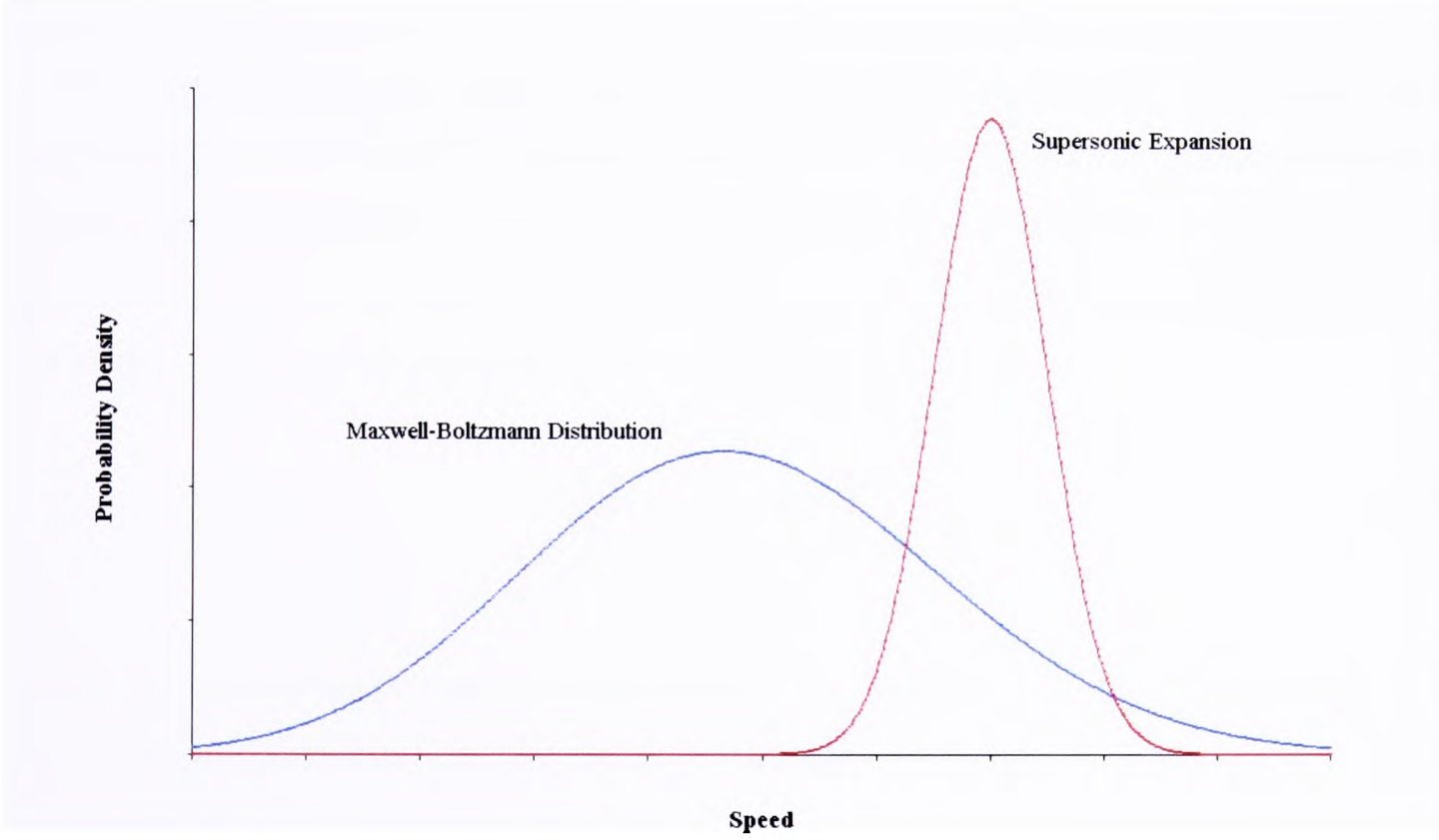

Figure 2.9: Speed distributions for a Maxwell-Boltzmann Distribution and a Supersonic Expansion

As the gas expands its speed distribution narrows and the temperature drops. The ratio of initial temperature, T_0, to the final temperature, T, is given by

$$\left(\frac{T}{T_0}\right) = \left(1 + \frac{\gamma - 1}{2} M^2\right)^{-1} \tag{2.14}$$

where γ is the ratio of heat capacities and M is the Mach number. The Mach number is defined as

$$M = \frac{\nu_o}{\nu_s} \tag{2.15}$$

where ν_o is the speed of the flow relative to the medium and ν_s is the speed of sound in the medium.

For a mono-atomic gas, which is used to drive the expansion, $\gamma = 5/3$. The Mach number can be modelled with a simple polynomial function based on the distance travelled downstream in multiples of the aperture diameter [13]. At the minimum constriction of the aperture, the gas become sonic, i.e. its speed reaches Mach number one, $M = 1$. The gas then expands into the chamber at a supersonic speed, $M > 1$, providing that

$$\frac{P_{ext}}{P_{int}} < \left(\frac{1}{2}(\gamma + 1)\right)^{\frac{\gamma}{\gamma - 1}} \tag{2.16}$$

where P_{int} is the pressure internal to the cavity, i.e. the pressure of the low pressure region. As the gas enters into the low pressure region, M increases, T decreases and $\nu \rightarrow \nu_\infty$, the limiting velocity of the gas. This can be calculated by

$$\nu_\infty = \sqrt{\left(\frac{2\gamma k T_0}{(\gamma - 1)m}\right)} \tag{2.17}$$

For argon, where $m = 40$ u, initially at room temperature, $\nu_\infty = 560$ ms^{-1}, whilst for the lighter neon, $m = 20$u, $\nu_\infty = 780$ ms^{-1}.

The whole expansion occurs within the "zone of silence". This is a region defined not including any shock waves that may develop as the high pressure gas interacts with the low pressure background gas. In front of the zone of silence a Mach disk shock wave develops. To locate the position of the shock wave one can estimate the extent of the zone of silence, x_m by using the formula

$$\frac{x_m}{d} = \frac{2}{3}\left(\frac{P_{ext}}{P_{int}}\right)^{\frac{1}{2}} \tag{2.18}$$

If, $d = 0.5$ mm, $P_{ext} = 1.0$ bar and $P_{int} = 1{\times}10^{-5}$ mbar, one obtains $x_m \approx 3$ m. This approximate extent of the zone of silence is greater than the size of the Fabry-Perot cavity, which is just less than 1 m at maximum extent, and hence the implications of the shock wave do not need to be considered.

Additionally, the shock wave will be diffuse. The shock wave extends over a region of the order of the mean free path, λ, so it is possible that the background molecules may pass through the shock wave, and interact with the expansion. However, this interaction will only cause an attenuation of the expansion, and hence the effect on the S/N ratio will be minimal.

Within the expansion the temperature and density both decrease until the density is so low that the gas can be considered to be in free molecular flow. Within the collision free zone there

can be no further drops in temperature due to a lack of molecular collisions. The temperature of the expansion within this region has been shown to be approximately 830 mK for argon and 310 mK for neon [14].

2.2.2 Expansion Modelling

To understand how the expansion favours the formation of weakly bound clusters, it is possible to calculate the thermodynamic properties of the expanding gas sample assuming ideal gas behaviour, negligible viscosity and negligible heat conduction. The equations used in the modelling need only be calculated downstream of the expansion since thermal information cannot be physically transmitted faster than the speed of sound. The calculations provide information on the temperature, the pressure and the Mach number of the expanding gas.

To accurately calculate the Mach number, M, one needs to solve various partial differential equations [15]. This level of accuracy is not required for the calculations undertaken in this thesis, and M can be modelled using a simple polynomial, as discussed above. Once the value of M is known it is possible to calculate all the other thermodynamic variables.

The variation of M with respect to $\frac{x}{d}$, where x is the distance from the nozzle and d is the nozzle diameter, is illustrated in figure 2.10. The values of M were calculated using the polynomial form

$$M = \left(\frac{x}{d}\right)^{\gamma-1}\left(C_1 + C_2\left(\frac{d}{x}\right) + C_3\left(\frac{d}{x}\right)^2 + C_3\left(\frac{d}{x}\right)^2\right) \tag{2.19}$$

where for a mono-atomic gas ($\gamma = 5/3$) C_1 = 3.2320, C_2 = -0.7563, C_3 = 0.3937 and C_4 = -0.0727 [13] The resulting calculations of temperature and density are illustrated in figures 2.11 and 2.12. These calculations were performed with an initial temperature of 300K and an initial gas density of 1000 in arbitrary units. Using the calculated temperature and density it is

possible to determine the number of residual binary and ternary collisions at each point in the expansion. These residual collisions and other selected data from the illustrations are given in table 2.1.

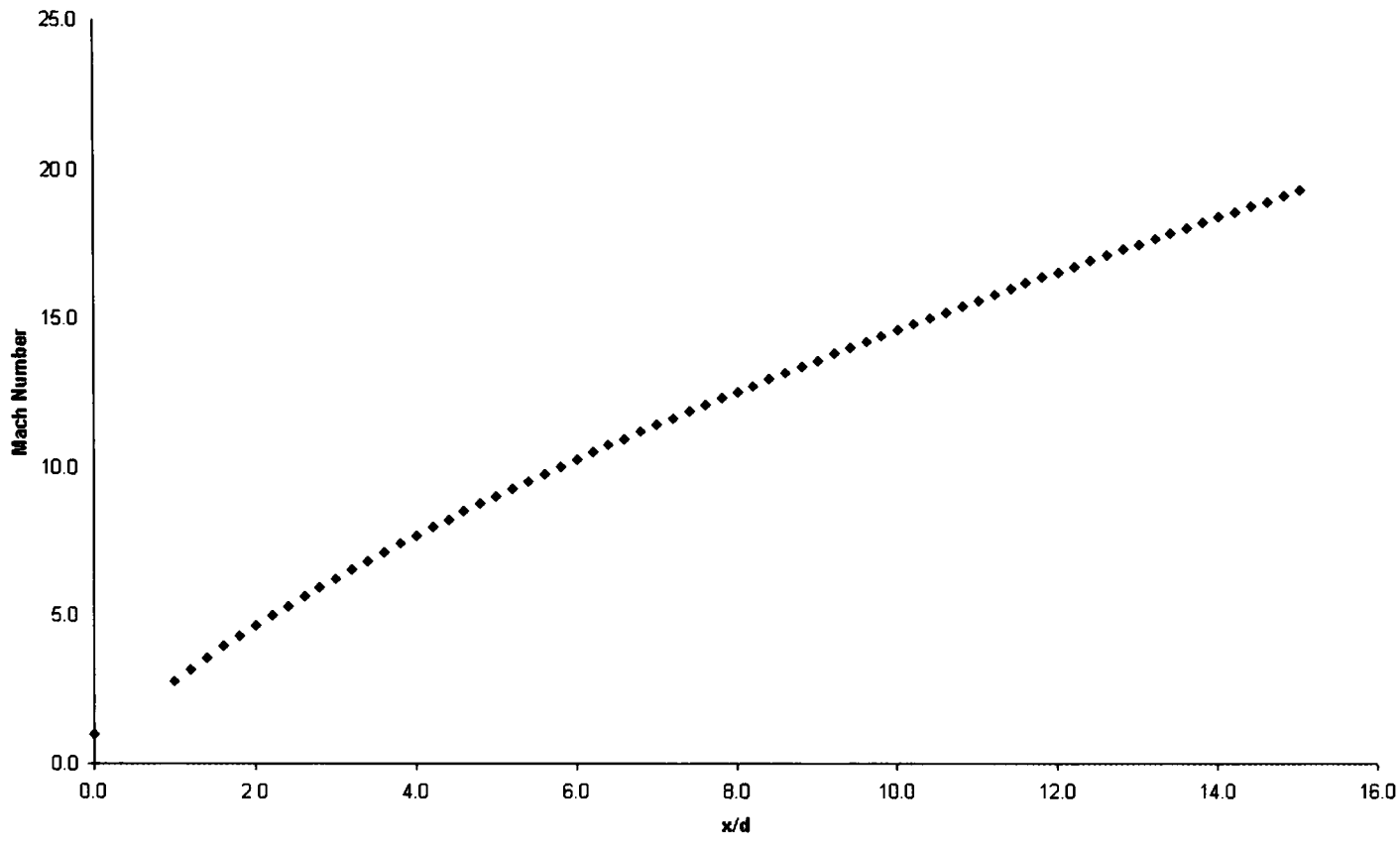

Figure 2.10: Variation in Mach number as expansion progresses

2.2.3 Cluster Formation

Supersonic expansions are used in the study of weakly bound complexes, since the thermal non-equilibrium conditions, as modelled above, lead to a high level of complex cluster formation. The formation of clusters is a result of the dropping of the sample's temperature and density. These two factors affect the rate of both the formation and destruction reactions of the clusters.

For any complex assuming that the formation occurs at a reasonable fraction of the collision

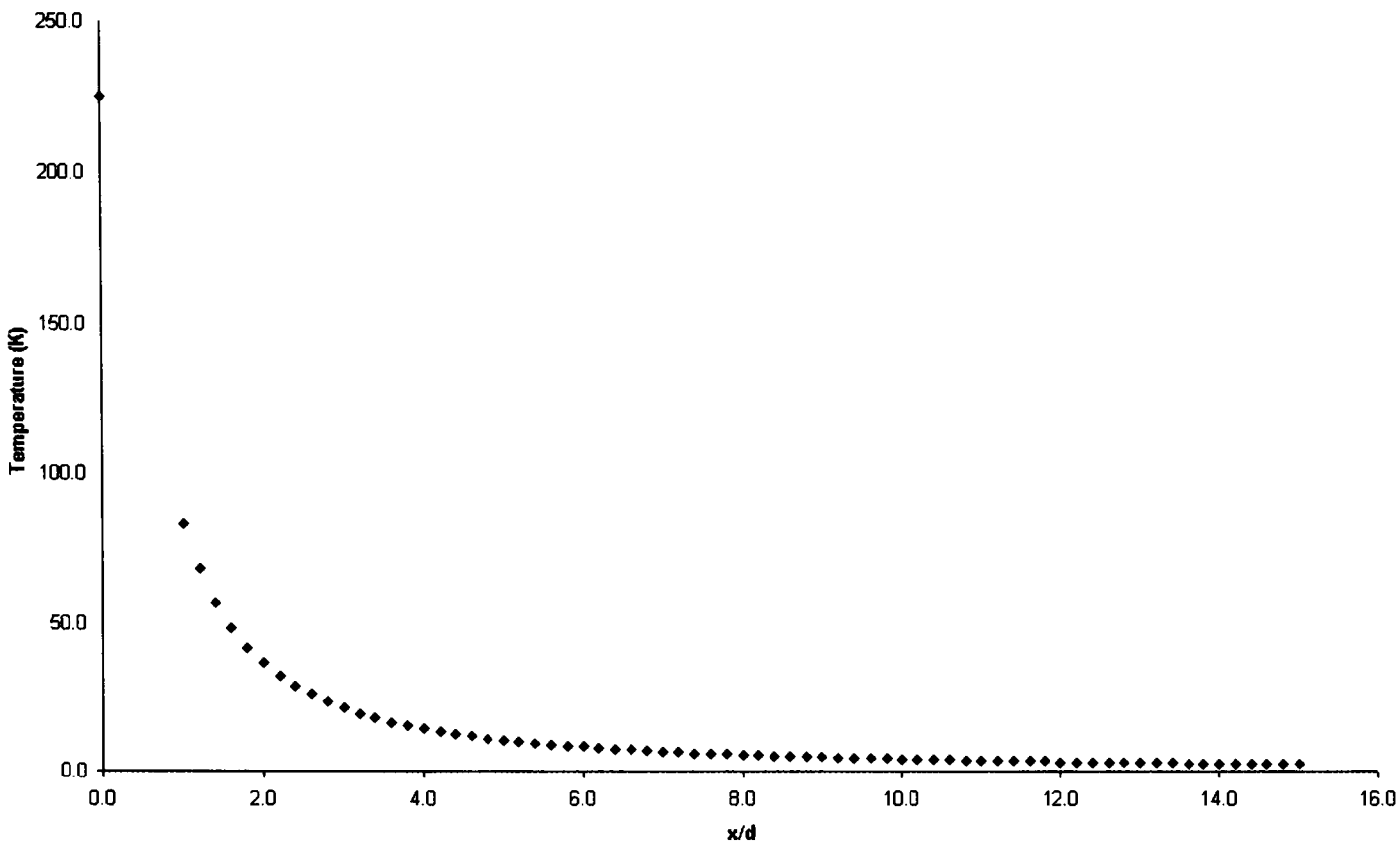

Figure 2.11: Variation in Temperature as expansion progresses

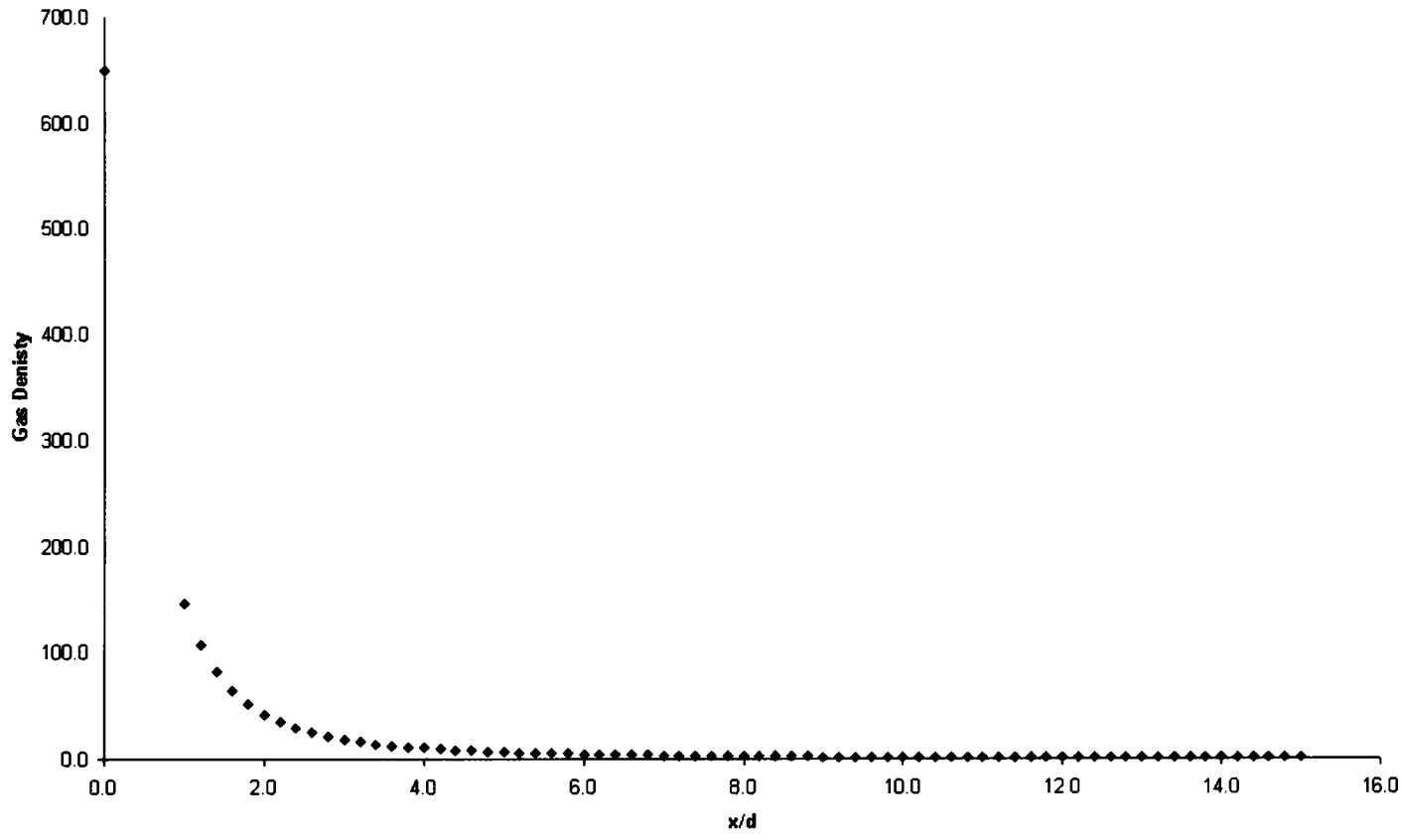

Figure 2.12: Variation in Gas Density as expansion progresses

$\frac{x}{d}$	Mach Number	Velocity (ms^{-1})	Temperature (K)	Density ρ/ρ_0	$\int_x^\infty Z_2 dx$	$\int_x^\infty Z_3 dx$
1.0	2.797	475.479	83.176	145.988	-	-
1.2	3.199	491.832	68.005	107.927	311.558	1.186×10^{-1}
1.4	3.587	503.644	56.728	82.227	237.295	6.724×10^{-2}
1.6	3.961	512.435	48.161	64.322	186.833	4.063×10^{-2}
1.8	4.322	519.155	41.512	51.473	151.085	2.590×10^{-2}
2.0	4.672	524.413	36.250	42.003	124.869	1.724×10^{-2}
3.0	6.284	539.184	21.183	18.763	60.015	3.555×10^{-2}
4.0	7.727	545.748	14.353	10.465	35.859	1.160×10^{-3}
5.0	9.053	549.327	10.595	6.637	24.142	4.893×10^{-4}
6.0	10.291	551.534	8.265	4.572	17.518	2.427×10^{-4}
7.0	11.460	553.011	6.700	3.337	13.379	1.345×10^{-4}
8.0	12.574	554.059	5.586	2.541	10.606	8.083×10^{-5}
9.0	13.641	554.837	4.760	1.999	8.648	5.167×10^{-5}
10.0	14.669	555.433	4.125	1.612	7.209	3.466×10^{-5}
15.0	19.362	557.067	2.382	0.707	3.595	7.528×10^{-6}

Table 2.1: Data from modelled expansion. Nozzle diameter, d, set at 5×10^{-4} m. Final two columns give the residual number of binary and ternary collisions out to infinity respectively. Collisions calculated with atomic mass of 40 u, a radius for binary collisions of 4.0 Å , an inner and outer radius for ternary collisions of 4.0 Å and 5.0 Å

rate, and the subsequent destruction step is limited by the exponential factor of binding energy of the complex, $e^{-\epsilon/RT}$, then in the first few nozzle diameters from the expansion there will be a pseudo-equilibrium with any complex formation balanced by destruction. Therefore

$$A + B + M \rightleftharpoons AB + M$$

This equilibrium can be modelled with statistical mechanics. As the temperature of the expansion drops the thermal equilibrium starts to favour the production of the two-body complex. However, as seen in table 2.1, as the distance from the nozzle increases the number of 3-body collisions, required to form any two-body complex, drops off sharply. This drop in the 3-body collision rate leads to the favourable thermodynamics being hampered by the poor kinetics. These opposing forces lead to an optimal range of distances within which the complex is formed. This optimal range is within the first few nozzle diameters of the expansion.

For a gas sample at room temperature in thermal equilibrium, the concentration of dimer

clusters is relatively low. For Ar, the concentration of Ar_2 is 0.09% [16], which has a binding energy of 99.2 cm^{-1} [17]. As detailed above, lowering the temperature of the sample leads to the thermal equilibrium moving in favour of the dimers and higher clusters. With Ar, the formation of higher clusters such as Ar_3 and Ar_4, which have overall binding energies of 298 cm^{-1} and 597 cm^{-1} respectively [18], occurs under some expansion conditions. This *snow balling* effect is also seen in the case of hydrogen bonded complexes [19]. In these cases the high binding energy of the complex allows initial complex formation in high density regions of the expansion and additional subsequent collisions allow trimers, tetramers and pentamers to form.

The use of the supersonic expansion allows for the trapping of the gas in a thermal non-equilibrium state between the initial formation of the dimers and the formation of the higher order complexes which would otherwise take place at low temperatures. This trapping is possible due to the lack of collisions within the collision free zone of the expansion. The conversion rate from monomer to dimer/complex can be controlled by varying the initial conditions of the gas, such as the temperature, composition, the pressure and the actual sample and carrier gas used in the expansion, or by varying the nature of the expansion, see below.

2.2.4 Pulsed Nozzle

The technique of FTMS is inherently pulsed, as the gas sample has to be excited, the exciting radiation has to ring-down within the cavity and finally the FID has to be collected. Thus using a continuous gas flow does not circumvent the pulsed nature of the data collection. Due to limitations in the pumping speeds of the vacuum pumps, if a continuous rather than pulsed gas flow is used then the diameter of the expansion aperture needs to be narrower, or P_{ext} reduced, to allow for the same P_{int} pressure to be maintained. Given that cluster formation falls rapidly with reduction in P_{ext}, lowering P_{ext} will cause a significant lowering of complex formation. If a narrower aperture is used, whilst P_{ext} is held at the same level, then the expanding gas will

experience fewer collisions and the 3-body formation reactions will drop off more rapidly and hence a reduction in the complex concentration will be observed. Either of these adjustments will lead to a lower S/N ratio and a degradation in the spectra recorded.

For these reasons a pulsed nozzle was used. This device delivers the gas into the chamber in rapid and controllable pulses with minimum turbulence. Once the gas has been introduced to the cavity the microwave spectroscopy takes place, as detailed above, before the vacuum chamber is pumped down for the next collection.

The nozzle consists of a small aperture which is opened and closed with a rapid solenoid action. The pulse widths are typically set at 500 μs, with gaps between pulses typically of the order of 100 ms. A diagram of the nozzles used in the experimental work can be seen in figure 2.13.

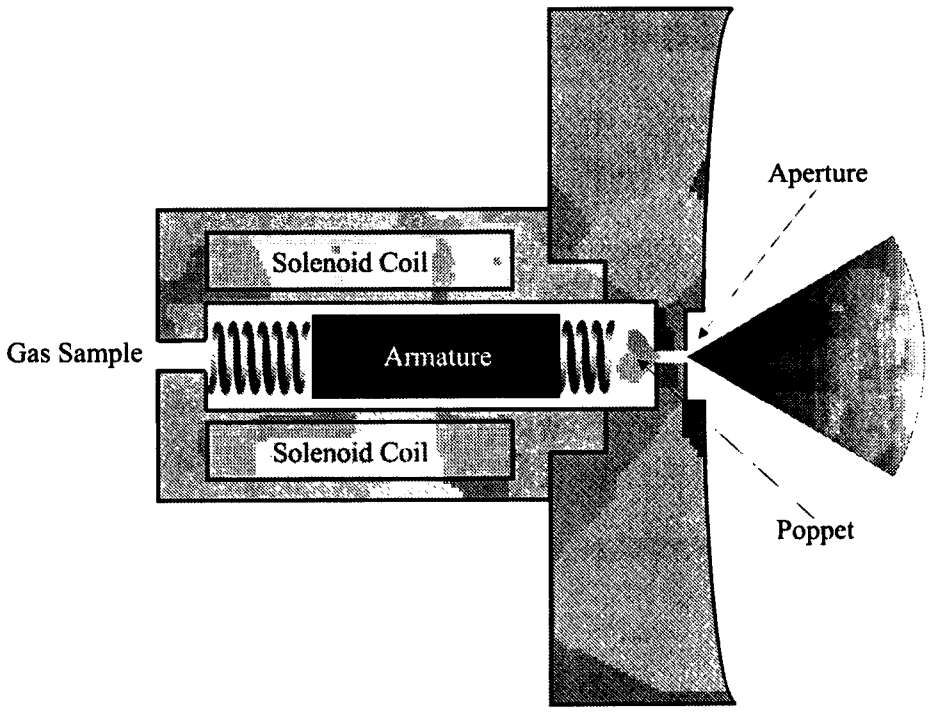

Figure 2.13: Pulsed Nozzle

2.3 Signal Production

The nature of the actual interaction of the microwave radiation and the complex species in the expansion has been studied extensively by Balle and Flygare [20]. Their work focused on the Fabry-Perot cavity, as used in this thesis, and the most relevant points are discussed here.

2.3.1 Absorption and Emission

The microwave pulse length used, τ_p, was set to 1-2 μs, which is sufficiently short that the translation of the molecules in the expansion is negligible within the pulse duration. The pulse contains a range of frequencies of approximately 1 MHz around the input frequency, due to the Fourier Transform of the input step wave. This creates a spatially dependent electric field, of strength ϵ. Within the cavity, when the pulse finishes the field strength decays with a characteristic decay time, $2\tau_c$.

For a polar species, with a transition between states a and b, with a electric-dipole transition moment $\mu_{ab} = \langle a|\mu|b\rangle$, which is resonant with the frequency range to which it is exposed, the interaction will lead to a change in the population difference between the states, and a bulk polarisation which oscillates at an angular frequency, the Rabi frequency, proportional to $\mu_{ab}\epsilon$, where μ_{ab} and ϵ are defined as above. The maximum polarization is achieved when [4]

$$\frac{\tau_p \mu_{ab} \epsilon}{2\hbar} = \frac{\pi}{2} \tag{2.20}$$

After the polarizing radiation decays the species emission can be detected. Equation 2.20 indicates that the strength of this signal is a function of the applied electric field, the electric-dipole transition moment, μ_{ab}, the pulse width, τ_p, and the size of the emitting population. In the case of weak signals, the strength can be improved by increasing the pulse width, and by increasing the electric field within the cavity. The emitted electric field strength within the

cavity is dependent on the cavity's Q-factor and the input power from the microwave circuit. With an input power of 100 milliwatts and a Q-factor of 1×10^4, it should be possible, with the correct pulse width, to observe transition dipole moments down to 0.030-0.025 Debye.

The emission from the species in question will have a decay time, the polarisation relaxation time, T_2, typically around 50 μs. The decay is a result of molecular collisions and the Doppler effect.

2.3.2 Line Shape

One might initially expect the line shape of a transition between two states to be a delta function. However, this is not the case. Observed line widths, quoted as the FWHH, are typically 10 to 20 kHz at the used microwave frequencies. The observed width of the lines determines the precision and resolution of the experiment. Since the integrated area of a transition is approximately constant, the sharper the line the greater the S/N ratio for a transition of the same intensity.

The factors which contribute to the line width are:

1. Natural Line Width

   The energy of the excited state of the transition is not accurately defined, as shown by the Heisenberg uncertainty principle. The uncertainty is inversely proportional to the lifetime of the state, $\Delta\mathrm{E}.\Delta t \approx \hbar$. The lifetime of the excited rotational state is determined by the rate of spontaneous emission which is inversely proportional to the Einstein coefficient A. Using the typical values for the coefficients, the natural line width for the microwave frequencies of interest is of the order of 1×10^{-5} Hz [21].

2. Pressure Broadening

   Hard molecular collisions in gas samples lead to perturbations in the energies of the species

present and hence lead to a broadening of the line width. Since the number of collisions is proportional to the pressure, this broadening effect becomes more considerable as the pressure of the sample increases. In the case of a supersonic expansion this effect is negligible, as the spectroscopic study takes place within the collision free zone which by definition has no molecular collisions [9].

It should be noted that soft molecular collisions in gas samples can lead to a change of phase of the wavefunction and hence reduce the in-phase emitted signal, leading to a lower S/N and a broader line width. A soft collision is one with a large collision cross-section. Clearly, the number of soft collisions vastly outnumbers the number of hard collisions due to relative size of their collision cross-sections.

3. Doppler Broadening

   When an emitting sample is moving in the direction of emission, a Doppler shift affects the frequency observed by a stationary observer. In a situation of random thermal movement, the emitting species will be moving in all directions relative to the observation and the line width for the transmission is broadened. In the supersonic expansion the molecular velocities are directed, but diverging, along the intermirror axis, and have a narrow distribution along the axis. This form of broadening is commonly the dominant form of line width broadening within the supersonic expansion. Typically the Doppler broadening for the microwave frequencies of interest is 1-10 kHz [21].

4. Residual Structure

   Splitting of a few tens of kHz are often observed, due to species specific factors. These factors can include methyl-rotational tunnelling [22], magnetic hyperfine and electric quadrupole interactions [2], nuclear spin-spin interactions [23] and the Zeeman effect [24], although these factors can be resolved in some cases and have proven critical in some spectroscopic assignments. In the specific case of open-shell molecules the Zeeman effect

is very important because of the interaction with the earth's magnetic field. For a magnetic field of roughly 0.5 Gauss, NO in the $^2\Sigma^+$ state is split to the order of 1.50 MHz [25]. These effect can be reduced with the use of Helmholtz coils, see section 2.6.3.

5. Instruments

   The quality of the instrument used in the detection process can have a significant effect on the line width. The most important instrumental effect in broadening the lines is often a lack of a monochromatic microwave source. The microwave radiation used during the experimental data collection was generated from a Wiltron 6769B microwave synthesiser which has an accuracy, from an external source, of 0.0025 Hz in the frequency ranges of the study [26]. This means that the synthesiser produced a very narrow, but not negligible, line width.

An important aspect of the experimental set up used, is that each signal is split into a Doppler doublet, see figure 2.14. This is a result of the emission been parallel or anti-parallel to the translation of the species. This splitting, $\Delta\nu$, difference of the two Doppler doublets, can be calculated using

$$\begin{aligned} \Delta\nu &= \nu_o\left(1+\frac{V}{c}\right) - \nu_o\left(1-\frac{V}{c}\right) \\ &= \nu_o\left(\frac{V}{c}+\frac{V}{c}\right) \\ &= \frac{2\nu_o V}{c} \end{aligned} \tag{2.21}$$

where ν_o is the frequency of the transmission, V is the speed of the gas and c is the speed of light. The speed of the gas expansion can be used as an indication of the composition of the gas.

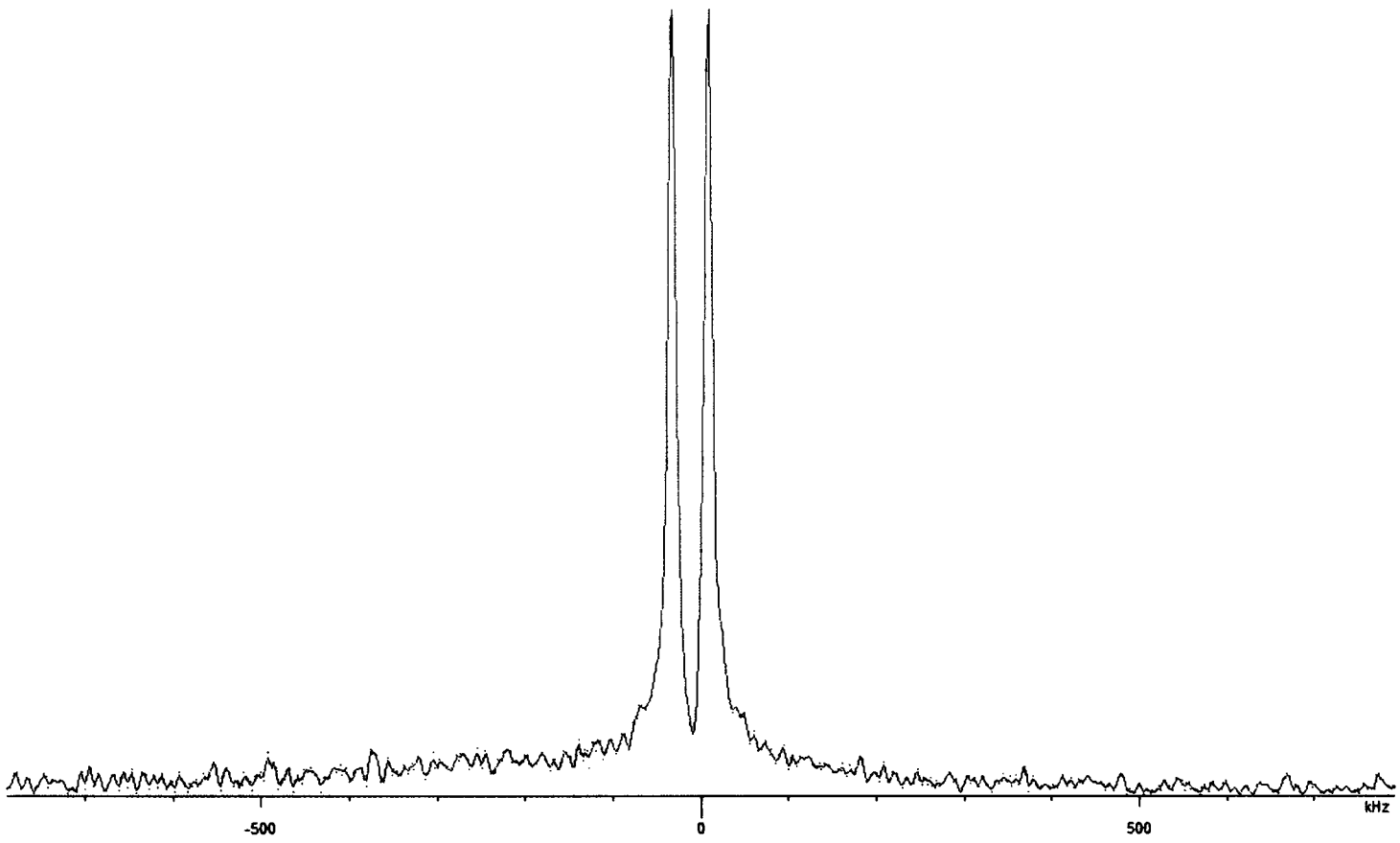

Figure 2.14: Typical Spectra

Species	Abundance	Transition (MHz)
$^{16}O^{12}C^{32}S$	9.4×10^{-1}	12,162.979
$^{16}O^{12}C^{34}S$	4.2×10^{-2}	11,865.662
$^{16}O^{13}C^{32}S$	1.1×10^{-2}	12,123.842
$^{18}O^{12}C^{32}S$	2.0×10^{-3}	11,409.708
$^{16}O^{13}C^{34}S$	4.7×10^{-4}	11,823.464
$^{16}O^{12}C^{36}S$	1.4×10^{-4}	11,599.372
$^{18}O^{12}C^{34}S$	9×10^{-5}	11,119.936
$^{18}O^{13}C^{32}S$	2×10^{-5}	11,382.125

Table 2.2: Abundances for various isotopomers of OCS

2.3.3 Sensitivity

The sensitivity of the spectrometer can be determined by the study of a stable species such as carbonyl sulfide (OCS) [27]. This molecule has a dipole moment of 0.715 Debye and the transmissions for $J = 0 \rightarrow 1$ for all the various isotopomers of the molecule all fall around 12 GHz. The use of a monomer, as opposed to a complex, means that the observations are not critical on the supersonic expansion. The natural abundances and transmission frequencies of the isotopomers of OCS are given in table 2.2.

The rarest isotopomer observed during initial sensitivity tests, whilst studying NO-O_2, was $^{16}O^{12}C^{36}S$, which has a natural abundance of 1.4×10^{-4}.

This compares reasonably to the other observations of the group, which recorded the signal of $^{16}O^{13}C^{34}S$ in 1997 [28] and $^{18}O^{12}C^{34}S$ in 2004 [6]. As each specific dipole moment requires specific optimisation, once $^{16}O^{12}C^{36}S$ had been observed no further time was spent optimising for OCS.

2.4 Signal Processing

The signal recorded from the microwave circuit is in the form of a FID. This decay represents the rotational spectra in the time domain rather than the more understandable frequency domain. To convert the FID to a frequency spectrum a Fourier Transform can be used. The various processes that the original FID is subjected to are detailed below.

2.4.1 Free-Induction Decay

The detection microwave circuit, see section 2.1.2, mixes the output of the cavity to $2.5 + \Delta$ MHz. The observed range of the final detection electronics covers the range of 0 to 5 MHz, which is sampled at a 10 MHz rate. Since the strongest signals decay with a maximum half-life

of approximately 100 μs, 4096 samples covering 409.6 μs will encompass the decay of even the strongest FID signals.

A typical recorded FID can be seen in figure 2.15. The Doppler doublet, which is always present for genuine signals, is seen in the FID by the cyclical pattern of intensities. This pattern oscillates at the frequency of the doublet splitting and results from the beating of the two signals with their distinct frequencies.

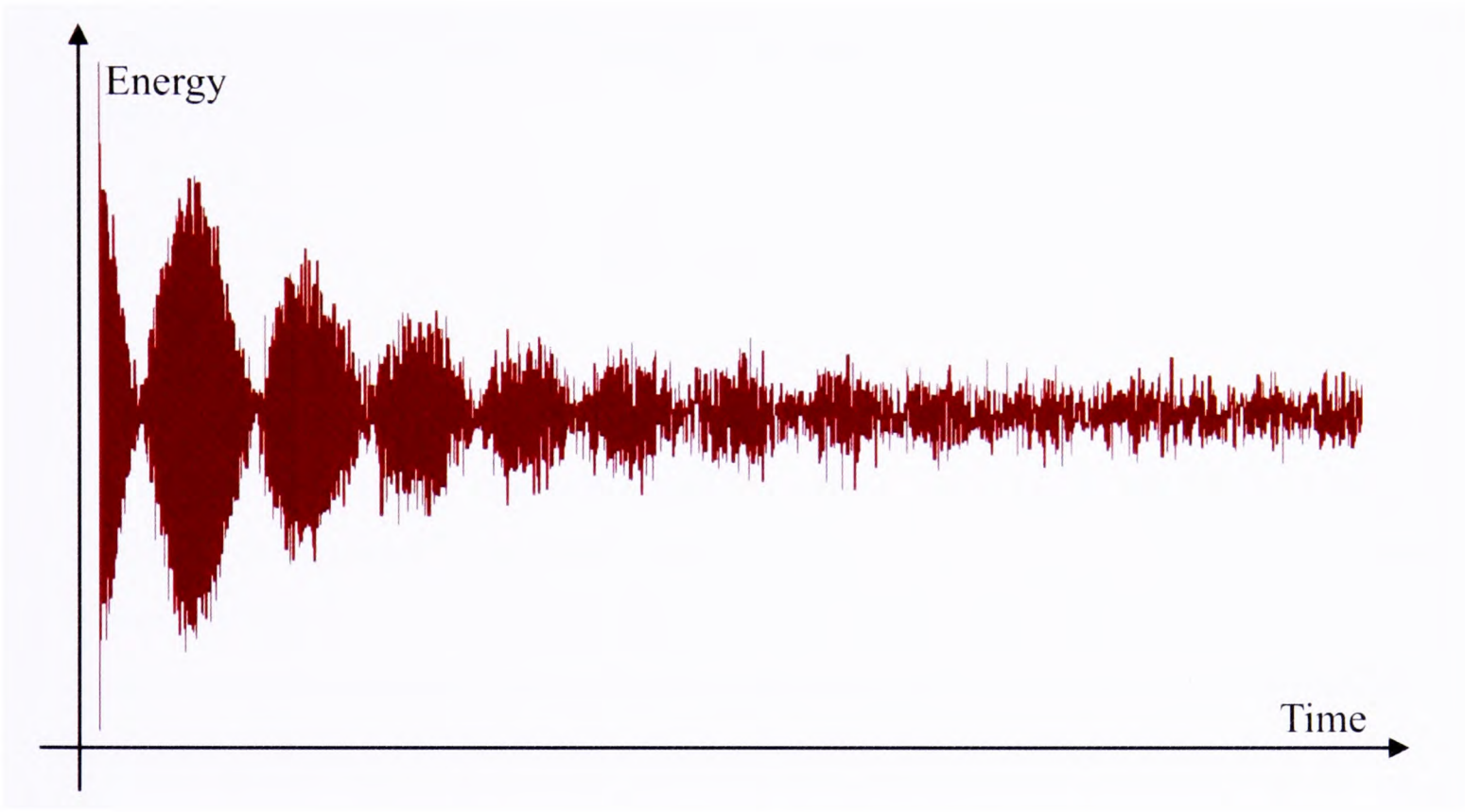

Figure 2.15: Typical FID, illustrating the Doppler doublet

The FID from separate collections are additive only if all the various collections are mutually in-phase. This condition is experimentally achieved by synchronising all the timing signals to a 5 MHz master clock and the data collection trigger to a 2.5 MHz clock. Even with these timings the separate collections can be dephased by mirror vibrations, so these are minimised at all times. This minimisation is accomplished by isolating the cavity from other vibrating

equipment in the laboratory.

2.4.2 Fourier Transform

To convert the time domain FID to the frequency domain spectra for further interpretation a Fourier Transform is used. In general a Fourier Transform converts a series of data points at equal time intervals into a linear combination of sine and cosine functions. The final spectrum is the coefficients of this linear combination.

Given a continuous function of time, $g(t)$, the transformation of this to a function of frequency, $f(\nu)$, is given by

$$f(\nu) = \int_{-\infty}^{\infty} g(t) e^{it\nu} dt \tag{2.22}$$

The algorithm that is used within the Fourier Transform Microwave Spectrometer Experimental Control and Data Acquisition (ECDA) software, see section 2.5, is a Fast Fourier Transform, developed by Tukey and Cooley in 1965 [29]. This is used as it reduces the number of computational steps from N^2 to $N\log N$ for N data points. The Fast Fourier Transform used is mathematically similar to that in equation 2.22 except that the data are discrete rather than continuous. Details on Fourier Transformations can be found in standard texts [30].

2.4.3 Data Processing

To increase the S/N ratio of observed transitions the raw FID is multiplied, within the ECDA software, by a function of time, $h(t)$, before it is transformed to the frequency domain. The purpose of this manipulation is to increase the importance of the most relevant section of the FID and reduce the importance of regions that contain little signal, but a large proportion of noise. Since the species signal will decay within a few multiples of its FID half-life after this point the recorded FID will mainly be noise. The simplest function form of $h(t)$ to accent the

most relevant sections of the FID would be

$$h(t < t_c) = 1, \quad h(t \geq t_c) = 0 \tag{2.23}$$

where t_c is the selected cut off point in the FID. The functional form of $h(t)$ can be varied, and it has been found that one of the most useful forms is that of a Gaussian

$$h(t < t_m) = e^{-((t-t_m)/k_1)^2}, \quad h(t \geq t_m) = e^{-((t-t_m)/k_2)^2} \tag{2.24}$$

where t_m is the centre of the Gaussian, and k_1 and k_2 are the decay times. If $k_1 = k_2$, then the Gaussian is symmetric. From varying the values of the variables, t_m, k_1 and k_2 within the ECDA software, it has been found that the greatest resolution of the signal is, in general, obtained with $t_m = 512$ μs, $k_1 = k_2 = 1024$ μs. These can be varied once the FID has been recorded if the default settings do not resolve the recorded signals well.

2.5 Experimental Controls

This section discusses the various controls used during the data collection process. The various controls have been tailored to increase the S/N ratio and to allow for more rapid data collection. The spectrometer controls affect the sample gas expansion, cavity tuning, circuit timings and automation.

Most of the experimental control is exercised by the use of ECDA software written by Ben Watson [6]. This communicates from the computer to electronic hardware via a multifunction PC card (Amplicon PC-30A). The microwave synthesiser is controlled with a different card, a GPIB interface card (National Instruments PCI-GPIB). Details on the ECDA software can be found in the thesis of Watson [6].

2.5.1 Gas Expansion and Mixing

The S/N ratio for a specific transition of a monomer species is normally very stable for a set P_{ext} as the signal is not a strong function of the kinetics of the expansion. Optimum conditions for the monomer signal are observed when the sample is seeded into a mono-atomic rare gas, to drive the expansion, in a ratio of a few percent. This low percentage of sample within the expansion reduces the number of reactive collisions and reduces unwanted clustering.

To allow the study of complexes the expansion is required to "trap" the system in a thermal non-equilibrium state, where there is a high concentration of complexes. Important experimental factors in the formation of the complexes are the value of P_{ext}, value of P_{int}, the composition of the mixture and the diameter of the aperture. These factors affect the total number of 2-body and 3-body collisions, see table 2.1.

Given that P_{int} and the nozzle aperture are fixed during the data collection process, variation of P_{ext} can be made to effect the relative rate of the formation and destruction reactions of NO-O_2. The optimal level for P_{ext} was found to be roughly 1.5 bar.

In addition to the expansion requirements for the formation of NO-O_2, the actual gas mixing arrangement "up-stream" of the nozzle is of critical importance. This is a result of the relatively rapid reaction of NO and O_2 to form NO_2. This oxidation problem was resolved in two separate ways, using an "active mixer" and a "passive mixer".

The initial solution involved the development of a 2-by-2 in-line active mixer. The mixer is illustrated in figure 2.16.

In the active mixer the mixing was accomplished in the following order. Firstly, the two sample gases, NO and O_2, are pulsed into the rare gas at independent ratios at the sub-slave

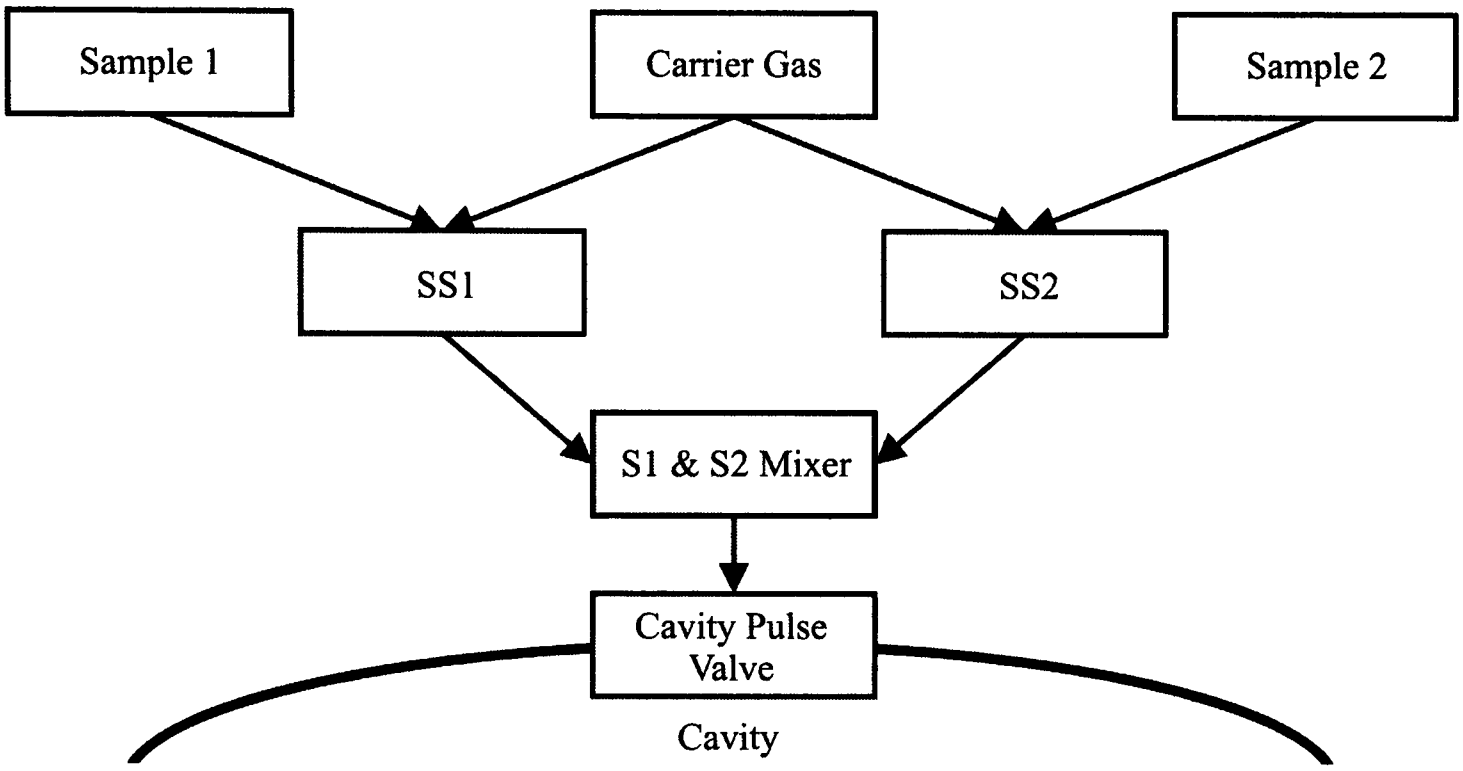

Figure 2.16: 2-by-2 in-line active gas mixing rig. SS1 = Sub-slave valve One, SS2 = Sub-slave valve Two, S1 = Slave One valve, S2 = Slave Two valve

valves. These valves are the same type of solenoid pulse valve used at the cavity valve. The sample gases are held at a higher pressure than the rare gas to control the direction of flow across the sub-slave valves. Secondly, the two seeded gas mixtures are then passed into a mixing volume, 100 cm^3, to allow a uniform gas mixture to be obtained. Finally, the two seeded gases are then mixed at the slave valves, just prior to the pulse valve on the cavity. The volume between the slave valves and the cavity valve is kept as small as possible to allow a minimal time for the NO and O_2 to react to give NO_2. All the slave and sub-slave valves are controlled from the pulse of the cavity valve to stop the development of any pressure build ups upstream of this valve.

Experimentally it was found that the active mixer outlined above was unreliable due to the requirement that all five pulse valves pulsed simultaneously. To overcome these complications a second passive mixing unit was developed that was not subject to the same mechanical issues as the active mixer. This relied on using continuous flow of sample gases through narrow bore capillaries. This rig is illustrated in figure 2.17.

In the passive mixer the two sample gases are mixed into the rare gas stream via long narrow bore capillaries. Assuming Poiseuille flow of the sample gases via the capillaries, the volume flow is modelled by Poiseuille's formula

$$V = \frac{\pi \Delta p r^4}{8 l \eta} \tag{2.25}$$

where Δp is the pressure difference along the length of the capillary, l, r is the radius of the capillary and η is the viscosity of the sample gas. This model is based on the assumption of negligible sample compression. Using capillaries of 0.5 m in length and an inner diameter of 50 μm equation 2.25 was used to predict the ideal Δp values needed for the mixing ratio required.

Since the passive mixer had no moving parts it was not subject to the reliability problems of the active mixer. The only practical issue with the passive mixed is that the sample gases had to be filtered prior to entry to the capillaries to stop any blockages occurring. Once setup the passive mixer could be used continuously with little maintenance during the data collection process of the research.

2.5.2 Cavity Tuning

The cavity exhibits a high Q-factor, see equation 2.6, when the cavity is in resonance with the wavelength of the radiation in the chamber. If the frequency and the cavity are not in resonance the power is not coupled into the cavity and reflects straight out into the external detection circuit. If the frequency and cavity are in resonance, then the radiation will form standing waves with a cavity ring down. Experimentally this resonance condition is essential.

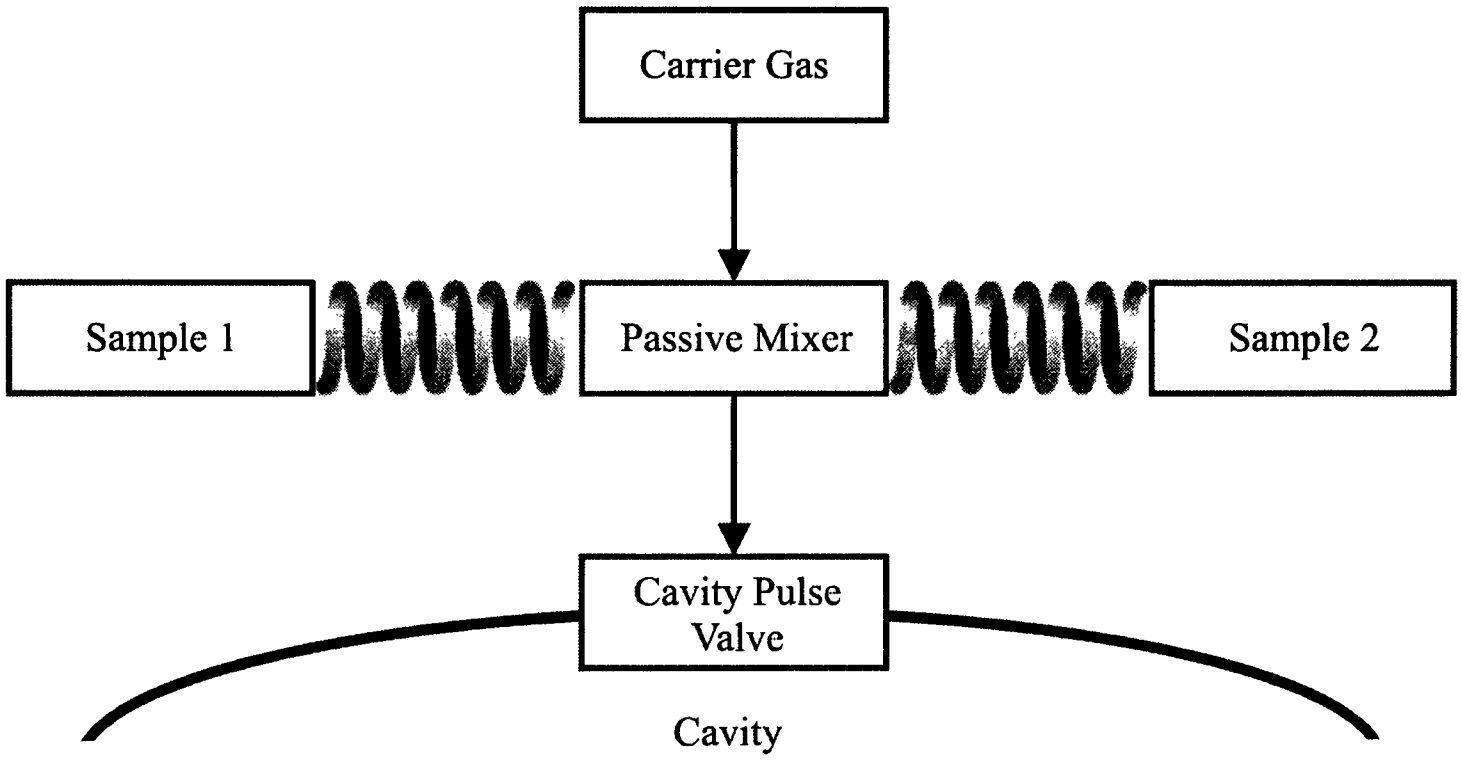

Figure 2.17: Passive gas mixing rig

The ECDA software controls the mirror separation via a stepping motor and can scan the synthesiser ± 200 MHz from the required frequency, thus allowing cavity resonances to be automatically established.

2.5.3 Timing

The pulse based experiment used is dependent on the ability to time accurately the repetition of the data collection stage. The timing issues for FTMS can be divided into two distinct groups, which have different accuracy requirements. The first group encompasses the timing during an experimental data collection cycle. The factors to be timed are the gas pulse into the chamber, the microwave pulse and the FID detection. The timing of these is of the order of a microsecond and therefore is controlled by in-house electronic hardware. The second group is the control triggers for the electronic hardware, which requires time accuracy of the order of a millisecond and therefore can be controlled by the ECDA software. Further details on timing issues are given by Watson [6]. The ECDA software has overall control of the experiment, and is used to conduct not only the actual data collection as a foreground collection, but also the background collections as explained below.

At the most basic an experimental run would consist of a trigger to the gas pulse system and a subsequent microwave sequence. The data collection would follow after the cavity had rung down. This is a foreground collection. These collections could be set to occur at a rate of 5-20 Hz, depending on the vacuum chambers pumping speed, etc. This arrangement would be subject to a 2.5 MHz signal leaking into the detection section of the microwave circuit and other coherent noise sources. The 2.5 MHz would be recorded as a strong single signal at the centre of the frequency range and would make the location of weak, yet genuine, signal impossible. By using background collections this 2.5 MHz signal, and other coherent noise, can be eliminated. Background collections are the same as the foreground collection, except that the gas pulse is not triggered. Since every additional collection introduces more thermal

noise into the spectrum, several background collections are averaged to reduce this effect. In practice ten background collections were used in this averaging process. The final recorded FID is the results of subtraction of the averaged background collections from the single foreground collection.

2.5.4 Automation

The ECDA software allows a large degree of automation in the experimental procedure. The software can be set to record a pre-determined number of collections at a set frequency, then shift the synthesiser to a new frequency, re-tune the cavity to the resonance and then repeat the data acquisition. This allows a frequency region of the spectrum to be automatically scanned and analysed subsequently.

2.6 Miscellaneous Apparatus

There are several pieces of additional apparatus that perform important tasks in allowing the FTMS experiment to be conducted. These are detailed below.

2.6.1 Gas-line

The gas lines were used to supply the sample and rare gases to the mixing units and then transfer the mixed gases to the chamber. The gas lines used were constructed from PTFE and stainless steel. Within the active mixer, see section 2.5.1, the mixing volumes were constructed from stainless steel cylinders. The sample and rare gases were regulated directly from the storage cylinders with pressures not exceeding 5 bar within the tubing as higher pressures can cause catastrophic failure.

2.6.2 Vacuum System

The chamber is of a stainless steel construction measuring 95 × 42 × 42 cm. The chamber is accessible using a number of removal flanges. The mirrors are mounted internally, one of which is on a movable mount, controlled by the stepping motor, allowing the chamber to be brought into resonance with the selected microwave frequency. The gas is introduced through a small aperture in the centre of the movable mirror. The antenna is mounted centrally on the static mirror.

The vacuum within the chamber is maintained by a diffusion pump coupled to a rotary pump. The diffusion pump (Edwards Diffstak MK.2 250/2000) is mounted centrally under the chamber and has a pumping speed of 2000 dm^3s^{-1}. The rotary pump (Trivac D40B) is connected to the diffusion pump and has a pumping speed of 10 dm^3s^{-1}. This combination can evacuate to 1×10^{-6} mbar with the running pressure normally set at 4.0 - 7.0×10^{-5} mbar.

2.6.3 Helmholtz Coils

The Helmholtz coils, originally discussed in section 2.3.2, are primarily used to reduce the effect of the earth's magnetic field on the open-shell species within the chamber. The coils can be used to remove any other stray magnetic field to which the chamber maybe subject. The zero field region generated is of a limited physical extent. The coils counter the magnetic fields by applying a counter field which can be varied in the three mutually orthogonal directions.

The coils are constructed from three pairs of square tracks and are positioned on opposite sides of the vacuum chamber. These are mounted around the chamber parallel to the three axes. The two tracks for each axis are wired in series and connected to a constant current generator. The three generators are then adjusted to produce a zero field within a small spatial region of the chamber. The centre of the zero field is located along the intermirror axis, around 1-10 cm from the nozzle within the movable mirror. This position is selected since this is the volume where the actual molecule-radiation interaction occurs. The magnetic field can be

determined with a magnetometer, which allows for the positioning of the zero field. Even for the near non-magnetic Ar-NO, there is some effect as seen in figures 2.18 and 2.19, where the coils are respectively on and off. As can been seen the signal is more clearly defined in figure 2.18 where the doublet has an average signal width of 11.43 kHz and S/N ratio of 115, compared to a average signal width of 14.55 kHz and S/N ratio of 86 in figure 2.19. This reduction in signal width and increase in S/N ratio comes at the cost of losing the magnetic field hyperfine information.

Conclusion

Overall, the experimental setup used is very similar to that used by other research groups and previous members of the Howard group. The resonant cavity, see section 2.1.1, has been used extensively for many years. As has the technique of using a supersonic jet, see section 2.2. The signal processing has been conducted using the same software as previous group members, see section 2.3.

The main addition in to the experimental setup, during the study of NO-O_2, has being the development of the passive gas mixing rig, see section 2.5.1. This new mixing arrangement has proved reliable and once setup ran without any serious issues.

The experimental setup is under constant review and additions are discussed within the group at regular intervals, but the basic design remains the same.

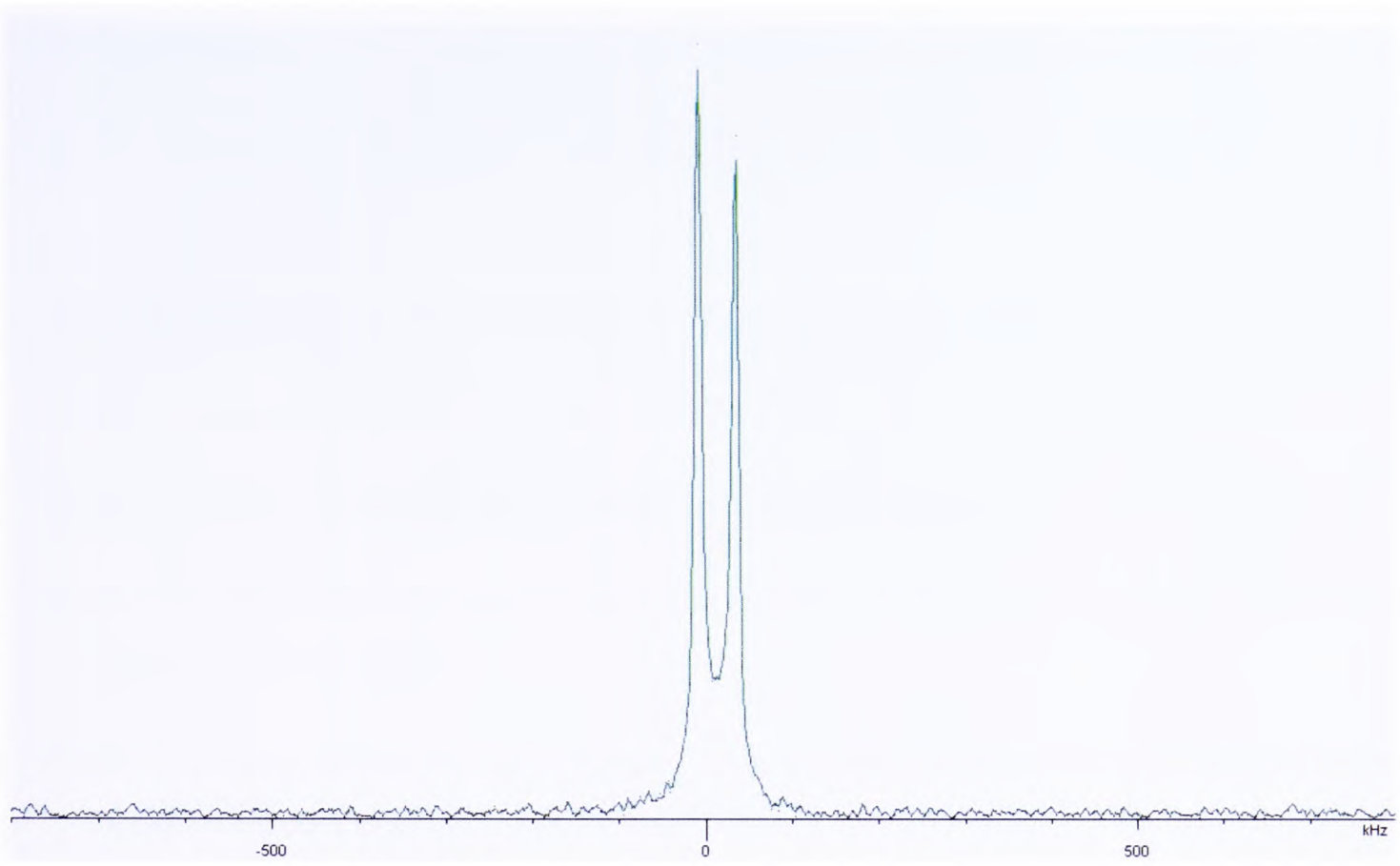

Figure 2.18: Ar-NO J = $\frac{1}{2} \rightarrow \frac{3}{2}$ F = $\frac{3}{2} \rightarrow \frac{5}{2}$. Helmholtz coils on

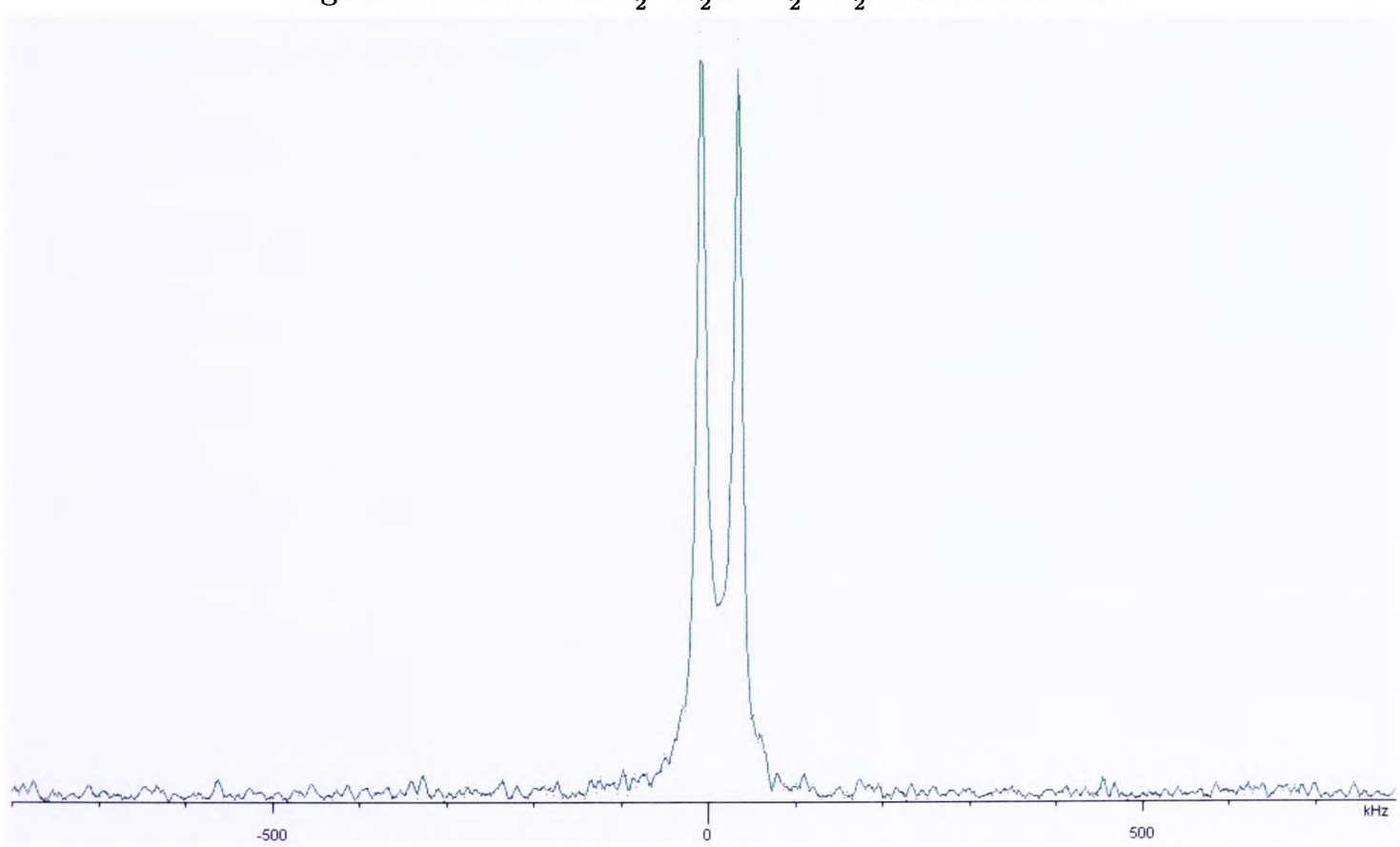

Figure 2.19: Ar-NO J = $\frac{1}{2} \rightarrow \frac{3}{2}$ F = $\frac{3}{2} \rightarrow \frac{5}{2}$. Helmholtz coils off

References

[1] T. J. Balle, E. J. Campbell, M. R. Keenan and W. H. Flygare, J. Chem. Phys. **71**, 2723 (1979)

[2] C. R. Dennis, C. J. Whitham and B. J. Howard, J. Chem. Phys. **115**, 1367 (2001)

[3] M. Schäfer, T. Ha and A. Bauder, J. Chem. Phys. **119**, 8404 (2003)

[4] N. F. Ramsey *Molecular Beams.* Oxford University Press (1969)

[5] P. D. A. Mills *Molecular Beam Investigation of Open-Shell Van der Waals Molecules.* D.Phil Thesis, Oxford University (1983)

[6] B. J. Watson *Microwave Spectroscopy of Open-Shelled Weakly Bound Complexes.* D.Phil Thesis, Oxford University (2004)

[7] M. S. Snow *Spectroscopic Investigation of Chiral and Induced Chiral Interactions.* D.Phil Thesis, Oxford University (2006)

[8] A. E. Siegman *An Introduction to Lasers and Masers.* McGraw-Hill, Inc (1971)

[9] A. E. Siegman *Lasers.* University Science Books (1986)

[10] B. L. Henke, E. M. Gullikson and J.C. Davis, Atomic Data and Nuclear Data Tables **54**, 181 (1993)

[11] S. J. Orfanidis *Electromagnetic Waves and Antennas.* ECE Department Rutgers University. http://www.ece.rutgers.edu/~orfanidi/ewa/ (accessed April 2007)

[12] P. Lorrain, D. P. Corson and F. Lorrain *Electromagnetic Fields and Waves.* W. H. Freeman and Company (1988)

[13] B. J. Howard *The Structure and Dynamics of Van der Waals Molecules.* Iberdrola Lectures, Consejo Superior de Investigaciones Cientificas (CSIC), Madrid (2001)

[14] M. Hillenkamp, S. Keinan and U. Even, J. Chem. Phys. **118**, 8699 (2003)

[15] U. G. Pirumov and G. S. Roslyakov *Gas Flow in Nozzles.* Springer-Verlag (1986)

[16] E. Buluggiu and C. Foglia, Chem. Phys. Lett. **1**, 82 (1967)

[17] P. R. Herman, P. E. LaRocque and B. P. Stoicheff, J. Chem. Phys. **89**, 4535 (1988)

[18] L. L. Lohr, Molec. Phys. **85**, 607 (1995)

[19] B. Ouyang, T. G. Starkey and B. J. Howard, *High-resolution microwave spectroscopy study of ring-structured trifluoroacetic acid and water complexes.* Manuscript submitted for publication.

[20] E. J. Campbell, L. W. Buxton, T. J. Balle, M. R. Keenan and W. H. Flygare, J. Chem. Phys. **74**, 829 (1981)

[21] J. M. Hollas *High Resolution Spectroscopy.* John Wiley & Sons (1998)

[22] L. Martinache, W. Kresa, N. Wegener, U. Vonmont and A. Bauder, Chem. Phys. **148**, 129 (1990)

[23] H. Qian, D. Seccombe and B. J. Howard, J. Chem. Phys. **107**, 7658 (1997)

[24] C. K. Jen, Phys. Rev. **74**, 1396 (1948)

[25] K. Takazawa, H. Abe and H. Wada, Chem. Phys. Lett. **329**, 405 (2000)

[26] *Series 67XXB Swept Frequency Synthesizer Operation Manual.* Wiltron Co. (1989)

[27] K. Tanaka, T. Tanaka and I. Suzuki, J. Chem. Phys. **82**, 2835 (1985)

[28] C. D. Dennis *High Resolution Spectroscopy of Open Shell Clusters*, D.Phil Thesis, Oxford University (1997)

[29] J. W. Cooley and J. W. Tukey, Math. Comput. **19**, 297 (1965)

[30] W. H. Press, B. P. Flannery, S. A. Teukolsky and W. T. Vetterling *Numerical Recipes.* Cambridge University Press (1987)

Chapter 3

Ab initio Calculations

"There will be little rubs and disappointments everywhere, and we are all apt to expect too much; but then, if one scheme of happiness fails, human nature turns to another; if the first calculation is wrong we make a second better: we find comfort somewhere"

Jane Austen

Introduction

With the development of computers capable of fast numerical calculations it became possible to consider using numerical quantum mechanical techniques to solve the Schrödinger equation of a molecule

$$\hat{\mathscr{H}}\Psi = E\Psi \tag{3.1}$$

All of the computational methods used are based on the Born-Oppenheimer (BO) and adiabatic approximations. The BO approximation states that due to the large difference in the mass of electrons and nuclei, the electrons respond instantaneously to any change in the nuclei positions and therefore the electronic wavefunction, Ψ_{el}, of the system can be solved for at a particular set of nuclei coordinates to give the Potential Energy Surface (PES) representing the energy of the wavefunction. This allows the overall wavefunction to be separated into two wavefunctions one for the electrons and another for the nuclei.

$$\Psi(\mathbf{r},\mathbf{R}) = \Psi_{el}(\mathbf{r};\mathbf{R})\Psi_{nuc}(\mathbf{R}) \tag{3.2}$$

where the electron and nuclei coordinates are given by $\mathbf{r}$ and $\mathbf{R}$ respectively. The electronic wavefunction is still parametrically dependent on the nuclei coordinates, but can be solved for each fixed nuclear geometry.

The adiabatic approximation is that the nuclear motion is restricted to a single PES. The combination of these two approximations usually give reasonable solutions to the Schrödinger equation. However, these approximations can fail if two or more solutions to the Schrödinger equation are too close together energetically. This complication does not occur within the work of this thesis, and will not be further considered. Relativistic contributions to the form of the Hamiltonian are also not considered.

Solutions for the electronic wavefunction generated without reference to experimental data are a result of *ab initio* methods. There are various *ab initio* methods available all with different advantages and disadvantages. The most commonly used methods are Hartree-Fock, Perturbation, Multi-reference, Coupled Cluster, Configuration Interactions and Density Functional Theory.

This chapter describes the theory of the relevant *ab initio* methods, the general factors to consider when undertaking any *ab initio* calculations and the actual programs and specific methods used in the prediction of energies, structures and rotational constants of NO-O_2 and NO_2-O_2.

3.1 Hartree-Fock Method

The most basic method used in *ab initio* calculations is the Hartree-Fock method. This is also the starting point for all the other methods described in this chapter.

Using the BO and adiabatic approximations, described above, the Hamiltonian operator, $\hat{\mathscr{H}}$, can be viewed as a combination of two separate operators, the first operating on the electronic wavefunction and the second operating on the nuclear wavefunction

$$\hat{\mathscr{H}} = \hat{\mathscr{H}}_{el} + \hat{\mathscr{H}}_{nuc} \tag{3.3}$$

where

$$\hat{\mathscr{H}}_{el} = \mathbf{T}_e + \mathbf{V}_{ne} + \mathbf{V}_{ee} + \mathbf{V}_{nn} \tag{3.4}$$

$$\hat{\mathscr{H}}_{nuc} = \mathbf{T}_n \tag{3.5}$$

where $\mathbf{T}_e$ is the electron kinetic operator, $\mathbf{T}_n$ is the nuclear kinetic operator, and the other terms,$\mathbf{V}_{ne}$,$\mathbf{V}_{ee}$ and $\mathbf{V}_{nn}$ represent the potential energy operators arising from the mutual interactions of the nuclei and electrons. Since the nuclear kinetic operator is assumed to operate only on the nuclear wavefunction, this operator can be factored out as solutions to the electronic wavefunction are functions of the nuclei's positions.

Therefore solutions are required for

$$\hat{\mathscr{H}}_{el}\Psi_{el}(\mathbf{r};\mathbf{R}) = E\Psi_{el}(\mathbf{r};\mathbf{R}) \tag{3.6}$$

For the sake of brevity following references to Hamiltonians and wavefunctions will, unless otherwise stated, be referring to the electronic Hamiltonian and the electronic wavefunction.

Analytical solutions for the energy in equation 3.6 can only be obtained for isolated H_2^+ and other isolated one electron systems. Solving this equation for other systems is accomplished by the use of numerical *ab initio* methods. The Hamiltonian operator ignores relativistic effects, requiring electron spin to be taken account of in an *ad hoc* manner.

The energy of an approximate wavefunction, $\tilde{\Psi}$, is given by the expectation of the Hamiltonian operator

$$E = \frac{\left\langle \tilde{\Psi} \middle| \hat{\mathscr{H}} \middle| \tilde{\Psi} \right\rangle}{\left\langle \tilde{\Psi} | \tilde{\Psi} \right\rangle} \tag{3.7}$$

where the denominator equals one for orthonormal wavefunctions.

To enable the construction of an approximate wavefunction one can make the orbital approximation. This approximation assumes that each electron can be assigned to a separate spatial wavefunction, an orbital.

Since electrons within the wavefunction are fermions, the total $\tilde{\Psi}$ is restricted in form to be antisymmetric with respect to electron exchange. One way to create valid antisymmetric

wavefunctions, is by the use of Slater Determinants (SD), Φ_{SD}.

SD are constructed from orthonormal single electron wavefunctions, ϕ_i, which are occupied by various electrons. The resulting single electron functions are a product of a spatial orbital function and a spin function. Each electron has a spin quantum number of 1/2. In an applied external field the electron's spin will either be aligned parallel or anti-parallel to the field. These two states are designated α and β. These states are orthonormal

$$\langle \alpha | \alpha \rangle = \langle \beta | \beta \rangle = 1 \tag{3.8}$$

$$\langle \alpha | \beta \rangle = \langle \beta | \alpha \rangle = 0 \tag{3.9}$$

The single electron wavefunctions used to construct the SD form the Molecular Orbitals (MO) of the system. A typical SD, with N electrons, has the form

$$\Phi_{SD} = \frac{1}{\sqrt{N!}} \begin{vmatrix} \phi_1(1) & \phi_2(1) & \dots & \phi_N(1) \\ \phi_1(2) & \phi_2(2) & \dots & \phi_N(2) \\ \dots & \dots & \dots & \dots \\ \phi_1(N) & \phi_2(N) & \dots & \phi_N(N) \end{vmatrix} \tag{3.10}$$

where $\phi_i(n)$ is the wavefunction for electron n in orbital i. The Hartree-Fock method assumes that only one SD is required to give a reasonable trial wavefunction. This assumption neglects the effects of electron correlation, see section 3.2. The other methods described within this chapter, Perturbation Theory and Multi Configurational Self Consistent Field, all account more accurately for this effect.

The detailed form of the Hamiltonian given in equation 3.4 is required to allow for the determination of the energy of a single SD. The four operators which comprise the overall

Hamiltonian have the following form [1]

$$\mathbf{T}_e = -\sum_i^N \frac{1}{2}\nabla_i^2 \tag{3.11}$$

$$\mathbf{V}_{ne} = -\sum_i^N \sum_a \frac{Z_a}{|\boldsymbol{R}_a - \boldsymbol{r}_i|} \tag{3.12}$$

$$\mathbf{V}_{ee} = \sum_i^N \sum_{j>i}^N \frac{1}{|\boldsymbol{r}_i - \boldsymbol{r}_j|} \tag{3.13}$$

$$\mathbf{V}_{nn} = \sum_a \sum_{b>a} \frac{Z_a Z_b}{|\boldsymbol{R}_a - \boldsymbol{R}_b|} \tag{3.14}$$

These have all been given in atomic units. Collecting these operators in terms of the number of electrons involved, one obtains

$$\hat{\mathscr{H}} = \sum_{i=1}^N \mathbf{h}_i + \sum_{i=1}^N \sum_{j>i}^N \mathbf{g}_{ij} + \mathbf{V}_{nn} \tag{3.15}$$

where

$$\mathbf{h}_i = -\frac{1}{2}\nabla_i^2 - \sum_a \frac{Z_a}{|\boldsymbol{R}_a - \boldsymbol{r}_i|} \tag{3.16}$$

$$\mathbf{g}_{ij} = \frac{1}{|\boldsymbol{r}_i - \boldsymbol{r}_j|} \tag{3.17}$$

Here $\mathbf{h}_i$ gives the Hamiltonian of electron i within the field of the nuclei and $\mathbf{g}_{ij}$ is the electron-electron electrostatic repulsion.

When evaluating the expectation value of equation 3.15 the final term is not a function of electron coordinates, and assuming that the SD are normalized

$$\langle \Psi | \, \mathbf{V}_{nn} \, | \Psi \rangle = V_{nn} \, \langle \Psi | \, \Psi \rangle = V_{nn} \tag{3.18}$$

By application of standard theory, as presented in the literature [1], [2], and with the use of *Lagrange multipliers*, it is possible to re-write Hamiltonian presented in equation 3.15 in terms of an effective one-electron operator, the *Fock operator*, $\mathbf{F}_i$ [1]

$$\mathbf{F}_i = \mathbf{h}_i + \sum_{j}^{N} (\mathbf{J}_j - \mathbf{K}_j) \tag{3.19}$$

where $\mathbf{h}_i$ is given in equation 3.16, $\mathbf{J}_j$ is the *Coulomb* integral and $\mathbf{K}_j$ is the *Exchange* integral. The *Coulomb* integral represents the classical repulsion between two charge distributions of electron 1 and electron 2, given by $\phi_1(1)^2$ and $\phi_2(2)^2$

$$\mathbf{J}_j \, |\phi_i(2)\rangle = \langle \phi_j(1) | \, \mathbf{g}_{12} \, | \phi_j(1) \rangle \, | \phi_i(2) \rangle \tag{3.20}$$

The *Exchange* integral is a purely quantum mechanical term with no classical equivalence or analogy

$$\mathbf{K}_j \, |\phi_i(2)\rangle = \langle \phi_j(1) | \, \mathbf{g}_{12} \, | \phi_i(1) \rangle \, | \phi_j(2) \rangle \tag{3.21}$$

The Fock operator describes the kinetic energy of the electron and its effective potential energy due to the attractive and repulsive interactions with the nuclei and other electrons in the system.

The final solution to the *Hartree-Fock equation* is given by

$$\mathbf{F}_i\phi_i = \sum_j^N \lambda_{ij}\phi_j \tag{3.22}$$

where λ_{ij} is a Lagrange multiplier. By uses of a unitary transformation on equation 3.22, the Lagrange multipliers can be diagonalized ($\lambda_{ij} \rightarrow 0$ and $\lambda_{ii} \rightarrow \epsilon_i$). This diagonalization gives a set of single electron wavefunctions, $\phi^{'}$, known as *canonical* MO

$$\mathbf{F}_i\phi_i^{'} = \epsilon_i\phi_i^{'} \tag{3.23}$$

The individual energies of each *canonical* MO can be determined by pre-multiplying by $\phi_i^{'*}$ and integrating. The Hartree-Fock equations give a set of pseudo-eigenvalue equations, with the Fock operator depending on all of the occupied MOs. From the above equations it is only possible to solve for a specific Fock orbital, once all the other orbitals are known. This paradox can be resolved by the use of an iterative approach, giving a set of functions called the *Self Consistent Field* (SCF) orbitals.

The energy for the system, under the Hartree-Fock method is not the sum of the MO energies as this counts the electron-electron repulsion twice. Also the energy is only an approximate value since the electron-electron repulsion is only taken in to account in an average manner, and hence this method is referred to as a *Mean Field* approximation. These limitations are due to the fact that the method only uses a single SD in the trial wavefunction.

None of the above places any restrictions on the form of the spatial orbitals used in the construction of the SD. If this unrestricted form is used in the calculation, then the method

is termed an *Unrestricted Hartree-Fock* (UHF) calculation. However, it is common to restrict the form of the spatial components in the SD to be the same function for each pair of α and β spins. This gives a *Restricted Hartree-Fock* (RHF) calculation. This approach is only valid for closed-shell systems, and hence of no relevance to NO-O_2 or NO_2-O_2. But, RHF can be extended to allow for open-shell systems with the *Restricted Open-Shell Hartree-Fock* (ROHF) method. The allowed states in these three methods are illustrated in figure 3.1

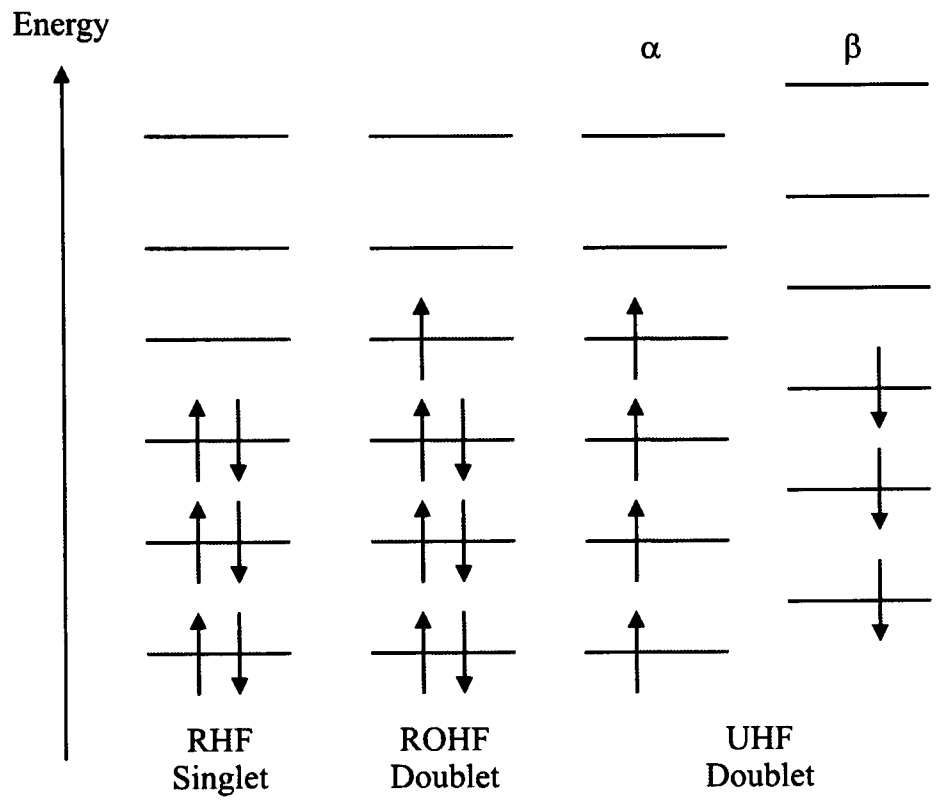

Figure 3.1: Spin states for Hartree-Fock wavefunctions

The RHF method can be used to give a usable approximation to the energy of the wavefunction around the equilibrium geometry, but this method is insufficient to model bond dissociations and the energetics of reactions. Taking the dissociation of H_2 as an example reaction, a RHF model will give a *dissociation catastrophe.* Here the final state is composed not of two hydrogen radicals, but a combination of an ionic and a covalent contribution on separation [3]. This clearly does not represent reality. The reason for this misrepresentation is that the spatial part of the two wavefunctions for the two bonding electrons, in RHF, is the same with equal proba-

bility of being on one hydrogen or the other. This leads to the ionic contribution on separation being allowed. If UHF is used to model the dissociation then this problem is avoided, but UHF does not give a state of definite overall spin. The UHF wavefunction for the separated state is said to suffer from *spin contamination* as it is composed of an unphysical mixture of a singlet and triplet spin state.

3.2 Electron Correlation Methods

In the Hartree-Fock method the actual electron-electron repulsion is replaced with an averaged repulsion. In the case of a large basis set, see section 3.5, this approximation leads to the calculated energy covering roughly 99% of the total energy, but does not account for the remaining 1%. This 1%, the difference between the Hartree-Fock limit and the real energy of the system being studied, is often critical in chemical processes and is termed the Electron Correlation (EC) [4]. The physically interpretation of the EC is that the electrons are actually correlated and are on average further apart than the simple Hartree-Fock solutions imply. The Hartree-Fock solution only allows the electrons to interact with an averaged electron field, but in reality the electrons interact with the instantaneous electron field. The EC accounts for this difference.

UHF accounts for the EC to a certain extent, by allowing electrons of different spin to occupy different spatial wavefunctions. In the case of RHF and ROHF, electron pairs in the same MO have a spatial overlap of one, whereas in different MO they have a spatial overlap of zero due to the orthonormal nature of the MO. There is still repulsion between electrons in different MO, despite there being a zero overlap, since the $\mathbf{g}_{ij}$ terms include the products of wavefunctions. Thus, the correlation between electrons can be both intra- and inter-orbital. Since the Pauli principle prevents two electrons in the same orbital having the same spin, intra-orbital EC is between electrons of opposite spins. This is termed *Coulomb correlation.* Inter-orbital EC can be between electrons of the same or opposite spins. The interaction between electrons of

the same spins is termed *Fermi correlation. Coulomb correlation* is the dominant form of EC [1].

Many methods have been developed in past decades that refine the Hartree-Fock method to take account of EC in more detail. These methods represent the same repulsion in different ways, but they should all ideally have the same four basic characteristics:

1. Continuous Potential Surface

   Given a particular geometry, the method should always produce the same energy, and give a continuous potential energy surface around that point.

2. Size Consistent

   When the method is applied to an ensemble of isolated systems, the calculated energies should be additive. For example, given a system composed of A and B

   $$E(AB) = E(A) + E(B)$$

   when the A-B separation tends to infinity. This requirement is critical for the calculation of binding energies as this value is calculated by subtracting the energies of the components from the energy of the complex.

3. Exact

   The method should be exact, equivalent to full *Configuration Interaction*, see section 3.4, when applied to a two electron system.

4. Variational

   The method should obey the variational principle. This principle is based on the variational theory which states that for any approximate wavefunction, $\tilde{\Psi}$, when compared to the true wavefunction, Ψ, it will have an energy greater than or equal to the that of Ψ. This theory only applies to the ground state wavefunction of each symmetry of the species.

Therefore by creating approximate wavefunctions containing various numerical coefficients, these can be adjusted to minimise the total energy of the $\tilde{\Psi}$ and therefore create a better approximation to the true wavefunction. This means that numerical techniques can be used to optimise solutions for Schrödingers equation by reducing their energy.

The advanced methods, such as Perturbation Theory and Multi Configurational SCF, all take account of EC by using multiple SD to construct the trial wavefunction, $\tilde{\Psi}$.

$$\tilde{\Psi} = a_o \Phi_{HF} + \sum_i a_i \Phi_i \tag{3.24}$$

Usually for a perturbative methods a_o is close to 1, but this is not the case for a Multi Configurational method. The values of a_i are calculated differently by the specific method.

The excited SD, Φ_i, are constructed by considering excitation of one or more electrons from their orbitals in the Hartree-Fock determinant, to formerly unoccupied, virtual MOs. Within any practical basis set, see section 3.5, there will be numerous virtual MO which can be swapped with the occupied MO in Φ_{HF}. The resulting determinants are classified with respect to the number of electrons that have been excited, i.e. *singly*, *doubly*, *triply* etc. Clearly, the number of excited electrons is limited to the number of electrons in the system. Examples of excited determinants, showing single, double and triple excitation from the Hartree-Fock configuration, are illustrated in figure 3.2.

3.3 Perturbation Theory

In perturbation theory multiple SD wavefunctions are used. The basic idea is that the exact solution to the problem is close to the Hartree-Fock solution. Within the context of solving the Schrödinger equation, the Hamiltonian is divided into a reference operator, $\hat{\mathscr{H}}_0$, which

represents the Hartree-Fock solution, and a perturbation, $\hat{\mathscr{H}'}$ operator. This method can be size consistent, allowing it to be used when calculating binding energies, but it is not variational.

Writing the true Hamiltonian as a sum of the reference and perturbation operators [2]

$$\hat{\mathscr{H}_0}\Phi_i = E_i\Phi_i \tag{3.25}$$

$$\hat{\mathscr{H}} = \hat{\mathscr{H}_0} + \lambda\hat{\mathscr{H}'} \tag{3.26}$$

where λ is a variable parameter which measures the strength of the perturbation to the reference Hamiltonian. This variable is used to track the order of the corrections made to the energy of the system. The solutions to the reference Hamiltonian, Φ_i, are a known completed set of orthonormal functions. The overall perturbed Schrödinger equation, becomes

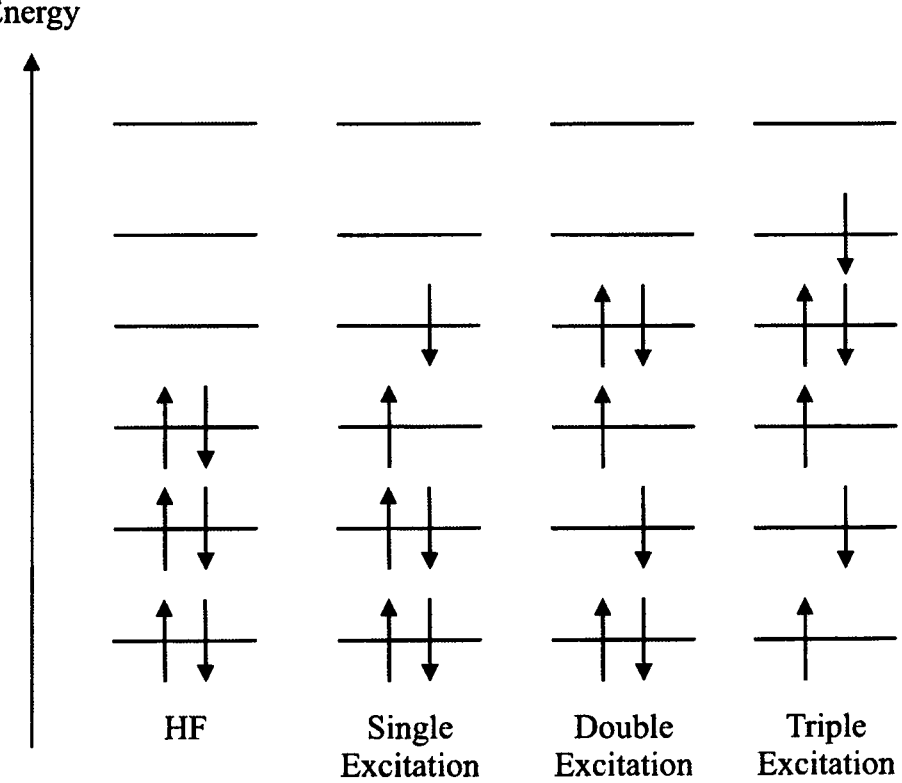

Figure 3.2: Excited SD generated from Hartree-Fock reference determinant

$$\hat{\mathscr{H}}\Psi = E\Psi \tag{3.27}$$

where the perturbed wavefunction and energy can be written as a Taylor series in powers of the parameter λ.

$$(\hat{\mathscr{H}_0} + \lambda\hat{\mathscr{H}'})(\lambda^0\Psi_0 + \lambda^1\Psi_1 + \lambda^2\Psi_2 + \ldots) =$$

$$(\lambda^0 E_0 + \lambda^1 E_1 + \lambda^2 E_2 + \ldots)(\lambda^0\Psi_0 + \lambda^1\Psi_1 + \lambda^2\Psi_2 + \ldots) \tag{3.28}$$

By making this expansion, and collecting terms in orders of λ, one obtains the *perturbation* equations

$$\lambda^0 \quad : \quad \hat{\mathscr{H}_0}\Psi_0 = E_0\Psi_0 \tag{3.29}$$

$$\lambda^1 \quad : \quad \hat{\mathscr{H}_0}\Psi_1 + \hat{\mathscr{H}'}\Psi_0 = E_0\Psi_1 + E_1\Psi_0 \tag{3.30}$$

$$\lambda^2 \quad : \quad \hat{\mathscr{H}_0}\Psi_2 + \hat{\mathscr{H}'}\Psi_1 = E_0\Psi_2 + E_1\Psi_1 + E_2\Psi_0 \tag{3.31}$$

$$\lambda^n \quad : \quad \hat{\mathscr{H}_0}\Psi_n + \hat{\mathscr{H}'}\Psi_{n-1} = \sum_{i=0}^{n} E_i\Psi_{n-i} \tag{3.32}$$

The solution for the n-order energy correction can be obtained by pre-multiplying by Φ_0 and integrating

$$\langle\Phi_0|\,\hat{\mathscr{H}_0}\,|\Psi_n\rangle + \langle\Phi_0|\,\hat{\mathscr{H}'}\,|\Psi_{n-1}\rangle = \sum_{i=0}^{n-1} E_i\,\langle\Phi_0|\,\Psi_{n-i}\rangle + E_n\,\langle\Phi_0|\,\Psi_0\rangle \tag{3.33}$$

$$E_0\,\langle\Phi_0|\,\Psi_n\rangle + \langle\Phi_0|\,\hat{\mathscr{H}'}\,|\Psi_{n-1}\rangle = E_n\,\langle\Phi_0|\,\Psi_0\rangle \tag{3.34}$$

Therefore, assuming an orthonormal relationship of Φ and Ψ, it can be seen that

$$E_n = \langle \Phi_0 | \hat{\mathscr{H}'} | \Psi_{n-1} \rangle \tag{3.35}$$

Equation 3.35 implies that to obtain the nth-order energy correction one needs to know the (n-1) order wavefunction correction. However, it can be shown that with the nth-order wavefunction correction, one can obtain the (2n+1) order energy correction [1].

To actually determine the wavefunction corrections, one expands the correction in terms of the set of functions generated by eigenfunctions of the unperturbed Schrödinger equation, Φ_i. This is *Rayleigh Schrödinger* perturbation theory [1]. For the first perturbation equation, in terms of λ^1

$$\Psi_1 = \sum_i c_i \Phi_i \tag{3.36}$$

$$(\hat{\mathscr{H}_0} - E_0) \left(\sum_i c_i \Phi_i \right) + (\hat{\mathscr{H}'} - E_1)\Phi_0 = 0 \tag{3.37}$$

By pre-multiplying equation 3.37 by Φ_0^* and integrating it can be seen that

$$E_1 = \langle \Phi_0 | \hat{\mathscr{H}'} | \Phi_0 \rangle \tag{3.38}$$

Thus to obtain the first order correction to the energy, one need to know the effect of the perturbed Hamiltonian on the unperturbed wavefunction. To obtain the first order correction to the wavefunction, one pre-multiplies equation 3.37 by any eigenfunction other than Φ_0^* and then integrates to give, for Φ_j^*

$$c_j = \frac{\langle \Phi_j | \hat{\mathscr{H}'} | \Phi_0 \rangle}{E_0 - E_j} \tag{3.39}$$

From equations 3.38 and 3.39 it is possible to determine the first order corrections to both the energy and wavefunction.

It is possible to extend the corrections beyond the first order, to the second, third etc order. However, the mathematics gets more and more complex as the level of correction is increased. Below are the relevant equations for the second order corrections

$$\Psi_2 = \sum_i d_i \Phi_i \tag{3.40}$$

$$(\hat{\mathscr{H}_0} - E_0)\left(\sum_i d_i \Phi_i\right) + \left(\hat{\mathscr{H}'} - E_1\right)\left(\sum_i c_i \Phi_i\right) - E_2 \Phi_0 = 0 \tag{3.41}$$

Thus with pre-multiplication of Φ_0^* and integration it can be seen that

$$E_2 = \sum_i c_i \langle \Phi_0 | \hat{\mathscr{H}'} | \Phi_i \rangle = \sum_{i \neq 0} \frac{\langle \Phi_0 | \hat{\mathscr{H}'} | \Phi_i \rangle \langle \Phi_i | \hat{\mathscr{H}'} | \Phi_0 \rangle}{E_0 - E_i} \tag{3.42}$$

With pre-multiplication of a function other than Φ_0^* and integration it can be seen that, for Φ_j^*

$$d_j = \sum_{i \neq 0} \frac{\langle \Phi_j | \hat{\mathscr{H}'} | \Phi_i \rangle \langle \Phi_i | \hat{\mathscr{H}'} | \Phi_0 \rangle}{(E_0 - E_j)(E_0 - E_i)} - \frac{\langle \Phi_j | \hat{\mathscr{H}'} | \Phi_0 \rangle \langle \Phi_0 | \hat{\mathscr{H}'} | \Phi_0 \rangle}{(E_0 - E_j)^2} \tag{3.43}$$

In the practical application of perturbation theory to the task of correcting for the EC of a system, the unperturbed Hamiltonian must be determined. The most common selection for

$\hat{\mathscr{H}}_0$ is a sum of Fock operators. This results in *Møller Plesset* (MP) perturbation theory [5]. Since the Fock operators count the electron-electron repulsion twice, the perturbation is the exact $\mathbf{V}_{ee}$ minus twice $\langle \mathbf{V}_{ee} \rangle$. This correction is in general not small compared to the current solution from the Hartree-Fock method, but it does have known solutions to the unperturbed state. With this selection of the perturbation

$$\begin{aligned}
\hat{\mathscr{H}}_0 &= \sum_{i=1}^{N} \mathbf{F}_i = \sum_{i=1}^{N} (\mathbf{h}_i + \sum_{j=1}^{N} (\mathbf{J}_{ij} - \mathbf{K}_{ij})) = \sum_{i=1}^{N} \mathbf{h}_i + 2 \langle \mathbf{V}_{ee} \rangle \\
&= \sum_{i=1}^{N} \mathbf{h}_i + \sum_{i=1}^{N} \sum_{j=1}^{N} \langle \mathbf{g}_{ij} \rangle \qquad (3.44) \\
\hat{\mathscr{H}}' &= \hat{\mathscr{H}} - \hat{\mathscr{H}}_0 = \mathbf{V}_{ee} - \sum_{i=1}^{N} \sum_{j=1}^{N} (\mathbf{J}_{ij} - \mathbf{K}_{ij}) = \mathbf{V}_{ee} - 2 \langle \mathbf{V}_{ee} \rangle \\
&= \sum_{i=1}^{N} \sum_{j>i}^{N} \mathbf{g}_{ij} - \sum_{i=1}^{N} \sum_{j=1}^{N} \langle \mathbf{g}_{ij} \rangle \qquad (3.45)
\end{aligned}$$

The zero order wavefunction is just the Hartree-Fock wavefunction and the zero order energy is just the sum of the occupied MO energies. The first order energy correction, E_1, is given by

$$E_1 = \langle \Phi_0 | \hat{\mathscr{H}}' | \Phi_0 \rangle = \langle \mathbf{V}_{ee} \rangle - 2 \langle \mathbf{V}_{ee} \rangle = - \langle \mathbf{V}_{ee} \rangle \qquad (3.46)$$

This correction removes the double counting of the electron-electron repulsion introduced at the zero order. The second order correction to the energy can be shown to only involve doublet excited determinants [1]. These determinants can be generated from two electrons been promoted from occupied MO, i and j, to virtual MO, a and b

$$E_2 = \sum_{i<j}^{occ} \sum_{a<b}^{vir} \frac{\langle \Phi_0 | \hat{\mathscr{H}}' | \Phi_{ij}^{ab} \rangle \langle \Phi_{ij}^{ab} | \hat{\mathscr{H}}' | \Phi_0 \rangle}{E_0 - E_{ij}^{ab}} \qquad (3.47)$$

This correction accounts for approximately 80-90% [1] of the EC. MP2 is a fairly inexpensive method, computationally speaking, for obtaining a correction for the EC, since the method only grows as M^5, where M is the number of basis functions used. If one extends to the third order, MP3, the energy correction recovers approximately 90-95% [1] of the EC, but the integrals grow as M^6. For the fourth order, MP4, the correction is approximately 95-98% [1], but at the cost of a integral growth of M^7. It is theoretically possible for the energies of various MP levels to oscillate about the limiting value of the system, the correction to ∞ order, due to the method being non-variational. However, this oscillation is rarely observed.

As with the Hartree-Fock method it is possible to use the MP methods for both closed-shell and open-shell systems. In the Hartree-Fock method the advantage of using UHF rather than RHF was that the UHF method takes account, to a degree, of the EC and results in a lowering of the wavefunctions energy. However, in the case of using Unrestricted MPn (UMPn), rather than Restricted MPn (RMPn) there is often an increase in the energy due to the effect of *spin contamination.* Given that RMPn cannot be used for an open-shell system, such as the complexes in this thesis, an alternative is to use ROHF as the reference wavefunction rather than the UHF. This selection of a different reference wavefunctions, leads to different equations from those derived above, but in practice the actual solutions obtained by using UHF or ROHF as the reference tend to be very similar.

3.4 Multi Configurational Self Consistent Field

As with perturbation theory, Multi Configurational Self Consistent Field (MCSCF) is an advanced method that tries to correct the Hartree-Fock wavefunctions and energy to take into account the EC. This method extends the description of the basic wavefunction, but does not perform the perturbative interactions over all of the MO as is done in the MPn method. MCSCF is an extended form of *Configuration Interaction* (CI). In CI the trial wavefunction is written

as a linear combination of determinants, where the expansion coefficients are selected so that the resulting energy is minimised. The MO for the excited SD are taken from the preliminary Hartree-Fock calculations. In MCSCF, in addition to the optimisation of expansion coefficients, the MO within the determinants are optimised to give an energy minimum.

For CI the excited SD are labelled with a subscript S, D, T etc to represent the level of the excitation of the determinant. The resulting trial wavefunction is given by

$$\Psi_{CI} = a_0\Phi_{SCF} + \sum_S a_S\Phi_S + \sum_D a_D\Phi_D + \ldots = \sum_{i=0}^{N} a_i\Phi_i \tag{3.48}$$

This is optimised to give a minimum energy, with the constraint that the overall wavefunction is normalized. This constrained optimisation is achieved, with the use of Lagrange Multipliers, in a similar manner to the optimisation in perturbation theory [1]. The expansion coefficients, in equation 3.48, can be solved for with the use of secular equations. Using $\mathscr{H}_{ij} = \langle\Phi_i|\,\hat{\mathscr{H}}\,|\Phi_j\rangle$, the secular equations in matrix form are given by

$$\begin{pmatrix} \mathscr{H}_{00}-E & \mathscr{H}_{01} & \ldots & \mathscr{H}_{0j} \\ \mathscr{H}_{10} & \mathscr{H}_{11}-E & \ldots & \mathscr{H}_{1j} \\ \ldots & \ldots & \ldots & \ldots \\ \mathscr{H}_{j0} & \ldots & \ldots & \mathscr{H}_{jj}-E \end{pmatrix} \begin{pmatrix} a_0 \\ a_1 \\ \ldots \\ a_j \end{pmatrix} = \begin{pmatrix} 0 \\ 0 \\ \ldots \\ 0 \end{pmatrix} \tag{3.49}$$

This matrix equation can be solved by diagonalizing the CI matrix, using methods detailed in standard texts [6]. The eigenvalues represent the CI energy, and the eigenvectors contain the coefficients a_j. The lowest eigenvalue corresponds to the ground state CI energy, the next is the first excited state and so on.

The elements within the CI matrix can evaluated by expanding the determinants as a sum

of products of MO and then the CI matrix can be expressed in terms of MO integrals. However, certain CI matrix elements are zero. Since the Hamiltonian operator, in equation 3.49, does not contain a spin operator, any elements connecting determinants of a different total spin are automatically zero. Such a zero element would be formed by the excitation of an α spin electron to a β spin. However, it is possible for the CI wavefunction to represent a mixture of spin states [7], if the Hamiltonian contains a spin-orbit operator. This problem can be removed by taking linear combinations of determinants to give proper spin eigenfunctions, called *Configurational State Functions* (CSF). For highly excited states the CSF can be a combination of several different determinants.

In CI calculations, one of the problems encountered is the fact that the number of CSF expands at a dramatic rate as the number of electrons and basis functions increases. For singlet CSF, the total number generated, Δ, for N electrons and M basis functions is

$$\Delta = \frac{M!(M+1)!}{(\frac{N}{2})!(\frac{N}{2}+1)!(M-\frac{N}{2})!(M-\frac{N}{2}+1)!} \tag{3.50}$$

Even for small systems with small basis sets this can lead to of the order of 10^9 singlet CSF. As a result of this rapid increase in the CSF that have to be included, it is common for the CI expansion to be truncated to a certain order. Truncation at the first level of excitation gives no improvement over the original Hartree-Fock calculation, and is therefore not used. Common points for truncation are at the second, third and fourth level of excitation. As more terms are added, reducing the level of truncation, the computation becomes more expensive and the resulting stepwise increase in accuracy of the EC is reduced. The EC correction follows the law of diminishing returns.

Within MCSCF solutions are obtained by an iterative process in a similar manner to SCF. In the original Hartree-Fock equations the MOs were optimised so that there was no change

in the energy on a variation in the MO. This process gives a zero in the first derivative of the energy with respect to the MO coefficient, but does not guarantee that this is an actual minimum. To determine that this is really a minimum rather than a maximum or a turning point, the second derivative is required to be positive. This second step of checking is rarely undertaken in SCF, but in MSCSF the wavefunctions are harder to converge and an expansion to second order is undertaken to help with the convergence.

MCSCF is rarely used purely for the purpose of recovering unaccounted EC. A better answer to unaccounted for EC is normally obtained by fixing the MO, not allowing them to relax as MCSCF does, and extending the number of levels of the CI excitation. However, MCSCF should be used when it is not possible to give a qualitatively correct description of the electron structure within the system with a single determinant. There are several examples of such systems, for example ozone [1]. With ozone there are two non-equivalent resonance structures which both equally well describe the electrons in the molecule. These resonance structures are illustrated in figure 3.3.

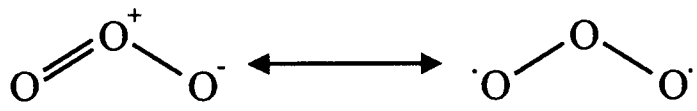

Figure 3.3: Resonance structures of ozone

Using MCSCF both of these resonance structures can be included in the basic wavefunction.

Within MCSCF, EC is explained with reference to RHF calculations. Using this reference, EC is composed of two components, the *static* and *dynamic* correlation [1]. The static correlation can be accounted for by allowing the orbitals to become partially occupied and not forcing them to be doubly occupied. The dynamic correlation is the remaining part of the EC. However, there is no means of accurately discriminating between these two effects. As an example consider the progression from RHF to UHF for ozone. The EC that is recovered as the method

changes is mainly static correlation. If one progresses further to MCSCF then, as more CSF are added, the additional EC recovered is mainly dynamic correlation.

The main problem with MCSCF is trying to determine which of the possible configurations are the relevant configurations to best describe the electron structure. There are two approaches that are commonly used, *Complete Active Space Self Consistent Field* (CASSCF) and *Restricted Active Space Self Consistent Field* (RASSCF). These two approaches are illustrated in figure 3.4. With CASSCF, the orbitals are divided into *active* and *inactive*. The inactive orbitals are either doubly occupied or totally virtual in all configurations selected. For the active orbitals a full CI is performed. As discussed above the number of CSF required for a full CI calculation for even a small system can be vast. This leads to using RASSCF as an alternative in some situations. Here the active orbitals are divided into three classes, RAS1, RAS2 and RAS3. RAS1 are doubly occupied in the original Hartree-Fock calculation, RAS2 are both occupied and virtual and RAS3 are totally virtual. For RAS2 orbitals a full CI calculation is undertaken and up to two electrons can be excited from RAS1 to RAS3. This reduces the number of CSF generated, but hopefully maintains the relative accuracy of the resulting energies and wavefunctions. The selection of the active orbitals in CASSCF, or RAS1-3 orbitals in RASSCF, is not an easy task. The use of MCSCF technique often requires an understanding of the underlying chemistry.

It is possible to couple the MCSCF method to that of MP2, or even MP3, to give a multi-reference basic wavefunction which it then couples to excited states with the use of perturbation theory [8]. Currently this coupling to a multi-reference wavefunction cannot be made to the more advanced Coupled Cluster method [3] in a problem-free manner. In general MP2 and MCSCF are the most commonly used combination.

3.5 Basis functions and sets

When undertaking any *ab initio* calculations one is expanding the unknown wavefunction, Ψ, in terms of a known set of functions, the basis functions. This expansion can be exact for a complete set of basis functions. In this case such a set would infinite and cannot be used for numeric calculations, thus a finite set must be selected. This is discussed in the next section.

3.5.1 Basis Functions

The two basic functional forms that are used to represent orbitals around each atom in *ab initio* calculations are *Slater Type Orbitals* (STO) and *Gaussian Type Orbitals* (GTO).

STO have the general form [7]

$$\chi_{\varsigma,n,l,m}(r,\theta,\phi) = NY_{l,m}(\theta,\phi)r^{n-1}e^{-\varsigma r} \tag{3.51}$$

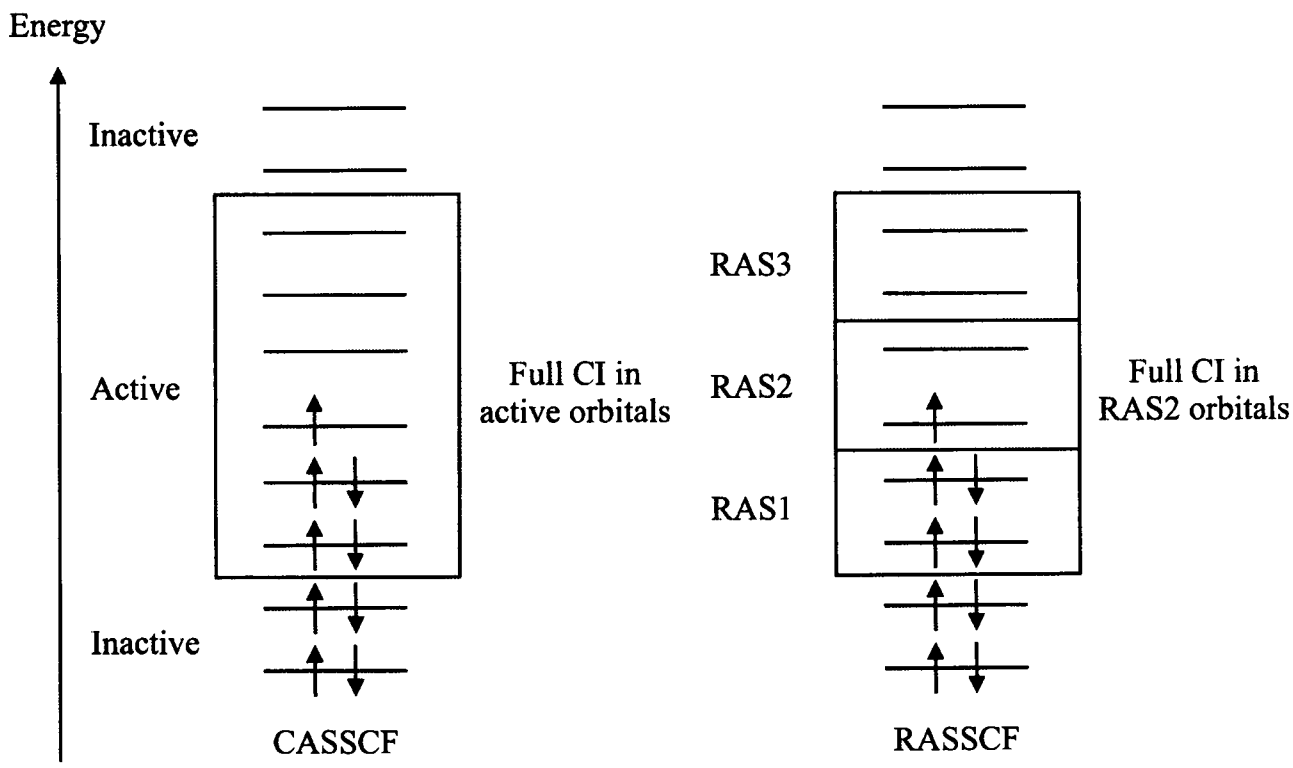

Figure 3.4: Excitation within the CASSCF and RASSCF approaches

where N is the normalisation constant and $Y_{l,m}$ is a spherical harmonic function. These are derived from the exact solutions to the hydrogen atom. They have the correct behaviour at large distances and near the nuclei. However, for computational reasons these are only used for atomic and diatomic systems where a very high level of accuracy is required.

GTO have the general form [7]

$$\chi_{\varsigma,n,l,m}(r,\theta,\phi) = NY_{l,m}(\theta,\phi)r^{2n-2-l}e^{-\varsigma r^2} \tag{3.52}$$

The r^2 term in the exponent in the GTO makes them inferior to the STO in that they have a zero gradient at the nucleus and do not represent the tail of the wavefunction as well as the STO. However, the functional limitations of the GTO can be reduced by taking linear combinations. As a rough approximation one requires about three times as many GTO to give the same accuracy as one STO. However, GTO are the most commonly used basis functions as the ease of integration of a GTO means that calculations can be performed more rapidly.

3.5.2 Basis Sets

The basis set is the collection of functions used for the wavefunction expansion. As a general rule the larger the basis set the more accurate is the expansion of the wavefunction and the calculated energy. A minimum basis set is one in which a minimum number of functions are included to accommodate the electrons of a neutral species. This initial set of functions can be extended by doubling, tripling, etc the number of functions of each type included in the set, to give the Double Zeta, Triple Zeta, etc type basis sets. It is possible to have a different number of duplications for the inner and outer valence orbitals, giving a split valence basis set. Another way of extending the minimal basis set is the inclusion of polarization functions. Polarization functions are used to polarize the existing functions in the system to give a better overall description of the MO. For example, s type orbitals are polarized with p type orbitals,

p are polarized with d and so on. It is possible to over polarize a basis set, which can lead to artefacts, and the basis set is said to be unbalanced. As a guide, to balance a basis set containing two p type orbitals, one would have to include one d type orbital, i.e. (n-1) functions of angular momentum (l+1) compared to n functions of angular momentum l. This means a basis set including 3s2p1d is balanced, whereas 3s2p2d2f1g is unbalanced.

Using GTO functions in the basis set can lead to a large number of functions being used and many coefficients being optimised to maintain accuracy. This computational issue can be reduced by using linear combinations of *primitive* GTO (PGTO) giving *contracted* GTO (CGTO). This contraction is particularly valid when applied to the inner orbitals, since these do not play a significant part in chemical bonding. The contraction is given by

$$\chi(CGTO) = \sum_{i}^{k} a_i \chi_i(PGTO) \tag{3.53}$$

The range of basis sets on commercially available *ab initio* packages is vast. The most regularly used include the Pople Style, Dunning-Huzinaga and the Atomic Natural Orbital basis sets.

The Pople Style basis sets include the STO-nG basis sets, which consist of n PGTOs for each orbital and the 6-311G basis set, which is a triple split valence basis, with the core orbitals formed from a contraction of 6 PGTO and valence orbitals split into three functions, represent by 3, 1 and 1 PGTOs. The 6-311G basis set can have diffuse functions added with diffuse s and p type orbitals added to the non-hydrogen atoms. This would be designated by 6-311+G. One can also add further diffuse orbitals, in the form of an s type orbitals on hydrogens. This would be designated by 6-311++G. Polarizations functions can also be added, to both the non-hydrogen and hydrogen atoms. These are denoted by listing the functions in parentheses after the G.

The Dunning-Huzinaga basis sets are based on CGTO. These basis sets are labelled with respect to their zeta, for example VDZ for a double zeta basis set, and VTZ for a triple zeta basis set. The contraction schemes used within the polarized VDZ basis sets, cc-pVDZ, is 6, 1, 1, 1 for s-functions, 4, 1 for p-functions and 3, 1 for hydrogen atoms. For the polarized VTZ basis sets, cc-pVTZ, the scheme is 5, 3, 1, 1, 1 for s-functions, 4, 1, 1 for p-functions and 3, 1, 1 for hydrogen atoms. The number of functions used within the cc-pVDZ and cc-pVTZ basis sets are

Atom	cc-pVDZ	cc-pVTZ
H-He	2s, 1p	3s, 2p, 1d
B-Ne	3s, 2p, 1d	4s, 3p, 2d, 1f
Al-Ar	4s, 3p, 1d	5s, 4p, 2d, 1f

With the Dunning-Huzinaga basis sets methods have been developed to extrapolate from a finite to an infinite basis set, which removes the practical limitations of the selected basis set.

3.5.3 Basis Set Extrapolation

As discussed above, an infinite or a Complete Basis Set (CBS) approximation to a complete basis set would provide an exact solution to wavefunction. The use of such a basis set is not practically possible, since the computational time for CBS calculations rises rapidly with the number of atoms in the system, n, and the total number of basis functions N. For the MP2 method the time, t, required for a calculation with N basis functions per atoms scales as [9]

$$t \propto nN^4 \tag{3.54}$$

It is possible to extrapolate to the CBS limit using finite basis sets if results converge in a uniform manner. The correlation consistent basis sets developed by Dunning et al. [10] con-

verge to the CBS limit in a uniform manner and therefore can be used to extrapolate.

Work has been performed on extrapolation using the Dunning basis sets by Truhlar [11] and Klopper [12]. It was found by Truhlar that the Hartree-Fock and the EC energies converge at different rates, leading to these energies having to be extrapolated separately. The EC energy is defined as the overall calculated energy minus the calculated Hartree-Fock energy. Both Truhlar and Klopper proposed using a power series expansion for the extrapolation, of the form

$$E_X^{HF} = E_\infty^{HF} + A^{HF} X^{-\alpha} \tag{3.55}$$

$$E_X^{Corr} = E_\infty^{Corr} + A^{Corr} X^{-\beta} \tag{3.56}$$

where X is the order of the Dunning basis set. For the aug-cc-pVDZ basis set $X = 2$, for aug-cc-pVTZ $X = 3$, etc. Different EC methods will have different values for the coefficients α and β. Truhlar found for the MP2 method, $\alpha = 3.39$ and $\beta = 1.91$ [11].

However, the form of the extrapolation does not seem to be in the form of a power series. Since the only constraint on the form is that $\mathrm{E}_X \rightarrow \mathrm{E}_\infty$ as $X \rightarrow \infty$, there are numerous possible functions that can be used.

Using the MP2 data from the Klopper paper [12], and Hartree-Fock and MP2 calculations performed on Gaussian 03 [13] it has been found that an exponential extrapolation provides a better convergence to the CBS limit than a power series.

Using the functional form

$$E_X^{HF} = E_\infty^{HF} + A^{HF} e^{-\beta' X + \gamma' X^2} \tag{3.57}$$

$$E_X^{Corr} = E_\infty^{Corr} + A^{Corr} e^{-\beta X + \gamma X^2} \tag{3.58}$$

it is possible to solve for the coefficients β', γ', β and γ using the expression for the difference between the current and ∞ level

$$\delta E_X = E_X - E_\infty = A e^{-\beta X + \gamma X^2} \tag{3.59}$$

$$\begin{aligned} ln\left(\frac{\delta E_{X+1}}{\delta E_X}\right) &= ln\left(\frac{e^{-\beta(X+1)+\gamma(X+1)^2}}{e^{-\beta X+\gamma X^2}}\right) \\ &= -\beta + \gamma(2X+1) \end{aligned} \tag{3.60}$$

A plot of the above equation will provide a straight line with an intercept of $-\beta$ and a gradient of γ. Plots of the MP2 E^{Corr} data from Klopper and E^{HF} from the Gaussian 03 calculations are illustrated in figures 3.5 and 3.6.

Linear regressions on these data sets give the following values for the extrapolation coefficients

β'	=	0.6154	β	=	1.2184
γ'	=	−0.1474	γ	=	0.0629
$\lvert r'^2 \rvert$	=	0.7620	$\lvert r^2 \rvert$	=	0.9880

Using the above coefficients, even with an extrapolation based on the smallest two basis

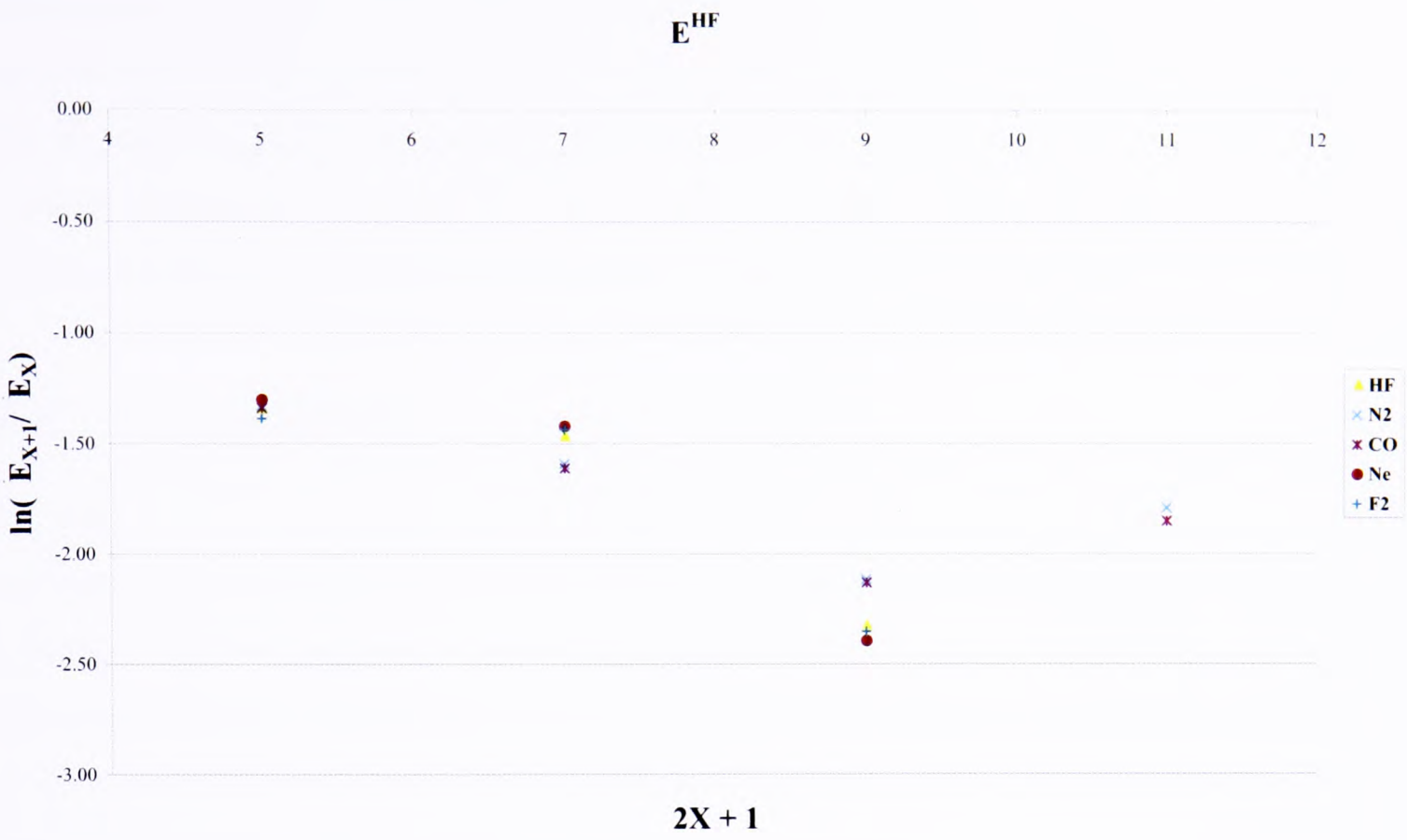

Figure 3.5: Extrapolation plot for Hartree-Fock energy

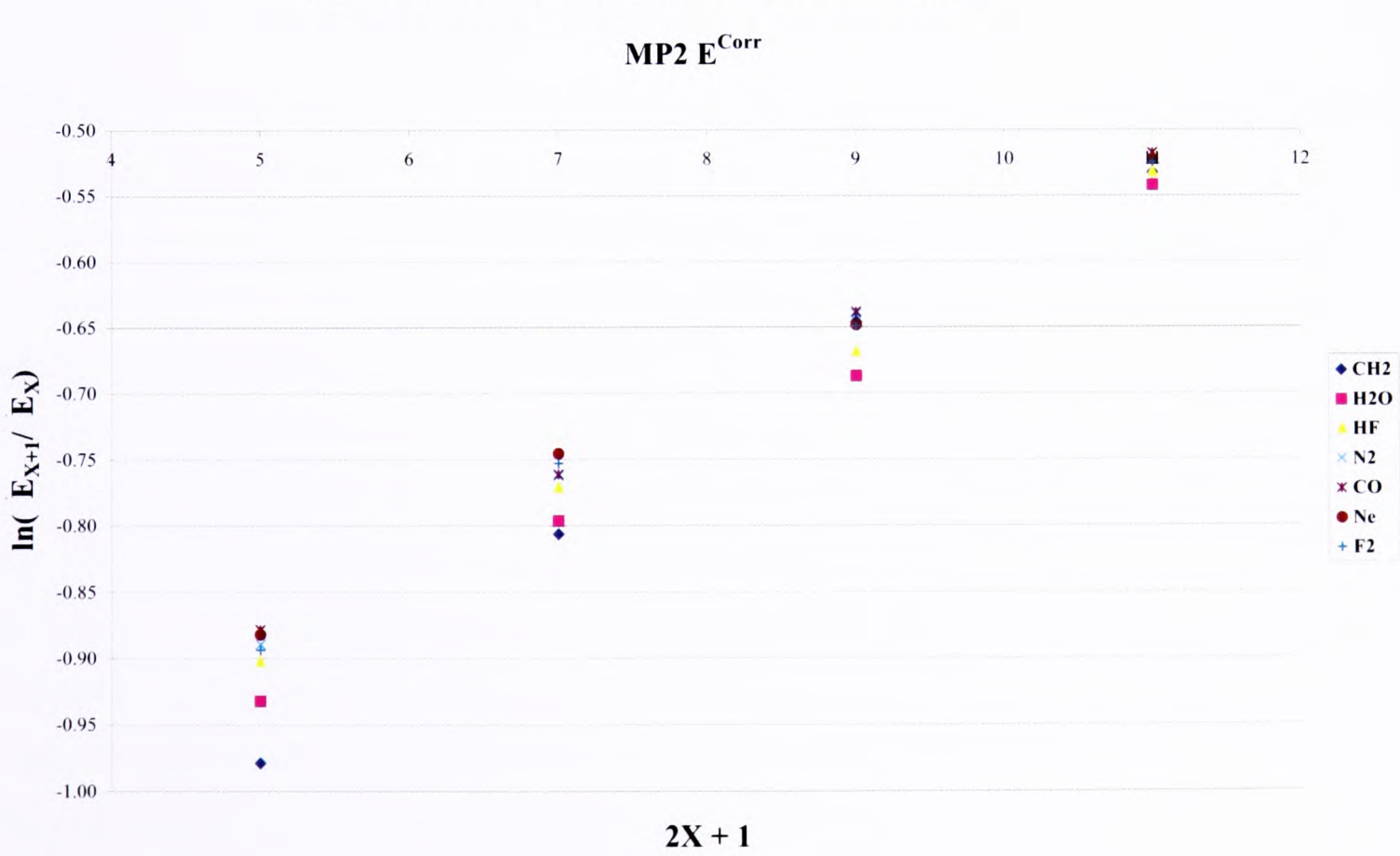

Figure 3.6: Extrapolation plot for MP2 EC energy

sets, aug-cc-pVDZ and aug-cc-pVTZ, the relative error between the extrapolation value and the true value, taken to be the CBS limit, is only of the order of 0.5 - 1.0 %. Most of this error, of a few milli Hartrees, is due to the extrapolation of the EC. These errors are considerably less than the errors from the power series extrapolation. The above values are the coefficients used for the extrapolation performed on the specific *ab initio* calculations undertaken in this thesis.

3.6 Corrections

In addition to the corrections made above for EC and finite nature of used basis sets, there are two further corrections that need to be taken into account when performing *ab initio* calculations. The first correction accounts for errors resulting from use of a finite basis set when calculating binding energies. The second correction accounts for size inconsistencies. Neither of these corrections can correct for the incomplete description of the EC as this limitation is dependent on the method selected.

3.6.1 Basis Set Superposition Error

Since all the available basis sets are of a finite size the expansion of the wavefunction and the resulting energy calculated will be inexact. If the number of functions included in the expansion increases the wavefunction should be more accurately defined and the resulting energy should be lower. However, when one is calculating intermolecular interactions there is another problem, the *Basis Set Superposition Error* (BSSE). This is of critical importance when one tries to calculated the binding energy of the Van der Waals complex such as NO or NO_2 and O_2. One calculates the binding energy to be the difference between the calculated energy of the complex and the sum of the energies of the separate components when at an infinite separation. This is the correct assuming that one is operating with a complete basis set. However, the basis sets used computationally are finite. Therefore, when the two monomers come together in the complex, and the basis functions start to overlap, there are more functions available to describe the wavefunction of each monomer and there is an overall lowering of the calculated energy of

the system. This has nothing to do with the chemistry and is simply a result of the limitation of the basis sets used. This effect can occur both intramolecularly and intermolecularly. There is no common procedure to relieve the problem for the intramolecular case, but for the intermolecular case an approximate correction can be made with *Counterpoise Correction* (CP) [14].

For CP correction four extra calculations are required in addition to the three for the complex and the two separate components. Considering the complex AB, composed of two diatomic species A and B. The species A and B will each have their own basis sets a and b and the resulting complex will have basis set ab. The basis sets used in each stage of the calculation are designated by the subscript. On complexation the geometries of A and B will change slightly and this is denoted by *. The initial step is to calculated the energy of complexation

$$\Delta E_{Complexation} = E(AB)^*_{ab} - E(A)_a - E(B)_b \tag{3.61}$$

where $E(AB)^*_{ab}$ is the energy of the complex at the geometry selected, and $E(A)_a$ and $E(B)_b$ are the energies of the monomers in isolation. The next stage is to calculate the energy of A, with basis set a at the geometry it has in the complex, and the energy of B, with basis set b in the complexed geometry. Then the energy of A and B are calculated, in the complexed geometries using the full basis set ab in the absence of the nuclei of B when A is calculated, and vice versa. The overall CP correction is then

$$\Delta E_{CP} = E(A)^*_{ab} + E(B)^*_{ab} - E(A)^*_a - E(B)^*_b \tag{3.62}$$

Giving the corrected binding energy of the complex as

$$\Delta E_{Binding} = \Delta E_{Complexation} - \Delta E_{CP} \tag{3.63}$$

As the basis sets increase in size the value of ΔE_{CP} will decrease until at an infinite basis set it would be equal to zero. By comparison to experimental data, it is found that in general the use of CP overestimates the BSSE. This overestimate is due to the fact that in the complex not all of the functions on the absent monomer are available to the other monomer.

The two values of $\Delta E_{Complexation}$ and $\Delta E_{Binding}$ bracket the true value of the complexes binding energy.

3.6.2 Size-Consistency Error

As mentioned earlier not all EC methods are inherently size consistent, see section 3.2. This can lead to calculated binding energies not tending to zero as the separation of the complex approaches infinite. To remove this error one can calculate the Size-Consistency Error (SCE) of the method used, following the work of Rintelman et al. [15].

The SCE is defined as the energy difference between the sum of separate monomer calculations and the energy of a calculation with all monomers presents, but at sufficient distances apart to guarantee that there is no interaction

$$SCE \approx E(A) + E(B) - E(A \ldots B) \tag{3.64}$$

The value of the SCE is dependent on *ab initio* method as well as several other factors and is crucial in calculating accurate binding energies. SCE is significant for MCSCF coupled to second order perturbation theory, and corrections were used in all practical applications of the above theory in this thesis.

3.7 Calculations

The actual calculations undertaken for this thesis were performed with two commercially available packages, Gaussian 03 [13] and MOLPRO [16]. The calculations were performed on Linux computers. Discussion and the relevant results presented in chapters 6 and 7 and Appendices B and C.

3.7.1 Z-matrix

When defining the geometry of the system for the computer calculation it is common to use a Z-matrix rather than Cartesian coordinates as it does not contain redundant structural degrees of freedom. The construction of a Z-matrix is illustrated in figure 3.7. The first atom is has no coordinates given. The second atom has just its distance from the first atom given. The third atom has a distance defined to either of the first two atoms and an angle to their line of centres. The fourth and subsequent atoms are defined as a distance from a previous atom and two angles relative to a plan containing three already specified atoms. This procedure removes the three degrees of freedom for the position of the centre of mass of the system and the three degrees of freedom for the orientation of the system, all of which are included in a Cartesian framework.

3.7.2 Methods

Ab initio calculations were undertaken for both NO-O_2 and NO_2-O_2.

The calculations for NO-O_2 were performed in two stages. Initially MP2 Counterpoise Corrected geometry optimisation using the 6-311++G(d,p) [17] basis set were performed. These calculations, detailed in Appendix B, illustrated convergence problems, and upon consideration it became clear that the system may not be fully represented by a single determinant, see chapter 6. This lead to the use of MCSCF coupled to second order perturbation theory.

The PES calculations for NO-O_2 using a multi-reference method are detailed in Appendix B and are discussed in more depth in chapter 6.

The calculations for NO_2-O_2 were performed using the same multi-reference method as for NO-O_2. These are discussed in depth in chapter 7.

Conclusion

The methods discussed in this chapter cover some of the techniques that are used in *ab initio* calculations. There are several other methods including Couple Cluster and Density Functional Theory that are commonly used but have not been discussed or used within this thesis. An excellent text for a more general overview of the whole subject of computational chemistry is "Introduction to Computational Chemistry" by Frank Jensen [1]. A specific section for Electron Correlation methods can be found in "Modern Methods and Algorithms of Quantum Chemistry" edited by J Grotendorst [3].

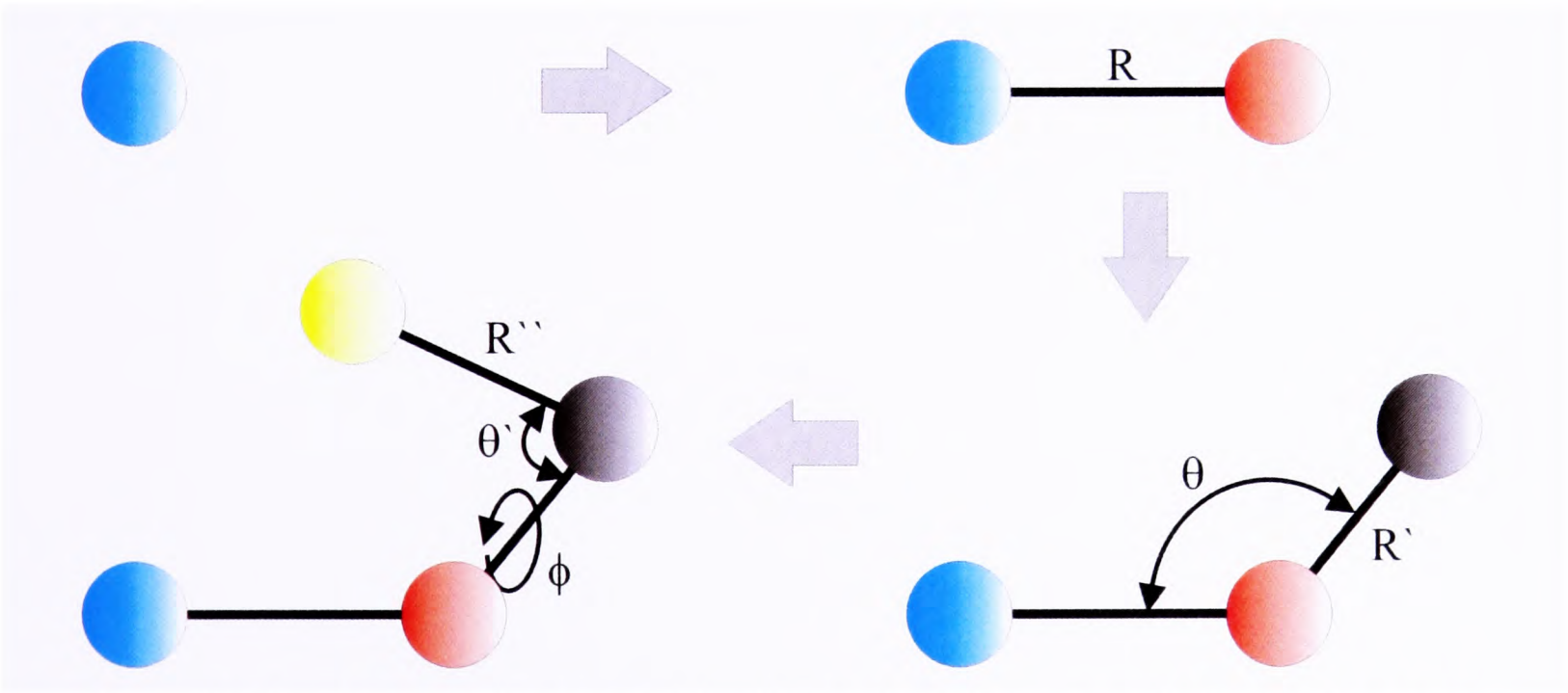

Figure 3.7: Construction of a Z-matrix: R, R′ and R″ are the defined inter-atomic distances, θ is the first atomic angle and Φ is the dihedral angle

The calculations were undertaken for several purposes. Firstly to check that the binding energy of the complexes were sufficiently large to enable them to be formed. Secondly the global minima geometries were used to generate the predicted spectra. Finally, with the full PES it has become possible to algebraically model the PES and with this dynamical model improve the accuracy of the fit of the predicted spectra. This dynamically modelling has not been used on NO-O_2 or NO_2-O_2.

References

[1] F. Jensen *Introduction to Computational Chemistry.* John Wiley & Sons (2002)

[2] P. W. Atkins *Molecular Quantum Mechanics.* Oxford University Press (1997)

[3] J. Grotendorst (Ed.) *Modern Methods and Algorithms of Quantum Chemistry.* John von Neumann Institute for Computing (2000)

[4] W. G. Richards and D. L. Cooper *Ab initio molecular orbital calculations for chemists.* Oxford University Press (1983)

[5] C. Møller and M. S. Plesset, Phys. Rev. **46**, 618 (1934)

[6] W. H. Press, B. P. Flannery, S. A. Teukolsky and W. T. Vetterling *Numerical Recipes.* Cambridge University Press (1987)

[7] C. J. Cramer *Essentials of Computational Chemistry: Theories and Models.* John Wiley & Son (2005)

[8] P. Jensen and P. R. Bunker *Computational Molecular Spectroscopy.* John Wiley & Sons (2000)

[9] J. B. Foresman and A. Frisch *Exploring Chemistry with Electronic Structure Methods.* Gaussian, Inc (1996)

[10] T. H. Dunning, J. Chem. Phys. **90**, 1007 (1989)

[11] P. L. Fast, M. L. Sanchez and D.G. Truhlar, J. Chem. Phys. **111**, 2921 (1999)

[12] W. Klopper, Mol. Phys. **99**, 481 (2001)

[13] Gaussian 03, Revision C.02, M. J. Frisch, G. W. Trucks, H. B. Schlegel, G. E. Scuseria, M. A. Robb, J. R. Cheeseman, J. A. Montgomery, Jr., T. Vreven, K. N. Kudin, J. C. Burant, J. M. Millam, S. S. Iyengar, J. Tomasi, V. Barone, B. Mennucci, M. Cossi, G. Scalmani, N. Rega, G. A. Petersson, H. Nakatsuji, M. Hada, M. Ehara, K. Toyota, R. Fukuda, J.

Hasegawa, M. Ishida, T. Nakajima, Y. Honda, O. Kitao, H. Nakai, M. Klene, X. Li, J. E. Knox, H. P. Hratchian, J. B. Cross, V. Bakken, C. Adamo, J. Jaramillo, R. Gomperts, R. E. Stratmann, O. Yazyev, A. J. Austin, R. Cammi, C. Pomelli, J. W. Ochterski, P. Y. Ayala, K. Morokuma, G. A. Voth, P. Salvador, J. J. Dannenberg, V. G. Zakrzewski, S. Dapprich, A. D. Daniels, M. C. Strain, O. Farkas, D. K. Malick, A. D. Rabuck, K. Raghavachari, J. B. Foresman, J. V. Ortiz, Q. Cui, A. G. Baboul, S. Clifford, J. Cioslowski, B. B. Stefanov, G. Liu, A. Liashenko, P. Piskorz, I. Komaromi, R. L. Martin, D. J. Fox, T. Keith, M. A. Al-Laham, C. Y. Peng, A. Nanayakkara, M. Challacombe, P. M. W. Gill, B. Johnson, W. Chen, M. W. Wong, C. Gonzalez, and J. A. Pople, Gaussian, Inc., Wallingford CT, 2004.

[14] F. B. van Duijneveldt, J. G. C. M. van Duijneveldt-van de Rijdt and J. H. van Lethe, Chem. Rev. **94**, 1873 (1994)

[15] J. M. Rintelman, I. Adamovic, S. Varganov and M. S. Gordon, J. Chem. Phys. **122**, 44105 (2005)

[16] MOLPRO, Version 2002.6, H.-J. Werner, P. J. Knowles, R. Lindh, F. R. Manby, M. Schtz, P. Celani, T. Korona, G. Rauhut, R. D. Amos, A. Bernhardsson, A. Berning, D. L. Cooper, M. J. O. Deegan, A. J. Dobbyn, F. Eckert, C. Hampel, G. Hetzer, A. W. Lloyd, S. J. McNicholas, W. Meyer, M. E. Mura, A. Nickla, P. Palmieri, R. Pitzer, U. Schumann, H. Stoll, A. J. Stone, R. Tarroni, and T. Thorsteinsson, University College Cardiff Consultants Limited, 2004

[17] R. Krishnan, J. S. Binkley, R. Seeger and J. A. Pople, J. Chem. Phys. **72**, 650 (1980)

Chapter 4

Rotational Theory I

"There is a theory which states that if ever anybody discovers exactly what the universe is for and why it is here, it will instantly disappear and be replaced by something even more bizarre and inexplicable. There is another theory which states that this has already happened"

Douglas Adams

Introduction

The original theory of the rotation of three-dimensional bodies was developed in the 18^{th} century by Leonhard Euler with the development of Euler angles, which allow a description of a rigid-rotor within three-dimensional Euclidean space [1]. The development of quantum mechanics in the early 20^{th} century led to the development of the angular momentum operators based on the earlier work.

The derivation of these operators and their characteristics are detailed below. The treatment of the various forms of molecules is explained and then extended to take account of selection rules and transition intensities. Chapter 5 extends this basic theory to take account of fine and hyperfine structure, covering spin-orbit interactions, spin-spin interactions and nuclear coupling. These additional structure effects have a considerable impact on the observed spectra.

4.1 Rigid Rotor

A rigid rotor is a soluble, yet hypothetical system. The system is composed of a collection of constant masses, in a fixed three-dimensional structure, rotating about their centre of mass. This can be treated using classical mechanics. Clearly, this model does not represent a "real world" situation but can be extended to take account of its shortcomings.

Within the rigid rotor model, it is possible to define for each atom i, a tangential velocity, ν_i

$$\nu_i = \boldsymbol{r}_i \times \omega \tag{4.1}$$

where $\boldsymbol{r}_i$ is the radius of rotation and ω is the angular velocity of the rotor. Each rotating particle, of mass m_i, will have a kinetic energy given by

$$\begin{aligned} \mathbf{E}_T &= \frac{1}{2} m_i \nu_i^2 \\ &= \frac{1}{2} m_i (\boldsymbol{r}_i \times \omega) . (\boldsymbol{r}_i \times \omega) \end{aligned} \tag{4.2}$$

For the whole system in an arbitrary cartesian framework, the overall kinetic energy will be

$$\begin{aligned}
\mathbf{E}_T &= \sum_i \frac{1}{2} m_i \left(\boldsymbol{r}_i \times \omega\right) . \left(\boldsymbol{r}_i \times \omega\right) \\
&= \sum_i \frac{1}{2} m_i \left[\left(x_i^2 + y_i^2 + z_i^2\right)\left(\omega_x^2 + \omega_y^2 + \omega_z^2\right) - \left(x_i\omega_x + y_i\omega_y + z_i\omega_z\right)^2\right] \qquad (4.3) \\
&= \sum_i \frac{1}{2} m_i \left[\left(y_i^2 + z_i^2\right)\omega_x^2 + \left(x_i^2 + z_i^2\right)\omega_y^2 + \left(x_i^2 + y_i^2\right)\omega_z^2 - 2x_iy_i\omega_x\omega_y - 2x_iz_i\omega_x\omega_z - 2y_iz_i\omega_y\omega_z\right]
\end{aligned}$$

By using the definition of terms of the *moment of inertia tensor* [2], **I**, it is possible to write equation 4.3 in terms of this tensors elements

$$\begin{aligned}
\mathbf{E}_T &= \frac{1}{2} I_{xx}\omega_x^2 + \frac{1}{2} I_{yy}\omega_y^2 + \frac{1}{2} I_{zz}\omega_z^2 \\
&+ \frac{1}{2}\left(I_{xy} + I_{yx}\right)\omega_x\omega_y + \frac{1}{2}\left(I_{xz} + I_{zx}\right)\omega_x\omega_z + \frac{1}{2}\left(I_{yz} + I_{zy}\right)\omega_y\omega_z \qquad (4.4)
\end{aligned}$$

where

$$I_{xx} = \sum_i \left(y_i^2 + z_i^2\right) m_i \qquad (4.5)$$

$$I_{yy} = \sum_i \left(x_i^2 + z_i^2\right) m_i \qquad (4.6)$$

$$I_{zz} = \sum_i \left(x_i^2 + y_i^2\right) m_i \qquad (4.7)$$

$$I_{xy} = I_{yx} = -\sum_i x_i y_i m_i \tag{4.8}$$

$$I_{xz} = I_{zx} = -\sum_i x_i z_i m_i \tag{4.9}$$

$$I_{yz} = I_{zy} = -\sum_i y_i z_i m_i \tag{4.10}$$

By writing equation 4.4 in matrix form it can be seen that

$$\mathbf{E}_T = \frac{1}{2}\omega^T.\mathbf{I}.\omega \tag{4.11}$$

Given that the *moment of inertia tensor* is symmetric it is possible to diagonalize this tensor, with a similarity transformation, to reduce the number of non-zero elements to three

$$\mathbf{I}' = \tilde{\mathbf{S}}.\mathbf{I}.\mathbf{S} \tag{4.12}$$

where $\mathbf{S}$ is a matrix formed from the three mutually orthogonal eigenvectors of $\mathbf{I}$. The resulting *moment of inertia tensor* is now diagonal

$$\mathbf{I}' = \begin{pmatrix} I_{xx} & 0 & 0 \\ 0 & I_{yy} & 0 \\ 0 & 0 & I_{zz} \end{pmatrix} \tag{4.13}$$

The axes for this tensor are a unique set of molecule fixed axes, called the Principal Axes. The Principal Axes are labelled a, b and c, with moments of inertia, I_{aa}, I_{bb} and I_{cc} respectively. By convention a, b and c are matched to x, y and z so that $I_{aa} \leq I_{bb} \leq I_{cc}$.

Based on the values of the moments of inertia molecules can be grouped into four classes.

1. Linear Molecules

   This group represents all diatomic molecules and other linear molecules such as CO_2 and OCS. Rotation can be in a parallel or perpendicular sense with respect to the linear axis of the molecule. The moment of inertia of a rotation parallel to the linear axis will be zero. The magnitude of any two moments of rotation about distinct axes perpendicular to the linear axis are equal, and will be much greater in magnitude than for the parallel rotation. Therefore for a linear molecule

$$I_{bb} = I_{cc} \tag{4.14}$$

$$I_{aa} = 0 \tag{4.15}$$

2. Spherical Tops

   This group represents molecules such as CH_4 and CCl_4 where all three moments of inertia are equal

$$I_{aa} = I_{bb} = I_{cc} \tag{4.16}$$

   This class of molecules is not observable in pure rotational spectroscopy as by symmetry they cannot have a permanent dipole moment. Thus any rotation does not produce a change in the direction of the dipole moment of the molecule which is a requirement for a rotational spectrum.

3. Symmetric Tops

   This group covers molecules such as CH_3Cl, NH_3 and BCl_3. Here, as for the linear molecules, the moment of any rotation perpendicular to the principal axis will be the

same regardless of the exact axis selected. A rotation parallel to the principal axis will no longer have a zero moment of inertia, due to the off-axis atoms. Therefore for a symmetric top molecule two of the moments of inertia are equal, with the third being distinct, but non-zero. Based on the relative value of the third moment of inertia, this class can be further sub-divided into *prolate* and *oblate* tops. For a *prolate* top

$$I_{aa} < I_{bb} = I_{cc} \tag{4.17}$$

And for an *oblate* top

$$I_{aa} = I_{bb} < I_{cc} \tag{4.18}$$

Examples of *prolate* tops include NH_3 and CH_3CN, and examples of oblate tops include BCl_3 and C_6H_6.

4. Asymmetric Tops

   This group covers most multi-atomic molecules in which the three moments of inertia are distinct

$$I_{aa} < I_{bb} < I_{cc} \tag{4.19}$$

   Examples of such molecules include H_2O and CHClFBr. Given the distinct values of the three moments of inertia, the asymmetric top represents the most complex type of molecule to study.

4.2 Rigid Rotor Hamiltonian

Solving for a rigid framework around the centre of mass of the system in question, the kinetic energy of the system within the rigid rotor approximation is given by

$$\mathbf{E}_T = \frac{1}{2} I_{aa} {\omega_a}^2 + \frac{1}{2} I_{bb} {\omega_b}^2 + \frac{1}{2} I_{cc} {\omega_c}^2 \tag{4.20}$$

By defining the angular momentum about a principal axis, i, as

$$N_i = I_{ii}.\omega_i \tag{4.21}$$

One can rewrite equation 4.20 as

$$\mathbf{E}_T = \frac{{N_a}^2}{2I_{aa}} + \frac{{N_b}^2}{2I_{bb}} + \frac{{N_c}^2}{2I_{cc}} \tag{4.22}$$

It is now possible, with the above equations, to move from the classical description of the systems to a quantum mechanical description. The relevant form of the Schrödinger equation is

$$\hat{\mathscr{H}}_{rot} \Psi_i = E_{rot} \Psi_i \tag{4.23}$$

where $\hat{\mathscr{H}}_{rot}$ is the rotational Hamiltonian operator, Ψ_i is the rotational wavefunction and E_{rot} is the rotational energy. Solving Schrödinger's equation is not a trivial task, but with appropriate approximations more manageable expressions can be derived.

The form of $\hat{\mathscr{H}}_{rot}$ will be

$$\hat{\mathscr{H}}_{rot} = \hat{T} + \hat{V} \tag{4.24}$$

where $\hat{T}$ and $\hat{V}$ are the separate operators for the kinetic and potential energy. Assuming the system is in free space and hence not subject to any external potential energy, then the operator for the potential energy is zero. This means that substitution of equation 4.22 into equation 4.24 gives

$$\hat{\mathscr{H}}_{rot} = \frac{\hat{N}_a{}^2}{2I_{aa}} + \frac{\hat{N}_b{}^2}{2I_{bb}} + \frac{\hat{N}_c{}^2}{2I_{cc}} \tag{4.25}$$

The three operators in the above equation have standard commutation relationships between themselves and the total angular momentum, given in standard texts [1], [3] within the lab fixed axis system. However, in the less common molecule fixed axis system the relationships become "anomalous" [3]

$$\hat{J}^2 = \hat{J}_a{}^2 + \hat{J}_b{}^2 + \hat{J}_c{}^2 \tag{4.26}$$

$$\left[\hat{J}_a, \hat{J}_b\right] = -\mathbf{i}\hat{J}_c \tag{4.27}$$

$$\left[\hat{J}^2, \hat{J}_g\right] = 0 \tag{4.28}$$

where $\hat{J}$ is $\hat{N}$ in units of $\hbar$ and g is one of the principal axes, a, b or c. Clearly, it is only possible to experimentally determine two parameters within the molecule fixed system: the total angular momentum, and one of its components. If the system being studied is near-prolate in nature, then $\hat{J}_a$ is commonly chosen as the component to be determined, but if the system is near-oblate, then $\hat{J}_c$ is chosen. Without the external application of a field to the system, the molecule fixed

axis system and the lab fixed axis system are independent. This means that it is possible to determine a third parameter from the lab fixed axis system, $\hat{J}_Z$. This commutes with $\hat{J}^2$ and $\hat{J}_a$. As found in the literature [4] for the near prolate system

$$\hat{J}^2\Psi_i = J(J+1)\Psi_i \tag{4.29}$$

$$\hat{J}_a\Psi_i = K\Psi_i \tag{4.30}$$

$$\hat{J}_Z\Psi_i = M_J\Psi_i \tag{4.31}$$

where the quantum numbers have the following ranges

$$J = 0, 1, 2, 3, 4, 5 \ldots \tag{4.32}$$

$$K = 0, \pm 1, \pm 2, \pm 3, \ldots, \pm J \tag{4.33}$$

$$M_J = 0, \pm 1, \pm 2, \pm 3 \ldots, \pm J \tag{4.34}$$

The wavefunctions, Ψ_i, form a "prolate rotor basis set", where each wavefunction is specified by three independent, "good" quantum numbers: J, K and M_J

$$\Psi_i = |JKM_J\rangle \tag{4.35}$$

where J is the total angular momentum of the system, K is the component of angular momentum about the rotor's principal axis and M_J is the component of the angular momentum about the lab fixed axis $\boldsymbol{Z}$. Rearranging equation 4.25 gives

$$\hat{\mathscr{H}}_{rot} = A\hat{J}_a{}^2 + \frac{(B+C)}{2}(\hat{J}_b{}^2 + \hat{J}_c{}^2) + \frac{(B-C)}{2}(\hat{J}_b{}^2 - \hat{J}_c{}^2) \tag{4.36}$$

where A, B and C are the principal rotational constants, defined as

$$A = \frac{h^2}{8\pi^2 I_{aa}} \tag{4.37}$$

$$B = \frac{h^2}{8\pi^2 I_{bb}} \tag{4.38}$$

$$C = \frac{h^2}{8\pi^2 I_{cc}} \tag{4.39}$$

Two further operators, the shift operators, are required to allow the eigenvalues for the angular momentum operators to be determined. These are defined as

$$\hat{J}_+ = \hat{J}_b + \mathbf{i}\hat{J}_c \tag{4.40}$$

$$\hat{J}_- = \hat{J}_b - \mathbf{i}\hat{J}_c \tag{4.41}$$

$\hat{J}_+$ is the lowering operator and $\hat{J}_-$ is the raising operator due to the "anomalous" commutation relationships. These have the following commutation relationships with the other defined operators

$$\left[\hat{J}_a, \hat{J}_+\right] = -\hat{J}_+ \tag{4.42}$$

$$\left[\hat{J}_a, \hat{J}_-\right] = \hat{J}_- \tag{4.43}$$

$$\left[\hat{J}^2, \hat{J}_+\right] = 0 \tag{4.44}$$

$$\left[\hat{J}^2, \hat{J}_-\right] = 0 \tag{4.45}$$

$$\left[\hat{J}_+, \hat{J}_-\right] = -2\hat{J}_a \tag{4.46}$$

Using the raising and lowering operators, the Hamiltonian in equation 4.36 can be re-written as

$$\hat{\mathscr{H}}_{rot} = A\hat{J}_a{}^2 + \frac{(B+C)}{2}(\hat{J}^2 - \hat{J}_a{}^2) + \frac{(B-C)}{4}(\hat{J}_+{}^2 + \hat{J}_-{}^2) \tag{4.47}$$

4.2.1 Symmetric Rotor

With a symmetric rotor such as CH_3CCH, the form of the Hamiltonian can be simplified, since $I_{bb} = I_{cc}$ or $I_{aa} = I_{bb}$. Using the prolate equivalence in equation 4.36, one obtains

$$\begin{aligned} \hat{\mathscr{H}}_{rot} &= A\hat{J}_a{}^2 + B(\hat{J}_b{}^2 + \hat{J}_c{}^2) \\ &= B\hat{J}^2 + (A-B)\hat{J}_a{}^2 \end{aligned} \tag{4.48}$$

Using this Hamiltonian, the eigenvalues of the angular momentum operators $\hat{J}^2$, $\hat{J}_a$ and $\hat{J}_Z$ can be calculated with equations 4.29 and 4.30.

Given that 4.48 commutes with $\hat{J}^2$ and $\hat{J}_a$, the Hamiltonian matrix is diagonal in the J and K representation. The energy does not depend on the quantum number M_J in the absence of an applied external field. This means that the eigenvalues of the diagonal elements of the matrix are the quantized rotational energy levels of the rigid prolate symmetric rotor

$$\begin{aligned} E_{J,K} &= B\langle JK|\,\hat{J}^2\,|JK\rangle + (A-B)\langle JK|\,\hat{J}_a{}^2\,|JK\rangle \\ &= BJ(J+1) + (A-B)K^2 \end{aligned} \tag{4.49}$$

Since K and -K have the same energy all levels, except $K = 0$, are doubly degenerate.

4.2.2 Asymmetric Rotor

With the more general asymmetric rotor it is not possible to simplify equation 4.36 as done for the symmetric rotor. This means that one has to solve equation 4.47 directly. Using the "prolate rotor basis set" from standard texts [1], [3] the non-zero matrix elements of the Hamiltonian are

$$\langle JKM_J|\,\hat{J}^2\,|JKM_J\rangle = J(J+1) \tag{4.50}$$

$$\langle JKM_J|\,\hat{J}_a{}^2\,|JKM_J\rangle = K^2 \tag{4.51}$$

$$\begin{aligned}
\langle J\ K\text{-}2\ M_J|\,\hat{J}_+{}^2\,|JKM_J\rangle &= \langle JKM_J|\,\hat{J}_-{}^2\,|J\ K\text{-}2\ M_J\rangle \\
&= [(J+K)(J-K+1) \\
&\quad (J+K-1)(J-K+2)]^{\frac{1}{2}} \qquad (4.52)\\
\langle J\ K\text{+}2\ M_J|\,\hat{J}_-{}^2\,|JKM_J\rangle &= \langle JKM_J|\,\hat{J}_+{}^2\,|J\ K\text{+}2\ M_J\rangle \\
&= [(J-K)(J+K+1) \\
&\quad (J-K-1)(J+K+2)]^{\frac{1}{2}} \qquad (4.53)
\end{aligned}$$

With these four equations it is possible to construct the full Hamiltonian matrix. Since there is no connection for states of differing J, the Hamiltonian can be split into a series of sub-matrices, one for each value of J, of dimensions $2J+1$, for all the possible values of K. Below is an example of a sub-matrix for $J=3$

$$\mathbf{H} = \begin{pmatrix}
H_{+3+3} & 0 & H_{+3+1} & 0 & 0 & 0 & 0 \\
0 & H_{+2+2} & 0 & H_{+20} & 0 & 0 & 0 \\
H_{+1+3} & 0 & H_{+1+1} & 0 & H_{+1-1} & 0 & 0 \\
0 & H_{0+2} & 0 & H_{00} & 0 & H_{0-2} & 0 \\
0 & 0 & H_{-1+1} & 0 & H_{-1-1} & 0 & H_{-1-3} \\
0 & 0 & 0 & H_{-20} & 0 & H_{-2-2} & 0 \\
0 & 0 & 0 & 0 & H_{-3-1} & 0 & H_{-3-3}
\end{pmatrix} \qquad (4.54)$$

Here the Hamiltonians are labelled with respect to the two possible values of the K quantum number. The values of the non-zero Hamiltonian elements are

$$H_{+3+3} = H_{-3-3} = 12\alpha + 9(A - \alpha) \tag{4.55}$$

$$H_{+3+1} = H_{+1+3} = H_{-1-3} = H_{-3-1} = \beta\sqrt{60} \tag{4.56}$$

$$H_{+2+2} = H_{-2-2} = 12\alpha + 4(A - \alpha) \tag{4.57}$$

$$H_{+20} = H_{0+2} = H_{0-2} = H_{0+2} = \beta\sqrt{120} \tag{4.58}$$

$$H_{+1+1} = H_{-1-1} = 12\alpha + (A - \alpha) \tag{4.59}$$

$$H_{+1-1} = H_{-1+1} = \beta\sqrt{144} \tag{4.60}$$

$$H_{00} = 12\alpha \tag{4.61}$$

where

$$\alpha = \frac{B + C}{2} \tag{4.62}$$

$$\beta = \frac{B - C}{4} \tag{4.63}$$

To obtain the energy in the Schrödinger equation, one has to diagonalize the Hamiltonian matrix, given as an example in equation 4.54. However, a greater simplification can be made. As the Hamiltonian can only connect states which differ in K by 0 or ± 2, the matrix can be split into two parts one for odd K and the other for even K. Using the example of the $J = 3$ sub-matrix given above, one obtains

$$\mathbf{H}' = \left(\begin{array}{cccc|ccc} H_{+3+3} & H_{+3+1} & 0 & 0 & 0 & 0 & 0 \\ H_{+1+3} & H_{+1+1} & H_{+1-1} & 0 & 0 & 0 & 0 \\ 0 & H_{-1+1} & H_{-1-1} & H_{-1-3} & 0 & 0 & 0 \\ 0 & 0 & H_{-3-1} & H_{-3-3} & 0 & 0 & 0 \\ \hline 0 & 0 & 0 & 0 & H_{+2+2} & H_{+20} & 0 \\ 0 & 0 & 0 & 0 & H_{0+2} & H_{00} & H_{0-2} \\ 0 & 0 & 0 & 0 & 0 & H_{-20} & H_{-2-2} \end{array}\right) \tag{4.64}$$

The form of the above Hamiltonian matrix is still not diagonal. This can be improved by changing the selection of basis functions. The Hamiltonian matrix above has significant symmetry properties, which can be utilised by considering the symmetry properties of the ellipsoid of inertia of the asymmetric rotor [1]. This is a hypothetical ellipsoid representing the inertia of the system in three dimensions. This ellipsoid is symmetric under the identity operator, E, and under a C_2 rotation about the three principal axes of the system. These four symmetry operators form the D_2 point group. This group has four symmetry species, which are given in the character table below

Symmetry Species	E	$C_2{}^a$	$C_2{}^b$	$C_2{}^c$
A	1	1	1	1
B_a	1	1	−1	−1
B_b	1	−1	1	−1
B_c	1	−1	−1	1

If the basis functions used to construct the wavefunction belong to the D_2 point group, they will transform under the same symmetry operations and the resulting wavefunctions can be classified according to the symmetry species, A, B_a, B_b and B_c. This would mean that matrix

elements of the Hamiltonian in the energy matrix would only be non-zero if the wavefunctions were of the same symmetry species. If this is possible the sub-matrix given above in equation 4.64 would be factored into four independent units. The "prolate rotor basis set" used in the construction of the wavefunctions are not members of the D_2 point group. However, linear combinations of $|J \pm K\ M_J\rangle$ basis functions do belong to the D_2 point group. The relevant linear combinations are of the form [1]

$$|JKM_J\pm\rangle = \frac{1}{\sqrt{2}}\left(|JKM_J\rangle + (-1)^{\gamma}\,|J\ -K\ M_J\rangle\right) \tag{4.65}$$

where γ is even or odd, say 0 or 1. The exact form of the new basis set can be found in the standard texts. The new basis set is related to the old basis set, given in 4.35, by

$$|JKM_J\pm\rangle = W.\,|JKM_J\rangle \tag{4.66}$$

where W is the Wang transformation matrix [5]. This transformation matrix has the following form for an even number of dimensions of the energy matrix

$$\mathbf{W} = \frac{1}{\sqrt{2}}\begin{pmatrix} \nwarrow & & & & \nearrow \\ & -1 & 0 & 0 & 1 \\ & 0 & -1 & 1 & 0 \\ & 0 & 1 & 1 & 0 \\ & 1 & 0 & 0 & 1 \\ \swarrow & & & & \searrow \end{pmatrix} \tag{4.67}$$

If there is an odd number of dimensions in the energy matrix, the form is

$$\mathbf{W} = \frac{1}{\sqrt{2}} \begin{pmatrix} \nwarrow & & & & & \nearrow \\ & -1 & 0 & 0 & 0 & 1 \\ & 0 & -1 & 0 & 1 & 0 \\ & 0 & 0 & \sqrt{2} & 0 & 0 \\ & 0 & 1 & 0 & 1 & 0 \\ & 1 & 0 & 0 & 0 & 1 \\ \swarrow & & & & & \searrow \end{pmatrix} \tag{4.68}$$

Each asymmetric wavefunction is constructed from a linear combination of these symmetrised basis functions. The new overall energy matrix is given by

$$\mathbf{H''} = \mathbf{W}.\mathbf{H'}.\mathbf{W} = \mathbf{E}^+ + \mathbf{O}^+ + \mathbf{E}^- + \mathbf{O}^- \tag{4.69}$$

where **E** and **O** refer, respectively, to the even and odd nature of K and + and - refer, respectively, to the even and odd nature of γ, see equation 4.65, as defined by the King-Hainer-Cross notation [6]. The composition of these sub units is given below

$$\mathbf{E}^+ = \begin{pmatrix} H_{00} & \sqrt{2}H_{02} & 0 & \dots & \dots \\ \sqrt{2}H_{02} & H_{22} & H_{24} & 0 & \dots \\ 0 & H_{24} & H_{44} & H_{46} & \dots \\ \dots & 0 & H_{46} & H_{66} & \dots \\ \dots & \dots & \dots & \dots & \dots \end{pmatrix} \tag{4.70}$$

$$\mathbf{E}^{-} = \begin{pmatrix} H_{22} & H_{24} & 0 & \dots & \dots \\ H_{24} & H_{44} & H_{46} & 0 & \dots \\ 0 & H_{46} & H_{66} & H_{68} & \dots \\ \dots & 0 & H_{68} & H_{88} & \dots \\ \dots & \dots & \dots & \dots & \dots \end{pmatrix} \tag{4.71}$$

$$\mathbf{O}^{+} = \begin{pmatrix} H_{11} + H_{-11} & H_{13} & 0 & \dots & \dots \\ H_{13} & H_{33} & H_{36} & 0 & \dots \\ 0 & H_{35} & H_{55} & H_{57} & \dots \\ \dots & 0 & H_{57} & H_{77} & \dots \\ \dots & \dots & \dots & \dots & \dots \end{pmatrix} \tag{4.72}$$

$$\mathbf{O}^{-} = \begin{pmatrix} H_{11} - H_{-11} & H_{13} & 0 & \dots & \dots \\ H_{13} & H_{33} & H_{35} & 0 & \dots \\ 0 & H_{35} & H_{55} & H_{57} & \dots \\ \dots & 0 & H_{57} & H_{77} & \dots \\ \dots & \dots & \dots & \dots & \dots \end{pmatrix} \tag{4.73}$$

The results of the diagonalization of the above matrices are illustrated as the prolate limit in the correlation diagram in figure 4.1. To uniquely characterise energy levels between the prolate and oblate limits, the King-Hainer-Cross subscript notation [6] is used. The first subscript, K_a, is the limiting value of $|K|$ in the prolate limit. The second subscript, K_c, is the limiting value of $|K|$ in the oblate limit. The correlation diagram gives the connections between the limiting states.

The size of the diagonalization required to evaluate the final energy is reduced in complexity by the use of symmetry. As the complexity is reduced, so is the computational effort. However, as the level of J increases the functional form of the equations to be solved increases and

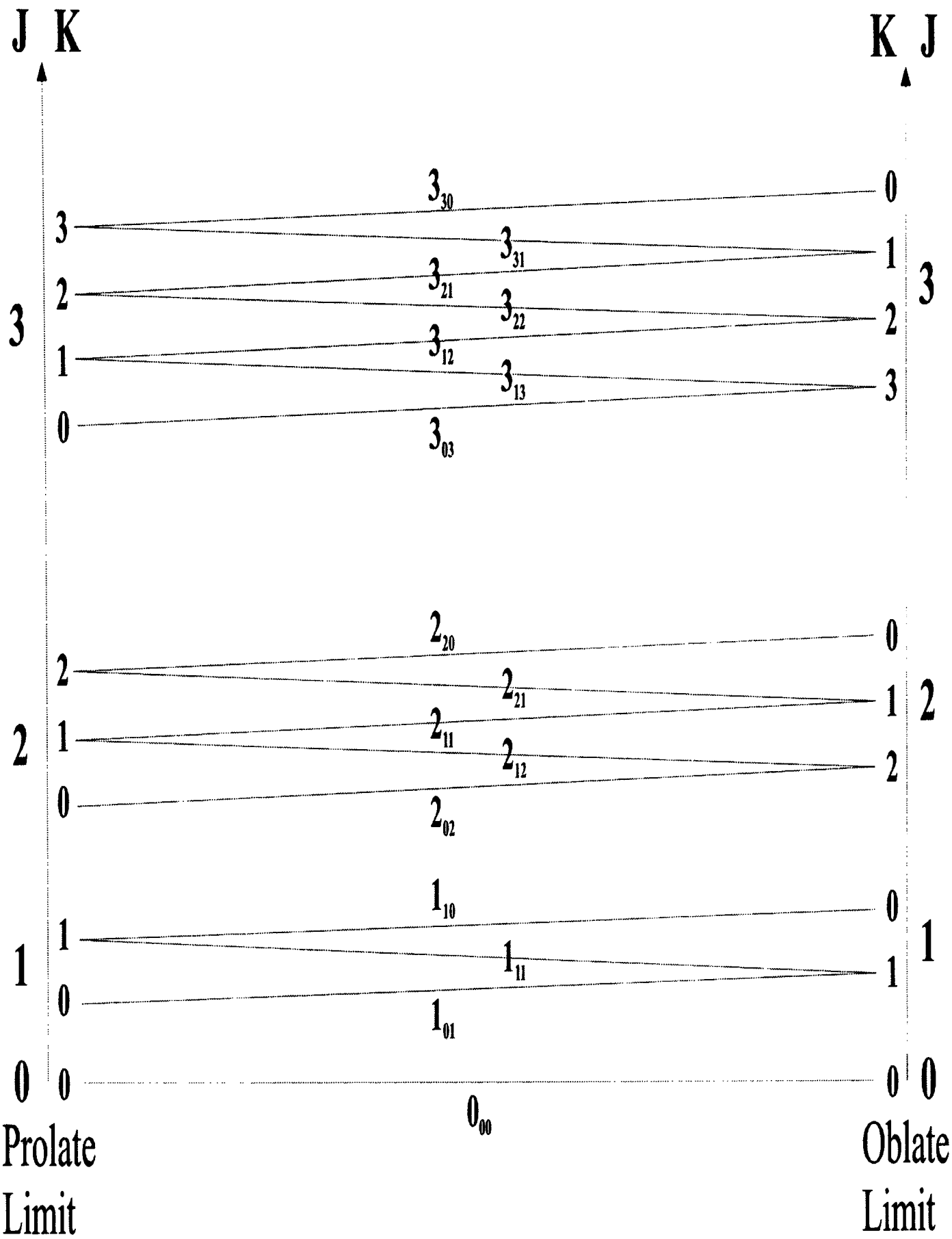

Figure 4.1: Correlation diagram of energy levels in asymmetric rotor in the limiting prolate and oblate forms. The subscript on J is defined as $K_a K_c$

$J_{K_a K_c}$	$E(A, B, C)$
0_{00}	0
1_{10}	$A+B$
1_{11}	$A+C$
1_{01}	$B+C$
2_{20}	$2\left(A+B+C+\left((B-C)^2+(A-C)(A-B)\right)^{\frac{1}{2}}\right)$
2_{21}	$4A+B+C$
2_{11}	$A+4B+C$
2_{12}	$A+B+4C$
2_{02}	$2\left(A+B+C-\left((B-C)^2+(A-C)(A-B)\right)^{\frac{1}{2}}\right)$
3_{30}	$5A+5B+2C+2\left(4(A-B)^2+(A-C)(B-C)\right)^{\frac{1}{2}}$
3_{31}	$5A+2B+5C+2\left(4(A-C)^2-(A-B)(B-C)\right)^{\frac{1}{2}}$
3_{21}	$2A+5B+5C+2\left(4(B-C)^2+(A-B)(A-C)\right)^{\frac{1}{2}}$
3_{22}	$4A+4B+4C$
3_{12}	$5A+5B+2C-2\left(4(A-B)^2+(A-C)(B-C)\right)^{\frac{1}{2}}$
3_{13}	$5A+2B+5C-2\left(4(A-C)^2-(A-B)(B-C)\right)^{\frac{1}{2}}$
3_{03}	$2A+5B+5C-2\left(4(B-C)^2+(A-B)(A-C)\right)^{\frac{1}{2}}$

Table 4.1: Asymmetric rotor energy levels

numerical methods have to be used [7]. The task of numerical diagonalization is possible on a standard personal computer. For the first three J levels the explicit expressions for the energy are given in terms of the principal moments in table 4.1

4.3 Selection Rules

The rotational spectrum represents an energy transition between two non-degenerate rotational states of the system. The transitions that are permitted are controlled by the *gross selection rules* and the *specific selection rules.* The *gross selection rules* cover the properties that a molecule must possess to allow the molecule to show a certain type of transition. This selection rule requires a dipole moment which can be interacted with an applied dipole to induce a tran-

sition between two states. The *specific selection rules* are the changes in the quantum numbers that are permissible during the transition.

The intensity of a transition is proportional to the square of the transition dipole moment, μ_{fi}, which is defined as

$$\mu_{fi} = \langle \psi_f | \, \mu \, | \psi_i \rangle \tag{4.74}$$

where ψ_i and ψ_f represent the initial and final wavefunctions of levels of the transition respectively. It is possible to have transitions induced by both magnetic and electric dipole moments. However, electric dipole transitions are more intense and these are the dipoles used in the studies undertaken in this thesis. The specific selection rules for "permitted" transitions for the total angular momentum quantum number J are

$$\Delta J = 0, \pm 1 \tag{4.75}$$

For the asymmetric rotor, only J and M_J are "good" quantum numbers: since there is no component of angular momentum that is constant with motion, $\hat{J}_a$ no longer commutes with the Hamiltonian. However, there are still specific selection rules for the pseudoquantum numbers K_a and K_c. These rules can be understood in terms of the symmetry of the dipole moment along axes fixed in space.

The component of the dipole moment along a space fixed axis F is given by

$$\mu_F = \sum_g \Phi_{Fg} \mu_g \tag{4.76}$$

where F = X, Y or Z, g = a, b, c and μ_g is the component of the permanent molecular dipole resolved along the principal axes. In experiments where the radiation is polarised, as is the case in this research, the radiation will parallel to one of the values of F. The Φ_{Fg} terms are the cosines of the angles between the fixed axes F and the rotation axis g. These direction cosines have an explicit form that can be derived from the Euler angles θ, ϕ and χ. These forms are discussed for NO-O_2 in section 6.2.5 of chapter 6. The relationship of fixed to rotating frameworks is covered in depth in many of standard texts, [1], [8].

For the case where the dipole moment lies parallel to the a principal axis, the condition for a permitted transition is given by

$$\langle JK_aK_c|\,\mu_F\,|J'K'_aK'_c\rangle = \mu_a\,\langle JK_aK_c|\,\Phi_{Fa}\,|J'K'_aK'_c\rangle \neq 0 \tag{4.77}$$

For the above expression to be correct, the integrand must transform according to the totally symmetric representation, A, of the D_2 point group. Given the symmetry constraints on the integrand, the symmetry of the states and Φ_{Fa} are themselves defined.

With the K_a and K_c notation it is possible to classify the states into the different symmetry representations of the D_2 point group. If K_a is even, then the total wavefunction is symmetric with respect to a rotation of π radians around the a axis. This even nature is represented by *e*. If K_a is odd, then the rotation of π radians about the a axis is asymmetric, which is represented by *o*. It is possible for the values of K_a and K_c to be any combination of even and odd. This means that there are four possible combinations of K_aK_c: *ee*, *eo*, *oe* and *oo*. By comparing the classifications based on the odd and even nature of K_a and K_c with the character table for the D_2 point group, it can be seen that

K_aK_c	*Symmetry Species*
ee	A
eo	B_a
oe	B_c
oo	B_b

In equation 4.77, the direction cosine, Φ_{Fa}, transforms as B_a. This means that the allowed symmetries of the energy levels are: $A(ee) \leftrightarrow B_a(eo)$ and $B_b(oo) \leftrightarrow B_c(oe)$. Extending this to the case where the dipole moment is parallel to the other principal axes, and noting the allowed changes in the labels K_a and K_c, the specific selections rules for a asymmetric rotor can be determined

Transition Type	*Dipole Component*	*Permitted Transitions*	ΔK_a	ΔK_c
$a-type$	$\mu_a \neq 0$	$ee \leftrightarrow eo$	$0, \pm 2, \ldots$	$\pm 1, \pm 3, \ldots$
		$oe \leftrightarrow oo$		
$b-type$	$\mu_b \neq 0$	$ee \leftrightarrow oo$	$\pm 1, \pm 3, \ldots$	$\pm 1, \pm 3, \ldots$
		$oe \leftrightarrow eo$		
$c-type$	$\mu_c \neq 0$	$ee \leftrightarrow oe$	$\pm 1, \pm 3, \ldots$	$0, \pm 2, \ldots$
		$eo \leftrightarrow oo$		

4.4 Transition Intensities

In section 4.3 the specific selection rules for an asymmetric rotor were derived. However, not all transitions will be observable due to differences in the intensities of the transitions. The intensity of an absorption line is proportional to the squares of absolute values of the direction cosines.

The intensity of an emitted transition, which is the actual observation in the experimental work of this thesis, will not necessarily match that of an absorption. However, it will provide an indication of rough signal strength. For an absorption transition caused by the dipole moment μ_g, a line strength can be defined

$$S(J;J') = \sum_{M_J M'_J} |\langle JK_aK_cM_J |\Phi_{Fg}| J'K'_aK'_cM'_J\rangle|^2 \tag{4.78}$$

where $|JK_aK_cM_J\rangle$ and $|J'K'_aK'_cM'_J\rangle$ are linear combinations of the basis set used. These combinations are given by the eigenvectors associated with the two states. The summation extends over all values of M_J and M'_J, but only one value of F since the radiation is assumed to be polarised. These matrix elements have been approximated in the limiting case and are discussed in the literature [9].

The exact theoretical calculation of the intensity of transitions, using the above equation as a starting point, is discussed in greater depth in several of the standard texts. However, within the practical data collections, it has been found that transitions are weak when there is a large ΔK_a or ΔK_c and/or when the dipole moment along the particular principal axis is small.

For NO-O_2 transition intensities were calculated for each transition between 5 and 20 GHz. The details of these calculations are given in chapter 6. Similar factors have also been calculated for NO_2-O_2, see chapter 7.

Conclusion

The above discussion details the derivation of the rigid rotor approximation for both symmetric and asymmetric rotors. The selection rules, both gross and specific, have been discussed. These topics are discussed at greater length in many of the standard texts where the effect of

centrifugal distortion is explained.

The following chapter extends the above discussion to take account of hyperfine structure of rotational spectra and the interaction of molecules with electric and magnetic fields. These effects have a dramatic effect on predicted and observed spectra and therefore these effects must be taken into account.

References

[1] R. N. Zare *Angular Momentum: Understanding Spatial Aspects in Chemistry and Physics.* John Wiley & Sons (1988)

[2] W. Gordy and R. L. Cook *Microwave Molecular Spectra.* John Wiley & Sons (1970)

[3] J. D. Graybeal *Molecular Spectroscopy.* McGraw-Hill, Inc (1988)

[4] P. W. Atkins *Molecular Quantum Mechanics.* Oxford University Press (1997)

[5] S. C. Wang, Phys. Rev. **34**, 243 (1929)

[6] G. W. King, R. M. Hainer and P. C. Cross, J. Chem. Phys. **11**, 27 (1943)

[7] W. H. Press, B. P. Flannery, S. A. Teukolsky and W. T. Vetterling *Numerical Recipes.* Cambridge University Press (1987)

[8] H. W. Kroto *Molecular Rotation Spectra.* Dover Publications, Inc. (1992)

[9] C. H. Townes and A. L. Schawlow *Microwave Spectroscopy.* Dover Publications, Inc. (1975)

Chapter 5

Rotational Theory II

"In theory, there is no difference between
theory and practice; In practice, there is."

Chuck Reid

Introduction

In the preceding chapter, the basic rigid rotor model of a closed-shell molecule was discussed and solved for the cases of the symmetric and asymmetric rotor. The model of the asymmetric rotor was then used to discuss selection rules and the intensity of the transitions.

This chapter builds on the work above and covers fine and hyperfine structures that can be observed within a rotational spectrum. These features arise from electron spin-orbital coupling, electron spin-spin coupling and nuclear quadrupole and magnetic coupling. These couplings are considered separately below, but they are given in terms of spherical tensor operators to allow straightforward mathematical manipulation. The combined interactions of the spin coupling and nuclear quadrupole and magnetic coupling are discussed within species specific applications

in the following chapters.

5.1 Spin Coupling

For open-shell systems there exists an interaction between the molecular rotation of the system and the unbalanced electronic angular momentum. This interaction has not been considered in the preceding chapter, yet it has an important effect on the observed rotational spectra.

For example, given that NO is a diatomic molecule with orbital angular momentum, the theory of spin coupling for diatomic molecule is relevant to the study of the complex NO-O_2. Thus, considering only diatomic systems the electronic orbital angular momentum will be strongly coupled to the interatomic axis of the molecule, due to the chemical bond. The vector $\boldsymbol{L}$, representing the direction and magnitude of the orbital angular momentum, will therefore precess rapidly around the interatomic axis, see figure 5.1. The precession of $\boldsymbol{L}$ means that it is not a constant of rotation, and $\boldsymbol{L}^2$ is not quantized. However, the projection of $\boldsymbol{L}$ onto the interatomic axis will have a definite, quantized value.

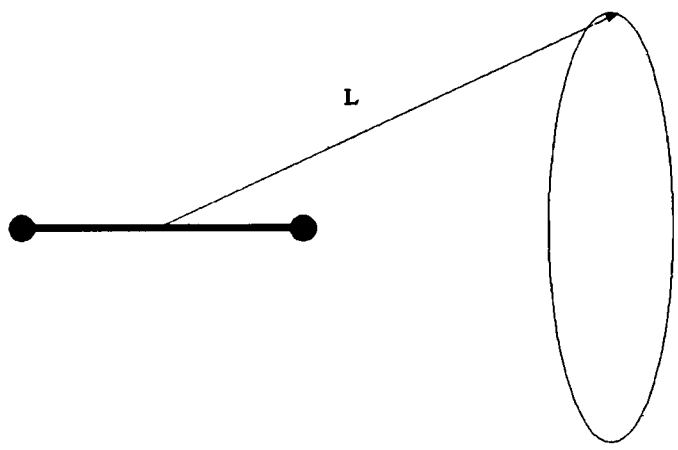

Figure 5.1: Precession of orbital angular momentum around interatomic axis

The electric force of the chemical bond will give a strong internal Stark Effect [1], which lifts the degeneracy of the orbital angular momentum, resolving it into components, M_L, along

the interatomic axis. See figure 5.2.

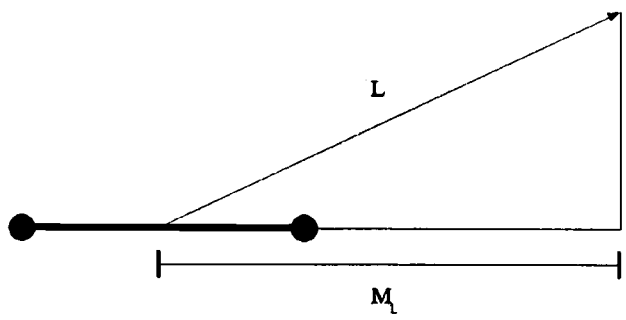

Figure 5.2: Resolution of $\boldsymbol{L}$ into components parallel to the interatomic axis

The resolution along the chemical bond is a second order effect and $+M_L$ is degenerate with $-M_L$. The magnitude of M_L is designated by Λ. Λ has the following values

$$\Lambda = |M_L| = 0, 1, 2, \ldots, L \tag{5.1}$$

Diatomic molecules with $\Lambda = 0$ have Σ electronic states, $\Lambda = 1$ have Π electronic states, $\Lambda = 2$ have Δ electronics states, and so on.

For open-shell diatomic molecules where $\Lambda \neq 0$, the magnetic field generated by the orbital motion interacts with the spin magnetic momentum and the spin angular momentum, $\boldsymbol{S}$, will be resolved along the chemical bond. The components of $\boldsymbol{S}$ along the bond are designated by Σ. Σ has the following values

$$\Sigma = S, S-1, S-2, \ldots, -S \tag{5.2}$$

Combining equations 5.1 and 5.2, the overall electronic angular momentum along the chemical bond is

$$\Omega = |\Lambda + \Sigma| \tag{5.3}$$

Ω is the total electronic angular momentum of the non-rotating diatomic, which corresponds to the projection of $\boldsymbol{J}$ for an atom. For a diatomic molecule, disregarding nuclear spin covered in section 5.2, $\boldsymbol{J}$ represents the overall electronic angular momentum with projection Ω, and the end-over-end rotation, O, of the of the molecule. The relationship of all the quantum numbers described above is illustrated in figure 5.3.

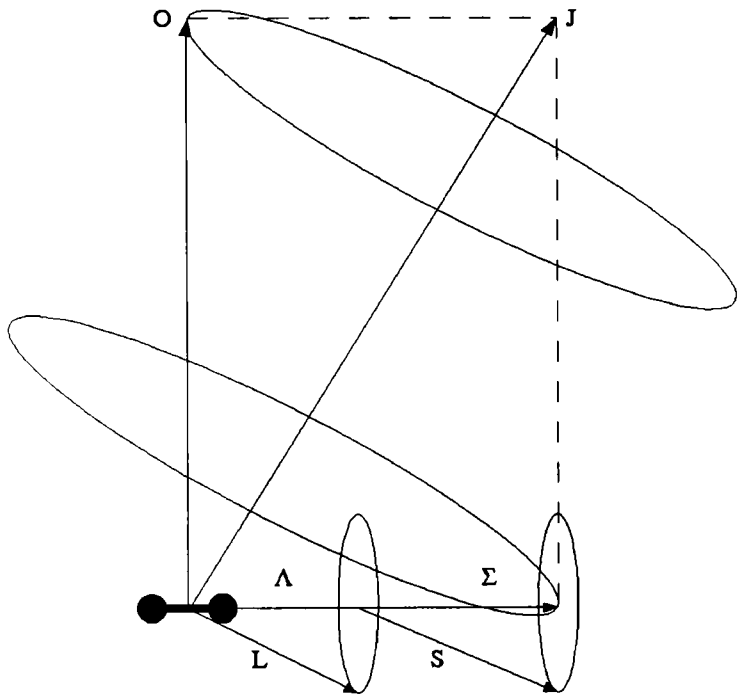

Figure 5.3: Vector diagram of Hund's case (a), illustrating all quantum numbers

In the case of NO, the low-lying electronic states are $^2\Pi_{3/2}$ and $^2\Pi_{1/2}$. These arise from differences in the coupling of the orbital and spin angular momentum. For O_2 the low-lying electronic states are $^3\Sigma_g^-$, $^1\Delta_g$ and $^1\Sigma_g^+$, which arise for different occupations of the ground state electron configuration.

The coupling together of the various angular momenta can occur in several ways. The five basic idealised types of coupling observed were designated Hund's Case (a), (b), (c), (d) and (e) by F. Hund, in the early 20^{th} century. These represent different basis sets which are used to describe the problem in question. By carefully selecting the case used, it is possible to make the overall Hamiltonian matrix more diagonal, and hence make the interpretation easier. However, assuming the system is fully represented, the actual selection of which basis set to use is of no critical importance. Hund's case (a) is described briefly below.

5.1.1 Hund's Case (a)

For a $\Lambda \neq 0$ state, where the magnetic field resulting from the molecular rotation is weak, both $\boldsymbol{S}$ and $\boldsymbol{L}$ will be resolved along the interatomic bond, resulting in Ω being a 'good' quantum number. This set of conditions represents Hund's Case (a), and is illustrated in figure 5.3.

As can be seen in the illustration of case (a), the interatomic axis precesses about the direction of the vector $\boldsymbol{J}$, as the z axis does in the case of a symmetric rotor. This means that the rotational energy for the open-shell diatomic can be found using the methods outlined in chapter 4.

The rotational Hamiltonian will have the form

$$\hat{\mathscr{H}}_{rot} = \frac{\hat{O}^2}{2I_{bb}} \tag{5.4}$$

where I_{bb} has its standard definitions. $\hat{O}$ is end-over-end rotation operator represented by

$$\begin{aligned} \hat{O} &= \hat{J} - \hat{P} \\ &= \hat{J} - \hat{L} - \hat{S} \end{aligned} \tag{5.5}$$

where $\hat{P}$ is the non-rotational angular momentum. By substitution of equation 5.5 into 5.4, it can be seen that

$$\begin{aligned} \hat{\mathscr{H}}_{rot} &= \frac{1}{2I_{bb}}\left(\hat{J} - \hat{L} - \hat{S}\right)^2 \\ &= \frac{1}{2I_{bb}}\left(\hat{J}^2 + \hat{L}^2 + \hat{S}^2 - 2\hat{J}.\hat{L} - 2\hat{J}.\hat{S} + 2\hat{L}.\hat{S}\right) \end{aligned} \tag{5.6}$$

The terms $\hat{J}.\hat{L}$ and $\hat{J}.\hat{S}$ represent a decoupling of the orbital and spin angular momentum from the interatomic bond, due the affect of rotation. $\hat{J}.\hat{L}$ causes lambda-doubling, and $\hat{J}.\hat{S}$ causes a coriolis interaction. If these terms are considerable, then the system will move from Hund's case (a) to Hund's case (b). The term $\hat{L}.\hat{S}$ represents a spin-orbit interaction. This final type of interaction is discussed in section 5.3.1.

These coupling schemes are covered in greater depth in the literature [2], [3].

5.2 Nuclear Coupling

For molecules and complexes composed of nuclei which have a nuclear spin, I, of $1/2$ or more there will be a nuclear hyperfine splitting of the rotational energy levels due to an interaction of the nuclear spin and the magnetic molecular field. If I is greater than or equal to 1, then nuclear hyperfine splitting can also occur due to interaction of the nuclear spin and the electrical

molecular field. These splittings are only observed for non-spherically symmetric nuclei which have a quadrupole or higher order moment.

Within NO-O_2 and NO_2-O_2, ^{14}N is the only predominant isotope with a quadrupole moment, $I = 1$. ^{16}O has $I = 0$, but ^{17}O has $I = 5/2$. Given that the natural abundance of ^{17}O is 0.037% [4], nuclear spin-spin interactions can be disregarded to a first approximation.

When the system is rotating, this rotation is coupled to the nuclear motion and hence the nuclear spin, $\boldsymbol{I}$, will couple to the molecular rotational angular momentum, $\boldsymbol{J}$, to give the resultant, $\boldsymbol{F}$. This is assuming that there is no external field to which the system is subject. Both $\boldsymbol{I}$ and $\boldsymbol{J}$ precess about the resultant, as illustrated in figure 5.4.

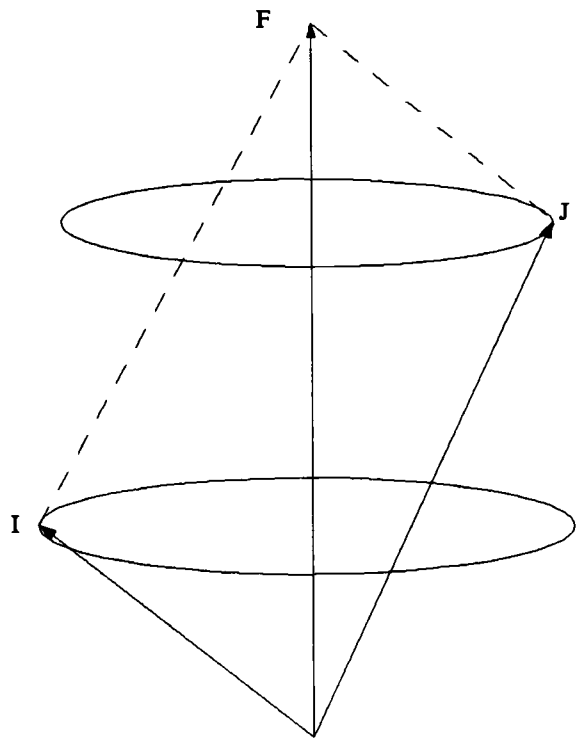

Figure 5.4: Precession of I and J around resultant F

This coupling means the total angular momentum of the molecule is represented by $\boldsymbol{F}$, rather than $\boldsymbol{J}$. However, to the first-order, $\boldsymbol{J}^2$ is still a constant of motion. Within this

coupling scheme the 'good' quantum numbers are F, M_F, J and I. The values that F and M_F can take are

$$F = J+I, J+I-1, J+I-2, \ldots, |J-I| \tag{5.7}$$

$$M_F = F, F-1, \ldots, -F \tag{5.8}$$

Just as for $\hat{J}$, the diagonal components of the total angular momentum are

$$\left\langle F, M_F \left| \hat{F}^2 \right| F, M_F \right\rangle = F(F+1) \tag{5.9}$$

$$\left\langle F, M_F \left| \hat{F}_Z \right| F, M_F \right\rangle = M_F \tag{5.10}$$

The nuclear coupling interaction places a twisting force on the nucleus, due to the non-spherical nature of the nuclear charge distribution, which will try to align the spin moment in the direction of the field gradient. The nuclear spin will precess around the field gradient.

In addition to the quadrupole coupling, magnetic coupling has a considerable effect on the observed spectra. These effects need to be taken into account to fully describe the hyperfine splitting observed for species with $I \geq 1$.

It is possible to represent the Hamiltonian for nuclear coupling within a cartesian framework using classical theory. However, the complexity of the mathematical notation can be greatly reduced with the use of spherical tensors, see section 5.3

5.3 Spherical Tensor Operators

As discussed in the above sections, often rotational spectra are complicated by the coupling of various forms of angular momenta. To fully describe these interactions, one has to be able to calculate matrix elements of operators between states of definite angular momentum, such as

$$\langle \alpha J M_J \,|T|\, \alpha' J' M'_J \rangle \tag{5.11}$$

where α represents all of the quantum numbers for the state other than J and its projection M_J. The best way to combine the various forms of angular momenta is through the use of *spherical tensor operators.* These are fully described in various texts [5], [6], and only the basics are detailed here.

An irreducible spherical tensor operator of rank k is defined as a set of $2k + 1$ functions, denoted as $T(k,q)$ or T^k_q, with components q = -k, -k + 1 , ... , k, that transform under a rotation of the reference frames as

$$\mathbf{R}T(k,q)\mathbf{R}^{-1} = \sum_{q'} D^k_{q'q}(R)\ T(k,q') \tag{5.12}$$

where $\mathbf{R}$ is the rotation operator, and $D^k_{q'q}$ is the *rotation matrix* [7]. The operator $T(k,q)$ behaves as a spherical harmonic. For a zero-rank spherical tensor operator, $T(0,0)$, any rotation leaves the function unchanged

$$\mathbf{R}T(0,0)\mathbf{R}^{-1} = D^0_{00}(R)\ T(0,0) = T(0,0) \tag{5.13}$$

These are termed *scalar operators.* The Hamiltonian is a scalar operator, as it is invariant

to rotation. First-rank operators behave under rotation as

$$\mathbf{R}T(1,q)\mathbf{R}^{-1} = D^1_{-1q}(R)\ T(1,-1) + D^1_{0q}(R)\ T(1,0) + D^1_{1q}(R)\ T(1,1) \tag{5.14}$$

These span three subspaces and hence behave as vectors. Hence they are termed *vector operators.* Angular momentum is a vector operator, as it operates within three dimensional space. Second rank operators behave under rotation as

$$\begin{aligned}\mathbf{R}T(2,q)\mathbf{R}^{-1} &= D^2_{-2q}(R)\ T(2,-2) + D^2_{-1q}(R)\ T(2,-1) \\ &\quad + D^2_{0q}(R)\ T(2,0) + D^2_{1q}(R)\ T(2,1) + D^2_{2q}(R)\ T(2,2)\end{aligned} \tag{5.15}$$

These span five subspaces and hence behave as the quadrupole moments of a charge distribution. Tensors with ranks greater than two appear rarely and in any case do not appear in the modelling of the species studied.

Using the spherical tensor operator representation, the angular momentum operators in the space-fixed frame are given by [8]

$$\hat{J}^1_1 = -\frac{1}{\sqrt{2}}(\hat{J}_x + i\hat{J}_y) = -\frac{1}{\sqrt{2}}\hat{J}_+ \tag{5.16}$$

$$\hat{J}^1_0 = \hat{J}_z \tag{5.17}$$

$$\hat{J}^1_{-1} = \frac{1}{\sqrt{2}}(\hat{J}_x - i\hat{J}_y) = \frac{1}{\sqrt{2}}\hat{J}_- \tag{5.18}$$

This relationship also applies to the molecule-fixed frame for non-rotational angular mo-

mentum. For rotational angular momentum the relationship becomes more complex [8]. Using the above definition of the angular momentum one can easily change between various reference frames, be they space-fixed, or molecule-fixed.

Wigner-Eckart Thorem

The Wigner-Eckart theorem [9] is powerful theorem that allows for the separation of matrix elements into a physical part, represented by a *reduced matrix element* and a geometric part represented by a Clebsch-Gordan coefficient or Wigner symbol. With the use of this theorem, the use of tensors greatly simplifies the calculation of matrix elements related by angular momentum operators.

For a system with a basis set

$$|\alpha J M_J\rangle \tag{5.19}$$

the application of Wigner-Eckart theorem gives [9]

$$\begin{aligned}\langle \alpha J M_J \,|T(k,q)|\, \alpha' J' M'_J\rangle &= \langle kq, J' M'_J | J M_J\rangle \left\langle \alpha J \left|\left|T^k\right|\right| \alpha' J'\right\rangle \\ &= (-1)^{J-M_J} \begin{pmatrix} J & k & J' \\ -M_J & q & M'_J \end{pmatrix} \left\langle \alpha J \left|\left|T^k\right|\right| \alpha' J'\right\rangle \end{aligned} \tag{5.20}$$

The *reduced matrix element* is $\left\langle \alpha J \left|\left|T^k\right|\right| \alpha' J'\right\rangle$. This theorem is used extensively below. This result and the general tensor algebra relationships used are presented in Appendix A.

5.3.1 Spin Coupling

The spin orbital coupling described in section 5.1 can be represented by first-rank tensor operators. The Hamiltonian for the interaction is given by

$$\hat{\mathscr{H}}_{SO} = \zeta T^1(\mathbf{L}).T^1(\mathbf{S}) \tag{5.21}$$

where $T^1(\mathbf{L})$ represents the first-rank orbital operator, and $T^1(\mathbf{S})$, is the first-rank spin operator. By expanding equation 5.21 and converting into the cartesian framework, it can be seen that

$$\hat{\mathscr{H}}_{SO} = \zeta \left(\hat{L}_z \hat{S}_z + \frac{1}{2} \left(\hat{L}^+ \hat{S}^- + \hat{L}^- \hat{S}^- \right) \right) \tag{5.22}$$

The second and third term connect different electronic states, and are commonly disregarded due to the high excitation energy to these states. Considering a basis set of

$$|\eta \Lambda S \Sigma\rangle \tag{5.23}$$

The dominant matrix element for $\hat{\mathscr{H}}_{SO}$ is

$$\left\langle \eta \Lambda S \Sigma \left| \zeta \hat{L}_z \hat{S}_z \right| \eta \Lambda' S \Sigma' \right\rangle = \delta_{\Lambda,\Lambda'} \delta_{\Sigma,\Sigma'} \zeta \Lambda' \Sigma' \tag{5.24}$$

5.3.2 Electric Quadrupole

As shown for spin coupling, spherical tensors can be used to simplify the calculation of matrix elements between definite states be they spin or nuclear related. The Hamiltonian for the

nuclear quadrupole interaction can be written as a scalar product of two second-rank spherical tensor operators [10] [11]

$$\hat{\mathscr{H}}_Q = \sum_p (-1)^p T_p^2(\mathbf{Q}) T_{-p}^2(\nabla\nabla\mathbf{V}) \tag{5.25}$$

where $T_p^2(\mathbf{Q})$ is the nuclear quadrupole tensor and $T_{-p}^2(\nabla\nabla\mathbf{V})$ is the field gradient tensor due to the electrons and other nuclei present within the molecule. Considering the molecular case for an appropriate basis set could be

$$|\eta J K_a I F M_F\rangle \tag{5.26}$$

Therefore, by application of tensor algebra, it is possible to derive a general matrix element

$$\begin{aligned}
&\left\langle \eta J K_a I F M_F \left| \hat{\mathscr{H}}_Q \right| \eta' J' K_a' I' F' M_F' \right\rangle \\
&\quad = \left\langle \eta J K_a I F M_F \left| T^2(\mathbf{Q}) T^2(\nabla\nabla\mathbf{V}) \right| \eta' J' K_a' I' F' M_F' \right\rangle \\
&\quad = (-1)^{(J'+I+F')} \delta_{F'F} \delta_{M_F' M_F} \begin{Bmatrix} F' & I & J \\ 2 & J' & I' \end{Bmatrix} \\
&\qquad \left\langle \eta J K_a \left|\left| T^2(\nabla\nabla\mathbf{V}) \right|\right| \eta' J' K_a' \right\rangle \left\langle I \left|\left| T^2(\mathbf{Q}) \right|\right| I \right\rangle
\end{aligned} \tag{5.27}$$

Using standard relationships, presented in Appendix A, it is possible to determine expressions for the two reduced matrix elements in equation 5.27. Considering initially the field gradient term, one has to convert from the space-fixed frame to the molecule-fixed frame [10]

$$\begin{aligned}\left\langle \eta J K_a \left|\left| T^2(\nabla\nabla\mathbf{V}) \right|\right| \eta' J' K_a' \right\rangle \\ = (-1)^{(J-K_a)} \left((2J'+1)(2J+1)\right)^{\frac{1}{2}} \\ \sum_q \begin{pmatrix} J & 2 & J' \\ -K_a & q & K_a' \end{pmatrix} \left\langle \eta \left| T_q^2(\nabla\nabla\mathbf{V}) \right| \eta' \right\rangle \end{aligned} \tag{5.28}$$

where $\left\langle \eta \left| T_q^2(\nabla\nabla\mathbf{V}) \right| \eta' \right\rangle$ is a molecular component of the field gradient, and can be determined for the specific system in question.

To determine the expression for the quadrupole reduced matrix element, initially a definition is required for the quadrupole moment of the nucleus, Q

$$\begin{aligned} eQ &= 2\left\langle IM_I = I \left| T_0^2(\mathbf{Q}) \right| IM_I = I \right\rangle \\ &= 2(-1)^{(I-I)} \begin{pmatrix} I & 2 & I \\ -I & 0 & I \end{pmatrix} \left\langle I \left|\left| T^2(\mathbf{Q}) \right|\right| I \right\rangle \end{aligned} \tag{5.29}$$

Therefore it can be seen by substitution that

$$\left\langle I \left|\left| T^2(\mathbf{Q}) \right|\right| I \right\rangle = \frac{eQ}{2\begin{pmatrix} I & 2 & I \\ -I & 0 & I \end{pmatrix}} = \frac{1}{2} eQ \left[\frac{(2I+3)(2I+2)(2I+1)}{(2I)(2I-1)}\right]^{\frac{1}{2}} \tag{5.30}$$

By combining equations 5.28 and 5.30 and substituting the result into 5.27, it can be seen that

$$\left\langle \eta J K_a I F M_F \left| T^2(\mathbf{Q}) T^2(\nabla\nabla\mathbf{V}) \right| \eta' J' K'_a I' F' M'_F \right\rangle$$

$$\begin{aligned} = \; & (-1)^{(J'+I+F')} (-1)^{(J-K_a)} \left((2J'+1)(2J+1)\right)^{\frac{1}{2}} \delta_{F'F} \delta_{M'_F M_F} \\ & \left\{ \begin{array}{ccc} F' & I & J \\ 2 & J' & I' \end{array} \right\} \frac{1}{2} eQ \left[\frac{(2I+3)(2I+2)(2I+1)}{(2I)(2I-1)} \right]^{\frac{1}{2}} \\ & \sum_q \left(\begin{array}{ccc} J & 2 & J' \\ -K_a & q & K'_a \end{array} \right) \left\langle \eta \left| T^2_q(\nabla\nabla\mathbf{V}) \right| \eta' \right\rangle \end{aligned} \tag{5.31}$$

Specific application of electric quadrupole interactions is left until chapters 6 and 7.

5.3.3 Magnetic Dipole

The Hamiltonian for the magnetic hyperfine interaction is given by [12] the first rank tensor scalar product of the nuclear spin angular momentum operator, $T^1(\mathbf{I})$, and an operator, $T^1(\mathbf{X})$, combining the NO spin-orbit interaction, $T^1(\mathbf{I}).T^1(\mathbf{L})$, the Fermi contact interaction, $T^1(\mathbf{I}).T^1(\mathbf{S})$, and the interaction of the electron and nuclear dipole-dipole, $T^1(\mathbf{I}).T^1(\mathbf{S}, C^2)$ [12]

$$\begin{aligned} \hat{\mathscr{H}}_{mag} &= T^1(\mathbf{I}).T^1(\mathbf{X}) \\ &= T^1(\mathbf{I}).\left[g_I \mu_B \mu_I \left(\frac{2}{r^3} T^1(\mathbf{L}) + \frac{8\pi}{3} g_e \left| \Psi(r=0)^2 \right| T^1(\mathbf{S}) - \sqrt{10} g_e \frac{1}{r^3} T^1(\mathbf{S}, C^2) \right) \right] \end{aligned} \tag{5.32}$$

By application of the above tensor algebra it is possible to evaluate matrix elements of the Hamiltonian given in 5.32 using as a basis set

$$|\eta L \Lambda S \Sigma J K_a I F M_F\rangle \tag{5.33}$$

The matrix elements are given by

$$\langle \eta L \Lambda S \Sigma J K_a I F M_F | \, T^1(\mathbf{I}).T^1(\mathbf{X}) \, | \eta' L' \Lambda' S' \Sigma' J' K'_a I F' M'_F \rangle$$

$$= \delta_{F'F}(-1)^{(J'+I+F)} \left\{ \begin{array}{ccc} J & I & F \\ I & J' & 1 \end{array} \right\} \langle I \, || T^1(\mathbf{I}) || \, I \rangle \, \langle \eta L \Lambda S \Sigma J K_a \, || T^1(\mathbf{X}) || \, \eta' L' \Lambda' S' \Sigma' J' K'_a \rangle \quad (5.34)$$

Using the standard expression detailed in Appendix A, it can be seen that

$$\langle I \, || T^1(\mathbf{I}) || \, I \rangle = [(2I+1)\, I \, (I+1)]^{\frac{1}{2}} \quad (5.35)$$

The second reduced matrix element, $\langle \eta L \Lambda S \Sigma J K_a \, || T^1(\mathbf{X}) || \, \eta' L' \Lambda' S' \Sigma' J' K'_a \rangle$, can be shown to be equal to [10]

$$\sum_q (-1)^{(J-K_a)} \, [(2J+1)(2J'+1)]^{\frac{1}{2}} \left(\begin{array}{ccc} J & 1 & J' \\ -K_a & q & K'_a \end{array} \right) \langle \eta L \Lambda S \Sigma | \, T^1_q(\mathbf{X}) \, | \eta' L' \Lambda' S' \Sigma' \rangle \quad (5.36)$$

where $T^1(\mathbf{X})$ is now expressed in terms of the molecule-fixed frame. Therefore, by combining equations 5.34, 5.35 and 5.36, a general matrix element is given by

$$\langle \eta L \Lambda S \Sigma J K_a I F M_F | \, T^1(\mathbf{I}).T^1(\mathbf{X}) \, | \eta' L' \Lambda' S' \Sigma' J' K'_a I F' M'_F \rangle$$

$$= \delta_{F'F}(-1)^{(J'+I+F)} \begin{Bmatrix} J & I & F \\ I & J' & 1 \end{Bmatrix}$$
$$[(2I+1)\,I\,(I+1)]^{\frac{1}{2}}\,[(2J+1)(2J'+1)]^{\frac{1}{2}}$$
$$\sum_q (-1)^{(J-K_a)} \begin{pmatrix} J & 1 & J' \\ -K_a & q & K'_a \end{pmatrix} \langle \eta L \Lambda S \Sigma |\, T^1_q(\mathbf{X}) \,| \eta' L' \Lambda' S' \Sigma' \rangle \qquad (5.37)$$

The exact form of the final integral, $\langle \eta L \Lambda S \Sigma |\, T^1_q(\mathbf{X}) \,| \eta' L' \Lambda' S' \Sigma' \rangle$ is dependent on the exact species being studied. The different components of $T^1_q(\mathbf{X})$ give different spectral constants, and therefore provide distinct information about the observed species. The details of the application of equation 5.37 to NO-O_2 are discussed in chapter 6, but the general form can be found in previous papers by the group [13].

Spherical tensors provide an easy manner in which to combine the various forms of angular momentum which are present in molecular systems and which affect rotational spectra that are recorded at high resolution. The above treatment gives a general introduction to the use of spherical tensor operators, whilst their application to specific systems is presented in chapters 6 and 7.

Conclusion

This chapter has extended the initial theory of rotation discussed in chapter 4, to include the effects of electron and nuclear spin. These effects were considered in abstract isolation, but they have been expressed in terms of spherical tensor operators to allow for subsequent manipulation. The open-shell species NO-O_2 and NO_2-O_2, as mentioned above, are subject to both spin coupling and nuclear coupling. The combination of these two interactions leads to further complication of the rotational spectra. The specific application and combination of the above theory is detailed in the following species-specific chapters. The additional effects of

nuclear spin-spin coupling, nuclear spin-rotation coupling and the external Stark and Zeeman effect have not been considered as these do not arise at significant levels in the species studied within this thesis.

References

[1] G. Herzberg *Molecular Spectra and Molecular Structure: Spectra of Diatomic Molecules.* D. Van Nostrand Company, Inc. (1963)

[2] R. N. Zare *Angular Momentum: Understanding Spatial Aspects in Chemistry and Physics.* John Wiley & Sons (1988)

[3] J. D. Graybeal *Molecular Spectroscopy.* McGraw-Hill, Inc (1988)

[4] R. C. Weast (Ed.) *Handbook of Chemistry and Physics.* CRC Press, Inc. (1974)

[5] M. L. Boas *Mathematical Methods in the Physical Sciences.* John Wiley & Sons (1983)

[6] G. Arfken *Mathematical Methods for Physicists.* Academic Press, Inc. (1985)

[7] R. N. Zare *Angular Momentum: Understanding Spatial Aspects in Chemistry and Physics* (pp. 85-91). John Wiley & Sons (1988)

[8] R. N. Zare *Angular Momentum: Understanding Spatial Aspects in Chemistry and Physics* (pp. 177-180). John Wiley & Sons (1988)

[9] R. N. Zare *Angular Momentum: Understanding Spatial Aspects in Chemistry and Physics* (pp. 180-186). John Wiley & Sons (1988)

[10] B. J. Howard, *by personal communication*

[11] A. R. Edmonds *Angular momentum in quantum mechanics.* Princeton University Press (1960)

[12] C. R. Dennis, C. J. Whitham and B.J. Howard, J. Chem. Phys. **115**, 1355 (2001)

[13] P. D. A. Mills, C. M. Western and B. J. Howard, J. Phys. Chem. **90**, 3331 (1986)

Chapter 6

Calculations and Theory of $NO\text{-}O_2$

"Never make anything simple and efficient when a way can be found to make it complex and wonderful."

Anonymous

Introduction

Detailed *ab initio* calculations have been performed on $NO\text{-}O_2$, based on the methods outlined in chapter 3. The details on the exact methods used are presented below with the results presented in Appendix B.

Specific theory has been developed to fully describe the rotational spectra of $NO\text{-}O_2$. Relevant fine and hyperfine structure terms have been taken into account using the methods outlined in chapter 5 and below.

Using the Fourier Transform Microwave Spectroscopy (FTMS) techniques detailed above, the region from 7 to 18 GHz have been scanned to record transitions from NO-O_2. The results of the experiments and their connection to the developed theory are discussed.

6.1 *Ab initio* Calculations

The calculations on the NO-O_2 complex were performed in two stages. Initially, single-reference *Møller Plesset* second order perturbation theory (MP2) calculations were performed with Gaussian 03 [1] using the 6-311++G(d,p) basis set. These initial calculations could not fully represent the ground state of NO-O_2, and led to unsound results. The reasons for this poor representation are discussed below. Subsequent calculations were performed with MOLPRO [2] using a multi-reference Multi-Configuration Self Consistent Field (MCSCF) coupled to second order perturbation theory using the Dunning basis sets. The details of these calculations and their inherent limitations are outlined below with presentation of the salient data.

6.1.1 Single-reference Calculations

Initial *ab initio* calculations were performed using the standard MP2 method and the 6-311++G(d,p) basis set using Gaussian 03 [1]. This has been the standard method used within the group for weak interactions.

As NO-O_2 has three unpaired electrons, it can take on the form of a spin state doublet (S = 1/2) and quartet (S = 3/2). These two spin states were calculated separately. Preliminary Potential Energy Surface (PES) calculations were performed to locate local energy minima. The doublet spin state gave seven distinct local minima, and the quartet gave twenty seven. These thirty four geometries were geometrically optimised using a full counterpoise correction, as detailed in chapter 3. The optimisation process was hampered by convergence problems. It proved impossible to numerically converge one of the doublet and four of the quartet geometries. With hindsight it is clear that these calculations are inappropriate as these states are poorly

described by a single-reference configuration.

The relevant data from the three highest binding energy calculations for the two spin states are listed below

Doublet Spin State

Geometry	Corrected Energy (Hartree)	Binding Energy (cm^{-1})	Rotational Constant A (GHz)	Rotational Constant B (GHz)	Rotational Constant C (GHz)
a	-279.65530203	-65.68	56.500	1.885	1.824
b	-279.65530201	-65.67	56.478	1.884	1.823
c	-279.65530200	-65.67	56.717	1.883	1.822

Quartet Spin State

Geometry	Corrected Energy (Hartree)	Binding Energy (cm^{-1})	Rotational Constant A (GHz)	Rotational Constant B (GHz)	Rotational Constant C (GHz)
a′	-279.65526613	-57.80	50.182	1.846	1.780
b′	-279.65525566	-55.50	53.331	1.799	1.740
c′	-279.65525497	-55.35	53.308	1.800	1.741

The data for all of the converged calculations and illustrations of the physical form of geometries a, b, c, a′, b′ and c′ are located in Appendix B.

Considering just geometries a, b and c in the above tables, it can be seen that the doublet has converged to two separate geometries, with b and c representing the same geometry and a being distinct. Consideration of a′, b′ and c′ illustrates that the quartet has three distinct geometries of similar energies. The other calculated geometries for the doublet and quartet had distinct structural forms. The poor convergence of geometry optimisation led to careful consideration of the theoretical framework underlying the *ab initio* methods used.

6.1.2 Multi-reference Calculations

The various electronic states of NO-O_2 are best understood, by relating them to the occupancy of orbitals in both NO and O_2. For O_2 the ground state is $^3\Sigma^-$, but there are two low lying excited states, $^1\Delta$ and $^1\Sigma^+$, at 7,918 and 13,195 cm^{-1} [3] respectively, derived from the ground state electron configuration of π^{*2}. The ground state and first two excited states of O_2 are illustrated in figure 6.1. These low-lying states are of importance in these calculations since they arise from the same electron configuration as the ground state. The ground state of NO is $^2\Pi$, with the first excited state, $^2\Sigma^+$, at 43,965 cm^{-1} [3]. This initial excitation represents an excitation of the unpaired electron from the π^* orbital to a σ^* orbital. These two states are illustrated in figure 6.2. The impact of the NO first excited state can be accounted for with perturbation theory due to its high level of excitation.

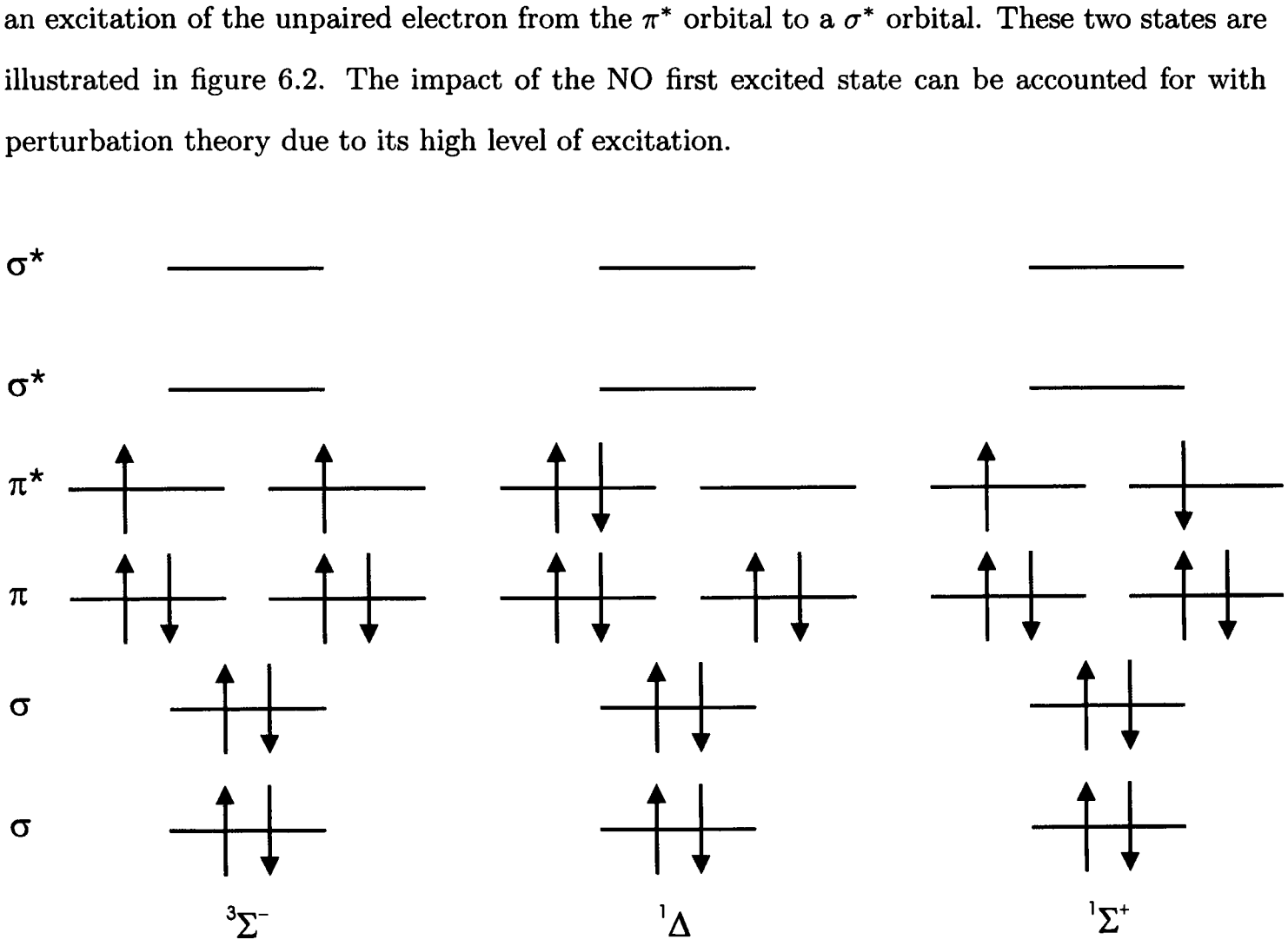

Figure 6.1: Three lowest electronic states of O_2

It can be seen that there are many possible combinations of NO and O_2 that are conceivable. Classing the non π^* orbital electrons as core electrons, the states of the complex can be

constructed by populating the four π^* orbitals with three electrons. Initially there are $C_3^8 = 56$ determinant wave functions. However, of these 56 determinants, only four distinct states are possible within the Van der Waals complex where the NO and O_2 retain their respective ground states, $^2\Pi$ and $^3\Sigma^-$. The occupancy of the π^* orbitals for these four states are illustrated in figure 6.3.

The four possible states for NO-O_2 are divided into two doublets (S = 1/2) and two quartets (S = 3/2). The doublet results from an anti-parallel alignment of the O_2 and NO spins, and the quartet results from a parallel alignment. These pairs can be further sub-divided, if the complex is planar. In a planar geometry the complex will have a C_s symmetry allowing the π^* orbitals to the separated into A' and A'' symmetries. In a planar geometry the π^* orbitals on the O_2 are A' and A'', giving an overall A'' $^3\Sigma^-$ state. The NO π^* orbital can be either of A' or A'' symmetry. Combining the symmetries of the two diatomic molecules, the overall symmetry of the complex wavefunction is controlled by the NO π^* orbital. An NO A' π^* occupation gives

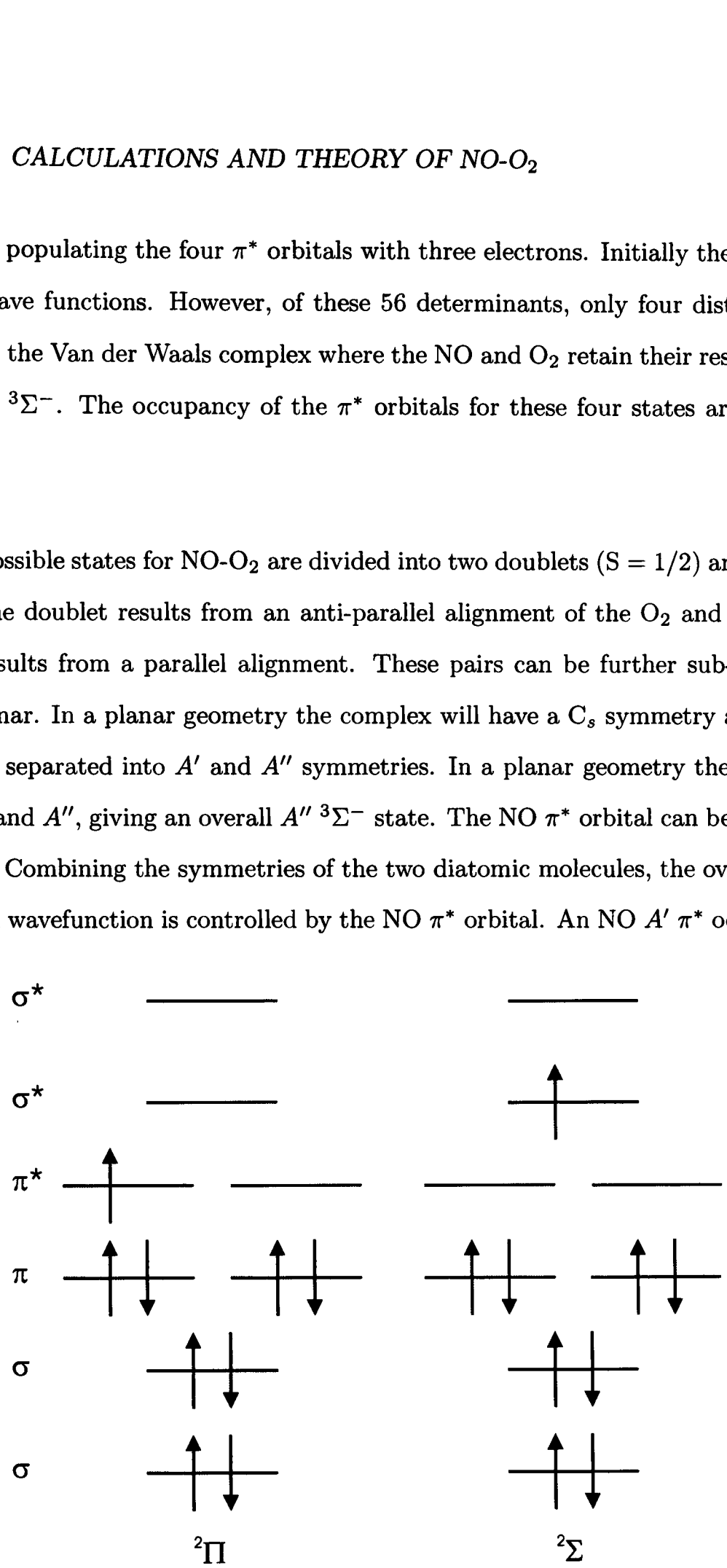

Figure 6.2: Two lowest electronic states for NO

an A'' overall wavefunction and vice versa. Thus, assuming a planar geometry, the four possible electronic states for NO-O_2 can be classified as $^2A''$, $^4A''$, $^2A'$ and $^4A'$. This division of the possible states into distinct multiplicities and symmetries greatly simplifies the *ab initio* calculations.

The quartet states for NO-O_2 can only be formed by a combination of the ground state diatomic molecules: $^2\Pi + {}^3\Sigma^-$. Since there is only one way to form the quartet, when all of the unpaired electrons are α, this state can be fully represented by a single-reference *ab initio* methods.

The doublet states can be formed not only from the combination of the ground state diatomic molecules, $^2\Pi + {}^3\Sigma^-$, but also from a combination of $^2\Pi$ NO and the first or second excited states of O_2, $^1\Delta$ or $^1\Sigma^+$. This leads to a lack of clarity in determining the progenitors of the doublet spin state. To fully represent this state a multi-reference *ab initio* method has to be used. The reason for this is illustrated below, with the case of two electrons.

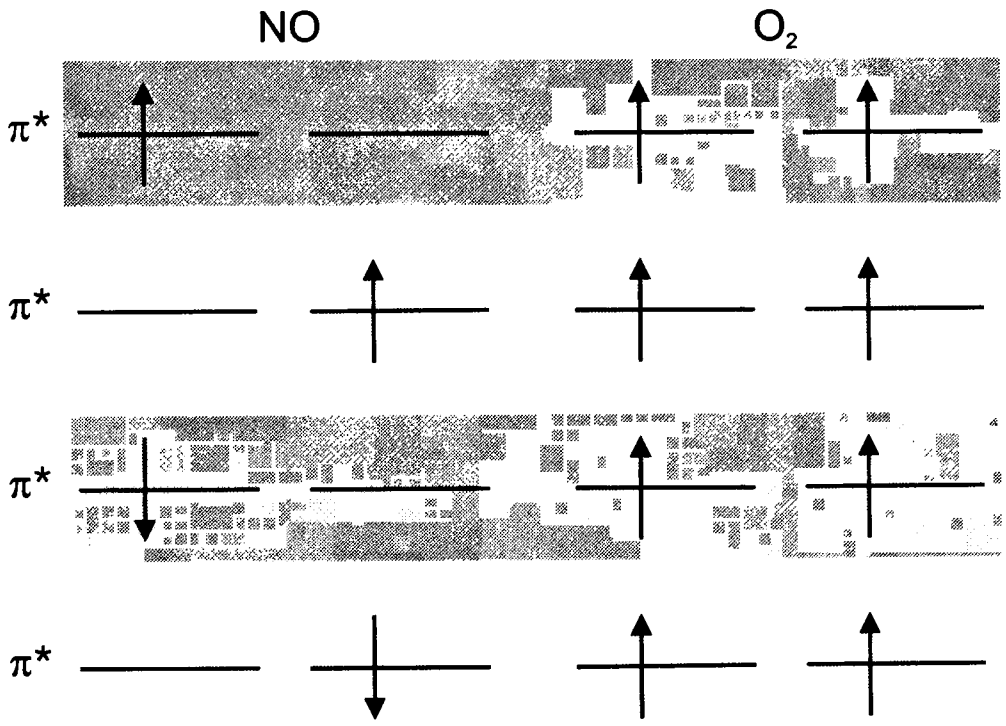

Figure 6.3: Four possible electronic states for NO-O_2

Considering a system with just two unpaired electrons, electrons 1 and 2, occupying one of two distinct orbitals, A or B, with one of two distinct spins, α or β. For each electron, 1 or 2, there are four possible spin orbitals

$$A(1)\alpha_1, \qquad A(1)\beta_1, \qquad B(1)\alpha_1, \qquad B(1)\beta_1,$$

$$A(2)\alpha_2, \qquad A(2)\beta_2, \qquad B(2)\alpha_2, \qquad B(2)\beta_2$$

These one electron orbitals can combine to give two orbitals by taking product combinations. For example

$$A(1)\alpha_1 \times A(2)\alpha_2 = A(1)\alpha_1 A(2)\alpha_2 \tag{6.1}$$

The 16 resulting overall two electron states, generated by taking all possible products, are

$$A(1)\alpha_1 A(2)\alpha_2, \qquad A(1)\alpha_1 A(2)\beta_2, \qquad A(1)\alpha_1 B(2)\alpha_2, \qquad A(1)\alpha_1 B(2)\beta_2,$$

$$A(1)\beta_1 A(2)\alpha_2, \qquad A(1)\beta_1 A(2)\beta_2, \qquad A(1)\beta_1 B(2)\alpha_2, \qquad A(1)\beta_1 B(2)\beta_2,$$

$$B(1)\alpha_1 A(2)\alpha_2, \qquad B(1)\alpha_1 A(2)\beta_2, \qquad B(1)\alpha_1 B(2)\alpha_2, \qquad B(1)\alpha_1 B(2)\beta_2,$$

$$B(1)\beta_1 A(2)\alpha_2, \qquad B(1)\beta_1 A(2)\beta_2, \qquad B(1)\beta_1 B(2)\alpha_2, \qquad B(1)\beta_1 B(2)\beta_2$$

By taking combinations of the above states to form a singlet spin states with unpaired electrons, omitting states forbidden by the Pauli exclusion principle, the resulting wavefunctions can be written as

$$\begin{aligned}\Psi &= [A(1)B(2)\,(\alpha_1\beta_2 \pm \beta_1\alpha_2) \mp B(1)A(2)\,(\alpha_1\beta_2 \pm \beta_1\alpha_2)] \\ &= \left[\left| \begin{array}{cc} A(1)\alpha_1 & A(1)\beta_1 \\ B(2)\alpha_2 & B(2)\beta_2 \end{array} \right| \mp \left| \begin{array}{cc} B(1)\alpha_1 & B(1)\beta_1 \\ A(2)\alpha_2 & A(2)\beta_2 \end{array} \right|\right]\end{aligned} \tag{6.2}$$

which cannot be represented in terms of a single Slater Determinant (SD), see chapter 3. The inability to represent the basic wavefunction with a single SD means that the Hartree-Fock and MP2 methods are invalid and would not be expected to calculate meaningful results.

This simple model illustrates the problems of calculations for an open-shell system where the spin is less than the maximum. This reasoning accounts for many of the problems encountered with O_2 and can be extended to three unpaired electrons giving a low-spin doublet. Having realised this problem with the initial MP2 calculations, multi-reference calculations were performed.

The exact method used for the calculations of NO-O_2 was Restricted Open-Shell Hartree-Fock (ROHF) followed by Multi-reference Rayleigh Schrödinger Second Order Perturbation Theory (RSPT2) using the MOLPRO[2] package. RSPT2 was selected as it takes account, by second order perturbation theory, of dispersion forces, which are of crucial importance in weakly bound complexes. The more basic Complete Active Space Self-Consistent Field (CASSCF) only partially accounts for these forces, and hence will give an inaccurate representation of the binding. The Complete Active Space (CAS) that was used in the RSPT2 calculations was generated from the three unpaired electrons and the four π^* orbitals on the NO and O_2. ROHF was used instead of Unrestricted Hartree-Fock to minimize spin-contamination effects.

Because of the 'flatness' of the potential energy surface and the variation of the counterpoise

correction with geometry, it was difficult to determine the equilibrium geometry of the complex by geometry optimisation methods. Instead the PES of the complex was calculated. Calculations were performed over a range of geometries, using the parameters illustrated in figure 6.4.

The bond lengths of NO and O_2 are fixed to their calculated monomer values of 1.1347 Å and 1.2234 Å respectively. This does not permit relaxation of the monomer geometries, and may slightly underestimate the overall binding energy (BE), but reduces the number of dimensions of the PES from six to four. The NO and O_2 are placed with their centre of mass on the z axis of the complex. θ_{NO} is the angle between the z axis and the line of atomic centres of NO. The angle θ_{O_2} is the equivalent for the O_2 diatomic. The angle ϕ represents the difference between the rotation of the two monomers, ϕ_{NO} and ϕ_{O_2}, about the z axis, see figure 6.5. R is the separation of the centre of masses of NO and O_2 along the z axis.

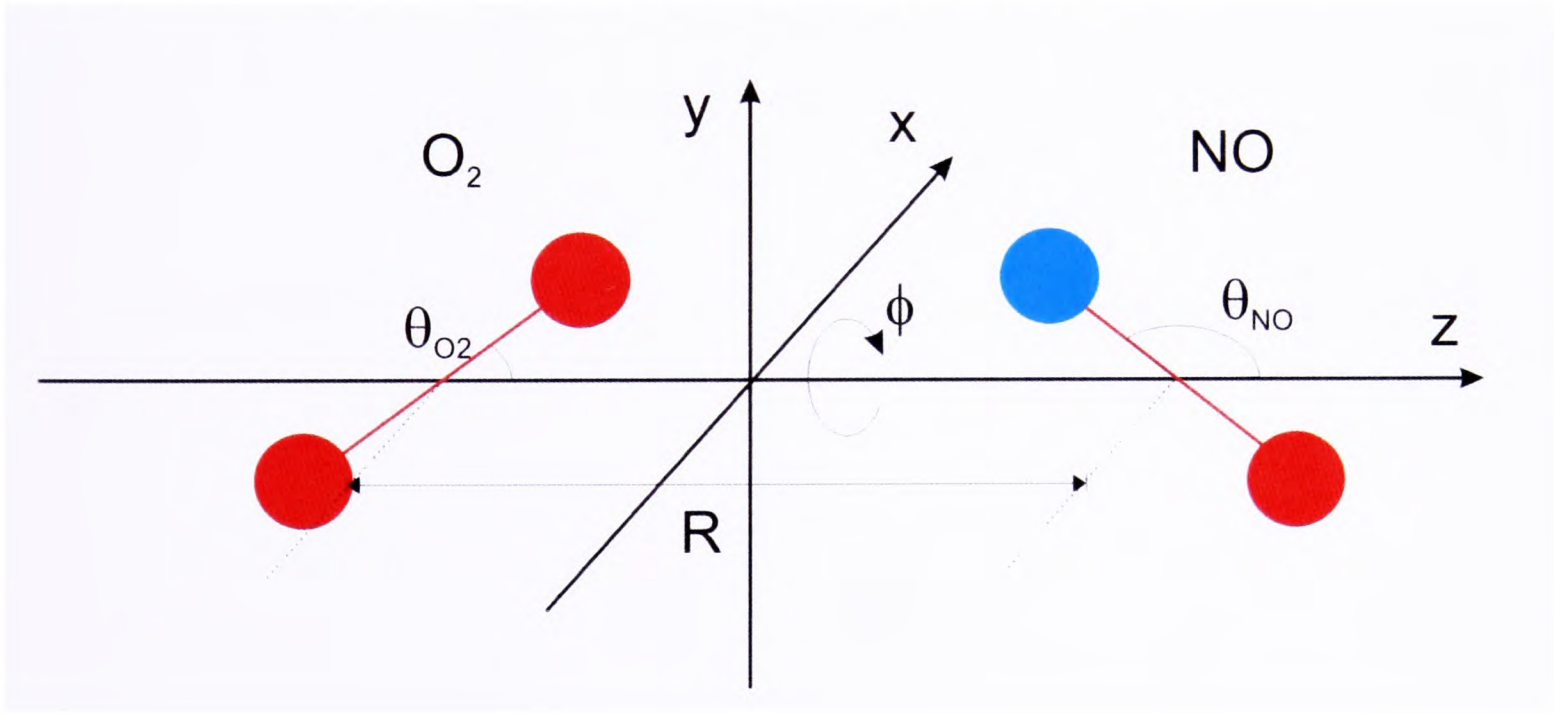

Figure 6.4: Geometry of NO-O_2 for calculations

The calculations were performed with both the Dunning's aug-cc-pVDZ and aug-cc-pVTZ basis sets. Two basis sets were used to enable basis set extrapolation to be performed. See original discussion in chapter 3. This extrapolation approximates the energy that would be calculated using a Complete Basis Set (CBS). Previous work has been preformed on extrapo-

lation using the Dunning basis sets by Truhlar [4] and Klopper [5]. Both Truhlar and Klopper proposed using a separate power series expansion for the extrapolation of the Hartree-Fock and Electron Correlation (EC) energies. However, the functional form of the extrapolation does not need to be a power series, since the only constraint is that $E_X \rightarrow E_\infty$ as $X \rightarrow \infty$, where X is the level of the Dunning basis set. This means there are numerous functional forms are possible, which should be evaluated by the relative accuracy of their convergence to the CBS limit. Using the data from the Klopper paper [5], and MP2 calculations it has been found that an exponential extrapolation provides a better convergence to the CBS limit than a power series expansion.

Using the functional form

$$E_X^{HF} = E_\infty^{HF} + A^{HF} e^{-\beta' X + \gamma' X^2} \tag{6.3}$$

$$E_X^{EC} = E_\infty^{EC} + A^{EC} e^{-\beta X + \gamma X^2} \tag{6.4}$$

and if the CBS limit is known it is possible to solve for the coefficients β, γ, β' and γ' using

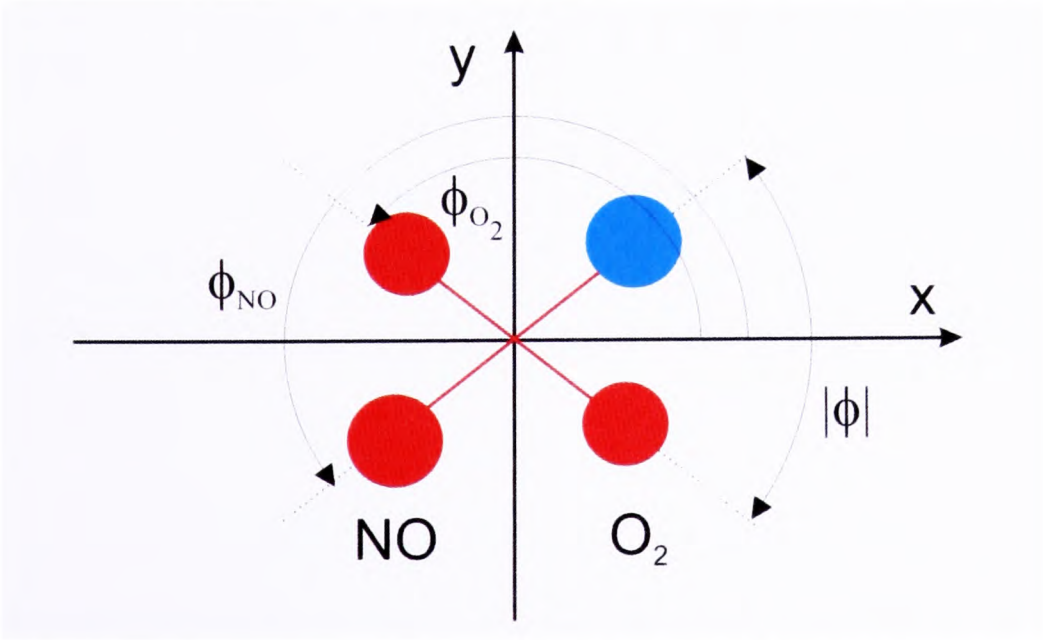

Figure 6.5: Geometry of NO-O_2 for calculations - Viewed parallel to z axis. $\phi = \phi_{NO} - \phi_{O_2}$

equations for the energy difference

$$\delta E_X = E_X - E_\infty = Ae^{-\beta X+\gamma X^2} \tag{6.5}$$

$$\begin{aligned} ln\left(\frac{\delta E_{X+1}}{\delta E_X}\right) &= ln\left(\frac{e^{-\beta(X+1)+\gamma(X+1)^2}}{e^{-\beta X+\gamma X^2}}\right) \\ &= -\beta+\gamma(2X+1) \end{aligned} \tag{6.6}$$

Thus, a plot of the above equation will provide a straight line with an intercept of $-\beta$ and a gradient of γ. Linear regressions on the extensive data sets from Klopper's paper [5] and additional Hartree-Fock calculations, gives β = 1.2184, γ = 0.0629 and β' = 0.6154, γ' = -0.1474, with correlations coefficients of the fits of $|r^2|$ = 0.9880 and $|r'^2|$ = 0.7620 respectively. Using these extrapolation coefficients, even with an extrapolation based on the smallest two basis sets, aug-cc-pVDZ and aug-cc-pVTZ, the relative error between the extrapolation value and the true value, taken to be the CBS limit, is of the order of 0.5 - 1.0 %. Most of this error, of a few milli Hartrees, is due to the EC extrapolation. This error is considerably better than the relative errors from the power series extrapolation. The extrapolation coefficients, calculated with MP2 theory, were used for the extrapolation performed on the RSPT2 PES calculations.

For the doublet calculations, ideally both the ROHF and RSPT2 calculations would have been based on the low spin doublet. However, with MOLPRO this low spin is only achievable within multi-reference methods. Therefore the doublet RSPT2 calculations were based on quartet ROHF orbitals.

The RSPT2 method is not inherently size consistent, as detailed in chapter 3, with the size inconsistency being dependent on the choice of zeroth-order Hamiltonian. Using the methods outlined by Rintelman et al. [6], the Size-Consistency Error (SCE) was calculated for all four

electronic states of NO-O_2, as defined in chapter 3. The results of these calculations for the planar system are

Electronic State	SCE cm^{-1}
$^2A'$	45.2968
$^2A''$	45.2968
$^4A'$	15.4809
$^4A''$	15.4809

The SCE are, as expected, the same for both symmetries of the doublet and quartet complex. These SCE have been quoted to six significant figures to illustrate their consistency across the different symmetries. These SCE were used to adjust the extrapolated potential so they tend to zero at large R.

The methods detailed above were used for calculations not only for $\phi = 0.0°$ of the complex geometry, but also for $\phi \neq 0.0°$. With the complex non-planar, the symmetry of the system is lowered from C_s to C_1. This means that it is not possible to trivially separate the two distinct forms of the NO π^* occupancy which can lead to cross-contaminations between the formally A' and A'' states. To reduce the effect of cross-contamination, the calculations for $\phi \neq 0.0°$ were initially performed with $\phi = 0.0°$, where is is possible to distinguish the A' and A'' states, and then the complex was twisted, with ϕ incremented in steps of 30° until the desired value of ϕ was reached, carrying forward orbitals of the preceding calculations. This method gave the expected continuous change in the potential of the system with no discontinuities, for $0.0° \leq \phi \leq 60.0°$, and was therefore taken as a reasonable approximation. For ϕ greater that 60.0° discontinuities were encountered. This led to hesitation in using these calculated values. Given that $\phi > 60.0°$ represented a high energy region of the PES which would not be accessible by the weakly bound complex, ϕ was limited to 60.0°.

The full PES can be found in electronic form on the attached CD. The PES covers the range R = 2.8 to 4.8 Å , θ_{O_2} = 0.0 to 180.0°, θ_{NO} = 0.0 to 180.0° and ϕ = 0.0 to 60.0°. ϕ was varied in steps of 30.0°. When $\phi = 0.0°$, the step size of θ_{O_2} and θ_{NO} was 10.0°, but when $\phi \neq 0.0°$. the step size was increased to 20.0°. The step size for R is 0.2 Å , regardless of the value of ϕ. Calculations were only performed for $90.0° > \phi > 0.0°$ since energies for other values of ϕ, 90.0 - 360.0, can be determined by symmetries in θ_{O_2} and θ_{NO}.

Having completed the PES calculation, the global minimum of the calculated points was found to be on the $^2A''$ surface, at R = 3.0 Å , $\theta_{O_2} = \theta_{NO}$ = 90.0° and ϕ = 0.0°, with a BE = -325.1 cm^{-1}. Plots of the three partial occupied molecular orbital at this H-shaped geometry are given in figures 6.6, 6.7 and 6.8. The minima for the $^2A'$, $^4A''$ and $^4A'$ surfaces were not at a planar geometry.

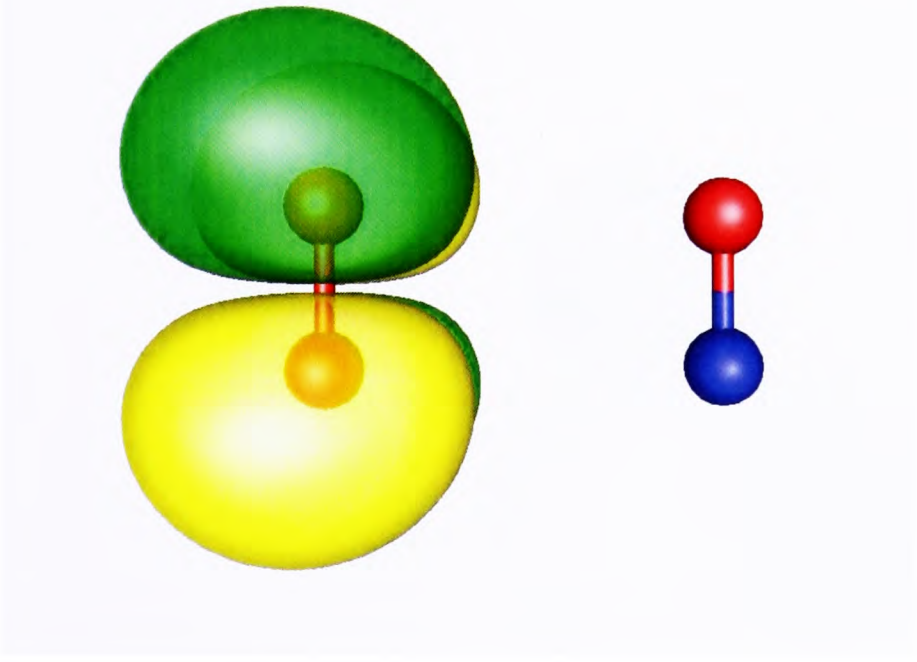

Figure 6.6: Partially occupied A'' Hartree-Fock molecular orbital - RSPT2 occupancy = 1.027

The BE of the global minimum clearly does not indicate a chemical bond. The strength of

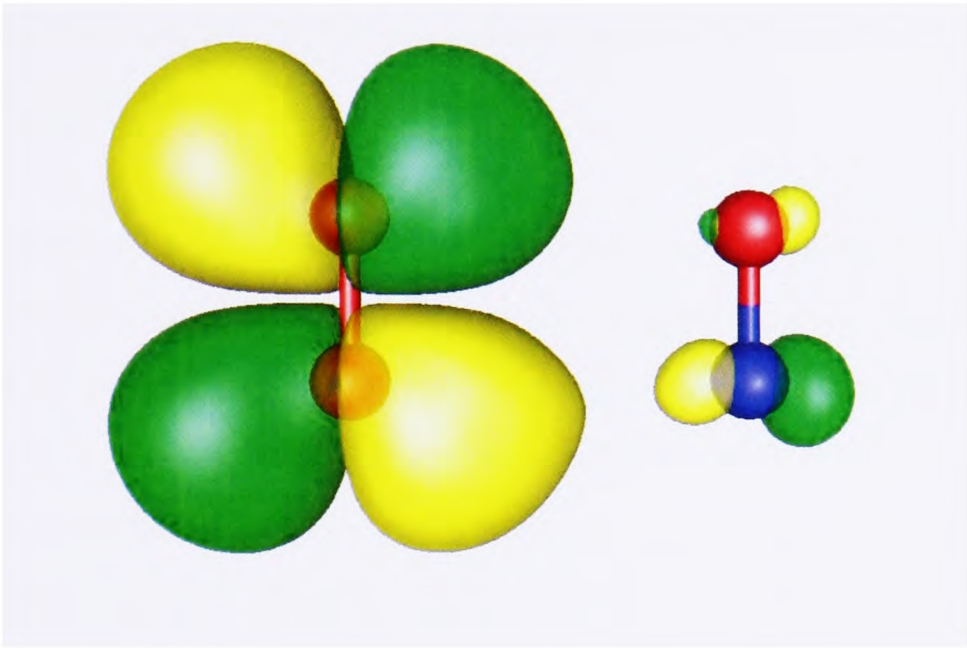

Figure 6.7: Partially occupied A' Hartree-Fock molecular orbital - RSPT2 occupancy = 1.121

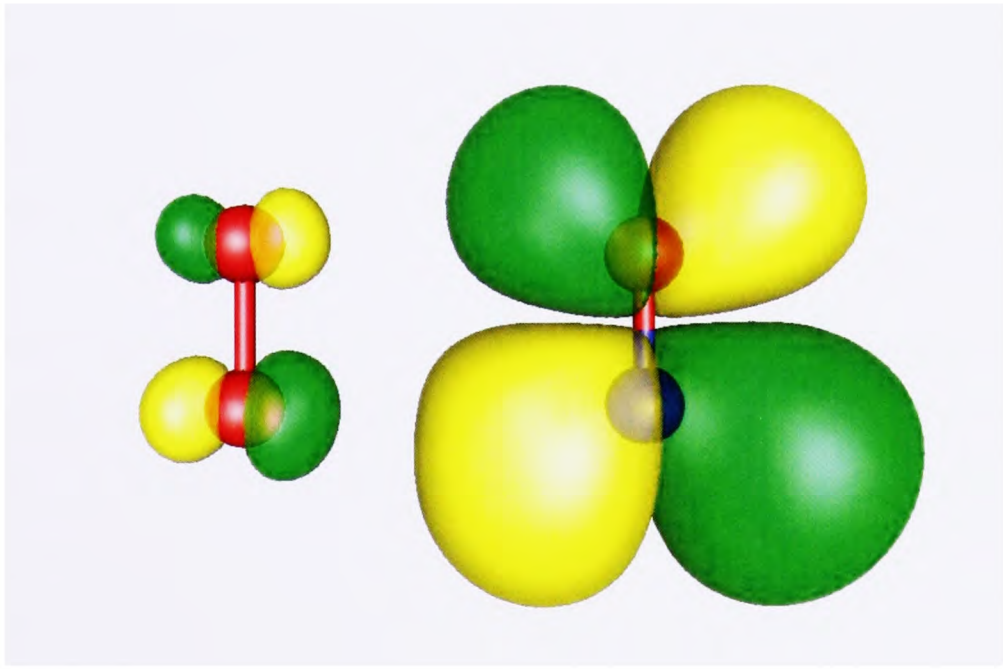

Figure 6.8: Partially occupied A' Hartree-Fock molecular orbital - RSPT2 occupancy = 0.915

this interaction suggests a Van der Waals class of interaction. However, as discussed earlier, this complex may be a potential reactive intermediate in the oxidation of NO to NO_2 [7], as the intermediate complex in the conventional model of this reaction, $(NO)_2$, is bound with a similar BE of 600-700 cm^{-1}.

Given that the calculated PES covers four dimensions, illustrating the surfaces in an understandable form is complicated. Representative geometries have been selected to provide a framework for the subsequent discussion. A plot of the potentials for the global minimum H-shaped geometry versus R, with $\theta_{O_2} = \theta_{NO} = 90.0°$ and $\phi = 0.0°$ is presented in figure 6.9. At large R the different surfaces converge to the same energy. The precise functional form of the attraction cannot be determined, due to overlapping repulsion, but this general functional form is suggestive of dipole-quadrupole, quadrupole-quadrupole and/or dispersion interactions varying respectively as R^{-4}, R^{-5} and R^{-6}. These are the long-range interactions that are found in other Van der Waals complexes.

As R is decreased the $^2A''$ potential drops considerably lower than any other state. The $^4A'$ and $^2A'$ virtually coincide across all calculated R. The $^4A''$ resides above the $^2A''$ at all R. This relative ordering of the spin states and symmetries can be rationalized by considering the overlap and occupancy of the π^* orbitals on the NO and O_2.

In the states of A'' symmetry the NO occupied π^* is parallel to the plane of the complex and therefore overlaps considerably with the singly occupied in-plane π^* orbital on the O_2. One might initially expect, by the application of Hund's rules, that the quartet, with its maximum multiplicity, would be lower in energy than the doublet. However, as can be seen this is not the case. Of course this reversal of Hund's rules is seen when one brings two hydrogen atoms together and a chemical bond is formed, with a singlet spin state due to exchange correlation, whilst the weakly bound triplet state resides at a higher energy. The same process

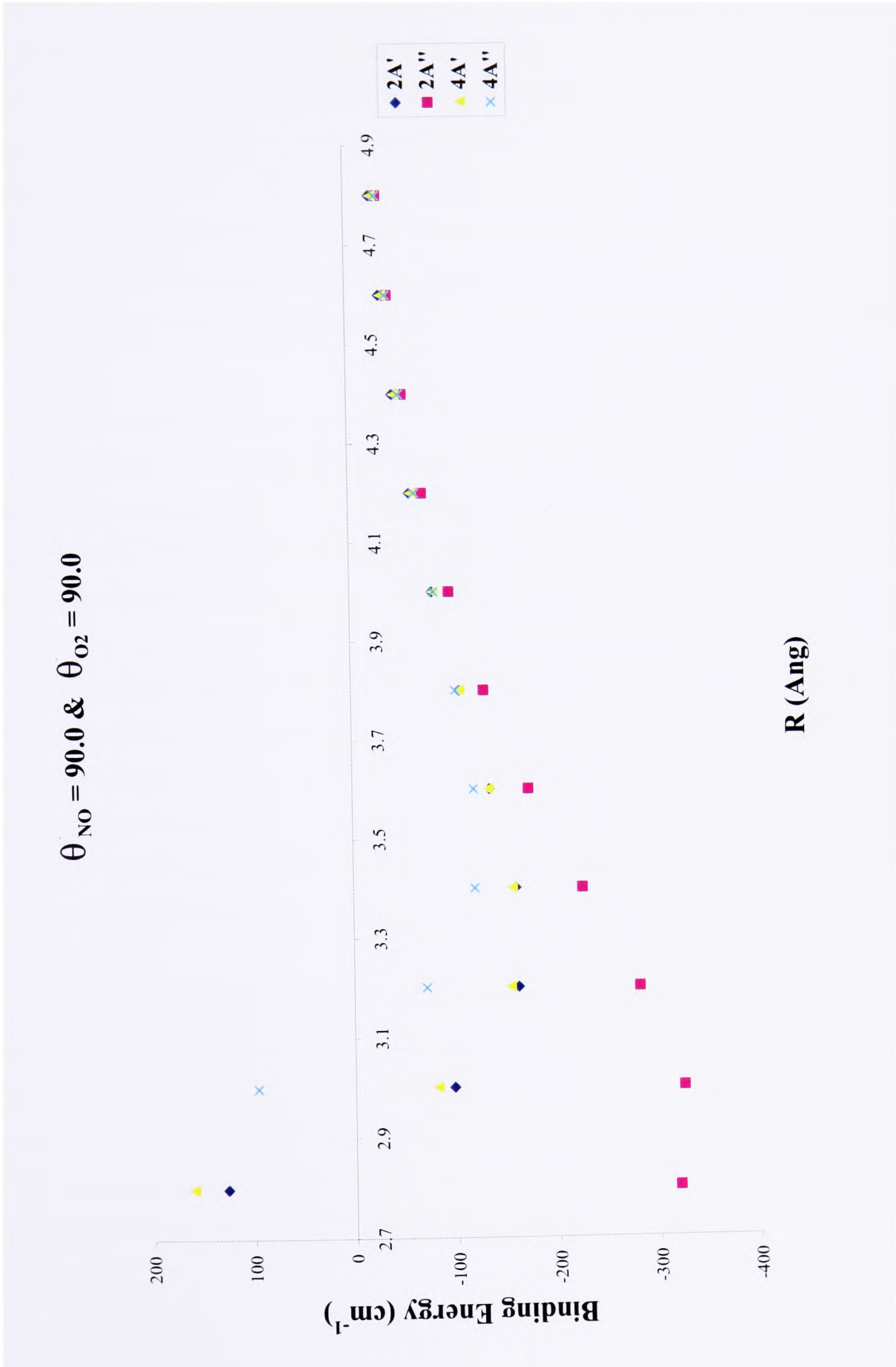

Figure 6.9: Calculated H-shaped Binding Energies (cm^{-1}) versus R (Å)

is occurring in NO-O_2, where the doublet, with an α electron on O_2 and β electron on NO, can form what appears to be a pseudo-chemical bond leading to a deeper potential well with its minimum at a shorter inter-diatomic distance than one might expect. In the quartet, the benefits of the exchange correlation cannot occur as both electrons in the π^* orbitals are α in nature, and a repulsive contribution results. Thus, this configuration has a higher energy than the doublet. This separation of doublet and quartet states varies approximately exponentially with intermolecular distance, as expected from the overlap of the interacting molecular orbitals.

In the A' symmetry the NO occupied π^* is perpendicular to the plane of the nuclei, and the attraction and repulsion will typically be governed by Van der Waals forces. Any overlap of the molecular orbitals will be non-bonding due to the perpendicular arrangement of the O_2 A' and NO A'' orbitals and the small overlap of the O_2 and NO A'' orbitals. The spin state in this case would not be expected to have a dramatic effect on the potential.

If this exchange correlation effect is the sole reason for the separation of the doublet and quartet states, then by taking a weighted average of the A'' symmetry states, the effect of the exchange correlation can be removed. If these data are compared to the A' data, it is found that the sets almost coincide, over all θ_{O_2}, θ_{NO} and ϕ. This coincidence implies that the exchange correlation effects are an additional effect to the typical dispersion and electrostatic forces that one expects between two diatomic molecules.

The PES illustrates the existence of secondary minima in T-shaped and linear geometries. These secondary minima all have BE $<$ -170 cm^{-1}. An illustration of the potentials of the T-shaped geometry, $\theta_{O_2} = 0.0°$, $\theta_{NO} = 90.0°$ and $\phi = 0.0°$, versus R can be seen in figure 6.10. Again, as with the H-shaped geometry, as R is decreased there is a separation of the potentials of the spin states and symmetries, which can be rationalized by considering the overlap and occupancy of the π^* orbitals. In A'' the NO π^* orbital is in the plane of the O_2, and can

overlap with the π^* orbital on the O_2. This overlap will be in-phase. This means, by use of the argument presented for the H-shaped geometry, the $^2A''$ will form a pseudo-chemical bond, due to exchange correlation, and will be lowered in energy, whilst the $^4A''$ will be raised in energy. In the A' the NO π^* orbital is perpendicular to the O_2 plane and thus any interaction will be governed by Van der Waals forces. This means that, as expected, the $^2A'$ and $^4A'$ coincide over all R.

The two other possible T-shaped geometries, $\theta_{O_2} = 90.0°$, $\theta_{NO} = 0.0°$ or $180.0°$ and $\phi = 0.0°$, illustrate the same behaviour as discussed above.

In the linear geometry, $\theta_{O_2} = \theta_{NO} = 0.0°$ and $\phi = 0.0°$, there is no separation of the A' and A'' as, because of the cylindrical symmetry of the system, the NO π^* orbital can interact in the same manner with either of the O_2 π^* orbitals. This is illustrated in figure 6.11 where the potentials as this geometry are plotted against R. As expected from the above discussions, relating to exchange correlation effects, in the linear geometry the $^2A'$ and $^2A''$ potential reside below those of the $^4A'$ and $^4A''$ states.

The PES variation in the angular parameters θ_{O_2} and θ_{NO} can be explored with the use of contour plots of the potentials. This have been calculated for the separate spin states and symmetries for $R = 3.4$ to 4.4 Å where the potentials were calculated for the full range of θ_{O_2} and θ_{NO}. Contour plots for $R = 3.4$ and 3.6 Å of the $^2A''$ state are illustrated in figures 6.12 and 6.13. The plots for the other values of R and states can be found on the attached CD.

The contour plots in figures 6.12 and 6.13 and on the attached CD all follow the same overall form, regardless of their specific spin state or symmetry. They indicate a rise in the potential energy of the system as θ_{NO} and θ_{O_2} simultaneously tend to $0.0°$ or $180.0°$, which is most pronounced at lower values of R. This is expected by the Pauli exclusion principle, as

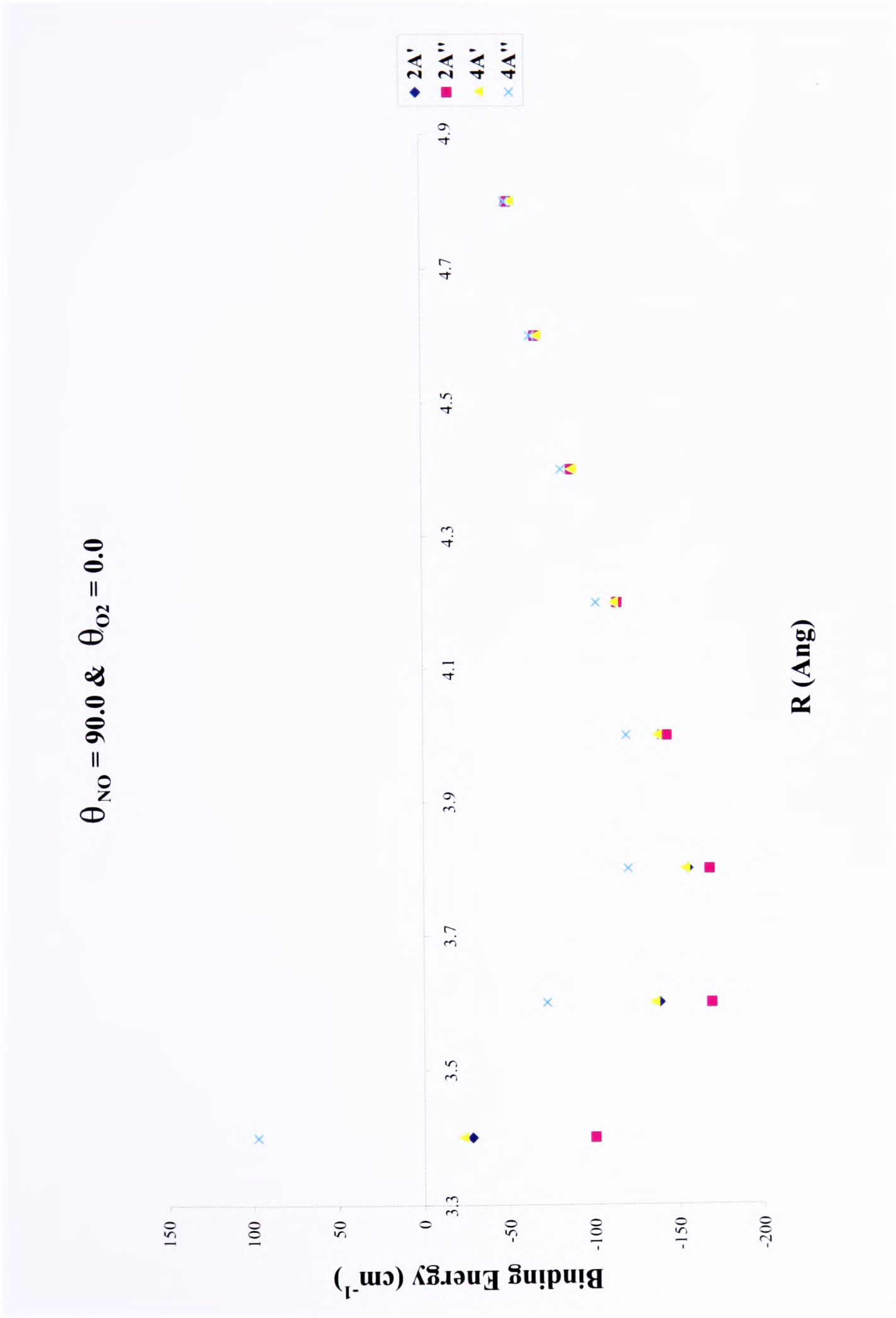

Figure 6.10: Calculated T-shaped Binding Energies (cm^{-1}) versus R (A)

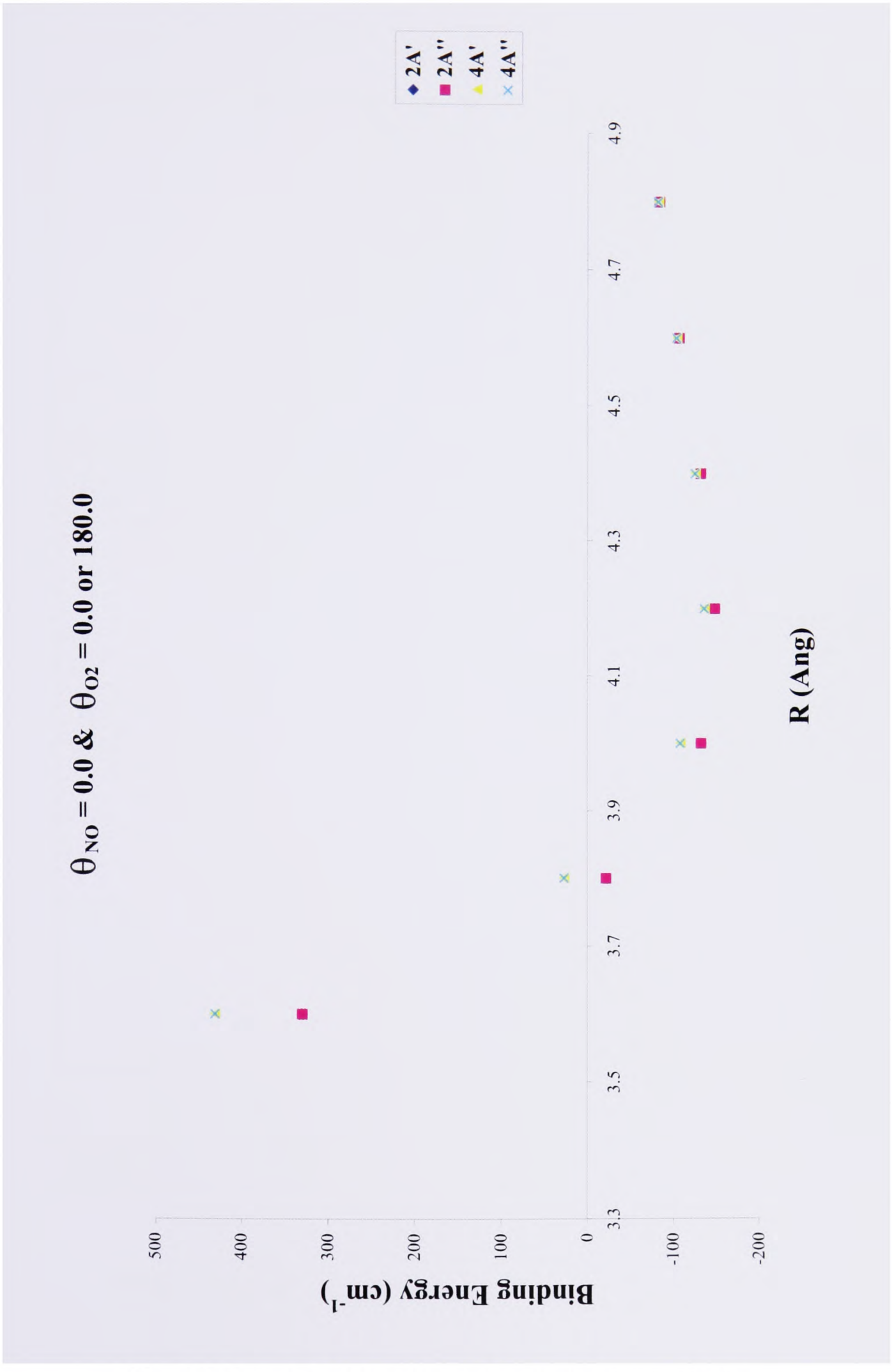

Figure 6.11: Calculated Linear Binding Energies (cm^{-1}) versus R (Å)

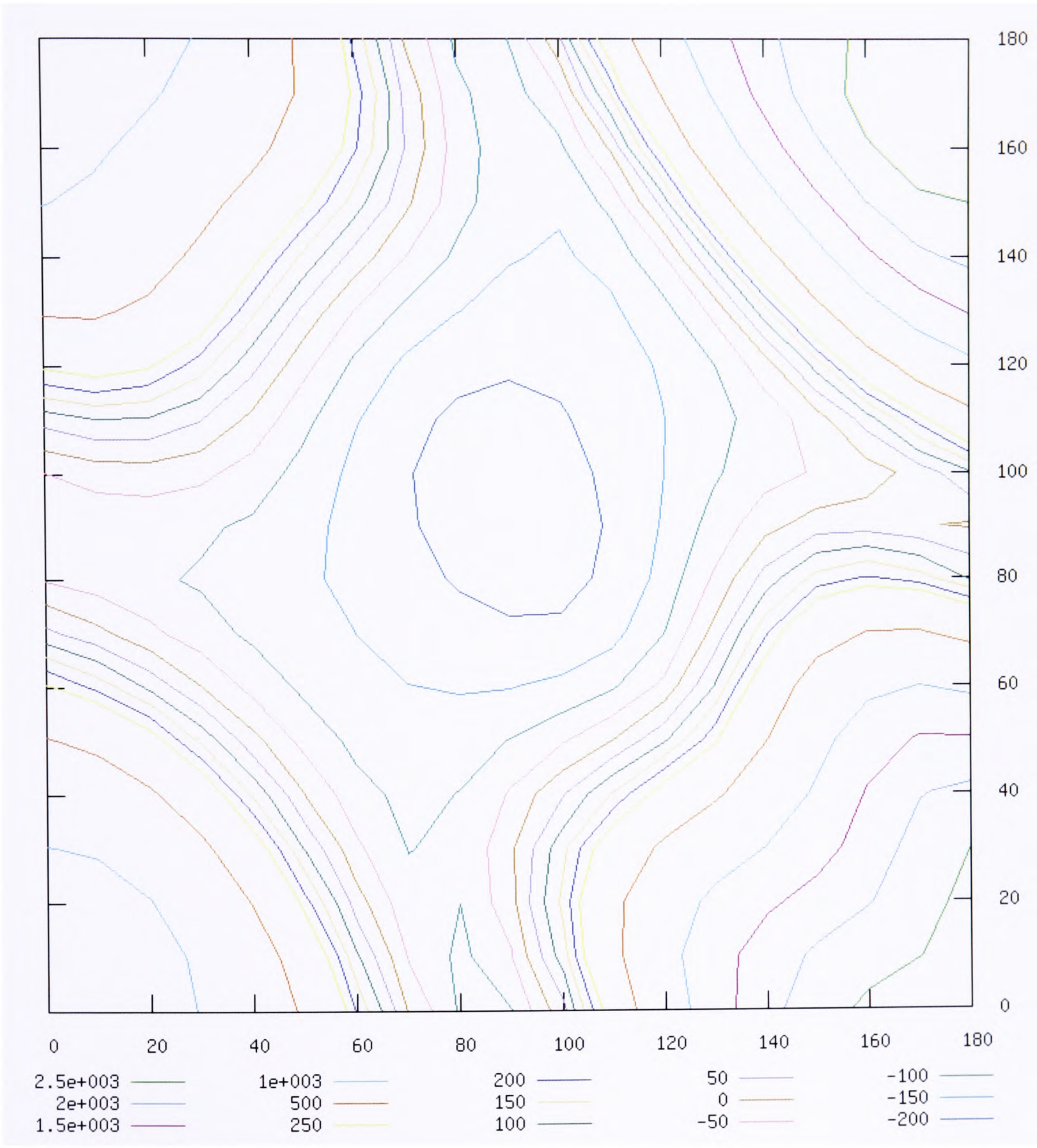

Figure 6.12: Potential contour plot of θ_{NO} versus θ_{O_2} for $^2A''$. $R = 3.4$ Å

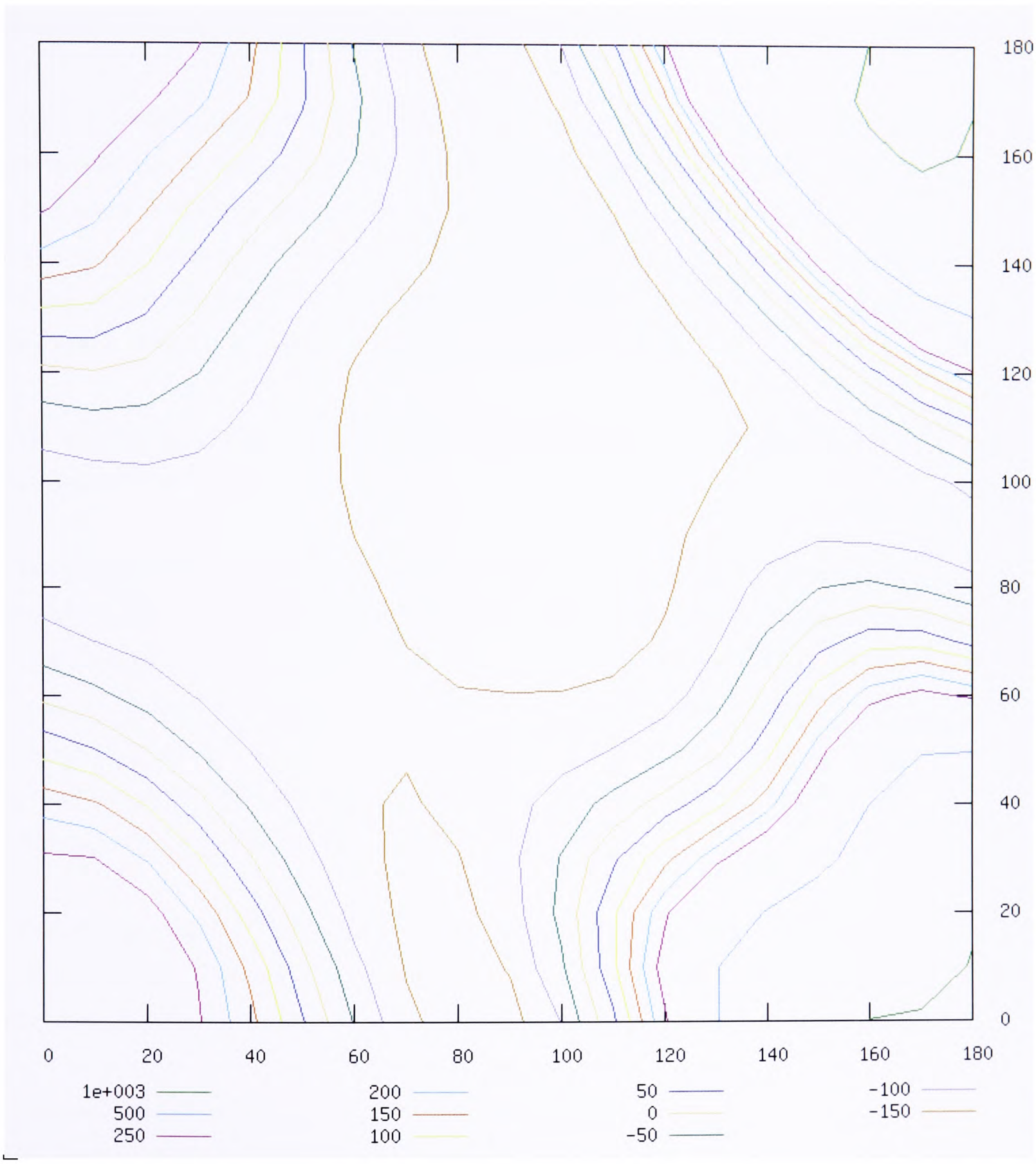

Figure 6.13: Potential contour plot of θ_{NO} versus θ_{O_2} for $^2A''$. $R = 3.6$ Å

these geometries represent a close spatial proximity of the interacting atoms of the diatomic molecules at a fixed separation of the centres of mass.

The contour plots are almost circular with respect to θ_{NO} and θ_{O_2}, which is not what one might initially expect. A symmetric motion of both diatomic molecules could be expected to be of a lower force constant than an asymmetric motion. However, this would give a narrow valley in the potential, which is not observed. This can be account for by the fact that the symmetric motion will disrupt the favourable exchange correlation effects, leading to a higher force constant, which is comparable to that for the asymmetric motion.

The variation of the PES with respect to ϕ is indicated by figure 6.14. In this figure $\theta_{O_2} = \theta_{NO} = 90.0°$ and $R = 3.0$ Å .

As ϕ deviates from zero the exchange correlation effects that favour the $^2A''$ state, but disfavour the $^4A''$ state, are dramatically reduced leading to the $^2A''$ state rising in energy and the $^4A''$ state dropping in energy. Additionally as the symmetry of the system is reduced from C_s to C_1 the symmetry that stopped the NO π^* orbital from interacting significantly with the O_2 is removed. This means that the $^2A'$ and $^4A'$ diverge and tend towards the state of a matching spin. Similar patterns of the potential are observed for other R, θ_{NO} and θ_{O_2}. When $\phi \neq 0.0°$ the binding of NO and O_2 is governed by Van der Waals forces.

The PES also indicated additional secondary minima at other geometries. However, on a close inspection these are misleading as they result purely from the relationship of the topography of the PES and the manner in which is has been parameterised.

From second order polynomial fits in the region around the global minimum, the values of the geometric parameters derived for NO-O_2 at minimum energy are: $R = 2.9$ Å , $\theta_{O_2} = 90.8°$,

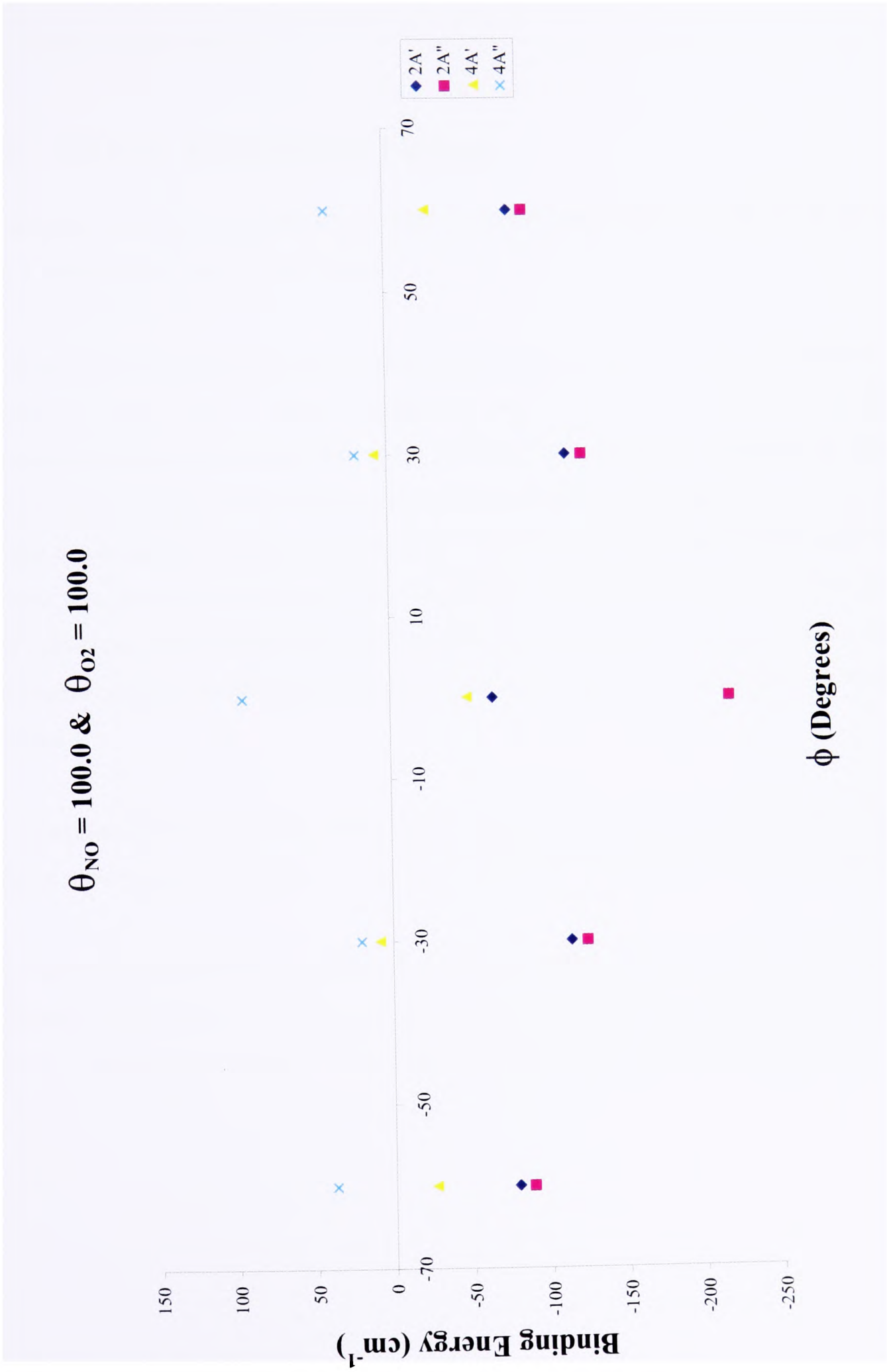

Figure 6.14: Calculated T-shaped Binding Energies (cm^{-1}) versus R (Å)

$\theta_{NO} = 89.2°$ and $\phi = 0.0°$.

6.2 NO-O_2 Rotational Theory

To develop an accurate model for the rotational energy levels of NO-O_2 an effective Hamiltonian and a well selected basis set are required.

The effective Hamiltonian can be constructed in one of several ways, see chapter 1. The most basic model would be that is a rigid-rotor, where the system is assumed to be fixed in an undistorting geometry, regardless of the rotation it is undergoing. To check the validly of this simplistic model, one can estimate the root mean square (RMS) variation of the geometry of the system, from is global minimum, due to the effects of zero-point energy, assuming the system is in its ground vibrational state. The smaller the RMS deviation of the more accurate the rigid-rotor model will be, the lower the effects of vibrational averaging on the rotational parameters and the smaller any potential Coriolis effects due to the coupling of vibrations and rotations.

Using the calculated PES for NO-O_2 and assuming that the normal modes for the vibrations can be approximated by figure 6.15, one can calculate the RMS of δR, $\delta\theta_{NO}$, $\delta\theta_{O_2}$ and $\delta\phi$.

Further, assuming that the potential is locally harmonic, then by the virial theorem the potential energy of the vibration is half of the zero-point energy. One can express this potential energy, E_x, as a function of the vibrational force constant, k_x, and the reduced mass, μ

$$\begin{aligned} E_x &= \frac{1}{2}\left(\frac{1}{2}h\nu_x\right) \\ &= \frac{1}{4}h\left(\frac{1}{2\pi}\sqrt{\frac{k_x}{\mu}}\right) \\ &= \frac{\hbar}{4}\sqrt{\frac{k_x}{\mu}} \end{aligned} \tag{6.7}$$

Modelling ν_1 as a simple stretch, then the potential energy of this vibration is given by

$$E_1 = \frac{1}{2}k_1\left\langle R^2\right\rangle = \frac{\hbar}{4}\sqrt{\frac{k_1}{\mu}} \tag{6.8}$$

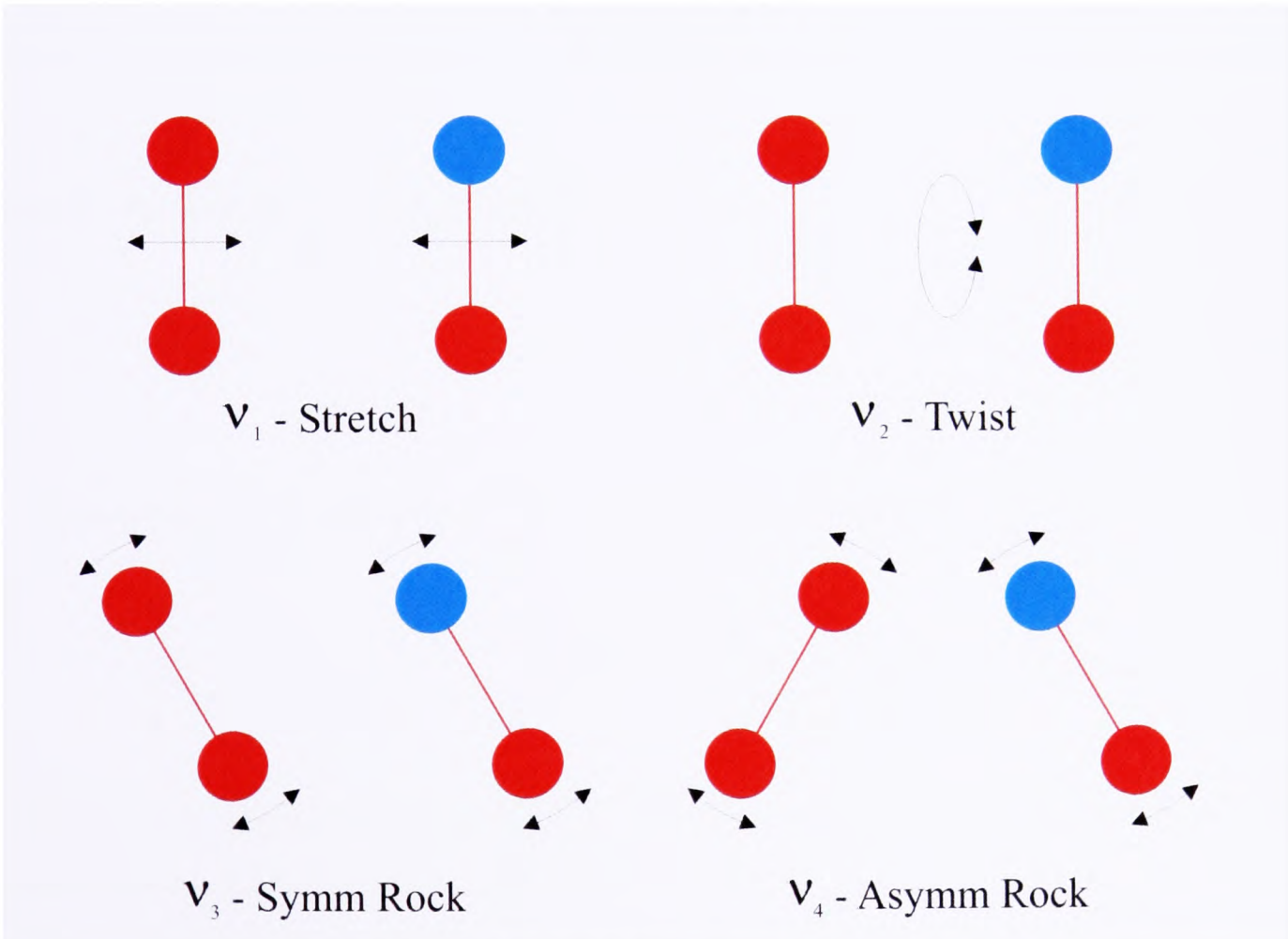

Figure 6.15: Approximate Normal Modes for NO-O_2

Thus

$$\langle R^2 \rangle = \frac{\hbar}{2}\sqrt{\frac{1}{k_1 \mu}} \tag{6.9}$$

Using the PES one can determine a numerical value for k_1, by determining the energy rise for a set displacement of R. This value can then be substituted into equation 6.9 to determine the RMS value of δR as 0.18 Å .

For ν_2 one replaces the reduced mass, μ, with a reduced moment of inertia for the two diatomic molecules. Therefore 6.7 becomes

$$E_x = \frac{\hbar}{4}\sqrt{\frac{k_x}{I_r}} \tag{6.10}$$

where I_r, the reduced moment of inertia, is defined as

$$I_r = \frac{I_{NO} I_{O_2}}{I_{NO} + I_{O_2}} \tag{6.11}$$

By equating the kinetic energy of ν_2 with equation 6.10 it can be shown that

$$\langle \phi^2 \rangle = \sqrt{\frac{B_r}{2k_2}} \tag{6.12}$$

where B_r is the reduced rotational constant. Using equation 6.12, and the PES, the calculated value of RMS of $\delta\phi$ can be shown to be 14°.

The kinetic energy of the zero-point angular vibrations in the plane can be represented by

the normal modes as illustrated in figure 6.15. However, given that the potential is circular with respect to θ_{NO} and θ_{O_2}, one can approximately determine the RMS of $\delta\theta_{NO}$ and $\delta\theta_{O_2}$ by inspecting their motions separately.

Using equation 6.12, where B_r is replaced with the rotational constants of the individual diatomic molecules, and the PES, is can be shown that the RMS of $\delta\theta_{NO}$ and $\delta\theta_{O_2}$ are 7.4° and 7.3° respectively.

The calculated RMS values of the parameters are non-zero, but are sufficiently close to zero to allow the rigid-rotor, at the equilibrium geometry, to be used as a valid starting model, see section 6.3

6.2.1 Coupling Scheme

Open-shell complexes can have non-zero electron spin due to the unpaired electrons. In the Hamiltonian, it is possible to couple the different angular momenta, or to use a decoupled form. The angular momentum of importance in NO-O_2 are the rotational, electron spin, orbital and nuclear spin angular momenta. The basis set used, be it either coupled or decoupled, is equally valid as they both fully represent the angular momentum in the system. However, for mathematical simplicity, it is common to use a coupled representation.

In previous work by the group on O_2 complexes [8] and NO complexes [9], the electron spin has been quantized along the internuclear axis of the open-shell diatomic molecule. Therefore for NO-O_2 there are three candidate axes systems for the quantization of the electron spin: the principal axis of the complex, the internuclear axis of O_2 or the internuclear axis of NO. For simplicity the electron spins of both NO and O_2 should be quantized along the same axis. For NO in isolation, there is a strong coupling of the electron spin to its internuclear axis which is best represented by Hund's case (a). In isolated O_2, the coupling of the electron spin to

its internuclear axis is much weaker and the electron spin cannot follow the rotation of the molecular framework. This leads to the best representation for O_2 being given by Hund's case (b).

Since the coupling of the NO electron spin to its internuclear axis is much stronger than that of O_2 and because the O_2 spin is quite strongly coupled to that of NO through spin correlation, see equation 6.21, it is most convenient to reduce the complexity of the effective Hamiltonian by quantizing the O_2 electron spins along the NO internuclear axis. Using this coupling scheme the relevant basis set is

$$|\eta\Lambda; S_1\Sigma_1; S_2\Sigma_2; JM_JK_a\rangle = |\eta\Lambda\rangle\,|S_1\Sigma_1\rangle\,|S_2\Sigma_2\rangle\,|JM_JK_a\rangle \tag{6.13}$$

where η is the label for the ground vibronic state, Λ, Σ_1 and Σ_2 are the projections of $\boldsymbol{L}$, $\boldsymbol{S}_1$ and $\boldsymbol{S}_2$ respectively along the atomic centre axis, the z axis, of the NO, J is the total angular momentum quantum number and K_a is the projection of $\boldsymbol{J}$ along the a axis of the complex. Assigning $\boldsymbol{S}_1$ and $\boldsymbol{S}_2$ to O_2 and NO respectively, the projection quantum numbers will have the following values: $\Lambda = \pm 1$, $\Sigma_1 = 0, \pm 1$ and $\Sigma_2 = \pm\frac{1}{2}$.

6.2.2 Effective Hamiltonian

The effective Hamiltonian, constructed to model the rigid system, will be composed of three classes of terms. Initially there is the rotational Hamiltonian, $\hat{\mathscr{H}}_{rot}$, representing the actual rotation of the complex. The second class of terms is the fine structure terms, the spin-orbital, $\hat{\mathscr{H}}_{so}$, the spin-spin, $\hat{\mathscr{H}}_{ss}$, the spin-correlation, $\hat{\mathscr{H}}_{sc}$, and the Renner-Teller, $\hat{\mathscr{H}}_{q}$ Hamiltonians. These are discussed in section 6.2.3. The final class of terms is the hyperfine structure terms $\hat{\mathscr{H}}_{mag}$ and $\hat{\mathscr{H}}_{quad}$, see section 6.2.4. The overall effective Hamiltonian is given by the sum of these

$$\hat{\mathscr{H}} = \hat{\mathscr{H}}_{rot} + \hat{\mathscr{H}}_{so} + \hat{\mathscr{H}}_{ss} + \hat{\mathscr{H}}_{sc} + \hat{\mathscr{H}}_{q} + \hat{\mathscr{H}}_{mag} + \hat{\mathscr{H}}_{quad} \tag{6.14}$$

The rotational Hamiltonian for the complex is that of a rigid asymmetric top

$$\begin{aligned} \hat{\mathscr{H}}_{rot} &= A\hat{R}_a^2 + B\hat{R}_b^2 + C\hat{R}_c^2 \\ &= A(\hat{J}_a - \hat{L}_a - \hat{S}_{1a} - \hat{S}_{2a})^2 + B(\hat{J}_b - \hat{L}_b - \hat{S}_{1b} - \hat{S}_{2b})^2 \\ &\quad + C(\hat{J}_c - \hat{L}_c - \hat{S}_{1c} - \hat{S}_{2c})^2 \end{aligned} \tag{6.15}$$

where A, B and C are the rotational constants of the complex. In equation 6.15 the orbital and spin angular momenta are quantized in a rotating axis system. The relationship between the principal axes of the complex and those of NO and O_2 can be determined by reference to figure 6.16.

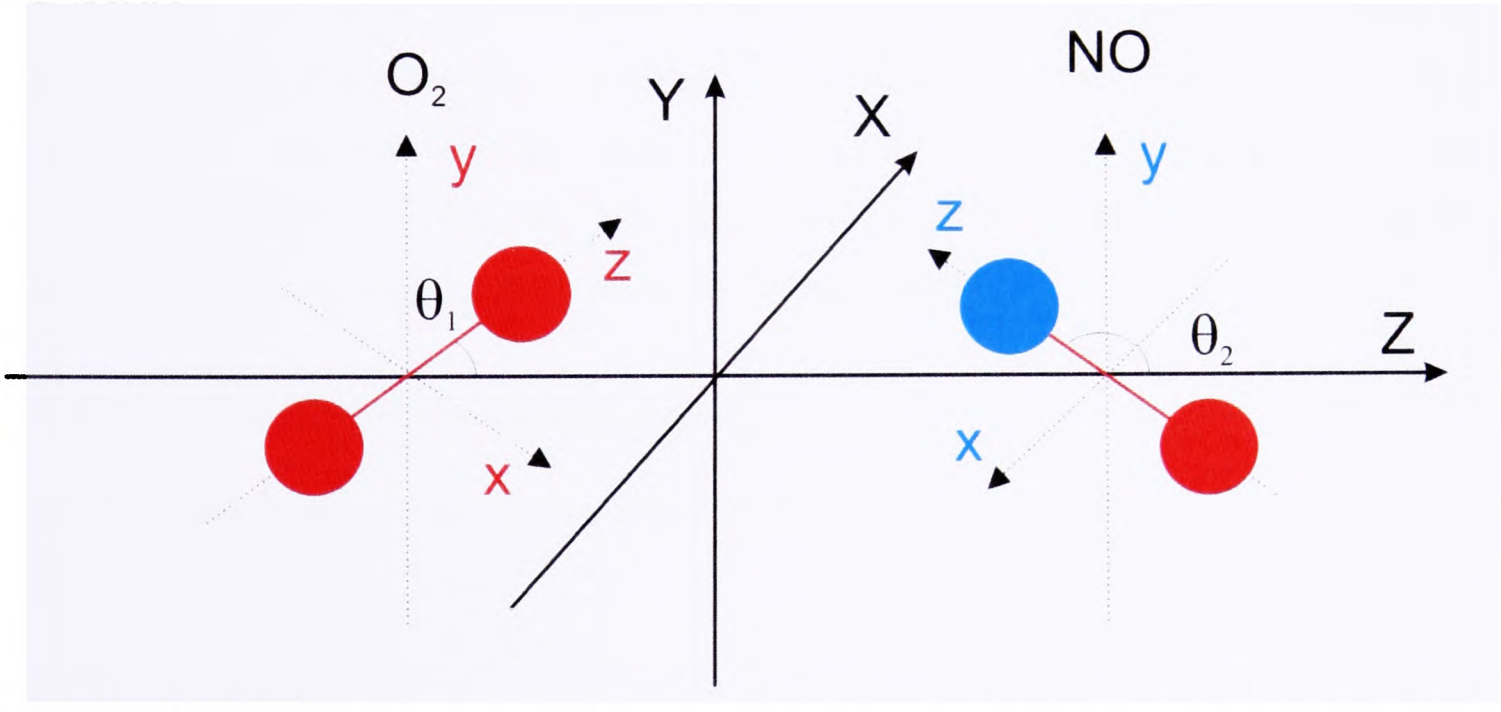

Figure 6.16: Orientation of NO-O_2. For free NO (x, y, z) corresponds to (b, c, a), for free O2 (x, y, z) corresponds to (b, c, a) and for the complex (X, Y, Z) corresponds to (B, C, A)

In figure 6.16 ϕ is defined as in figure 6.5, with $\theta_{NO} = \theta_2$ and $\theta_{O_2} = \theta_1$. With reference to figure 6.16 it can be determined that

$$\begin{aligned} P_a &= P_z \cos\theta_2 - P_x \sin\theta_2 \\ P_b &= P_z \sin\theta_2 \cos\phi_2 + P_x \cos\theta_2 \cos\phi_2 - P_y \sin\phi_2 \\ P_c &= P_z \sin\theta_2 \sin\phi_2 + P_x \cos\theta_2 \sin\phi_2 + P_y \cos\phi_2 \end{aligned} \tag{6.16}$$

where $P_{a,b,c}$ is equal to $\hat{L}_{a,b,c}$, $\hat{S}_{1a,1b,1c}$ or $\hat{S}_{2a,2b,2c}$ and $P_{x,y,z}$ are the projections of NO. A working assumption is made that the principal axes of the complex (A, B, C) coincide with the axes (Z, X, Y), in figure 6.16, regardless of the values of θ_1, θ_2 and ϕ. If $\phi = 0.0°$ then P_z is parallel to the NO atomic centre axis and in the A-B plane of the complex, P_x is in the A-B plane of the complex and P_y is parallel to the B-C plane of the complex. These relationships are based on the assumption that the principal axes do not deviate from the illustrated (Z, X, Y) axes. The results from the combination of 6.15 and 6.16 with the basis set given in 6.13 gives the matrix elements of the energy matrix. Expanding these equations gives terms including $\hat{L}_{\pm}$, which were taken to be zero since these will affect the energy at the second order and can be disregarded at this stage of analysis. The form of the non-zero matrix elements can be determined from basic angular momentum expressions [10].

6.2.3 Fine Structure Hamiltonian

The first fine structure term is the spin-orbit Hamiltonian. This is given by the standard expression [10]

$$\begin{aligned}\hat{\mathscr{H}}_{so} &= \zeta \hat{L}.\hat{S}_2 \\ &= \zeta \hat{L}_z \hat{S}_{2z} + \frac{1}{2}\zeta\left(\hat{L}^+\hat{S}_2^- + \hat{L}^-\hat{S}_2^+\right)\end{aligned} \tag{6.17}$$

where ζ is the spin-orbit coupling constant, which will be very close to that of free NO. The dominant term is $\hat{L}_z\hat{S}_{2z}$, which generates diagonal elements. The other terms connect different electronic states, and have been disregarded at this stage of analysis.

The second fine structure term is the spin-spin Hamiltonian of O_2. Again the standard expression [11] for this term is used

$$\hat{\mathscr{H}}_{ss} = \frac{2\lambda}{3}\left(3\hat{S}_{1z}^2 - \hat{S}_1^2\right) \tag{6.18}$$

where λ is the spin-spin coupling constant which will be very close to that of free O_2. Unfortunately this standard expression is written relative to the O_2 axis system, where as the coupling scheme used has the O_2 spin quantized about the NO axes system. This complication can be resolved using a second trigonometric relationship. Assuming that $\phi = 0.0°$, using figure 6.16, it can be seen that

$$\hat{\mathscr{H}}_{ss} = \frac{2\lambda}{3}\left(3\left(\hat{S}_{1z}\cos\left(\theta_2 - \theta_1\right) - \hat{S}_{1x}\sin\left(\theta_2 - \theta_1\right)\right)^2 - \hat{S}_1^2\right) \tag{6.19}$$

where the O_2 spin is now written relative to the NO internuclear axis.

The third and fourth fine structure terms, the fourth and fifth terms in equation 6.14, cannot

be represented by standard expressions. To represent the NO-O_2 in the most general form the effective Hamiltonian needs to be able to represent all four low lying states. To do this the model uses two terms. The first term represents the interaction of the NO and O_2 spins giving the overall doublet or quartet nature of the complex. The second term represents the quenching of the orbital angular momentum of the NO by the presence of the O_2.

The spin-correlation term represents the interaction of the spins using the geometry dependent parameter β defined as

$$\begin{aligned} \beta &= \frac{1}{2}\left(V_{4A''} + V_{4A'}\right) - \frac{1}{2}\left(V_{2A''} + V_{2A'}\right) \\ &= \bar{V}_4 - \bar{V}_2 \end{aligned} \tag{6.20}$$

where the values of $V_{4A''}$, etc, are derived from the PES calculations detailed above. Using β, the interaction can be represented with the following effective Hamiltonian

$$\begin{aligned} \hat{\mathscr{H}}_{sc} &= \frac{2\beta}{3}\left(\hat{S}_1.\hat{S}_2\right) \\ &= \frac{2\beta}{3}\left(\hat{S}_{1z}\hat{S}_{2z} + \frac{1}{2}\left(\hat{S}_{1+}\hat{S}_{2-} + \hat{S}_{1-}\hat{S}_{2+}\right)\right) \end{aligned} \tag{6.21}$$

The Renner-Teller term, represents the quenching of the orbital angular momentum with the use of two parameters, $\bar{\epsilon}$ and $\Delta\epsilon$. These are defined as

$$\bar{\epsilon} = \frac{2\Delta\epsilon_4 + \Delta\epsilon_2}{3} \tag{6.22}$$

$$\Delta\epsilon = \Delta\epsilon_4 - \Delta\epsilon_2 \tag{6.23}$$

where

$$\Delta\epsilon_4 = V_{4A''} - V_{4A'} \tag{6.24}$$

$$\Delta\epsilon_2 = V_{2A''} - V_{2A'} \tag{6.25}$$

The presence of the O_2 creates a barrier to free orbital motion of the unpaired electron on NO, removing the degeneracy of the NO π_x^* and π_y^* orbitals. This effect can be modelled with a Fourier expansion in electron coordinate about the NO internuclear axis

$$\hat{\mathscr{H}_q} = \epsilon_1 \cos\varphi_i + \epsilon_2 \cos 2\varphi_i + \ldots \tag{6.26}$$

where the expansion coefficients, ϵ_1, etc, are derived from the geometry of the Van der Waals complex and φ is the azimuthal angle of the unpaired electron about the NO axis. The second term in the above expansion is the most important since it has a first-order effect in a $^2\Pi$ state given by

$$\langle \Lambda = \pm 1 \,|\epsilon_2 cos 2\varphi_i|\, \Lambda = \mp 1\rangle = -\frac{1}{2}\epsilon_2 \tag{6.27}$$

The first term in equation 6.26 connects the $^2\Pi$ NO ground state with excited states differing by $\Delta\Lambda = \pm 1$ ($^2\Sigma$, $^2\Delta$). Since these excited states are relatively high in energy the effect on the energy of the ground state will be small. This term can also connect the $\Lambda = \pm 1$ states in the second order, but the net effect is indistinguishable from the second term above. Within the NO moiety the wavefunction is expressed as a linear combination of the π_x and π_y orbitals

$$\Pi_{\pm} = \mp \frac{1}{\sqrt{2}} (\pi_x \pm i\pi_y) \tag{6.28}$$

The Renner-Teller parameter ϵ_2 represents a shift in relative energy of the π_x and π_y orbitals. Within NO-O_2 the ϵ_2 coupling constant is defined, to represent all possible states of NO-O_2, as the combination of the constants $\bar{\epsilon}$ and $\Delta\epsilon$ given by

$$\begin{aligned} \epsilon_2 &= \bar{\epsilon} + \frac{2\Delta\epsilon}{3} \left(\hat{S}_1 . \hat{S}_2 \right) \\ &= \bar{\epsilon} + \frac{\Delta\epsilon}{3} \left(\hat{S}_{1z}\hat{S}_{2z} + \frac{1}{2} \left(\hat{S}_{1+}\hat{S}_{2-} + \hat{S}_{1-}\hat{S}_{2+} \right) \right) \end{aligned} \tag{6.29}$$

As with the rotational Hamiltonian, the non-zero fine structure matrix elements from the combination of the above equations with the basis set given in 6.13, can be determined from basic angular momentum expressions [10].

6.2.4 Hyperfine Structure Hamiltonian

The nitrogen nucleus in NO-O_2 has a non-zero nuclear spin, $I_N = 1$, that can couple to the magnetic field generated by the unpaired electrons present and the electric field gradient at the nucleus due to the rest of the complex. Given that the NO and O_2 are bound by a pseudo-chemical bond with a separation of approximately 3 Å , at this level of theory the effect of the O_2 electrons on the hyperfine terms relating to the nitrogen can be, to a good approximation, disregarded and theory developed previously by the group [9] based on Frosh and Foley can be used. To use this theory, one has to disregard any ϕ dependence and set $\phi = 0.0°$. This approximation is used as it greatly simplifies the expressions not only for the hyperfine terms, but also for the rotational terms.

The first hyperfine term in equation 6.14 represents the magnetic interaction between the nuclear spin angular momentum of nitrogen and the magnetic field due to the combination of the electron spin and orbital angular momenta on NO. This is given by a scalar product

$$\hat{\mathscr{H}}_{mag} = T^1(\mathbf{I}).T^1(\mathbf{X}) \tag{6.30}$$

The tensor $T^1(\mathbf{X})$ can be expanded into three terms representing the nuclear spin-orbit interaction, the Fermi contact interaction and the dipolar interaction of the electron and the nuclear magnetic dipoles

$$\begin{aligned}\hat{\mathscr{H}}_{mag} &= T^1(\mathbf{I}).T^1(\mathbf{X}) \\ &= g_I\mu_B\mu_I T^1(\mathbf{I}). \\ &\quad \left(\frac{2}{r^3}T^1(\mathbf{L}) + \frac{8\pi}{3}g_e\left|\Psi(r=0)^2\right|T^1(\mathbf{S}) - \sqrt{10}g_e\frac{1}{r^3}T^1(\mathbf{S}, C^2)\right)\end{aligned} \tag{6.31}$$

The second hyperfine term in equation 6.14 represents the nitrogen electric quadrupole interaction. This can be represented with second rank tensors

$$\hat{\mathscr{H}}_{quad} = T^2\left(\nabla\nabla\mathbf{V}\right).T^2\left(\mathbf{Q}\right) \tag{6.32}$$

Taking into account the hyperfine interactions, the former total angular momentum quantum number, J, is coupled to the nuclear spin quantum number, I, to give the final total angular momentum quantum number F

$$\boldsymbol{J} + \boldsymbol{I} = \boldsymbol{F} \tag{6.33}$$

Using this coupling the basis set has to be adjusted to take account of the new total angular momentum quantum number F

$$|\eta\Lambda; S_1\Sigma_1; S_2\Sigma_2; JM_JK_a; IFM_F\rangle = |\eta\Lambda\rangle\,|S_1\Sigma_1\rangle\,|S_2\Sigma_2\rangle\,|JM_JK_a; IFM_F\rangle \tag{6.34}$$

The non-zero hyperfine structure matrix elements from the combination of the expressions above with the basis set given in 6.34 are presented in section B.2 of Appendix B.

6.2.5 Energy levels and transition strength factors

Using the matrix elements detailed above it is possible to construct an energy matrix. In this system, as a result of the odd number of electrons, J the rotational quantum number is half integral. This leads to both F and K_a being half integral. K_a represents angular momentum about the a axis of a near prolate top. Although there are terms off-diagonal in K_a, this energy matrix was calculated with K_a limited to $\pm\frac{3}{2}$. This limitation disregards the effect of $K_a = \pm\frac{5}{2}$. This reduced the dimensions of the energy matrix and made the diagonalization more rapid. The energy matrix was constructed and diagonalized with a specifically written C++ program. Computer diagonalization was used due to the scale of the computation required, despite the fact that this method cloaks the relative importance of the terms in the ordering of the resulting energy levels. Using the geometric and energy dependent fine structure parameters from the PES and other fine and hyperfine parameters from isolated NO and O_2 [12], the energy of the rotational levels of NO-O_2 were calculated. The parameters used in the calculations are presented in table 6.1, and the resulting rotational energy levels are presented in figure 6.17.

The energy level pattern is not of the standard form that is obtained for a closed-shell

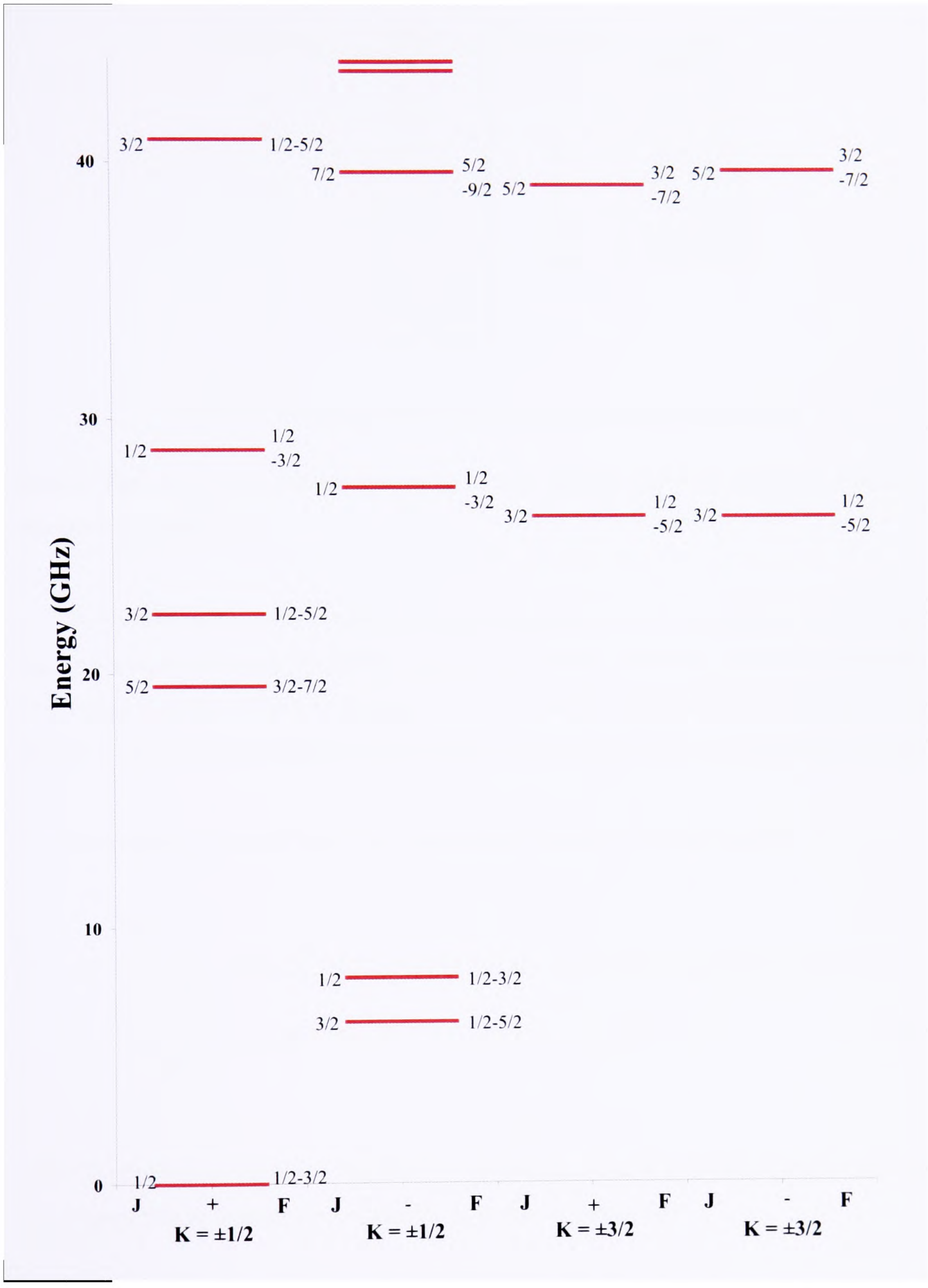

Figure 6.17: Rotational Energy Levels for NO-O_2. Hyperfine levels are not resolved

Parameter	Value	Parameter	Value
R	2.92 Å	ζ	123.0 cm^{-1}
θ_1	90.8°	λ	1.6 cm^{-1}
θ_2	89.2°	a	84.2 MHz
ϕ	0.0°	b_F	22.3 MHz
$V_{2_{A''}}$	-341.4 cm^{-1}	c	-58.8 MHz
$V_{2_{A'}}$	-88.8 cm^{-1}	d	112.6 MHz
$V_{4_{A''}}$	124.7 cm^{-1}	eQq_0	-1.86 MHz
$V_{4_{A'}}$	-71.5 cm^{-1}	eQq_2	23.05 MHz
A	23,361 MHz		
B	3,704 MHz		
C	3,191 MHz		

Table 6.1: Parameters used for NO-O_2 rotational energy level predictions

system. However, it does follow what seems to be a standard form for open-shell systems, as discussed in section 6.4.

The intensity of potential rotational energy transitions can be quantified by calculating the matrix elements of the electric dipole operator, μ, between the initial and final wavefunctions [10], taking care to get the correct phases. These transition strength factors can then be multiplied by approximate transition dipole moment components to give the transition strengths.

The transition strength factor for a directional excitation is defined as [13]

$$\begin{aligned} S &\propto \sum_{M'_F M_F} \left|\langle \eta' \Lambda' S'_1 \Sigma'_1 S'_2 \Sigma'_2 J' M'_J K'_a I' F' M'_F \left|\mu_Z\right| \eta \Lambda S_1 \Sigma_1 S_2 \Sigma_2 J M_J K_a I F M_F \rangle\right|^2 \\ &\propto \sum_{M'_F M_F} \left|\langle \eta' \Lambda' \Omega' J' M'_J K'_a I' F' M'_F \left|\mu_Z\right| \eta \Lambda \Omega J M_J K_a I F M_F \rangle\right|^2 \end{aligned} \tag{6.35}$$

where Ω represents spins of the NO and O_2. Writing μ_Z in terms of spherical tensors and using the Wigner-Eckart theorem, see Appendix A, it can be shown that

$$\langle \eta' \Lambda' \Omega' J' K'_a I F' M'_F \left| \mu_Z \right| \eta \Lambda \Omega J K_a I F M_F \rangle$$

$$= \left\langle \eta' \Lambda' \Omega' J' K'_a I F' M'_F \left| \sum_q D^{1*}_{0q}(\omega) T^1_q(\mu) \right| \eta \Lambda \Omega J K_a I F M_F \right\rangle$$

$$(-1)^{(F'-M'_F)} \begin{pmatrix} F' & 1 & F \\ -M'_F & 0 & M_F \end{pmatrix} \left\langle \eta' \Lambda' \Omega' J' K'_a I F' \left\| \sum_q D^{1*}_{.q}(\omega) T^1_q(\mu) \right\| \eta \Lambda \Omega J K_a I F \right\rangle \quad (6.36)$$

The initial phase factor and 3-j symbol in equations 6.36, when squared and summed overall M_F for $F = F'$ or $F = F' \pm 1$, has a value of $1/3$. By the application of standard tensor algebra, the reduced matrix element can be expanded

$$\left\langle \eta' \Lambda' \Omega' J' K'_a I F' \left\| \sum_q D^{1*}_{.q}(\omega) T^1_q(\mu) \right\| \eta \Lambda \Omega J K_a I F \right\rangle$$

$$\begin{aligned} &= (-1)^{(J'+I+F+1)} \left[(2F+1)(2F'+1) \right]^{\frac{1}{2}} \begin{Bmatrix} J' & F' & I \\ F & J & 1 \end{Bmatrix} \\ &\quad \left\langle \eta' \Lambda' \Omega' J' K'_a \left\| \sum_q \sum_q D^{1*}_{.q}(\omega) T^1_q(\mu) \right\| \eta \Lambda \Omega J K_a \right\rangle \\ &= (-1)^{(J'+I+F+1)} \left[(2F+1)(2F'+1) \right]^{\frac{1}{2}} \begin{Bmatrix} J' & F' & I \\ F & J & 1 \end{Bmatrix} \quad (6.37) \\ &\quad \sum_q (-1)^{(J'-K'_a)} \left[(2J+1)(2J'+1) \right]^{\frac{1}{2}} \begin{pmatrix} J' & 1 & J \\ -K'_a & q & K_a \end{pmatrix} \langle \eta' \Lambda' \Omega' \left| T^1_q(\mu) \right| \eta \Lambda \Omega \rangle \end{aligned}$$

The final matrix element in 6.37, $\langle \eta' \Lambda' \Omega' \left| T^1_q(\mu) \right| \eta \Lambda \Omega \rangle$, can have the electron spins factored out, and the remainder is diagonal in rotational transitions, meaning that it is equal to μ_q. By calculating the numerical value of 6.37 for each allowed transition and squaring the result,

it is possible to calculate approximate transition strength factors. It has been found that the majority of the allowed transitions in the frequency range 5 to 20 GHz are a-type with very low transition strength factors. From the initial *ab initio* calculations, the calculated dipole moments, in Debye, of the global minimum are

$$\begin{aligned} |\mu_a| &= 0.034 \\ |\mu_b| &= 0.091 \\ |\mu_c| &= 0.000 \end{aligned} \tag{6.38}$$

These low dipole moments are a result of the NO-O_2 complex lacking any significant internal electron transfer. The calculated dipole moments will be inaccurate, but they indicate that any rotational transitions will be very weak. Using the above transition strength factors, a predicted spectrum can be generated. This spectrum, in the ranging from 5 to 20 GHz, is presented in section B.3 of Appendix B. The transitions are given in terms of the rotational transition frequency and a hyperfine splitting from this base frequency. The transition strength factors are calculated as above and have not been multiplied by their respective dipole moment compenents.

The hyperfine splits presented in Appendix B are considerably more accurate than the rotational frequencies. Since that the effect of the electrons on O_2 on the hyperfine terms relating to the nitrogen can be disregarded due to the large NO to O_2 separation, the values used for the hyperfine constants, a, b_F, c, d, eQq_0 and eQq_2 are expected to be highly accurate. From accuracy tests, even if these constants are incorrect by 10%, the hyperfine splits change by at most 2 MHz, but generally only move by approximately 0.5 MHz. This high level of accuracy is the reason for quoting the hyperfine splits to the nearest 0.01 MHz.

6.3 Spectroscopic Results

Using FTMS and the passive gas mixing rig outlined in chapter 2, the region from 7.0 to 18.2 GHz has been scanned for species resulting from mixing NO and O_2. Using a previously unassigned signal the experiment was optimised to give a strong signal to noise (S/N) ratio.

In the range scanned, numerous assigned species, including $(NO)_2$, Ar-NO and Ar-NO_2, were observed. In addition to these anticipated signals, approximately 150 hyperfine split signals with varying S/N were observed. These signals were expected to be due to not only NO-O_2, but also $(NO)_x$. The full dataset of all observed lines recorded has been included on the attached CD.

Using the C++ program written to calculate the rotational energy levels as a base, see section 6.2.5, a program was developed to calculate allowed rotational transitions, then using observed transitions, the parameters within the program were adjusted to match the predictions to the observations. The program used the Levenberg-Marquardt method for multi-dimensional non-linear regression [14] to simultaneously fit the internal parameters. An outline of the logic of the program is given in figure 6.18.

In the program the transitions are fitted by variation of the separate parameters. The derivative of the transitions with respect to a parameter was calculated using the Hellman-Feynman Theorem. This theorem states that for a Hamiltonian dependent on parameter λ, $\hat{\mathscr{H}}(\lambda)$, with eigenvector $|\psi(\lambda)\rangle$, and eigenvalue $E(\lambda)$, then

$$\frac{\partial E}{\partial \lambda} = \left\langle \psi(\lambda) \left| \frac{\partial \hat{\mathscr{H}}}{\partial \lambda} \right| \psi(\lambda) \right\rangle \tag{6.39}$$

If the Hamiltonian is defined as

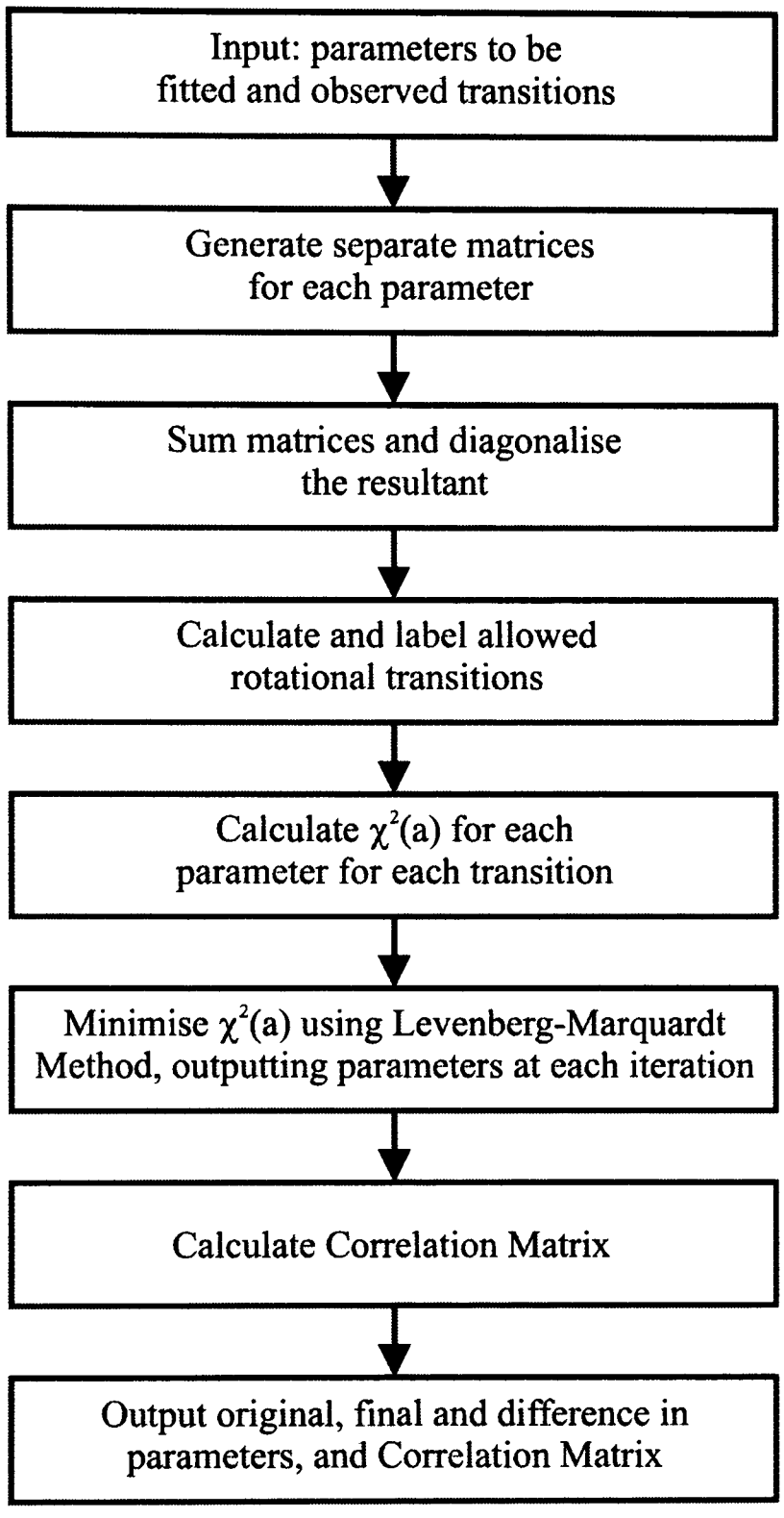

Figure 6.18: Logical structure of program used to assign data for NO-O_2

$$\hat{\mathscr{H}} = A.\mathbf{M}_A + B.\mathbf{M}_B + \ldots \tag{6.40}$$

Then

$$\frac{\partial \hat{\mathscr{H}}}{\partial A} = \mathbf{M}_A \tag{6.41}$$

$$\frac{\partial \hat{\mathscr{H}}}{\partial B} = \mathbf{M}_B \tag{6.42}$$

Assuming that the wavefunctions can be expressed as a linear combination of their basis functions

$$|\psi(\lambda)\rangle = \left|\sum_i c_i \phi_i\right\rangle \tag{6.43}$$

Then

$$\begin{aligned} \frac{\partial E}{\partial \lambda} &= \left\langle \sum_i c_i \phi_i \left| \frac{\partial \hat{\mathscr{H}}}{\partial \lambda} \right| \sum_j c_j \phi_j \right\rangle \\ &= \sum_{i,j} c_i^* M_{ij} c_j \end{aligned} \tag{6.44}$$

given that M_{ij} and c_i are all known from the initial stages of the calculation for the energy levels, it is a trivial task to determine the derivatives of the transitions with respect to each of the parameters to be fitted.

If the Hamiltonian is non-linearly dependent on a parameter, then one can either calculate the derivatives analytically and use the above equations, or one can simply determine a numerical derivative by adjusting the parameter and recalculating the energy.

Using the computer program and data from the 150 hyperfine clusters, numerous fittings were attempted. The correlation matrix was used to ensure that dependent parameters were not fitted simultaneously. The frequency range around the calculated transitions which was scanned, for observations to fit to, was an order of magnitude larger than the variation expected in the calculated transition frequencies due to the zero-point energy vibrations. Even after minimising the number of parameters to be fitted, no reasonable fits were found.

The frequency range about the calculated transitions which was scanned for observations to fit to was an order of magnitude larger than the variation expected in the calculated transition frequencies due to the zero-point energy vibrations.

On analysis, the lack of fit for NO-O_2 is not unexpected. The estimated sensitivity of the FTMS experiment was 0.030-0.025 Debye. The dipole moments calculated by the RSPT2 method, see 6.38, give the greatest value of 0.091 Debye to μ_b. However, most of the expected transitions are a-type. Given μ_a is 0.034 Debye, this means observations will be near the limit of sensitivity and hence detection and assignment of these transitions will be unfeasible.

6.4 Comparison of NO-O_2 and NO-HF

To test the validity of the calculated rotational energy levels of NO-O_2, one can compare them to the simplistic model developed by Kopp and Hougen [15] for NO-HF.

By examining the rotational energy levels given in figure 6.17, disregarding the hyperfine

structure, a simplistic relationship seems to present itself. Using the Kopp and Hougen model, [15], disregarding centrifugal distortion, the expected functional form of the energy levels would be

$$E = \alpha J\left(J+1\right) \pm \beta\left(J+\frac{1}{2}\right) \tag{6.45}$$

Using the lower lying calculated rotational energy levels, it is possible to solve for α and β. The average results, in MHz, for parameters are given below

K_a	α	β
$\pm\frac{1}{2}$	3426.098	3964.866
$\pm\frac{3}{2}$	3441.004	390.604

As expected, the form fits more accurately for $K_a = \pm\frac{1}{2}$ than for $K_a = \pm\frac{3}{2}$ where the model is invalid. The match of the calculated rotational energy levels to the simplistic model of Kopp and Hougen provides a degree of validation for the former.

Conclusion

Experimentally, it has not been possible to assign any of the observed transitions to NO-O_2. Many of the observed transitions are dependent on the presence of both NO and O_2, but their assignment to the complex has not been possible. This could imply that NO-O_2 is not present under the used experimental conditions. However, the *ab initio* calculations indicate that one would not anticipate having the required sensitivity to observe NO-O_2 even if this species was present in significant quantity.

In Appendix B, the transitions are given as a rotational transition and a hyperfine split since the there are represented by different levels of accuracy. The rotational frequency are based on

geometry predicted by the *ab initio* PES and the other fine structure constants. Given that the *ab initio* calculations are in effect MP2 calculations, the location of the global minimum may be inaccurate. If global minimum moved then the constants β, $\bar{\epsilon}$ and $\Delta\epsilon$ would all change, not to mention A, B, C, θ_1 and θ_2, leading to shifts in the rotational transition frequencies by several hundred MHz. This poor level of accuracy is the reason for only quoting the rotational transition frequencies to the nearest MHz.

References

[1] Gaussian 03, Revision C.02, M. J. Frisch, G. W. Trucks, H. B. Schlegel, G. E. Scuseria, M. A. Robb, J. R. Cheeseman, J. A. Montgomery, Jr., T. Vreven, K. N. Kudin, J. C. Burant, J. M. Millam, S. S. Iyengar, J. Tomasi, V. Barone, B. Mennucci, M. Cossi, G. Scalmani, N. Rega, G. A. Petersson, H. Nakatsuji, M. Hada, M. Ehara, K. Toyota, R. Fukuda, J. Hasegawa, M. Ishida, T. Nakajima, Y. Honda, O. Kitao, H. Nakai, M. Klene, X. Li, J. E. Knox, H. P. Hratchian, J. B. Cross, V. Bakken, C. Adamo, J. Jaramillo, R. Gomperts, R. E. Stratmann, O. Yazyev, A. J. Austin, R. Cammi, C. Pomelli, J. W. Ochterski, P. Y. Ayala, K. Morokuma, G. A. Voth, P. Salvador, J. J. Dannenberg, V. G. Zakrzewski, S. Dapprich, A. D. Daniels, M. C. Strain, O. Farkas, D. K. Malick, A. D. Rabuck, K. Raghavachari, J. B. Foresman, J. V. Ortiz, Q. Cui, A. G. Baboul, S. Clifford, J. Cioslowski, B. B. Stefanov, G. Liu, A. Liashenko, P. Piskorz, I. Komaromi, R. L. Martin, D. J. Fox, T. Keith, M. A. Al-Laham, C. Y. Peng, A. Nanayakkara, M. Challacombe, P. M. W. Gill, B. Johnson, W. Chen, M. W. Wong, C. Gonzalez, and J. A. Pople, Gaussian, Inc., Wallingford CT, 2004.

[2] MOLPRO, Version 2002.6, H.-J. Werner, P. J. Knowles, R. Lindh, F. R. Manby, M. Schtz, P. Celani, T. Korona, G. Rauhut, R. D. Amos, A. Bernhardsson, A. Berning, D. L. Cooper, M. J. O. Deegan, A. J. Dobbyn, F. Eckert, C. Hampel, G. Hetzer, A. W. Lloyd, S. J. McNicholas, W. Meyer, M. E. Mura, A. Nickla, P. Palmieri, R. Pitzer, U. Schumann, H. Stoll, A. J. Stone, R. Tarroni, and T. Thorsteinsson, University College Cardiff Consultants Limited, 2004

[3] G. Herzberg, *Molecular Spectra and Molecular Structure: I. Spectra of Diatomic Molecules.* D. Van Nostrand Company, Inc. (1963)

[4] P. L. Fast, M. L. Sanchez and D.G. Truhlar, J. Chem. Phys. **111**, 2921 (1999)

[5] W. Klopper, Mol. Phys. **99**, 481 (2001)

[6] J. M. Rintelman, I. Adamovic, S. Varganov and M. S. Gordon, J. Chem. Phys. **122**, 44105 (2005)

[7] H. Tsukahara, T. Ishida and M. Mayumi, Nitric Oxide **3**, 191 (1999)

[8] H. Qian, S. J. Low, D. Seccombe and B. J. Howard, J. Chem. Phys. **107**, 7651 (1997)

[9] C. R. Dennis, C. J. Whitham and B. J. Howard, J. Chem. Phys. **115**, 1355 (2001)

[10] R. N. Zare, *Angular Momentum: Understanding Spatial Aspects in Chemistry and Physics*, John Wiley & Son (1988)

[11] W. Gordy and R. L. Cook, *Microwave Molecular Spectra*, Interscience Publishers (1970)

[12] E. Klisch, S. P. Belov, R. Schieder, G. Winnewisser and E. Herbst, Mol. Phys. **97**, 65 (1999)

[13] B. J. Howard, *by personal communication*

[14] W. H. Press, B. P. Flannery, S. A. Teukolsky and W. T. Vetterling *Numerical Recipes.* Cambridge University Press (1987)

[15] I. Kopp and J.T. Hougen, Can. J. Phys. **45**, 2581 (1967)

Chapter 7

Calculations and Theory of NO_2-O_2

"If an idea's worth having once,

it's worth having twice."

Tom Stoppard

Introduction

Another potential weak interaction between two stable open-shell molecules is that between nitrogen dioxide and oxygen, NO_2-O_2. Using the theories and expertise developed during the research of NO-O_2, NO_2-O_2 has been investigated.

Using the *ab initio* methods developed for NO-O_2, detailed calculations have been performed on NO_2-O_2. The details on the exact methods used are presented below, with the results presented in Appendix C.

Specific theory has been developed to fully describe the rotational spectra of NO_2-O_2. Relevant fine and hyperfine structure terms have also been taken into account using the methods outlined below.

7.1 *Ab initio* Calculations

Based on arguments of chapter 3, the calculations for NO_2-O_2 complex were performed with a multi-reference Multi-Configuration Self Consistent Field (MCSCF) coupled to second order perturbation theory. The calculations were performed with MOLPRO [1] using Dunning basis sets.

7.1.1 Multi-reference Calculations

In NO_2-O_2 both of the monomers which form the complex are open-shell. NO_2 is $^2A_1$ [2] with its unpaired electron spatially localised on the nitrogen atom. O_2 is a $^3\Sigma^-$ in the ground state, but has two low lying excited states, $^1\Delta$ and $^1\Sigma^+$, at 7,918 and 13,195 cm^{-1} [3]. The combination of these two monomers can lead to either an overall doublet or quartet state. Given that the doublet is a low-spin state with unpaired electrons, a multi-reference *ab initio* method is required to accurately describe the basic wavefunction.

The method used was Restricted Open-Shell Hartree-Fock (ROHF), followed by Multi-reference Rayleigh Schrödinger Second Order Perturbation Theory (RSPT2). Five dimensional Potential Energy Surfaces (PES) were calculated using both the Dunning's aug-cc-pVDZ and aug-cc-pVTZ basis sets. Two basis sets were used to allow for basis set extrapolation to be performed, see chapter 3. All of these calculations were performed using a C_1 symmetry to make the results consistent. In the PES calculations the NO_2 and O_2 bond lengths and bond angles used were those of their monomer values. Separate PES calculations were performed for the complex and monomers allowing a binding energy (BE) to be calculated. The geometric setup used for the Z-matrix within the calculations is illustrated in figure 7.1.

NO_2 and O_2 are fixed at their calculated monomer geometries. NO_2 had bonds lengths of 1.1934 Å and a bond angle of 134.4°. O_2 had a bond length of 1.2234 Å . As in the case of NO-O_2, this does not permit relaxation of the monomer geometries, and may slightly underestimate the overall BE, but reduces the number of dimensions of the PES from nine to five. The O_2 is placed with its centre of mass on the x axis of the complex. The angle θ_2 gives the angle between the x axis and the line of atomic centres of O_2. The NO_2 is pivoted from the x axis at a distance of 1.0 Å . The angle of the pivot is given by θ_1. The angle ϕ_1 represents the rotation of the NO_2 about the pivot direction, from the plane of the nitrogen, the origin and the pivot point. The angle ϕ_2 represents the difference between the rotation of the O_2 and the NO_2 pivot direction about the x axis. See figure 7.2. R is the separation of the centre of mass of O_2 and the NO_2 pivot point along the x axis.

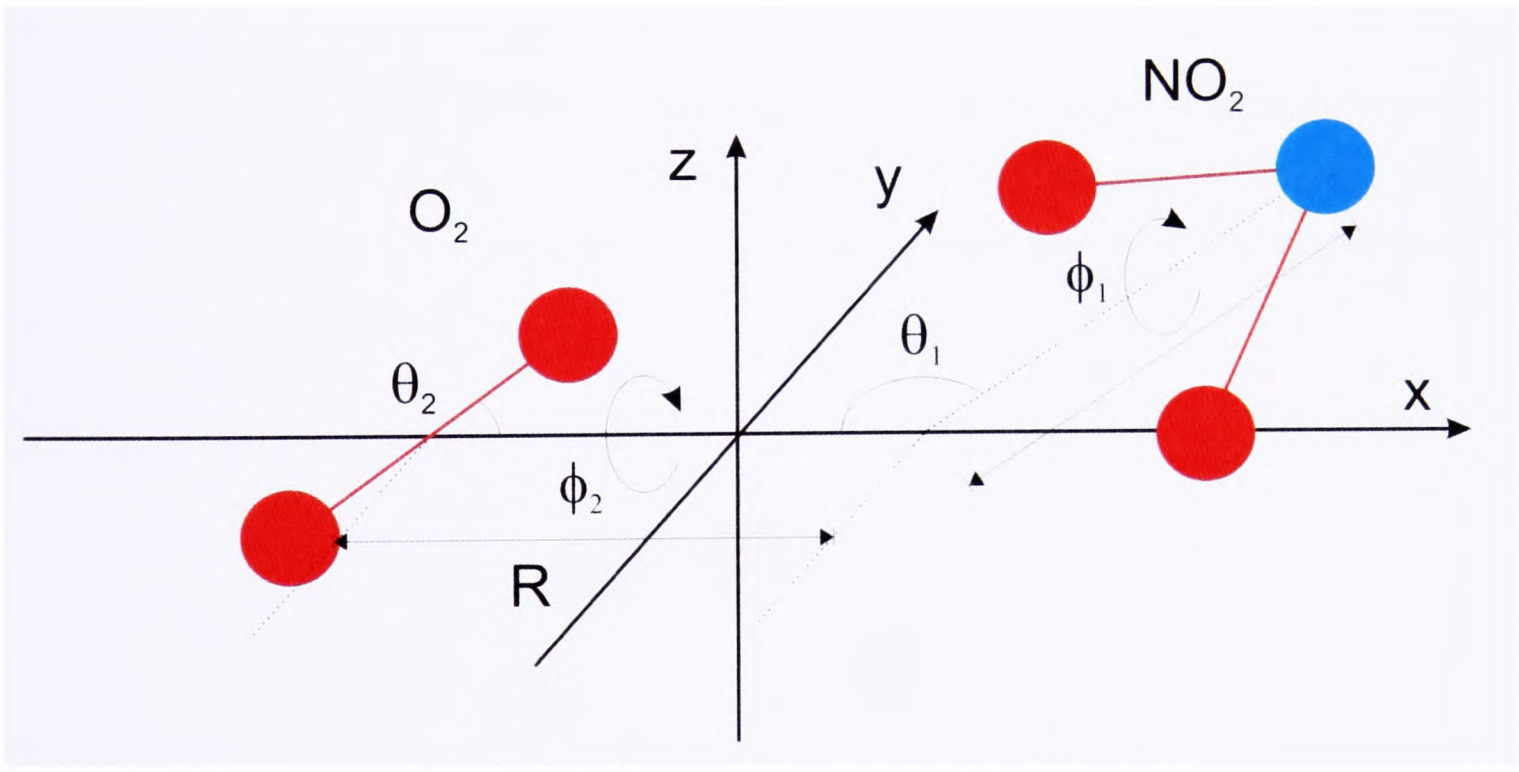

Figure 7.1: Geometry construction of NO_2-O_2

Given the inherent size inconsistency of the RSPT2 method, as detailed in chapter 3, the Size-Consistency Error (SCE) [4] has been calculated

Electronic State	SCE cm^{-1}
Doublet	24.28
Quartet	6.45

With these methods, crude yet extensive PES were calculated for the doublet and quartet spin states to determine the rough location of the global minima. Having located the approximate minima, more detailed PES were calculated, and full basis set extrapolation was performed.

The full detailed PES can be found in electronic form on the attached CD. The PES covers the range R = 2.8 to 3.1 Å in steps of 0.1 Å , θ_1 = 160.0 to 180.0°, θ_2 = 50.0 to 70.0°, ϕ_1 = 0.0 to 40.0° and ϕ_2 = 130.0 to 170.0°, all in steps of 10.0°.

Once the PES were completed, the lowest calculated point was found to be located on the doublet surface at R = 2.9 Å , θ_1 = 170.0°, θ_2 = 60.0°, ϕ_1 = 20.0° and ϕ_2 = 160.0°, with a BE = -410.6 cm^{-1}. Plots of the three partially occupied molecular orbitals at this geometry are given in figures 7.3, 7.4 and 7.5.

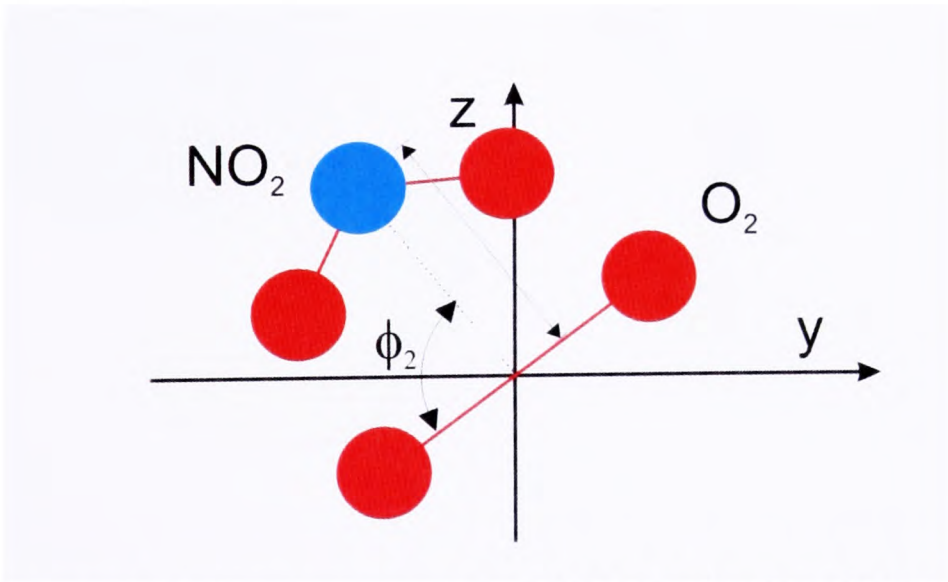

Figure 7.2: Geometry construction of NO_2-O_2 Viewed parallel to x axis

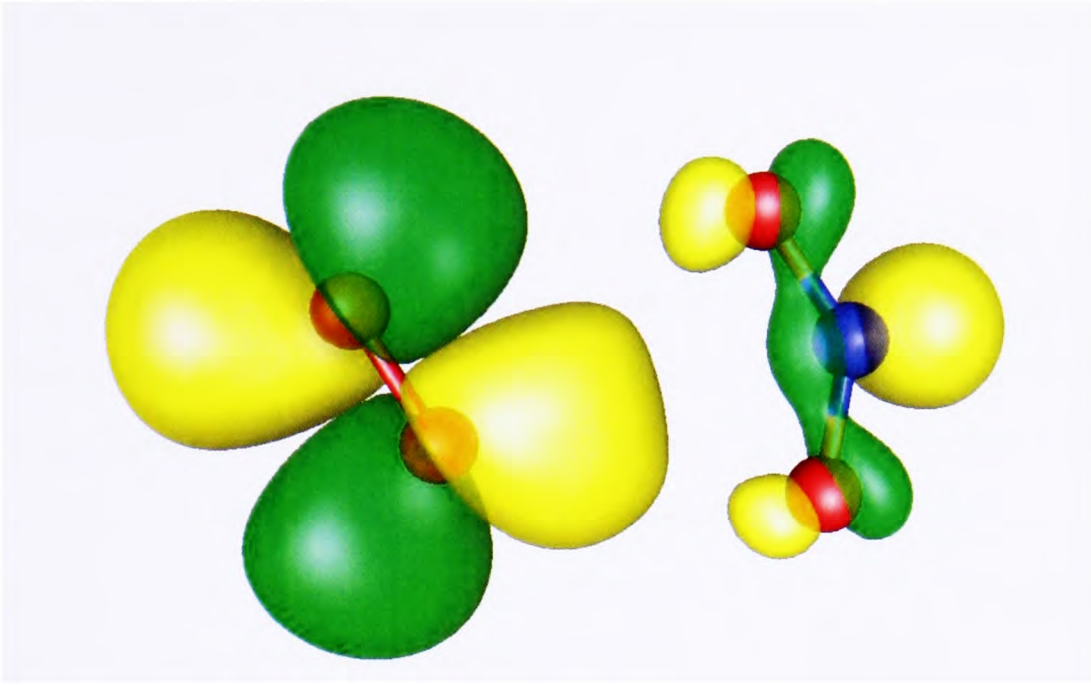

Figure 7.3: Partially occupied Hartree-Fock molecular orbital # 19 - RSPT2 occupancy = 1.069

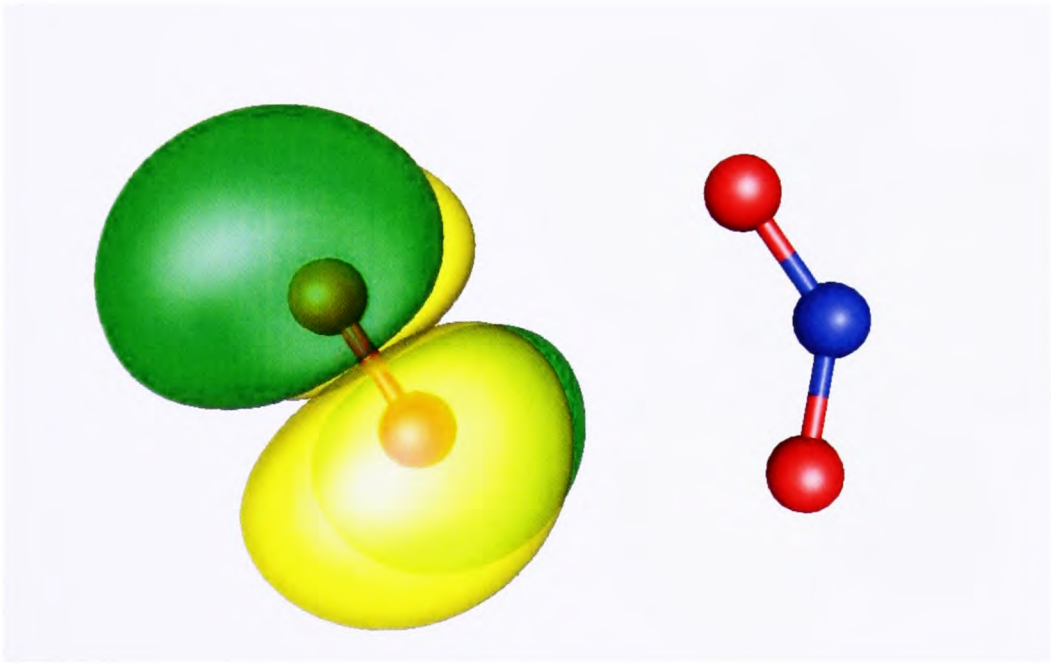

Figure 7.4: Partially occupied Hartree-Fock molecular orbital # 20 - RSPT2 occupancy = 1.026

In the range calculated the doublet surface resides below the quartet with an average separation of $\approx$ 200 cm^{-1}. The separation of the doublet and the quartet states illustrates an exponential increase as R decreases.

As observed in NO-O_2, the lowest state for NO_2-O_2 was a doublet which is in apparent contradiction of basic Hund's rules. However, as before, the most strongly bound point on the PES favours the formation of a what appears to be pseudo-chemical bond, due to exchange correlation, between the occupied π^* orbital on the O_2 and the in-plane orbital on NO_2. This geometry is favoured if exchange correlation is allowed, which is the case in the doublet where the two electrons on O_2 are α and the electron on NO_2 is β. In the quartet, where all of the unpaired electrons are α, this favourable interaction is not possible.

The calculated PES does not indicate the presence of any other genuine secondary minima. What may appear like minima in the PES are a result of the relationship of the topography of

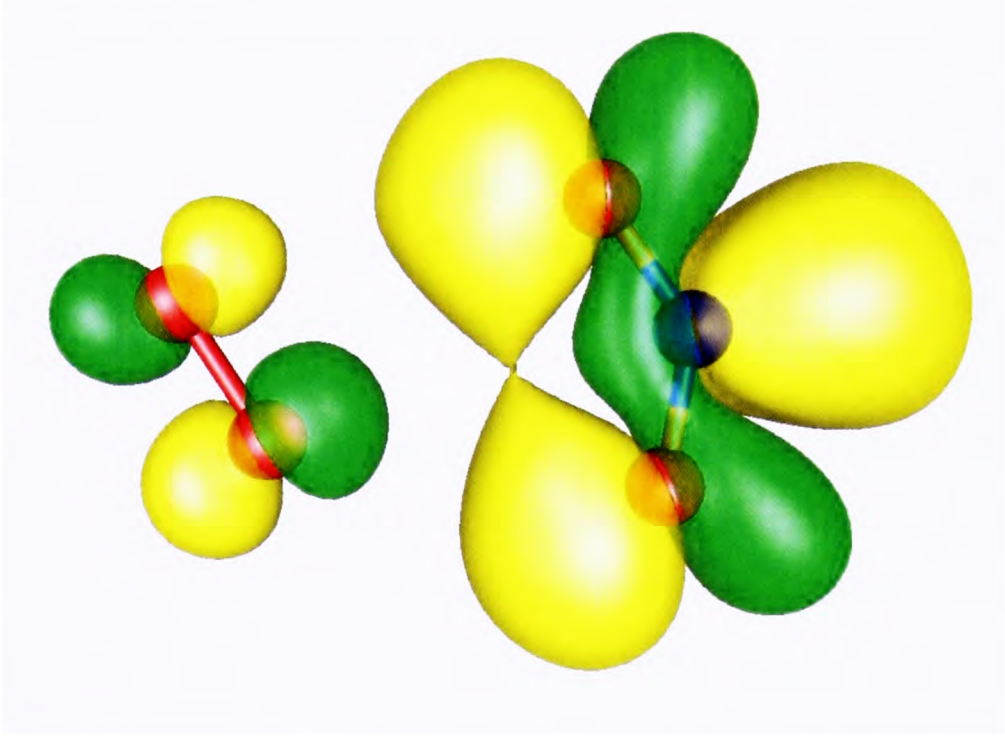

Figure 7.5: Partially occupied Hartree-Fock molecular orbital # 21 - RSPT2 occupancy = 0.977

the PES and the manner in which it has been parameterised. The lack of genuine secondary minima on the PES is a result of the small range of each dimension for which the PES was calculated. The detailed PES covers only four values of R, three of θ_1 and θ_2 and five of ϕ_1 and ϕ_2. As found for NO-O_2, one would expect secondary minima to occur at other geometries, including the T-shape and linear forms.

Given that the calculated PES covers five dimensions illustrating the surfaces in an understandable manner is complicated. Starting at the global minimum geometry, $R = 2.9$ Å , $\theta_1 = 170.0°$, $\theta_2 = 60.0°$, $\phi_1 = 20.0°$ and $\phi_2 = 160.0°$, the PES was extended to cover $R =$ 2.7 to 5.0Å . The results of these extended R calculations are given in figure 7.6. As can be seen in figure 7.6, the doublet resides below the quartet for all values of R, and both potential converge to zero at large R. This plot parallels that for NO-O_2 as illustrated in figure 6.9.

Given the small range of the detailed PES, and the complications of the coordinate system used to construct the system in the *ab initio* calculations it is not possible to generate meaningful contour plots of the potentials, as has been done for NO-O_2. However, by examination of the PES around the global minimum, it can be seen that the PES for the doublet state has a relatively high curvature, in terms of energy rise for a set displacement, with respect to R, θ_1 and θ_2, and relatively low curvature with respect to ϕ_1 and ϕ_2. This variation in the PES curvature can be rationalized in terms of the interaction of the NO_2 and the O_2.

Assuming that the interaction that favours the doublet in the geometry of the global minimum, is the spatial overlap and exchange correlation of the π^* orbital on O_2 and the in-plane orbital of the NO_2, then a rise in energy reflects the disruption of this overlap. Variation in R will move the moieties either apart, reducing the spatial overlap of the orbitals, or closer together, pushing the orbitals too close together. The first of these variations is disfavoured as it reduces the exchange correlation of the O_2 π^* orbital and NO_2 in-plane orbital. However,

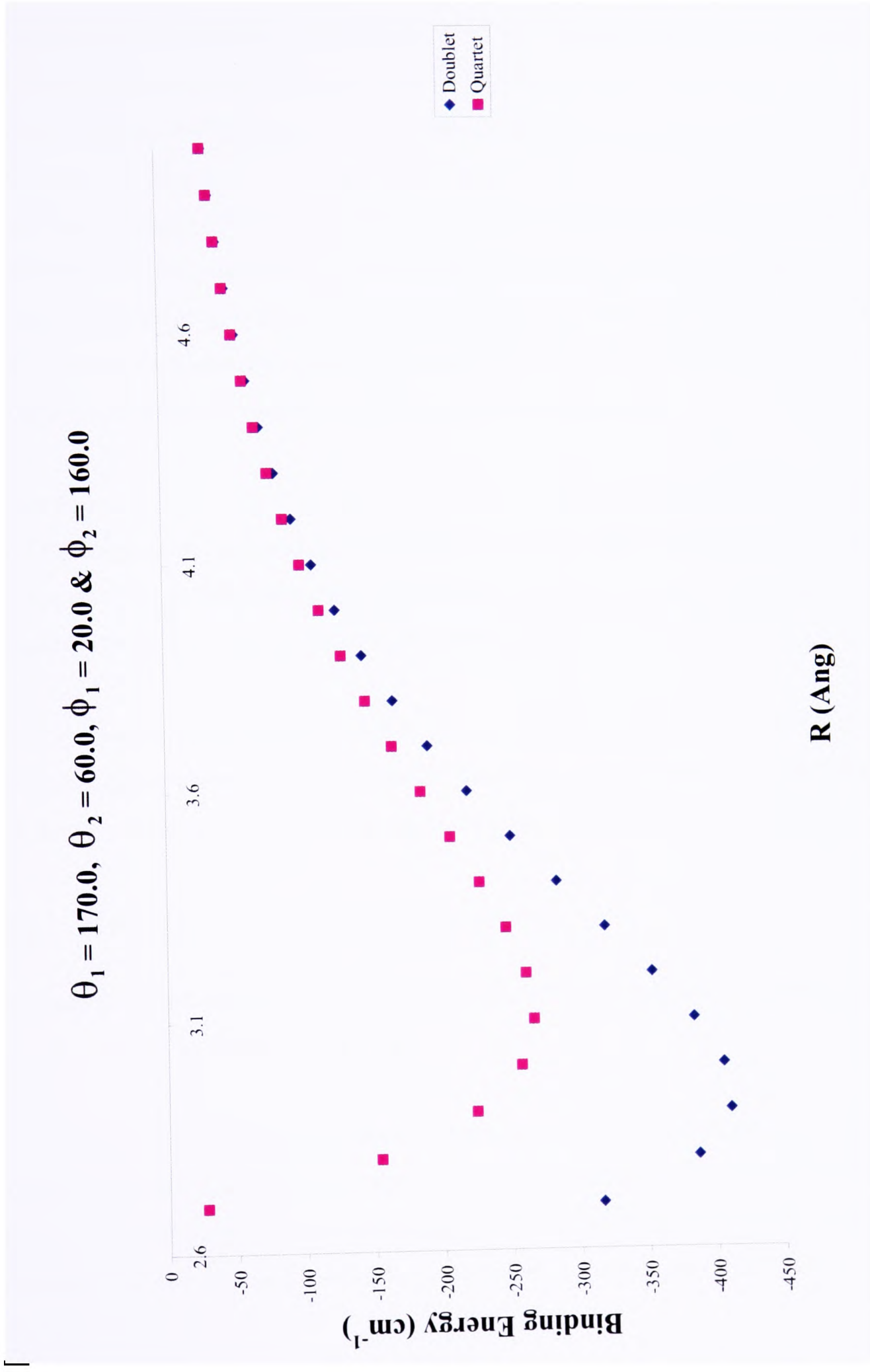

Figure 7.6: Calculated Binding Energies (cm^{-1}) versus R (A)

the separation of the moieties is favoured by the Pauli exclusion principle. The second variation increases the exchange correlation, but is significantly disfavoured by the Pauli exclusion principle. These variations lead to a pronounced potential well as a function of R. A variation in θ_1 moves the NO_2 out of the plane on the O_2 π^* orbital which is disfavoured. It should be noted that the global minimum geometry value of $\theta_1 = 170.0°$ gives a maximum out of plane displacement for the moieties of 0.017Å and the slight energy rise observed when θ_1 increases to 180.0° is thought to be an artefact of the calculations. Alteration in the value of θ_2 from 60.0° moves the in-phase lobe of the O_2 π^* orbital out of the centre of the NO_2 in-plane orbital, see figure 7.3, which will rapidly disrupt this favourable interaction.

Variations in ϕ_1 and ϕ_2 from their values at the global minimum both effectively rotate the NO_2 about vector connecting their centre of masses. These variations will simply rotate the in-plane NO_2 orbital about the in-phase lobe of the O_2 π^* orbital. This means that the potential will not be a sensitive function of either ϕ_1 or ϕ_2.

Given the additional degree of internal freedom of NO_2-O_2 compared to NO-O_2, it has not been possible to confirm this interpretation of the relative energy ordering of the two spin states, but the hypothesis of exchange correlation is consistent with the work in chapter 6.

7.2 NO_2-O_2 Rotational Theory

To develop an effective rotational model for NO_2-O_2, a Hamiltonian has to be constructed which represents all of the relevant interactions.

As was the case for NO-O_2 the effective Hamiltonian for NO_2-O_2 can be constructed in one of several manners. The most basic model to use for the system is that of rigid rotor, but this is only valid if the system's geometry is not dramatically modified by the effects of vibrational averaging over the rotational parameters due to zero-point energy. As presented in section

6.2 of the discussion of NO-O_2, one can test the validity of the rigid-rotor by determining the root mean square (RMS) deviation of the systems geometry due to zero-point energy vibrations. However, for NO_2-O_2, due to the five internal dimensions and the complicated parameterisation of the geometry, it is not easily possible to approximate the normal modes of the vibrations, beyond the stretch between NO_2 and O_2. Using the methods and approximations outlined in section 6.2, it can be shown that the RMS of δR is 0.11 Å , which is of comparable magnitude to that of NO-O_2.

In addition to the problems outlined above, as with all points on a PES, an *ab initio* calculation of the zero-point energies would not give meaningful results as the geometry is not geometrically optimised.

Therefore RMS amplitudes can only be estimated for NO_2-O_2 based on the PES. Given the high curvature of the potential well with respect to θ_1 and θ_2 a crude estimate of the RMS values of $\delta\theta_1$ and $\delta\theta_2$ would be in the range of 5-10°. The low curvature of the PES with respect to ϕ_1 and ϕ_2 leads to a crude estimate for the RMS values of $\delta\phi_1$ and $\delta\phi_2$ being of the order of a few tens of degrees. Thus, it can be seen that a rigid-rotor model would not be expected to reproduce the observed transitions to a high level of accuracy, but it would provide a starting model which can be refined once an initial assignment has been made.

Another feature of the PES for NO_2-O_2 is that at the lowest calculated point the separation of the doublet and the quartet states is 186.4 cm^{-1}. This separation is at least two orders of magnitude higher than other potential interaction terms in the Hamiltonian. The other interacting terms include the spin-spin coupling of O_2 but do not include spin-orbit coupling due to the lack of orbital angular momentum. The spin-spin coupling constant is approximately only 1.6 cm^{-1} and therefore would have a minor effect on the predicted spectrum. Additionally, the spin-spin coupling is modelled with a second-rank tensor which has a zero expectation value in

the doublet spin state.

Overall, this means that it is acceptable to disregard the quartet spin state and O_2 spin-spin coupling in the construction of the effective Hamiltonian.

7.2.1 Coupling Scheme

As outlined in chapter 6, the selection of the basis set used in the construction of the wavefunctions is crucial if one is to obtain solutions with meaningful quantum numbers. In addition, the use of a well selected basis set will reduce the number of off-diagonal terms in the overall matrices that have to be diagonalized to give the energies of the systems.

Since the interaction of the doublet and quartet spin states is disregarded, there is no requirement, at the rotational and fine structure level, to take account of the separate spins of the NO_2 and the O_2. This simplification allows the basis set to be constructed with a coupled system spin rather than with two distinct uncoupled spins for the moieties.

From previous work conducted on complexes containing NO_2 [5], [6], there are two potential coupling schemes for the angular momentum

$$\boldsymbol{N}+\boldsymbol{S}=\boldsymbol{J}, \quad \boldsymbol{J}+\boldsymbol{I}=\boldsymbol{F} \tag{7.1}$$

$$\boldsymbol{I}+\boldsymbol{S}=\boldsymbol{G}, \quad \boldsymbol{G}+\boldsymbol{N}=\boldsymbol{F} \tag{7.2}$$

where $\boldsymbol{N}$ is the rotational angular momentum, $\boldsymbol{S}$ is the electron spin angular momentum and $\boldsymbol{I}$ is the nuclear spin angular momentum. The selection of coupling scheme is of no consequence assuming that the basis set fully represents the system. Given this solution indifference, the work in this thesis has used the coupling scheme in equation 7.1, and hence assumes that the

coupling of the spin to the rotation is the dominate term. The basis set used is given by

$$|\eta N K S \Sigma J I F M_F\rangle \tag{7.3}$$

where η represents all unspecified quantum numbers such as vibration and electronic labels, N is the rotational quantum number, with internal projection K, J is the overall angular momentum neglecting nuclear spin, I is the nuclear angular momentum and F is the overall total angular momentum, with projection M_F. S has a value of $\frac{1}{2}$ since the system is assumed to be a doublet state.

7.2.2 Effective Hamiltonian

The effective Hamiltonian is composed of three types of terms. The first class of terms is the rotational term given by the rotational Hamiltonian $\hat{\mathscr{H}}_{rot}$. The second class of terms is the fine structure term, which is represented by the electron spin-rotation Hamiltonian $\hat{\mathscr{H}}_{sr}$, which will have contributions from both NO_2 and O_2. The final class of terms is the hyperfine terms which is comprised of the magnetic hyperfine, $\hat{\mathscr{H}}_{mag}$, and nuclear quadrupole $\hat{\mathscr{H}}_{quad}$. These are combined in the overall Hamiltonian

$$\hat{\mathscr{H}} = \hat{\mathscr{H}}_{rot} + \hat{\mathscr{H}}_{sr} + \hat{\mathscr{H}}_{mag} + \hat{\mathscr{H}}_{quad} \tag{7.4}$$

The rotational Hamiltonian is given by

$$\hat{\mathscr{H}}_{rot} = A\hat{N}_a^2 + B\hat{N}_b^2 + C\hat{N}_c^2 \tag{7.5}$$

where A, B and C are the rotational constants of the complex. As this Hamiltonian involves just the pure rotation there are none of the complications that were experienced with NO-O_2,

see chapter 6. The solution follows that outlined in chapter 4, with $\hat{J}$ replaced with $\hat{N}$.

The other terms in the overall Hamiltonian are discussed below.

7.2.3 Fine Structure Hamiltonian

The fine structure of the Hamiltonian for NO_2-O_2 is fully represented by the electron spin-rotation Hamiltonian. This represents the interaction of the spin dipole moment of the electron on NO_2 and electrons on O_2, with the magnetic field that is generated by the complex. This is given by a standard representation [7]

$$\hat{\mathscr{H}}_{sr} = \frac{1}{2}\sum_{\alpha\beta}\varepsilon_{\alpha\beta}\left(\hat{N}_\alpha\hat{S}_\beta + \hat{S}_\beta\hat{N}_\alpha\right) \tag{7.6}$$

where α and β run over the molecular fixed parameters x, y and z, and $\varepsilon_{\alpha\beta}$ is a specific term in the spin-rotation tensor. $\hat{N}$ is the rotational quantum operator of the complex and $\hat{S}$ is the overall spin quantum operator. This term is composed of two contributions, one from NO_2 and the other from O_2. However, these contributions will be dependent on their individual spins, $\boldsymbol{S}_1$ for NO_2 and $\boldsymbol{S}_2$ for O_2, rather than the overall spin.

The contribution of NO_2 can be represented by

$$\frac{1}{2}\sum_{\alpha\beta}\varepsilon'_{\alpha\beta}\left(\hat{N}_\alpha\hat{S}_{1\beta} + \hat{S}_{1\beta}\hat{N}_\alpha\right) \tag{7.7}$$

and that of O_2 can be represented by

$$\frac{1}{2}\sum_{\alpha\beta}\varepsilon''_{\alpha\beta}\left(\hat{N}_\alpha\hat{S}_{2\beta} + \hat{S}_{2\beta}\hat{N}_\alpha\right) \tag{7.8}$$

The spin coupling is given by

$$\boldsymbol{S}_1 + \boldsymbol{S}_2 = \boldsymbol{S} \tag{7.9}$$

Therefore we need to express matrix elements of $\boldsymbol{S}_1$ and $\boldsymbol{S}_2$ in terms of the matrix elements of the overall spin, $\boldsymbol{S}$, so that the Hamiltonian is defined with regards to the complex, rather than NO_2 or O_2. For the overall spin the matrix elements have the form

$$\left\langle S_1 S_2 S M_S \left| T_0^1(\mathbf{S}) \right| S_1 S_2 S M_S \right\rangle = M_S \tag{7.10}$$

It can be shown with the standard tensor algebra, see Appendix A, that the matrix elements of $\boldsymbol{S}_1$ can be expressed as

$$\begin{aligned}
&\left\langle S_1 S_2 S M_S \left| T_0^1(\mathbf{S}_1) \right| S_1 S_2 S M_S \right\rangle \\
= \;& (-1)^{(S-M_S)} \begin{pmatrix} S & 1 & S \\ -M_S & 0 & M_s \end{pmatrix} \left\langle S_1 S_2 S \left|\left| T_0^1(\mathbf{S}_1) \right|\right| S_1 S_2 S \right\rangle \\
= \;& (-1)^{(S-M_S)} \begin{pmatrix} S & 1 & S \\ -M_S & 0 & M_s \end{pmatrix} \\
& (-1)^{(S_1+S_2+S+1)} (2S+1) \begin{Bmatrix} S_1 & S & S_2 \\ S & S_1 & 1 \end{Bmatrix} \left\langle S_1 \left|\left| T_0^1(\mathbf{S}_1) \right|\right| S_1 \right\rangle \\
= \;& (-1)^{(S-M_S)} \begin{pmatrix} S & 1 & S \\ -M_S & 0 & M_s \end{pmatrix} \\
& (-1)^{(S_1+S_2+S+1)} (2S+1) \begin{Bmatrix} S_1 & S & S_2 \\ S & S_1 & 1 \end{Bmatrix} (S_1(S_1+1)(2S_1+1))^{\frac{1}{2}}
\end{aligned} \tag{7.11}$$

By using the algebraic expansions for the 3-j and 6-j symbols in terms of S_1, S_2, S and M_s given in the standard texts [9], it can be shown that for the doublet state of the complex

$$\begin{aligned}
&\left\langle S_1 S_2 S M_S \left| T_0^1(\mathbf{S}_1) \right| S_1 S_2 S M_S \right\rangle \\
&= M_S \ \frac{1}{2} \ \frac{(S(S+1)+S_1(S_1+1)-S_2(S_2+1))}{S(S+1)} \\
&= M_S \ \frac{1}{2} \ \frac{(\frac{1}{2}(\frac{1}{2}+1)+\frac{1}{2}(\frac{1}{2}+1)-1(1+1))}{\frac{1}{2}(\frac{1}{2}+1)} \\
&= -\frac{1}{3} \ M_S
\end{aligned} \tag{7.12}$$

By a similar expression it can be seen that

$$\left\langle S_1 S_2 S M_S \left| T_0^1(\mathbf{S}_2) \right| S_1 S_2 S M_S \right\rangle = +\frac{4}{3} \ M_S \tag{7.13}$$

This means for expressions in the Hamiltonian that are dependent on the spin of NO_2, a pre-multiplying factor of $-1/3$ is required for the constants to take account of the spin coupling in the complex. For terms dependent on the spin of O_2 the constant pre-multiplier is $+4/3$. Therefore in the spin-rotation Hamiltonian the parameter $\varepsilon_{\alpha\beta}$ can be determined as a sum of the parameters of NO_2 and O_2, with the appropriate pre-multipliers

$$\varepsilon_{\alpha\beta} = \frac{-\varepsilon'_{\alpha\beta}}{3} + \frac{4\varepsilon''_{\alpha\beta}}{3} \tag{7.14}$$

For the spin-rotation Hamiltonian even if one disregards the influence of quartic spin-rotation terms, there are still nine terms in the general expression for $\hat{\mathscr{H}}_{sr}$ [7]. If the complex has sym-

metry then the number of terms in $\hat{\mathscr{H}}_{sr}$ decreases due to the requirement that $\hat{\mathscr{H}}_{sr}$ transforms according to the symmetric representations of the complex's point group. If the complex has a plane of symmetry, then $\hat{\mathscr{H}}_{sr}$ has only five terms, and if the system is of the D_{2h} point group than there are only three terms [7].

The determination of the number of and values of the spin-rotation parameters is discussed in section 7.2.5, where the geometry of the complex is related to that of the NO_2 and O_2 monomer.

7.2.4 Hyperfine Structure Hamiltonian

Within NO_2-O_2 the non-zero nitrogen nuclear spin, I_N, will couple to magnetic field and electric field gradients generated by the rest of the complex. Given that the O_2 and NO_2 are separated by greater than 3.7 Å , it is reasonable to assume that the impact of the O_2 on the electron distribution near to the nitrogen nucleus is negligible and that the through space effect of the O_2 electrons is small. This means that the hyperfine constants of NO_2 are little affected, allowing the effect to O_2 to be disregarded. Specifically, the hyperfine interaction for NO_2-O_2 has been developed using the standard theory [8] as the effect of the two unpaired electrons on the O_2 can be neglected. The hyperfine is composed of two parts, the magnetic and quadrupole interactions, which are discussed separately below.

The magnetic hyperfine term represents the magnetic interaction of the nitrogen nuclear spin with the spin and orientation of the unpaired electron. The magnetic term is composed of two parts. The first part represents the isotropic Fermi contact interaction and the second part represents the dipole-dipole interaction of the nucleus and the unpaired electrons. Both of these terms have a standard form when written with spherical tensors [10]

$$\hat{\mathscr{H}}_{mag} = b'_F T^1(\mathbf{I}).T^1(\mathbf{S}_1) - \sqrt{10}T^1(\mathbf{I}).T^1(\mathbf{S}_1, C'^2) \tag{7.15}$$

As in section 7.2.3, in equation 7.15 $\boldsymbol{S}_1$ refers to the NO_2 monomer. Using the relationship derived in the preceding section, it is possible to re-write equation 7.15 in terms of the complex

$$\hat{\mathscr{H}}_{mag} = b_F T^1(\mathbf{I}).T^1(\mathbf{S}) - \sqrt{10}T^1(\mathbf{I}).T^1(\mathbf{S}, C^2) \tag{7.16}$$

where $b_F = -b'_F/3$ and $T^1(\mathbf{S}, C^2) = -(T^1(\mathbf{S}_1, C'^2))/3$.

In equation 7.16, the tensor product, $T^1(\boldsymbol{S}, C^2)$, has components [10]

$$T^1_p(\mathbf{S}, C^2) = -\sqrt{3}(-1)^p g\mu_B g_N \mu_N \sum_{p_1 p_2} T^1_{p_1}(\mathbf{S}) T^2_{p_2}(C) \begin{pmatrix} 1 & 2 & 1 \\ p_1 & p_2 & -p \end{pmatrix} \tag{7.17}$$

where g and g_N are the electron and nuclear g-factors, and μ_B and μ_N are the Bohr and nuclear magnetons.

$T^2_{p_2}(C)$ are the parameters describing the dipolar interaction [8] and for a planar molecule, such as NO_2, can be related in any axes system to three independent cartesian components

$$\begin{aligned} g\mu_B g_N \mu_N T^2_0(C) &= \frac{1}{2}T_{zz} = -\frac{1}{2}(T_{xx} + T_{yy}) \\ g\mu_B g_N \mu_N T^2_1(C) &= -g\mu_B g_N \mu_N T^2_{-1}(C) = -\frac{T_{xz}}{\sqrt{6}} \\ g\mu_B g_N \mu_N T^2_2(C) &= g\mu_B g_N \mu_N T^2_{-2}(C) = \frac{(T_{xx} - T_{yy})}{\sqrt{24}} \end{aligned} \tag{7.18}$$

The electric interaction takes the form of a quadrupole interaction which can be represented by [10]

$$\hat{\mathscr{H}}_{quad} = eT^2(\nabla\nabla\mathbf{V}).T^2(\mathbf{Q}) \tag{7.19}$$

where e is the electronic charge. In this case, given that there is no $\boldsymbol{S}$ dependence, there is no requirement to adjust the parameters in this standard Hamiltonian.

As with the magnetic interaction it can be shown [10] that for a planar molecule the cartesian components of $T^2(\mathbf{Q})$, $\chi_{\alpha\beta}$, can be related to the components $T^2(\nabla\nabla\mathbf{V})$ by

$$\begin{aligned} \chi_{zz} &= \frac{2eQ}{2I(2I-1)}T_0^2(\nabla\nabla\mathbf{V}) \\ \chi_{xx}-\chi_{yy} &= \frac{2\sqrt{6}eQ}{2I(2I-1)}T_{\pm 2}^2(\nabla\nabla\mathbf{V}) \end{aligned} \tag{7.20}$$

where Q is defined in chapter 5.

7.2.5 Energy levels and transition strength factors

To calculate the energy levels for NO_2-O_2 one has to determine the various constants for the complex. For the fine and hyperfine structure, the constants will be based on those of the NO_2 and O_2 monomers. However, it is not possible in general to simply use the monomer values, as the axes used for the monomers are not orientated as the principal axes of the complex. This leads to the requirement of projecting the monomer axis systems onto the complex.

The spin-rotation tensor elements, and the magnetic and quadrupole cartesian components all transform as x^2, y^2 and z^2. It is common practice to denote these transformations as xx, yy and zz. The Fermi contact term is a scalar and thus can be taken from the monomer to the complex without having to consider the axis system.

The projections of xx, yy and zz can be determined in several different ways. The most general manner makes use of the Euler angles, ϕ, θ and χ [9]. Using $[x, y, z]$ to represent the monomers axes in the their principal axes, and $[X, Y, Z]$ as the complex principle axes, it can be seen from the standard texts [9] that the relationship between these two axes is given by

$$\begin{bmatrix} X \\ Y \\ Z \end{bmatrix} = \begin{bmatrix} c(\phi)c(\theta)c(\chi) - s(\phi)s(\chi) & -c(\phi)c(\theta)s(\chi) - s(\phi)c(\chi) & c(\phi)s(\theta) \\ s(\phi)c(\theta)c(\chi) + c(\phi)s(\chi) & -s(\phi)c(\theta)s(\chi) + c(\phi)c(\chi) & s(\phi)s(\theta) \\ -s(\theta)c(\chi) & s(\theta)s(\chi) & c(\theta) \end{bmatrix} \begin{bmatrix} x \\ y \\ z \end{bmatrix} \quad (7.21)$$

where c = cos and s = sin, and elements represent the direction cosines. The relationship is expressed as above, due to the subsequent requirement for numerical solutions. Using this relationship it is possible to determine not only how x, y, and z transform to X, Y and Z, but also how xx, yy and zz transform. In the monomers the off-diagonal terms are zero. In the complex the off-diagonal terms maybe of comparable magnitude to those on-diagonal, but they will have a negligible impact on the final predicted spectrum, and can therefore be disregarded. Therefore it can be seen that [11]

$$
\begin{aligned}
X^2 = XX &= xx\,(c(\phi)c(\theta)c(\chi) - s(\phi)s(\chi))^2 \\
&\quad + yy\,(-c(\phi)c(\theta)s(\chi) - s(\phi)c(\chi))^2 \\
&\quad + zz\,(c(\phi)s(\theta))^2 \qquad (7.22) \\
Y^2 = YY &= xx\,(s(\phi)c(\theta)c(\chi) + c(\phi)s(\chi))^2 \\
&\quad + yy\,(-s(\phi)c(\theta)s(\chi) + c(\phi)c(\chi))^2 \\
&\quad + zz\,(s(\phi)s(\theta))^2 \qquad (7.23) \\
Z^2 = ZZ &= xx\,(-s(\theta)c(\chi))^2 + yy\,(s(\theta)s(\chi))^2 \\
&\quad + zz\,(c(\theta))^2 \qquad (7.24)
\end{aligned}
$$

The expressions above can be used for the magnetic and quadrupole terms. However, the spin-rotation terms depend upon the speed of rotation around the different axes and hence are proportional to the rotational constants. Thus, the constants for the complex and monomers need to be scaled by their rotational constants, R^C and R^M. Therefore the general expressions for the spin-rotation terms are

$$\begin{aligned}
\left(\frac{\varepsilon_{XX}}{R^C_{XX}} - \bar{\varepsilon}\right) &= \left(\frac{\varepsilon_{xx}}{R^M_{xx}} - \bar{\varepsilon}\right)(c(\phi)c(\theta)c(\chi) - s(\phi)s(\chi))^2 \\
&\quad + \left(\frac{\varepsilon_{yy}}{R^M_{yy}} - \bar{\varepsilon}\right)(-c(\phi)c(\theta)s(\chi) - s(\phi)c(\chi))^2 \\
&\quad + \left(\frac{\varepsilon_{zz}}{R^M_{zz}} - \bar{\varepsilon}\right)(c(\phi)s(\theta))^2 \qquad (7.25) \\
\left(\frac{\varepsilon_{YY}}{R^C_{YY}} - \bar{\varepsilon}\right) &= \left(\frac{\varepsilon_{xx}}{R^M_{xx}} - \bar{\varepsilon}\right)(s(\phi)c(\theta)c(\chi) + c(\phi)s(\chi))^2 \\
&\quad + \left(\frac{\varepsilon_{yy}}{R^M_{yy}} - \bar{\varepsilon}\right)(-s(\phi)c(\theta)s(\chi) + c(\phi)c(\chi))^2 \\
&\quad + \left(\frac{\varepsilon_{zz}}{R^M_{zz}} - \bar{\varepsilon}\right)(s(\phi)s(\theta))^2 \qquad (7.26) \\
\left(\frac{\varepsilon_{ZZ}}{R^C_{ZZ}} - \bar{\varepsilon}\right) &= \left(\frac{\varepsilon_{xx}}{R^M_{xx}} - \bar{\varepsilon}\right)(-s(\theta)c(\chi))^2 + \left(\frac{\varepsilon_{yy}}{R^M_{yy}} - \bar{\varepsilon}\right)(s(\theta)s(\chi))^2 \\
&\quad + \left(\frac{\varepsilon_{zz}}{R^M_{zz}} - \bar{\varepsilon}\right)(c(\theta))^2 \qquad (7.27)
\end{aligned}$$

where

$$\bar{\varepsilon} = \frac{1}{3}\left(\frac{\varepsilon_{xx}}{R^M_{xx}} + \frac{\varepsilon_{yy}}{R^M_{yy}} + \frac{\varepsilon_{zz}}{R^M_{zz}}\right) \qquad (7.28)$$

For O_2, where $\chi = 0.0$

$$\begin{aligned}
R^M_{zz} &= 0, \qquad R^M_{xx} = R^M_{yy} \\
\varepsilon_{zz} &= 0, \qquad \varepsilon_{xx} = \varepsilon_{yy} \qquad (7.29)
\end{aligned}$$

This means that the expressions for the O_2 spin-rotation parameters simplify to

$$\begin{aligned}
\left(\frac{\varepsilon_{XX}}{R^C_{XX}}\right) &= \left(\frac{\varepsilon_{xx}}{R^M_{xx}}\right)\left(c^2(\phi)c^2(\theta)+s^2(\phi)\right) \\
\left(\frac{\varepsilon_{YY}}{R^C_{YY}}\right) &= \left(\frac{\varepsilon_{xx}}{R^M_{xx}}\right)\left(s^2(\phi)c^2(\theta)+c^2(\phi)\right) \\
\left(\frac{\varepsilon_{ZZ}}{R^C_{ZZ}}\right) &= \left(\frac{\varepsilon_{xx}}{R^M_{xx}}\right)\left(s^2(\theta)\right)
\end{aligned} \tag{7.30}$$

From the lowest calculated point on the NO_2-O_2 PES, it is possible to numerically solve for the Euler angles for NO_2 and O_2. The stepwise rotations of the Euler angles are illustrated in standard texts [9].

Based on the orientations presented in figure 7.7 [12], the numerically calculated values of the Euler angles, for NO_2 and O_2, are

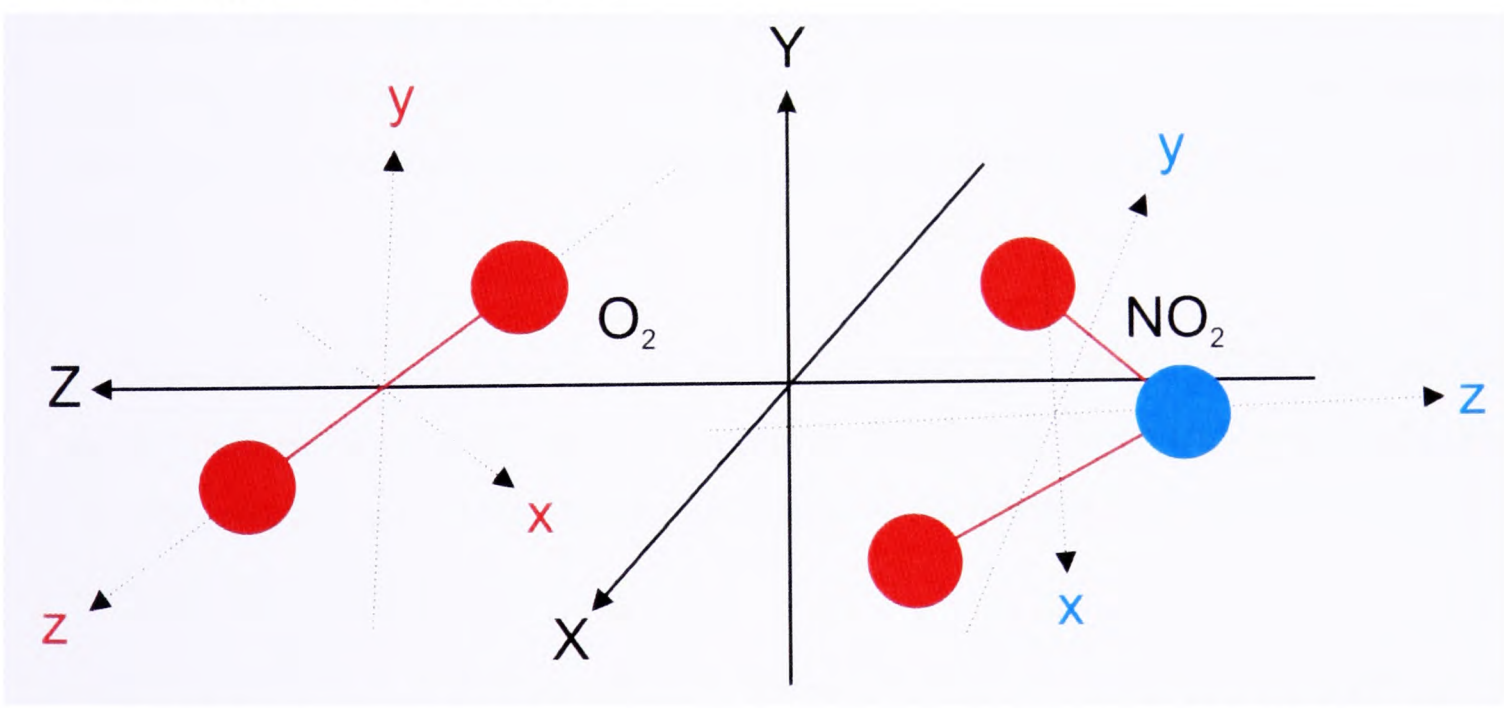

Figure 7.7: Orientation of NO_2-O_2. For free NO_2 (x, y, z) corresponds to (c, a, b), for free O_2 (x, y, z) corresponds to (b, c, a) and for the complex (X, Y, Z) corresponds to (B, C, A)

Parameter	Value (MHz)	Parameter	Value (MHz)
A	10,947	T_{AA}	-12.18
B	2,682	T_{BB}	6.33
C	2,154	T_{CC}	5.86
ε_{AA}	-65.41	χ_{AA}	-1.51
ε_{BB}	-25.58	χ_{BB}	0.31
ε_{CC}	-11.29	χ_{CC}	1.20
b_F	-49.09		

Table 7.1: Parameters used for NO_2-O_2 rotational energy level predictions

Constant	NO_2	O_2
ϕ	13.8	0.3
θ	166.6	56.3
χ	-76.5	0.0

Using these values and the relationships given above and the spin conversion factors, the rotational constants and the projected fine and hyperfine constants for NO_2-O_2 can be calculated. Using monomer constants for NO_2 from the work of Bowman et al. [13] and monomer constants for O_2 from Brown and Carrington's work [14], calculations yield the results given in table 7.1.

Using the values from table 7.1 and the spectra prediction software SPFIT [15], one can predict the microwave spectra of NO_2-O_2. The calculated energy levels are presented in figure 7.8. The predicted spectra for low lying levels with $N \leq 3$ between 5 and 20 GHz is presented in section C.2 of Appendix C.

Relative transition strengths for the allowed transitions are given in section C.2. These have been calculated by the SPFIT program using the method outlined in chapter 6. Here the values of the dipole moment components are taken into account. Transitions are allowed for all three dipole moments, but the strongest are a-type due to the values of the dipole moment

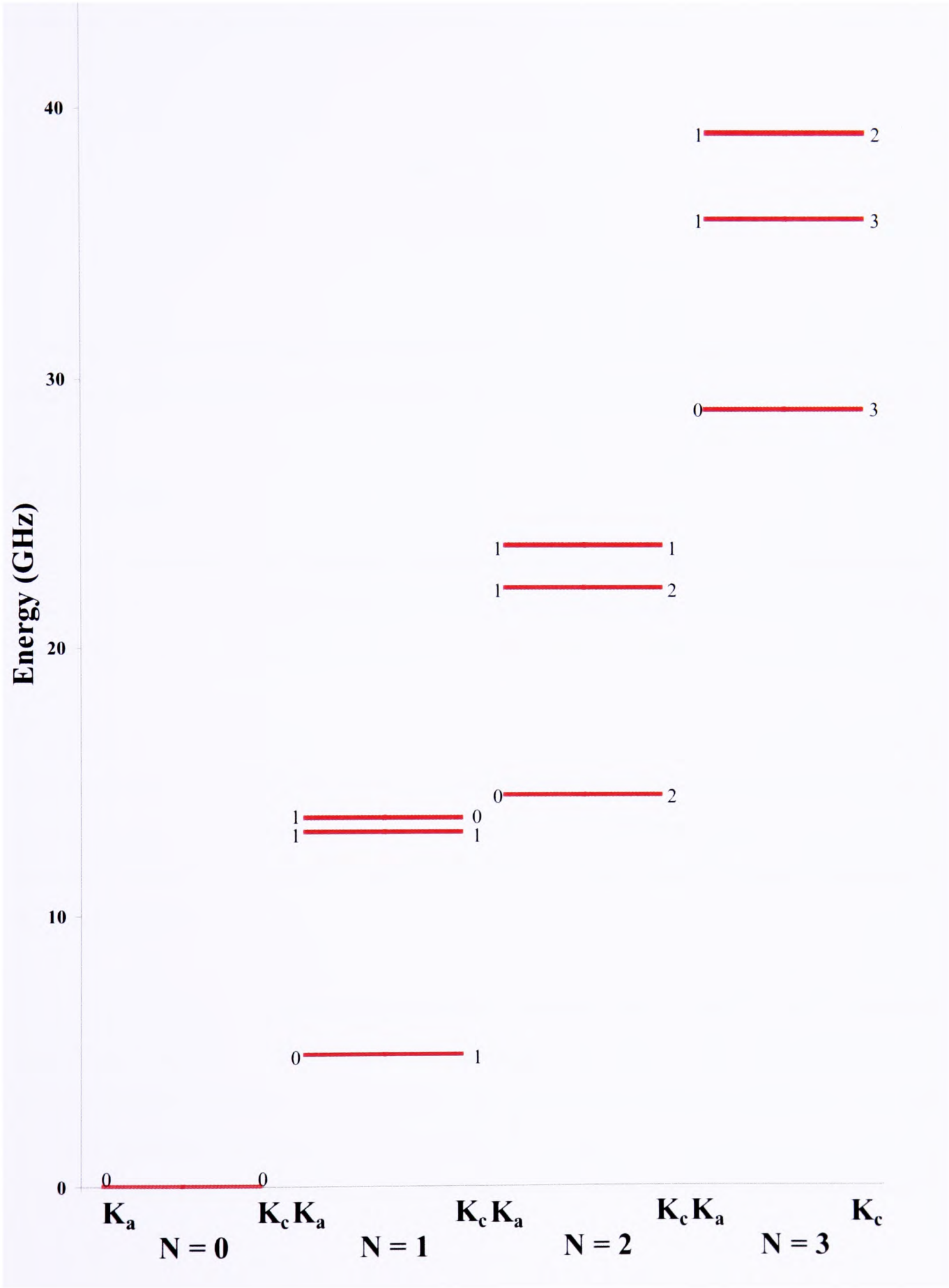

Figure 7.8: Rotational Energy Levels of NO_2-O_2

components. For the lowest point on the PES, the calculated dipole moments in Debye are

$$\begin{aligned} |\mu_a| &= 0.591 \\ |\mu_b| &= 0.128 \\ |\mu_c| &= 0.031 \end{aligned} \tag{7.31}$$

These relatively high values of the dipole moments in comparison to those of NO-O_2 mean that it should be possible to observe NO_2-O_2 with a Fourier transform microwave spectrometer.

Conclusion

From an examination of the calculated energy levels disregarding the fine and hyperfine structure, the pattern follows that of an asymmetric rotor. This is anticipated since the effects of the fine and hyperfine terms are minimal compared to the effect of the rotational constants.

Comparison of the calculated spectra and transition strengths with experimentally observed transitions indicate that NO_2-O_2 was not present in significant concentrations under the experimental conditions. The comparison was conducted over a sufficient range to encompass any variation in transition frequencies resulting from the zero-point energy vibrational averaging of the rotational constants.

In Appendix C, the transitions are presented as the rotational transition and a hyperfine split. The presentation of the transition frequencies has been split in this way to illustrate the differing levels of accuracy of the constants. The values of the rotational constants, A, B and C, which determine the position of the rotational transition are dependent on the accuracy of the *ab initio* PES. These calculations are based only on second order perturbation theory

and therefore the exact position of the global minimum may be inaccurate. These potential inaccuracies lead to the rotational transitions only been quoted to the nearest MHz.

The fine and hyperfine structure on each rotational level is based on NO_2 monomer values. These monomer values have been researched in depth by other groups and are therefore known to a high degree of accuracy. With this initial accuracy, it seems reasonable to quote the fine and hyperfine splits to the nearest 0.01 MHz.

References

[1] MOLPRO, Version 2002.6, H.-J. Werner, P. J. Knowles, R. Lindh, F. R. Manby, M. Schtz, P. Celani, T. Korona, G. Rauhut, R. D. Amos, A. Bernhardsson, A. Berning, D. L. Cooper, M. J. O. Deegan, A. J. Dobbyn, F. Eckert, C. Hampel, G. Hetzer, A. W. Lloyd, S. J. McNicholas, W. Meyer, M. E. Mura, A. Nickla, P. Pal mieri, R. Pitzer, U. Schumann, H. Stoll, A. J. Stone, R. Tarroni, and T. Thorsteinsson, University College Cardiff Consultants Limited, 2004

[2] V. Kurkal, P. Fleurat-Lessard and R. Schinke, J. Chem. Phys. **119**, 1489 (2003)

[3] G. Herzberg, *Molecular Spectra and Molecular Structure: I. Spectra of Diatomic Molecules.* D. Van Nostrand Company, Inc. (1963)

[4] J. M. Rintelman, I. Adamovic, S. Varganov and M. S. Gordon, J. Chem. Phys. **122**, 44105 (2005)

[5] J. M. Brown and T. J. Sears, Mol. Phys. **34**, 1595 (1977)

[6] R. J. Low *High Resolution Spectroscopy of Weakly Bound Molecular Complexes.* D.Phil Thesis, Oxford University (1995)

[7] J. M. Brown and T. J. Sears, J. Mol. Spectrosc. **75**, 111 (1979)

[8] I. C. Bowater, J. M. Brown and A. Carrington, Proc. Roy. Soc. Lond. **333**, 265 (1973)

[9] R. N. Zare, *Angular Momentum: Understanding Spatial Aspects in Chemistry and Physics*, John Wiley & Son (1988)

[10] T. J. Sears, Comput. Phys. Rep. **2**, 3 1984

[11] M. Schäfer, T. Ha and A. Bauder, J. Chem. Phys. **119**, 8404 (2003)

[12] R. J. Low, M. D. Brookes, C. J. Whitham and B. J. Howard, J. Chem. Phys. **105**, 6756 (1996)

[13] W. C. Bowman and F. C. De Lucia, J. Chem. Phys. **77**, 92 (1982)

[14] J. M. Brown and A Carrington, *Rotational Spectroscopy of Diatomic Molecules*, Cambridge University Press (2003)

[15] H. M. Pickett, J. Mol. Spectrosc. **148**, 371 (1991)

Chapter 8

Conclusion

"There is no greater mistake then the hasty conclusion that opinions are worthless because they are badly argued"

Thomas H Huxley

Overview

This thesis has detailed the work undertaken in the investigation of the open-shell open-shell Van der Waals complexes of nitric oxide (NO) - oxygen (O_2) and nitrogen dioxide (NO_2) - oxygen (O_2). Experimental data has been collected targeting NO-O_2, using a Fourier transform microwave spectrometer. Detailed *ab initio* calculations have been performed on both species to locate NO-O_2 and NO_2-O_2 global minimum geometries and to determine the strength of binding of the complexes. Hamiltonians for the rotational energy levels have been developed for both species, and selection rules have been used on these levels to generate predicted rotational spectra. The salient details of this work are presented below.

8.1 Experimental work

Experimental data were collected between 7.0 and 18.2 GHz using a passive gas mixing rig, to combine NO and O_2 into an Ar carrier gas. Once assigned species had been removed from the data set, approximately 150 hyperfine split signals, with varying Signal to Noise ratios, were observed. These signals are thought to be due not only to NO-O_2, but also NO_2-O_2, $(NO)_x$ and Ar-$(NO)_x$.

The passive gas mixing rig proved critical for reliable mixing of sample gases into the rare gas carrier. This new design has now been incorporated into the experimental work of other group members.

8.2 *Ab initio* Calculations

Given the low-spin open-shell nature of NO-O_2 and NO_2-O_2, it was not possible to use standard single-reference *ab initio* methods, such as second order *Møller Plesset* perturbation theory (MP2). Multi-reference methods are required to generate a valid representation of the basic wavefunction. Thus, Multi-reference Rayleigh Schrödinger Second Order Perturbation Theory (RSPT2) was used for the *ab initio* calculations, in conjunction with Dunning's aug-cc-pVDZ and aug-cc-pVTZ basis sets. Two basis sets were used to allow extrapolation to an infinite basis set. Given that RSPT2 is not inherently size-consistent, a size-consistency correction had to be made to the calculations.

For NO-O_2, the global minimum was located on the $^2A''$ surface. This can be rationalised by considering the overlap and occupancy of the π^* orbitals. The extrapolated binding energy of NO-O_2 at this point is -325.1 cm^{-1}.

For NO_2-O_2, the global minimum was located on the doublet surface. Again, this can be

rationalised by considering the overlap and occupancy of the π^* orbitals of O_2 and the orbitals on NO_2. The extrapolated binding energy of NO_2-O_2 at this point is -410.6 cm^{-1}.

8.3 NO-O_2 Rotational Theory

The effective Hamiltonian constructed for NO-O_2 was composed of three classes of terms: the rotational $\hat{\mathscr{H}}_{rot}$ Hamiltonian; the fine structure terms spin-orbital $\hat{\mathscr{H}}_{so}$, spin-spin $\hat{\mathscr{H}}_{ss}$, spin-correlation $\hat{\mathscr{H}}_{sc}$ and the Renner-Teller $\hat{\mathscr{H}}_{q}$ Hamiltonians; and the hyperfine structure $\hat{\mathscr{H}}_{mag}$ and $\hat{\mathscr{H}}_{quad}$ Hamiltonians.

These terms were used within a specifically written C++ spectra prediction program. Using this program, an energy level pattern was calculated and the allowed transitions were predicted. Relative transition strength factors were also determined.

A second C++ program was written to adjust the internal Hamiltonian parameters of NO-O_2 to optimise the fit between the predicted and observed spectra. The program uses the Levenberg-Marquardt method for multi-dimensional non-linear regression to simultaneously fit the parameters.

Despite performing numerous fittings, no reasonable matches were found. This inability to fit the data to the predicted spectra of NO-O_2 is now understood to be an inevitable result of the allowed transitions having very low transition strength factors. This means that any transitions were near the limit of experimental sensitivity and hence detection and assignment of these is impractical.

To determine which species were generating the 150 hyperfine signals, attention was moved to $(NO)_4$ and Ar-$(NO)_2$. Preliminary *ab initio* calculations were performed on these species. Given that these are low-spin open-shell in nature, any Electron Correlation method used has

to be multi-reference to correctly represent the basic wavefunction. Since, $(NO)_4$ and Ar-$(NO)_2$ have 18 and 9 internal parameters respectively, performing Potential Energy Surface calculations using RPST2 and the aug-cc-pVDZ and aug-cc-pVTZ basis sets was prohibitive. Geometry optimisation was attempted using RPST2, but this proved unstable. It was thus impossible to determine the global minimum geometries for $(NO)_4$ and Ar-$(NO)_2$, and hence their predicted rotational spectra could not be obtained.

8.4 NO_2-O_2 Rotational Theory

The final species investigated for a possible fit with experimental data was NO_2-O_2. The effective Hamiltonian constructed for NO_2-O_2 was composed of three types of terms: the rotational $\hat{\mathscr{H}}_{rot}$ Hamiltonian; the fine structure term which is represented by the $\hat{\mathscr{H}}_{sr}$ spin-rotation Hamiltonian; and the hyperfine terms which are comprised of the $\hat{\mathscr{H}}_{mag}$ magnetic hyperfine, and $\hat{\mathscr{H}}_{quad}$ nuclear quadrupole Hamiltonians. Within the effective Hamiltonian, the interaction of the doublet and quartet forms of NO_2-O_2 was disregarded due to their large energy separation.

Using standard software for the prediction of rotational spectra, an energy level pattern was calculated, allowed transitions were determined and relative transition strength factors were evaluated.

By comparing the predicted spectrum for NO_2-O_2 with experimental observations, it can be inferred that NO_2-O_2 was not present in significant concentrations under the experimental conditions.

Summary

1. Experimental data has been collected between 7.0 and 18.2 GHz in an attempt to observe NO-O_2

2. Detailed *ab initio* calculations have been performed for NO-O_2 and predicted rotational spectra calculated

3. Specifically written and standard computer programs have been used to attempt to fit observations with predicted spectra. This did not succeed and the probable reason for that is understood

4. Steps 1, 2 and 3 were repeated for NO_2-O_2 with the same result

5. More limited calculations were made for $(NO)_4$ and Ar-$(NO)_2$ which indicated that computer resources were insufficient to predict accurate spectra. Thus, no attempt was made to fit observations to these species

In conclusion the experimental techniques of the group have been extended, detailed theory for NO-O_2 and NO_2-O_2 complexes have been produced and observational sensitivity requirements to actually observe those complexes using microwave spectroscopy understood.

Appendix A

Tensor Algebra

$$(1) \qquad \langle \alpha j m \,|T(k,q)|\, \alpha' j' m' \rangle = (-1)^{j-m} \begin{pmatrix} j & k & j' \\ -m & q & m' \end{pmatrix} \langle \alpha j \,||T^k||\, \alpha' j' \rangle$$

$$(2) \qquad \left\langle I \left|\left| I^{(1)} \right|\right| I' \right\rangle = \delta_{II'} \left[(2I+1)I(I+1)\right]^{\frac{1}{2}}$$

$$(3) \qquad \left\langle \gamma j_1 j_2 j m \left| \mathbf{T}^k . \mathbf{U}^k \right| \gamma' j_1' j_2' j' m' \right\rangle$$

$$= \delta_{jj'} \delta_{mm'} (-1)^{j_1'+j_2+j} \begin{Bmatrix} j_1 & j_2 & j \\ j_2' & j_1' & k \end{Bmatrix} \sum_{\gamma''} \langle \gamma j_1 \,||T^k||\, \gamma'' j_1' \rangle \langle \gamma'' j_2 \,||U^k||\, \gamma' j_2' \rangle$$

$$(4) \qquad \langle \gamma j_1 j_2 j m \,||T^{k_1}||\, \gamma' j_1' j_2' j' m' \rangle$$

$$= \delta_{j_2 j_2'} (-1)^{j_1+j_2+j'+k_1} \left[(2j'+1)(2j+1)\right]^{\frac{1}{2}} \begin{Bmatrix} j_1 & j & j_2 \\ j' & j_1' & k_1 \end{Bmatrix} \langle \gamma j_1 \,||T^{k_1}||\, \gamma' j_1' \rangle$$

(5) $$\left\langle \gamma j_1 j_2 j m \left|\left| U^{k_2} \right|\right| \gamma' j_1' j_2' j' m' \right\rangle$$

$$= \delta_{j_1 j_1'} (-1)^{j_1 + j_2' + j + k_2} \left[(2j'+1)(2j+1)\right]^{\frac{1}{2}} \left\{ \begin{array}{ccc} j_2 & j & j_1 \\ j' & j_2' & k_2 \end{array} \right\} \left\langle \gamma j_2 \left|\left| U^{k_2} \right|\right| \gamma' j_2' \right\rangle$$

Appendix B

$NO\text{-}O_2$ Appendix

B.1 *Ab initio* data

B.1.1 Gaussian 03

Tabulated output of counterpoise corrected geometry optimisation calculations preformed on Gaussian 03 [1] using MP2/6-311++G(d,p)

Doublet Spin State

Geometry	Corrected Energy (Hartree)	Binding Energy (cm^{-1})	Rotational Constant A (GHz)	Rotational Constant B (GHz)	Rotational Constant C (GHz)
a	-279.6553	-65.6781	56.4999	1.8845	1.8237
b	-279.6553	-65.6749	56.4783	1.8840	1.8232
c	-279.6553	-65.6718	56.7174	1.8828	1.8223
d	-279.6552	-50.5740	42,411.5238	1.5375	1.5375
e	-279.6551	-30.9970	29.3452	1.8062	1.7481
f	-279.6551	-27.9306	31.5407	1.8280	1.7278

Quartet Spin State

Geometry	Corrected Energy (Hartree)	Binding Energy (cm^{-1})	Rotational Constant A (GHz)	Rotational Constant B (GHz)	Rotational Constant C (GHz)
a′	-279.6553	-57.7996	50.1819	1.8456	1.7802
b′	-279.6553	-55.5022	53.3309	1.7988	1.7401
c′	-279.6553	-55.3502	53.3075	1.8001	1.7413
d′	-279.6553	-55.2313	53.3298	1.7986	1.7399
e′	-279.6552	-53.2630	42.2149	1.8038	1.7299
f′	-279.6552	-53.2007	42.2102	1.8015	1.7277
g′	-279.6552	-52.1147	376.9080	1.5427	1.5364
h′	-279.6552	-51.6537	40.2976	1.9329	1.8455
i′	-279.6552	-48.2419	36.7004	1.9875	1.8867
j′	-279.6552	-46.7210	92,690.9586	1.5065	1.5065
k′	-279.6552	-46.6980	23,164.9299	1.5068	1.5067
l′	-279.6552	-46.6552	134,176.2005	1.5185	1.5185
m′	-279.6552	-42.2066	42.1981	1.8988	1.8170
n′	-279.6552	-42.1734	42.2073	1.8860	1.8054
o′	-279.6552	-38.6130	377,025.8997	1.3654	1.3654
p′	-279.6552	-33.3157	28.1847	2.0587	1.9186
q′	-279.6551	-31.9398	29.3788	1.9490	1.8277
r′	-279.6551	-31.5892	25.9121	1.9905	1.8485
s′	-279.6551	-28.8244	31.2595	1.8008	1.7027
t′	-279.6551	-28.7232	31.6037	1.8294	1.7293
u′	-279.6551	-28.5513	28.1841	1.7946	1.6872
v′	-279.6551	-23.9095	31.2281	1.8309	1.7295

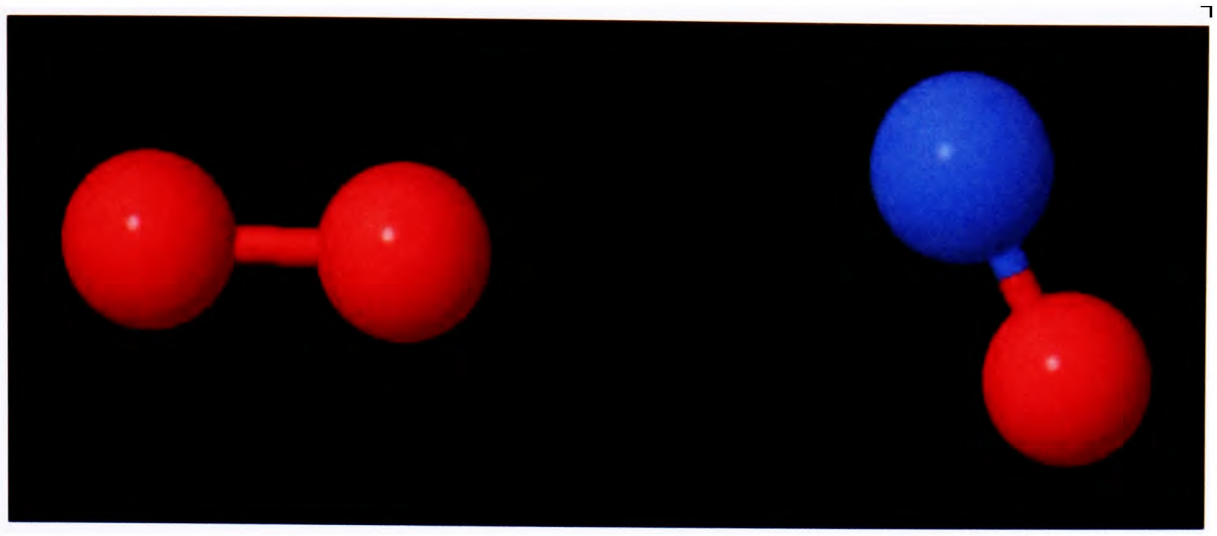

Figure B.1: Doublet Spin State - Geometry a

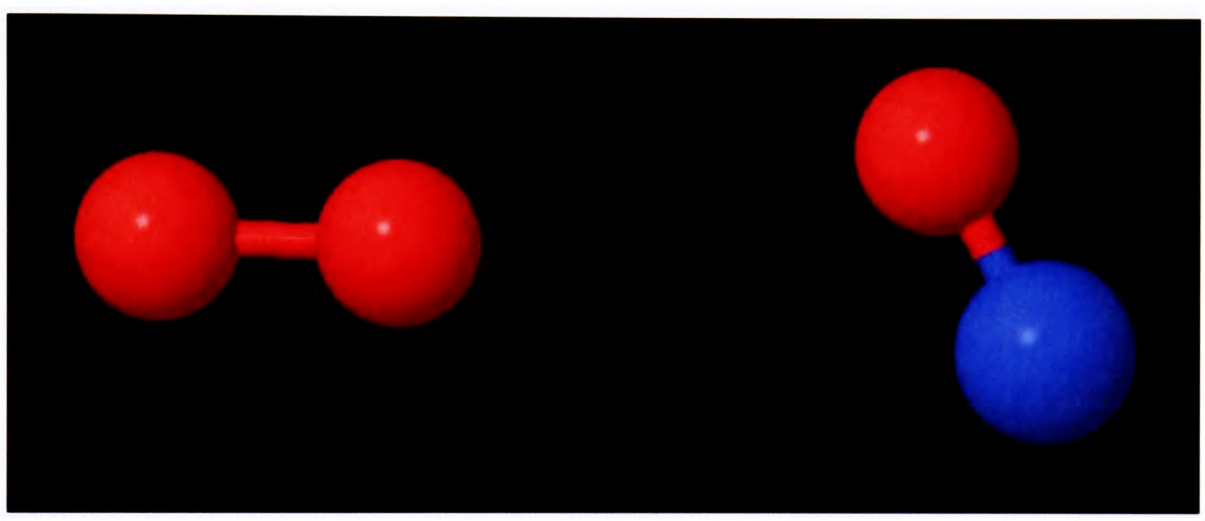

Figure B.2: Doublet Spin State - Geometry b

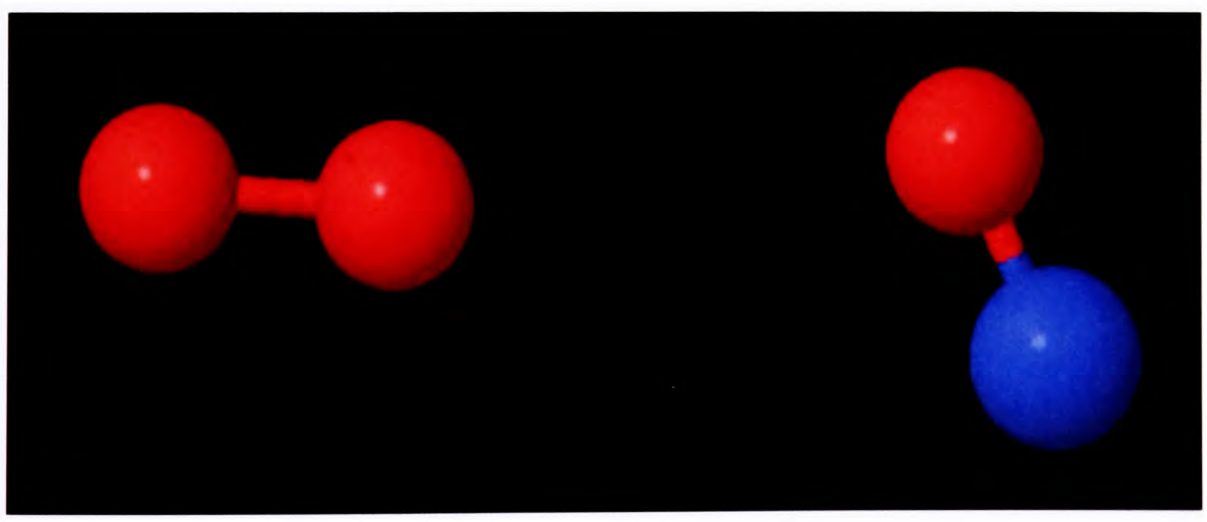

Figure B.3: Doublet Spin State - Geometry c

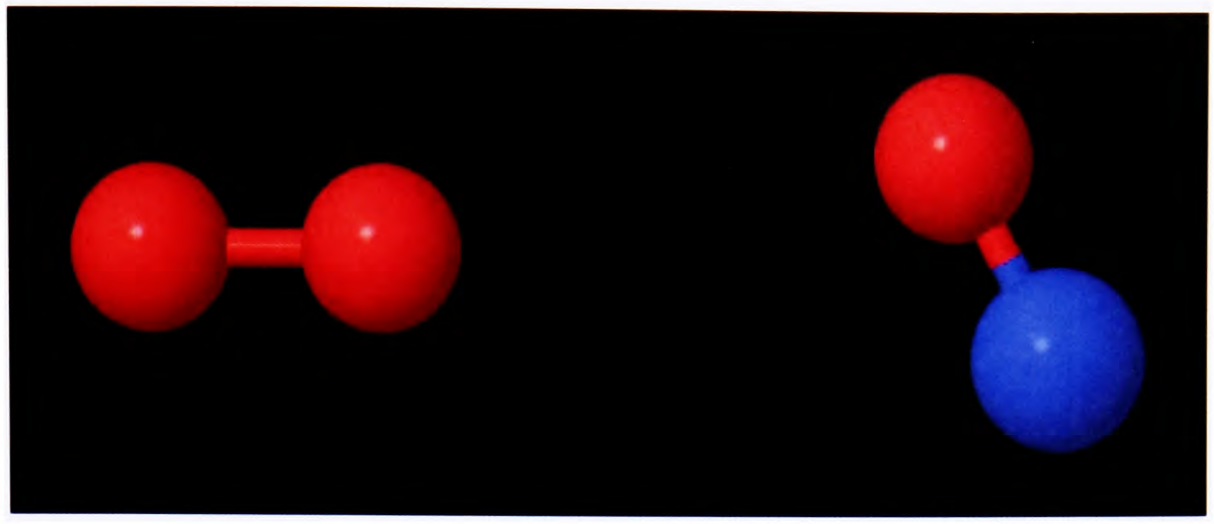

Figure B.4: Quartet Spin State Geometry a′

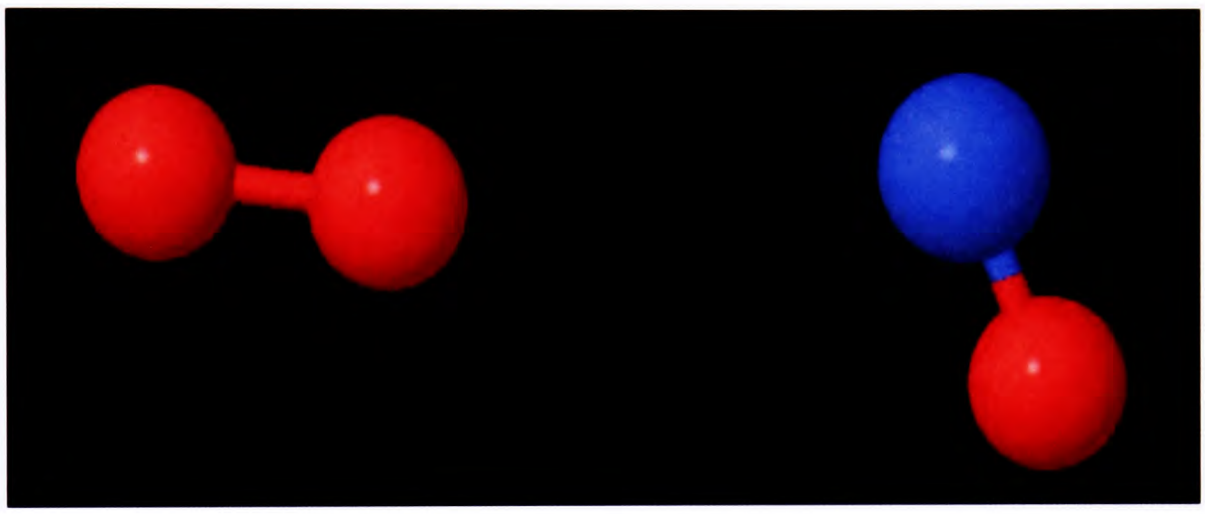

Figure B.5: Quartet Spin State - Geometry b′

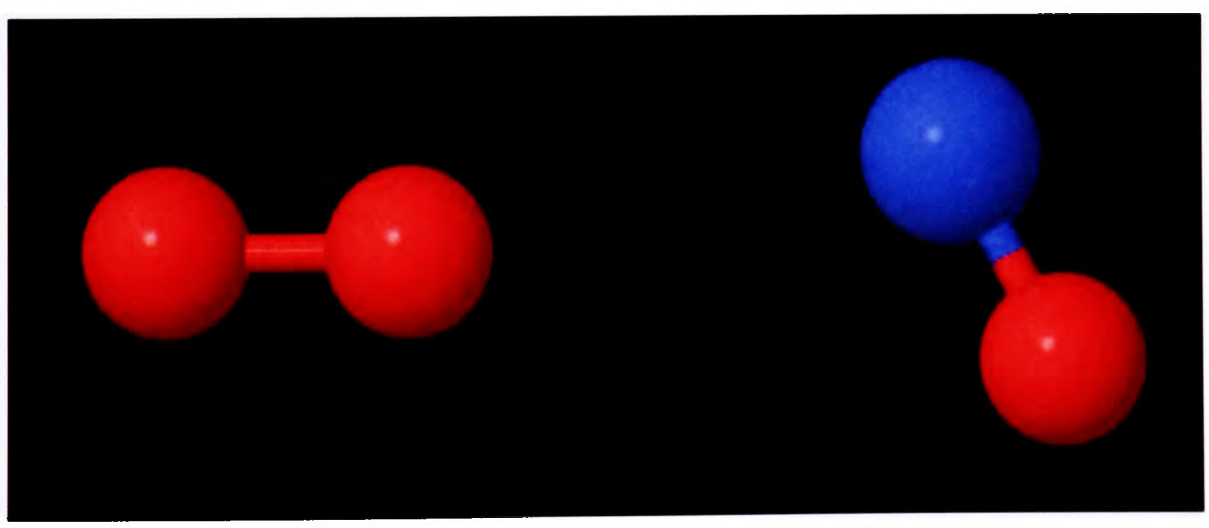

Figure B.6: Quartet Spin State - Geometry c′

B.1.2 MOLPRO

Tabulated global minima for planar NO-O_2 performed on MOLPRO [2] using counterpoise corrected RSPT2, aug-cc-pVDZ and aug-cc-pVTZ exponential basis set extrapolation and Size-Consistency Error correction on Binding Energy

State	Complex Energy (Hartree)	Binding Energy (cm^{-1})	Rotational Constant A (GHz)	Rotational Constant B (GHz)	Rotational Constant C (GHz)
$^2A'$	-280.2013	167.2012	26.9338	2.7802	2.5200
$^2A''$	-280.0222	325.1061	23.4141	3.6272	3.1407
$^4A'$	-280.0212	160.7225	25.6448	2.7947	2.5200
$^4A''$	-280.0211	155.7583	30.7130	2.4561	2.2743

B.2 Hamiltonian Matrix Elements

Magnetic hyperfine matrix elements for nitrogen nucleus in NO-O_2

$$\left\langle \eta\Lambda; S_1\Sigma_1; S_2\Sigma_2; JM_JK_a; IFM_F \right| \mathscr{H}_{mag} \left| \eta\Lambda'; S_1\Sigma_1'; S_2\Sigma_2'; J'M_J'K_a'; IF'M_F' \right\rangle$$

$$= \delta_{F,F'} (-1)^{J'+I+F} \left((2J'+1)(2J+1) \right)^{1/2} \left(I(I+1)(2I+1) \right)^{1/2}$$

$$\times \begin{Bmatrix} F & I & J \\ 1 & J' & I \end{Bmatrix} \sum_q (-1)^{J-K_a} \begin{pmatrix} J & 1 & J' \\ -K_a & q & K_a \end{pmatrix}$$

$$\left\{ \delta_{\Lambda,\Lambda'} \delta_{\Sigma_2,\Sigma_2'} a\Lambda \begin{Bmatrix} \frac{1}{\sqrt{2}} \sin\theta_2 \delta_{q,-1} \\ +\cos\theta_2 \delta_{q,0} \\ -\frac{1}{\sqrt{2}} \sin\theta_2 \delta_{q,1} \end{Bmatrix} \left[\begin{Bmatrix} \cos^2\frac{\theta_2}{2} \begin{pmatrix} S_2 & 1 & S_2 \\ -\Sigma_2 & -1 & \Sigma_2' \end{pmatrix} \\ +\frac{1}{\sqrt{2}} \sin\theta_2 \begin{pmatrix} S_2 & 1 & S_2 \\ -\Sigma_2 & 0 & \Sigma_2' \end{pmatrix} \\ +\sin^2\frac{\theta_2}{2} \begin{pmatrix} S_2 & 1 & S_2 \\ -\Sigma_2 & 1 & \Sigma_2' \end{pmatrix} \end{Bmatrix} \delta_{q,-1} \right.$$

$$+ \begin{Bmatrix} -\frac{1}{\sqrt{2}} \sin\theta_2 \begin{pmatrix} S_2 & 1 & S_2 \\ -\Sigma_2 & -1 & \Sigma_2' \end{pmatrix} \\ +\cos\theta_2 \begin{pmatrix} S_2 & 1 & S_2 \\ -\Sigma_2 & 0 & \Sigma_2' \end{pmatrix} \\ +\frac{1}{\sqrt{2}} \sin\theta_2 \begin{pmatrix} S_2 & 1 & S_2 \\ -\Sigma_2 & 1 & \Sigma_2' \end{pmatrix} \end{Bmatrix} \delta_{q,0}$$

$$\left. + \begin{Bmatrix} \sin^2\frac{\theta_2}{2} \begin{pmatrix} S_2 & 1 & S_2 \\ -\Sigma_2 & -1 & \Sigma_2' \end{pmatrix} \\ -\frac{1}{\sqrt{2}} \sin\theta_2 \begin{pmatrix} S_2 & 1 & S_2 \\ -\Sigma_2 & 0 & \Sigma_2' \end{pmatrix} \\ +\cos^2\frac{\theta_2}{2} \begin{pmatrix} S_2 & 1 & S_2 \\ -\Sigma_2 & 1 & \Sigma_2' \end{pmatrix} \end{Bmatrix} \delta_{q,1} \right]$$

$$\left. + \delta_{\Lambda,\Lambda'} b_F \left(S_2(S_2+1)(2S_2+1) \right)^{1/2} (-1)^{S_2-\Sigma_2} \right\}$$

$$
\left\{ \right.
+\delta_{\Lambda,\Lambda'} \tfrac{c}{3} \left(S_2\left(S_2+1\right)\left(2S_2+1\right)\right)^{1/2} (-1)^{S_2-\Sigma_2}
\left[
\left\{
\begin{array}{l}
-\cos^2\frac{\theta_2}{2} \begin{pmatrix} S_2 & 1 & S_2 \\ -\Sigma_2 & -1 & \Sigma_2' \end{pmatrix} \\
+\sqrt{2}\sin\theta_2 \begin{pmatrix} S_2 & 1 & S_2 \\ -\Sigma_2 & 0 & \Sigma_2' \end{pmatrix} \\
-\sin^2\frac{\theta_2}{2} \begin{pmatrix} S_2 & 1 & S_2 \\ -\Sigma_2 & 1 & \Sigma_2' \end{pmatrix}
\end{array}
\right\} \delta_{q,-1}
\right.
$$

$$
\left.
+
\left\{
\begin{array}{l}
\frac{1}{\sqrt{2}}\sin\theta_2 \begin{pmatrix} S_2 & 1 & S_2 \\ -\Sigma_2 & -1 & \Sigma_2' \end{pmatrix} \\
+2\cos\theta_2 \begin{pmatrix} S_2 & 1 & S_2 \\ -\Sigma_2 & 0 & \Sigma_2' \end{pmatrix} \\
-\frac{1}{\sqrt{2}}\sin\theta_2 \begin{pmatrix} S_2 & 1 & S_2 \\ -\Sigma_2 & 1 & \Sigma_2' \end{pmatrix} \\
-\sin^2\frac{\theta_2}{2} \begin{pmatrix} S_2 & 1 & S_2 \\ -\Sigma_2 & -1 & \Sigma_2' \end{pmatrix} \\
-\sqrt{2}\sin\theta_2 \begin{pmatrix} S_2 & 1 & S_2 \\ -\Sigma_2 & 0 & \Sigma_2' \end{pmatrix} \\
-\cos^2\frac{\theta_2}{2} \begin{pmatrix} S_2 & 1 & S_2 \\ -\Sigma_2 & 1 & \Sigma_2' \end{pmatrix}
\end{array}
\right\} \delta_{q,0}
\right.
$$

$$
\left.
+
\left\{
\begin{array}{l}
-\cos^2\frac{\theta_2}{2} \begin{pmatrix} S_2 & 1 & S_2 \\ -\Sigma_2 & -1 & \Sigma_2' \end{pmatrix} \\
+\sqrt{2}\sin\theta_2 \begin{pmatrix} S_2 & 1 & S_2 \\ -\Sigma_2 & 0 & \Sigma_2' \end{pmatrix} \\
-\sin^2\frac{\theta_2}{2} \begin{pmatrix} S_2 & 1 & S_2 \\ -\Sigma_2 & 1 & \Sigma_2' \end{pmatrix}
\end{array}
\right\} \delta_{q,1}
\right]
$$

$$
+\delta_{\Lambda,\Lambda'+2} d \left(S_2\left(S_2+1\right)\left(2S_2+1\right)\right)^{1/2} (-1)^{S_2-\Sigma_2}
\left\{
\begin{array}{l}
\sin^2\frac{\theta_2}{2} \begin{pmatrix} S_2 & 1 & S_2 \\ -\Sigma_2 & -1 & \Sigma_2' \end{pmatrix} \delta_{q,-1} \\
+\frac{1}{\sqrt{2}}\sin\theta_2 \begin{pmatrix} S_2 & 1 & S_2 \\ -\Sigma_2 & -1 & \Sigma_2' \end{pmatrix} \delta_{q,0} \\
+\cos^2\frac{\theta_2}{2} \begin{pmatrix} S_2 & 1 & S_2 \\ -\Sigma_2 & -1 & \Sigma_2' \end{pmatrix} \delta_{q,1}
\end{array}
\right\}
$$

$$
+\delta_{\Lambda,\Lambda'-2} d \left(S_2\left(S_2+1\right)\left(2S_2+1\right)\right)^{1/2} (-1)^{S_2-\Sigma_2}
\left\{
\begin{array}{l}
\cos^2\frac{\theta_2}{2} \begin{pmatrix} S_2 & 1 & S_2 \\ -\Sigma_2 & 1 & \Sigma_2' \end{pmatrix} \delta_{q,-1} \\
-\frac{1}{\sqrt{2}}\sin\theta_2 \begin{pmatrix} S_2 & 1 & S_2 \\ -\Sigma_2 & 1 & \Sigma_2' \end{pmatrix} \delta_{q,0} \\
+\sin^2\frac{\theta_2}{2} \begin{pmatrix} S_2 & 1 & S_2 \\ -\Sigma_2 & 1 & \Sigma_2' \end{pmatrix} \delta_{q,1}
\end{array}
\right\}
\left. \right\}
$$

where

$$
\begin{aligned}
a &= 2g_I\mu_B\mu_I\left\langle\frac{1}{r_i^3}\right\rangle \\
b_F &= \frac{8\pi}{3}g_e g_I\mu_B\mu_I\left|\Psi(0)\right|^2 \\
c &= \frac{3}{2}g_e g_I\mu_B\mu_I\left\langle\frac{3\cos^2\theta_i-1}{r_i^3}\right\rangle \\
d &= \frac{3}{2}g_e g_I\mu_B\mu_I\left\langle\frac{\sin^2\theta_i}{r_i^3}\right\rangle
\end{aligned}
$$

Electric quadrupole hyperfine matrix elements for nitrogen nucleus in NO-O_2

$$\langle \eta\Lambda; S_1\Sigma_1; S_2\Sigma_2; JM_JK_a; IFM_F | \mathscr{H}_Q | \eta\Lambda'; S_1\Sigma_1'; S_2\Sigma_2'; J'M_J'K_a'; IF'M_F' \rangle$$

$$= \delta_{F,F'}\delta_{\Sigma_1,\Sigma_1'}\delta_{\Sigma_2,\Sigma_2'}(-1)^{J'+I+F}\begin{Bmatrix} J & I & F \\ I & J' & 2 \end{Bmatrix}\frac{1}{2}\left(\frac{(2I+3)(2I+2)(2I+1)}{2I(2I-1)}\right)^{1/2}\left((2J+1)(2J'+1)\right)^{1/2}$$

$$\times\sum_q(-1)^{J-K_a}\begin{pmatrix} J & 2 & J' \\ -K_a & q & K_a' \end{pmatrix}\left\{\begin{array}{c} \delta_{q,-2}\begin{pmatrix} \delta_{\Lambda,\Lambda'-2}\frac{1}{2\sqrt{6}}eQq_2\cos^4\frac{\theta_2}{2} \\ +\delta_{\Lambda,\Lambda'}\frac{1}{2}eQq_0\sqrt{\frac{3}{8}}\sin^2\theta_2 \\ +\delta_{\Lambda,\Lambda'+2}\frac{1}{2\sqrt{6}}eQq_2\sin^4\frac{\theta_2}{2} \end{pmatrix} \\ +\delta_{q,-1}\begin{pmatrix} -\delta_{\Lambda,\Lambda'-2}\frac{1}{2\sqrt{6}}eQq_2\frac{1}{2}\sin\theta_2(\cos\theta_2+1) \\ +\delta_{\Lambda,\Lambda'}\frac{1}{2}eQq_0\sqrt{\frac{3}{2}}\sin\theta_2\cos\theta_2 \\ -\delta_{\Lambda,\Lambda'+2}\frac{1}{2\sqrt{6}}eQq_2\frac{1}{2}\sin\theta_2(\cos\theta_2-1) \end{pmatrix} \\ +\delta_{q,0}\begin{pmatrix} \delta_{\Lambda,\Lambda'-2}\frac{1}{2\sqrt{6}}eQq_2\sqrt{\frac{3}{8}}\sin^2\theta_2 \\ +\delta_{\Lambda,\Lambda'}\frac{1}{2}eQq_0\left(3\cos^2\theta_2-1\right) \\ +\delta_{\Lambda,\Lambda'+2}\frac{1}{2\sqrt{6}}eQq_2\sqrt{\frac{3}{8}}\sin^2\theta_2 \end{pmatrix} \\ +\delta_{q,1}\begin{pmatrix} \delta_{\Lambda,\Lambda'-2}\frac{1}{2\sqrt{6}}eQq_2\frac{1}{2}\sin\theta_2(\cos\theta_2-1) \\ -\delta_{\Lambda,\Lambda'}\frac{1}{2}eQq_0\sqrt{\frac{3}{2}}\sin\theta_2\cos\theta_2 \\ +\delta_{\Lambda,\Lambda'+2}\frac{1}{2\sqrt{6}}eQq_2\frac{1}{2}\sin\theta_2(\cos\theta_2+1) \end{pmatrix} \\ +\delta_{q,2}\begin{pmatrix} \delta_{\Lambda,\Lambda'-2}\frac{1}{2\sqrt{6}}eQq_2\sin^4\frac{\theta_2}{2} \\ +\delta_{\Lambda,\Lambda'}\frac{1}{2}eQq_0\sqrt{\frac{3}{8}}\sin^2\theta_2 \\ +\delta_{\Lambda,\Lambda'+2}\frac{1}{2\sqrt{6}}eQq_2\cos^4\frac{\theta_2}{2} \end{pmatrix} \end{array}\right\}$$

B.3 Predicted Rotational Transitions

J''	J'	Rotational Frequency (MHz)	F''	F'	Hyperfine Shift (MHz)	Parity$''$	Parity$'$	Transition Type	Transition Strength Factors
$\frac{1}{2}$	$\frac{3}{2}$	6,307	$\frac{3}{2}$	$\frac{1}{2}$	-5.15	+	−	a	0.05
			$\frac{3}{2}$	$\frac{3}{2}$	-3.72				0.20
			$\frac{1}{2}$	$\frac{1}{2}$	-3.24				0.20
			$\frac{1}{2}$	$\frac{3}{2}$	-1.80				0.25
			$\frac{3}{2}$	$\frac{5}{2}$	2.92				0.67
$\frac{1}{2}$	$\frac{1}{2}$	8,035	$\frac{3}{2}$	$\frac{3}{2}$	-9.20	+	−	a	0.74
			$\frac{1}{2}$	$\frac{3}{2}$	-7.28				0.59
			$\frac{3}{2}$	$\frac{1}{2}$	16.53				0.59
			$\frac{1}{2}$	$\frac{1}{2}$	18.45				0.07
$\frac{3}{2}$	$\frac{5}{2}$	12,955	$\frac{1}{2}$	$\frac{3}{2}$	-3.31	−	+	a	0.30
			$\frac{3}{2}$	$\frac{5}{2}$	-2.67				0.50
			$\frac{3}{2}$	$\frac{3}{2}$	-0.22				0.10
			$\frac{5}{2}$	$\frac{5}{2}$	0.91				0.10
			$\frac{5}{2}$	$\frac{7}{2}$	2.86				0.79
			$\frac{5}{2}$	$\frac{3}{2}$	3.37				0.00
$\frac{3}{2}$	$\frac{5}{2}$	13,199	$\frac{5}{2}$	$\frac{3}{2}$	-9.07	−	+	a	0.01
			$\frac{5}{2}$	$\frac{5}{2}$	-6.34				0.13
			$\frac{3}{2}$	$\frac{3}{2}$	-2.43				0.13
			$\frac{1}{2}$	$\frac{3}{2}$	-1.00				0.40
			$\frac{3}{2}$	$\frac{5}{2}$	0.30				0.67
			$\frac{5}{2}$	$\frac{7}{2}$	1.29				1.07

J''	J'	Rotational Frequency (MHz)	F''	F'	Hyperfine Shift (MHz)	Parity''	Parity'	Transition Type	Transition Strength Factors
$\frac{3}{2}$	$\frac{5}{2}$	13,482	$\frac{5}{2}$	$\frac{3}{2}$	-9.00	+	−	*a*	0.00
			$\frac{3}{2}$	$\frac{3}{2}$	-8.10				0.10
			$\frac{1}{2}$	$\frac{3}{2}$	-3.89				0.30
			$\frac{5}{2}$	$\frac{5}{2}$	-2.87				0.10
			$\frac{3}{2}$	$\frac{5}{2}$	-1.97				0.51
			$\frac{5}{2}$	$\frac{7}{2}$	4.06				0.80
$\frac{1}{2}$	$\frac{3}{2}$	13,551	$\frac{3}{2}$	$\frac{3}{2}$	-10.58	−	+	*a*	0.14
			$\frac{3}{2}$	$\frac{5}{2}$	-8.77				0.49
			$\frac{3}{2}$	$\frac{1}{2}$	-8.03				0.02
			$\frac{1}{2}$	$\frac{3}{2}$	17.15				0.18
			$\frac{1}{2}$	$\frac{1}{2}$	19.70				0.14
$\frac{1}{2}$	$\frac{3}{2}$	14,312	$\frac{1}{2}$	$\frac{3}{2}$	-13.00	−	+	*a*	0.25
			$\frac{1}{2}$	$\frac{1}{2}$	-3.41				0.20
			$\frac{3}{2}$	$\frac{5}{2}$	1.23				0.67
			$\frac{3}{2}$	$\frac{3}{2}$	12.73				0.20
			$\frac{3}{2}$	$\frac{1}{2}$	22.32				0.02
$\frac{3}{2}$	$\frac{3}{2}$	14,732	$\frac{1}{2}$	$\frac{3}{2}$	-5.66	−	+	*a*	0.02
			$\frac{1}{2}$	$\frac{1}{2}$	-3.11				0.02
			$\frac{3}{2}$	$\frac{3}{2}$	-2.57				0.04
			$\frac{3}{2}$	$\frac{5}{2}$	-0.76				0.02
			$\frac{3}{2}$	$\frac{1}{2}$	-0.02				0.02
			$\frac{5}{2}$	$\frac{3}{2}$	1.02				0.02
			$\frac{5}{2}$	$\frac{5}{2}$	2.82				0.10
$\frac{1}{2}$	$\frac{3}{2}$	15,056	$\frac{3}{2}$	$\frac{5}{2}$	-7.33	+	−	*a*	0.52
			$\frac{1}{2}$	$\frac{3}{2}$	3.62				0.19
			$\frac{3}{2}$	$\frac{3}{2}$	7.11				0.15
			$\frac{1}{2}$	$\frac{1}{2}$	11.38				0.15
			$\frac{3}{2}$	$\frac{1}{2}$	14.87				0.02

J''	J'	Rotational Frequency (MHz)	F''	F'	Hyperfine Shift (MHz)	Parity$''$	Parity$'$	Transition Type	Transition Strength Factors
$\frac{3}{2}$	$\frac{3}{2}$	16,040	$\frac{5}{2}$	$\frac{5}{2}$	-10.90	$-$	$+$	a	0.11
			$\frac{3}{2}$	$\frac{5}{2}$	-4.26				0.02
			$\frac{5}{2}$	$\frac{3}{2}$	0.61				0.02
			$\frac{3}{2}$	$\frac{3}{2}$	7.25				0.05
			$\frac{1}{2}$	$\frac{3}{2}$	8.69				0.02
			$\frac{3}{2}$	$\frac{1}{2}$	16.84				0.02
			$\frac{1}{2}$	$\frac{1}{2}$	18.27				0.02
$\frac{3}{2}$	$\frac{5}{2}$	17,304	$\frac{1}{2}$	$\frac{3}{2}$	-21.62	$+$	$-$	b	0.05
			$\frac{3}{2}$	$\frac{3}{2}$	-12.03				0.02
			$\frac{3}{2}$	$\frac{5}{2}$	-5.89				0.09
			$\frac{5}{2}$	$\frac{3}{2}$	-0.51				0.00
			$\frac{5}{2}$	$\frac{5}{2}$	5.62				0.02
			$\frac{5}{2}$	$\frac{7}{2}$	12.55				0.15
$\frac{3}{2}$	$\frac{5}{2}$	17,321	$\frac{5}{2}$	$\frac{7}{2}$	-7.24	$+$	$-$	b	0.00
			$\frac{5}{2}$	$\frac{5}{2}$	1.05				0.00
			$\frac{3}{2}$	$\frac{5}{2}$	1.95				0.00
			$\frac{5}{2}$	$\frac{3}{2}$	9.95				0.00
			$\frac{3}{2}$	$\frac{3}{2}$	10.85				0.00
			$\frac{1}{2}$	$\frac{3}{2}$	15.06				0.00
$\frac{3}{2}$	$\frac{3}{2}$	17,677	$\frac{5}{2}$	$\frac{5}{2}$	-9.65	$+$	$-$	a	0.06
			$\frac{3}{2}$	$\frac{5}{2}$	-8.75				0.01
			$\frac{5}{2}$	$\frac{3}{2}$	4.79				0.01
			$\frac{3}{2}$	$\frac{3}{2}$	5.69				0.03
			$\frac{1}{2}$	$\frac{3}{2}$	9.89				0.01
			$\frac{3}{2}$	$\frac{1}{2}$	13.45				0.01
			$\frac{1}{2}$	$\frac{1}{2}$	17.65				0.01
$\frac{1}{2}$	$\frac{3}{2}$	18,133	$\frac{1}{2}$	$\frac{1}{2}$	-21.13	$-$	$+$	b	0.09
			$\frac{1}{2}$	$\frac{3}{2}$	-16.92				0.11
			$\frac{3}{2}$	$\frac{1}{2}$	4.60				0.01
			$\frac{3}{2}$	$\frac{3}{2}$	8.81				0.09
			$\frac{3}{2}$	$\frac{5}{2}$	9.71				0.31

References

[1] Gaussian 03, Revision C.02, M. J. Frisch, G. W. Trucks, H. B. Schlegel, G. E. Scuseria, M. A. Robb, J. R. Cheeseman, J. A. Montgomery, Jr., T. Vreven, K. N. Kudin, J. C. Burant, J. M. Millam, S. S. Iyengar, J. Tomasi, V. Barone, B. Mennucci, M. Cossi, G. Scalmani, N. Rega, G. A. Petersson, H. Nakatsuji, M. Hada, M. Ehara, K. Toyota, R. Fukuda, J. Hasegawa, M. Ishida, T. Nakajima, Y. Honda, O. Kitao, H. Nakai, M. Klene, X. Li, J. E. Knox, H. P. Hratchian, J. B. Cross, V. Bakken, C. Adamo, J. Jaramillo, R. Gomperts, R. E. Stratmann, O. Yazyev, A. J. Austin, R. Cammi, C. Pomelli, J. W. Ochterski, P. Y. Ayala, K. Morokuma, G. A. Voth, P. Salvador, J. J. Dannenberg, V. G. Zakrzewski, S. Dapprich, A. D. Daniels, M. C. Strain, O. Farkas, D. K. Malick, A. D. Rabuck, K. Raghavachari, J. B. Foresman, J. V. Ortiz, Q. Cui, A. G. Baboul, S. Clifford, J. Cioslowski, B. B. Stefanov, G. Liu, A. Liashenko, P. Piskorz, I. Komaromi, R. L. Martin, D. J. Fox, T. Keith, M. A. Al-Laham, C. Y. Peng, A. Nanayakkara, M. Challacombe, P. M. W. Gill, B. Johnson, W. Chen, M. W. Wong, C. Gonzalez, and J. A. Pople, Gaussian, Inc., Wallingford CT, 2004.

[2] MOLPRO, Version 2002.6, H.-J. Werner, P. J. Knowles, R. Lindh, F. R. Manby, M. Schtz, P. Celani, T. Korona, G. Rauhut, R. D. Amos, A. Bernhardsson, A. Berning, D. L. Cooper, M. J. O. Deegan, A. J. Dobbyn, F. Eckert, C. Hampel, G. Hetzer, A. W. Lloyd, S. J. McNicholas, W. Meyer, M. E. Mura, A. Nickla, P. Palmieri, R. Pitzer, U. Schumann, H. Stoll, A. J. Stone, R. Tarroni, and T. Thorsteinsson, University College Cardiff Consultants Limited, 2004

Appendix C

NO_2-O_2 Appendix

C.1 *Ab initio* data

C.1.1 MOLPRO

Tabulated global minima, for calculated Potential Energy Surfaces, for NO_2-O_2 performed on MOLPRO [1] using counterpoise corrected RSPT2, aug-cc-pVDZ and aug-cc-pVTZ exponential basis set extrapolation and Size-Consistency Error correction on Binding Energy

State	Complex Energy (Hartree)	Binding Energy (cm^{-1})	Rotational Constant A (GHz)	Rotational Constant B (GHz)	Rotational Constant C (GHz)
^{2}A	-354.9930	410.6113	10.9474	2.6816	2.1541
^{4}A	-354.9922	280.1386	10.4530	2.5499	2.0502

C.2 Predicted Rotational Transitions

$N''_{K_aK_c}$	$N'_{K_aK_c}$	Rotational Frequency (MHz)	J''	J'	F''	F'	Hyperfine Shift (MHz)	Transition Type	Relative Transition Strength
0_{00}	1_{01}	4,836	$\frac{1}{2}$	$\frac{3}{2}$	$\frac{1}{2}$	$\frac{3}{2}$	-74.69	*a*	0.01
			$\frac{1}{2}$	$\frac{1}{2}$	$\frac{1}{2}$	$\frac{1}{2}$	-54.98	*a*	0.01
			$\frac{1}{2}$	$\frac{3}{2}$	$\frac{3}{2}$	$\frac{5}{2}$	-7.92	*a*	0.70
			$\frac{1}{2}$	$\frac{3}{2}$	$\frac{1}{2}$	$\frac{1}{2}$	-2.96	*a*	0.22
			$\frac{1}{2}$	$\frac{3}{2}$	$\frac{3}{2}$	$\frac{3}{2}$	-1.05	*a*	0.45
			$\frac{1}{2}$	$\frac{1}{2}$	$\frac{1}{2}$	$\frac{3}{2}$	5.10	*a*	0.45
			$\frac{1}{2}$	$\frac{1}{2}$	$\frac{3}{2}$	$\frac{1}{2}$	18.65	*a*	0.22
			$\frac{1}{2}$	$\frac{3}{2}$	$\frac{3}{2}$	$\frac{1}{2}$	70.67	*a*	0.01
			$\frac{1}{2}$	$\frac{1}{2}$	$\frac{3}{2}$	$\frac{3}{2}$	78.73	*a*	0.01

$N''_{K_aK_c}$	$N'_{K_aK_c}$	Rotational Frequency (MHz)	J''	J'	F''	F'	Hyperfine Shift (MHz)	Transition Type	Relative Transition Strength
2_{11}	3_{03}	5,064	$\frac{3}{2}$	$\frac{7}{2}$	$\frac{5}{2}$	$\frac{7}{2}$	-111.00	c	0.00
			$\frac{3}{2}$	$\frac{7}{2}$	$\frac{5}{2}$	$\frac{5}{2}$	-92.84	c	0.00
			$\frac{3}{2}$	$\frac{7}{2}$	$\frac{3}{2}$	$\frac{5}{2}$	-74.05	c	0.00
			$\frac{3}{2}$	$\frac{5}{2}$	$\frac{5}{2}$	$\frac{3}{2}$	-56.55	c	0.00
			$\frac{3}{2}$	$\frac{5}{2}$	$\frac{3}{2}$	$\frac{3}{2}$	-37.76	c	0.00
			$\frac{3}{2}$	$\frac{5}{2}$	$\frac{5}{2}$	$\frac{5}{2}$	-21.04	c	0.00
			$\frac{3}{2}$	$\frac{5}{2}$	$\frac{1}{2}$	$\frac{3}{2}$	-6.99	c	0.00
			$\frac{3}{2}$	$\frac{5}{2}$	$\frac{5}{2}$	$\frac{7}{2}$	-5.89	c	0.00
			$\frac{5}{2}$	$\frac{7}{2}$	$\frac{3}{2}$	$\frac{5}{2}$	-5.01	c	0.00
			$\frac{3}{2}$	$\frac{5}{2}$	$\frac{3}{2}$	$\frac{5}{2}$	-2.26	c	0.00
			$\frac{5}{2}$	$\frac{7}{2}$	$\frac{5}{2}$	$\frac{7}{2}$	-2.09	c	0.00
			$\frac{5}{2}$	$\frac{7}{2}$	$\frac{7}{2}$	$\frac{9}{2}$	4.17	c	0.00
			$\frac{5}{2}$	$\frac{7}{2}$	$\frac{7}{2}$	$\frac{7}{2}$	15.54	c	0.00
			$\frac{5}{2}$	$\frac{7}{2}$	$\frac{5}{2}$	$\frac{5}{2}$	16.07	c	0.00
			$\frac{5}{2}$	$\frac{5}{2}$	$\frac{3}{2}$	$\frac{3}{2}$	31.27	c	0.00
			$\frac{5}{2}$	$\frac{7}{2}$	$\frac{7}{2}$	$\frac{5}{2}$	33.71	c	0.00
			$\frac{5}{2}$	$\frac{5}{2}$	$\frac{5}{2}$	$\frac{3}{2}$	52.36	c	0.00
			$\frac{5}{2}$	$\frac{5}{2}$	$\frac{3}{2}$	$\frac{5}{2}$	66.78	c	0.00
			$\frac{5}{2}$	$\frac{5}{2}$	$\frac{5}{2}$	$\frac{5}{2}$	87.87	c	0.00
			$\frac{5}{2}$	$\frac{5}{2}$	$\frac{5}{2}$	$\frac{7}{2}$	103.02	c	0.00
			$\frac{5}{2}$	$\frac{5}{2}$	$\frac{7}{2}$	$\frac{5}{2}$	105.50	c	0.00
			$\frac{5}{2}$	$\frac{5}{2}$	$\frac{7}{2}$	$\frac{7}{2}$	120.65	c	0.00

$N''_{K_aK_c}$	$N'_{K_aK_c}$	Rotational Frequency (MHz)	J''	J'	F''	F'	Hyperfine Shift (MHz)	Transition Type	Relative Transition Strength
2_{12}	3_{03}	6,647	$\frac{3}{2}$	$\frac{7}{2}$	$\frac{5}{2}$	$\frac{7}{2}$	-103.29	*b*	0.00
			$\frac{3}{2}$	$\frac{7}{2}$	$\frac{5}{2}$	$\frac{5}{2}$	-85.13	*b*	0.00
			$\frac{3}{2}$	$\frac{7}{2}$	$\frac{3}{2}$	$\frac{5}{2}$	-68.73	*b*	0.00
			$\frac{3}{2}$	$\frac{5}{2}$	$\frac{5}{2}$	$\frac{3}{2}$	-48.85	*b*	0.00
			$\frac{3}{2}$	$\frac{5}{2}$	$\frac{3}{2}$	$\frac{3}{2}$	-32.44	*b*	0.00
			$\frac{3}{2}$	$\frac{5}{2}$	$\frac{5}{2}$	$\frac{5}{2}$	-13.34	*b*	0.00
			$\frac{5}{2}$	$\frac{7}{2}$	$\frac{3}{2}$	$\frac{5}{2}$	-6.73	*b*	0.01
			$\frac{5}{2}$	$\frac{7}{2}$	$\frac{5}{2}$	$\frac{7}{2}$	-6.19	*b*	0.02
			$\frac{5}{2}$	$\frac{7}{2}$	$\frac{7}{2}$	$\frac{9}{2}$	-2.95	*b*	0.03
			$\frac{3}{2}$	$\frac{5}{2}$	$\frac{5}{2}$	$\frac{7}{2}$	1.82	*b*	0.02
			$\frac{3}{2}$	$\frac{5}{2}$	$\frac{3}{2}$	$\frac{5}{2}$	3.06	*b*	0.01
			$\frac{3}{2}$	$\frac{5}{2}$	$\frac{1}{2}$	$\frac{3}{2}$	3.76	*b*	0.01
			$\frac{5}{2}$	$\frac{7}{2}$	$\frac{7}{2}$	$\frac{7}{2}$	8.42	*b*	0.00
			$\frac{5}{2}$	$\frac{7}{2}$	$\frac{5}{2}$	$\frac{5}{2}$	11.97	*b*	0.00
			$\frac{5}{2}$	$\frac{7}{2}$	$\frac{7}{2}$	$\frac{5}{2}$	26.58	*b*	0.00
			$\frac{5}{2}$	$\frac{5}{2}$	$\frac{3}{2}$	$\frac{3}{2}$	29.56	*b*	0.00
			$\frac{5}{2}$	$\frac{5}{2}$	$\frac{5}{2}$	$\frac{3}{2}$	48.25	*b*	0.00
			$\frac{5}{2}$	$\frac{5}{2}$	$\frac{3}{2}$	$\frac{5}{2}$	65.07	*b*	0.00
			$\frac{5}{2}$	$\frac{5}{2}$	$\frac{5}{2}$	$\frac{5}{2}$	83.76	*b*	0.00
			$\frac{5}{2}$	$\frac{5}{2}$	$\frac{7}{2}$	$\frac{5}{2}$	98.38	*b*	0.00
			$\frac{5}{2}$	$\frac{5}{2}$	$\frac{5}{2}$	$\frac{7}{2}$	98.91	*b*	0.00
			$\frac{5}{2}$	$\frac{5}{2}$	$\frac{7}{2}$	$\frac{7}{2}$	113.53	*b*	0.00

$N''_{K_aK_c}$	$N'_{K_aK_c}$	Rotational Frequency (MHz)	J''	J'	F''	F'	Hyperfine Shift (MHz)	Transition Type	Relative Transition Strength
3_{03}	3_{13}	7,054	$\frac{5}{2}$	$\frac{7}{2}$	$\frac{7}{2}$	$\frac{9}{2}$	-118.21	c	0.00
			$\frac{5}{2}$	$\frac{7}{2}$	$\frac{7}{2}$	$\frac{7}{2}$	-105.16	c	0.00
			$\frac{5}{2}$	$\frac{7}{2}$	$\frac{5}{2}$	$\frac{7}{2}$	-90.01	c	0.00
			$\frac{5}{2}$	$\frac{7}{2}$	$\frac{7}{2}$	$\frac{5}{2}$	-86.46	c	0.00
			$\frac{5}{2}$	$\frac{7}{2}$	$\frac{5}{2}$	$\frac{5}{2}$	-71.30	c	0.00
			$\frac{5}{2}$	$\frac{7}{2}$	$\frac{3}{2}$	$\frac{5}{2}$	-35.80	c	0.00
			$\frac{5}{2}$	$\frac{5}{2}$	$\frac{5}{2}$	$\frac{3}{2}$	-35.22	c	0.00
			$\frac{7}{2}$	$\frac{7}{2}$	$\frac{5}{2}$	$\frac{7}{2}$	-18.21	c	0.00
			$\frac{5}{2}$	$\frac{5}{2}$	$\frac{7}{2}$	$\frac{5}{2}$	-14.94	c	0.00
			$\frac{7}{2}$	$\frac{7}{2}$	$\frac{7}{2}$	$\frac{9}{2}$	-13.11	c	0.00
			$\frac{7}{2}$	$\frac{7}{2}$	$\frac{9}{2}$	$\frac{9}{2}$	-1.73	c	0.00
			$\frac{7}{2}$	$\frac{7}{2}$	$\frac{7}{2}$	$\frac{7}{2}$	-0.05	c	0.00
			$\frac{5}{2}$	$\frac{5}{2}$	$\frac{5}{2}$	$\frac{5}{2}$	0.21	c	0.00
			$\frac{5}{2}$	$\frac{5}{2}$	$\frac{3}{2}$	$\frac{3}{2}$	0.29	c	0.00
			$\frac{7}{2}$	$\frac{7}{2}$	$\frac{5}{2}$	$\frac{5}{2}$	0.49	c	0.00
			$\frac{5}{2}$	$\frac{5}{2}$	$\frac{7}{2}$	$\frac{7}{2}$	1.51	c	0.00
			$\frac{7}{2}$	$\frac{7}{2}$	$\frac{9}{2}$	$\frac{7}{2}$	11.32	c	0.00
			$\frac{5}{2}$	$\frac{5}{2}$	$\frac{5}{2}$	$\frac{7}{2}$	16.66	c	0.00
			$\frac{7}{2}$	$\frac{7}{2}$	$\frac{7}{2}$	$\frac{5}{2}$	18.65	c	0.00
			$\frac{5}{2}$	$\frac{5}{2}$	$\frac{3}{2}$	$\frac{5}{2}$	35.72	c	0.00
			$\frac{7}{2}$	$\frac{5}{2}$	$\frac{5}{2}$	$\frac{3}{2}$	36.57	c	0.00
			$\frac{7}{2}$	$\frac{5}{2}$	$\frac{5}{2}$	$\frac{5}{2}$	72.01	c	0.00
			$\frac{7}{2}$	$\frac{5}{2}$	$\frac{5}{2}$	$\frac{7}{2}$	88.45	c	0.00
			$\frac{7}{2}$	$\frac{5}{2}$	$\frac{7}{2}$	$\frac{5}{2}$	90.17	c	0.00
			$\frac{7}{2}$	$\frac{5}{2}$	$\frac{7}{2}$	$\frac{7}{2}$	106.62	c	0.00
			$\frac{7}{2}$	$\frac{5}{2}$	$\frac{9}{2}$	$\frac{7}{2}$	117.99	c	0.00

$N''_{K_aK_c}$	$N'_{K_aK_c}$	Rotational Frequency (MHz)	J''	J'	F''	F'	Hyperfine Shift (MHz)	Transition Type	Relative Transition Strength
2_{02}	2_{12}	7,763	$\frac{3}{2}$	$\frac{5}{2}$	$\frac{5}{2}$	$\frac{7}{2}$	-106.79	c	0.00
			$\frac{3}{2}$	$\frac{5}{2}$	$\frac{5}{2}$	$\frac{5}{2}$	-92.18	c	0.00
			$\frac{3}{2}$	$\frac{5}{2}$	$\frac{3}{2}$	$\frac{5}{2}$	-79.76	c	0.00
			$\frac{3}{2}$	$\frac{5}{2}$	$\frac{3}{2}$	$\frac{3}{2}$	-61.06	c	0.00
			$\frac{3}{2}$	$\frac{3}{2}$	$\frac{3}{2}$	$\frac{1}{2}$	-35.26	c	0.00
			$\frac{3}{2}$	$\frac{5}{2}$	$\frac{1}{2}$	$\frac{3}{2}$	-22.33	c	0.00
			$\frac{5}{2}$	$\frac{5}{2}$	$\frac{3}{2}$	$\frac{5}{2}$	-17.41	c	0.00
			$\frac{5}{2}$	$\frac{5}{2}$	$\frac{5}{2}$	$\frac{7}{2}$	-14.99	c	0.00
			$\frac{3}{2}$	$\frac{3}{2}$	$\frac{5}{2}$	$\frac{3}{2}$	-11.48	c	0.00
			$\frac{5}{2}$	$\frac{5}{2}$	$\frac{7}{2}$	$\frac{7}{2}$	-5.43	c	0.00
			$\frac{5}{2}$	$\frac{5}{2}$	$\frac{5}{2}$	$\frac{5}{2}$	-0.38	c	0.00
			$\frac{3}{2}$	$\frac{3}{2}$	$\frac{3}{2}$	$\frac{3}{2}$	0.94	c	0.00
			$\frac{5}{2}$	$\frac{5}{2}$	$\frac{3}{2}$	$\frac{3}{2}$	1.28	c	0.00
			$\frac{3}{2}$	$\frac{3}{2}$	$\frac{1}{2}$	$\frac{1}{2}$	3.47	c	0.00
			$\frac{3}{2}$	$\frac{3}{2}$	$\frac{5}{2}$	$\frac{5}{2}$	4.92	c	0.00
			$\frac{5}{2}$	$\frac{5}{2}$	$\frac{7}{2}$	$\frac{5}{2}$	9.19	c	0.00
			$\frac{3}{2}$	$\frac{3}{2}$	$\frac{3}{2}$	$\frac{5}{2}$	17.34	c	0.00
			$\frac{5}{2}$	$\frac{5}{2}$	$\frac{5}{2}$	$\frac{3}{2}$	18.32	c	0.00
			$\frac{5}{2}$	$\frac{3}{2}$	$\frac{3}{2}$	$\frac{1}{2}$	27.09	c	0.00
			$\frac{3}{2}$	$\frac{3}{2}$	$\frac{1}{2}$	$\frac{3}{2}$	39.67	c	0.00
			$\frac{5}{2}$	$\frac{3}{2}$	$\frac{3}{2}$	$\frac{3}{2}$	63.29	c	0.00
			$\frac{5}{2}$	$\frac{3}{2}$	$\frac{3}{2}$	$\frac{5}{2}$	79.69	c	0.00
			$\frac{5}{2}$	$\frac{3}{2}$	$\frac{5}{2}$	$\frac{3}{2}$	80.32	c	0.00
			$\frac{5}{2}$	$\frac{3}{2}$	$\frac{7}{2}$	$\frac{5}{2}$	106.29	c	0.00

$N''_{K_aK_c}$	$N'_{K_aK_c}$	Rotational Frequency (MHz)	J''	J'	F''	F'	Hyperfine Shift (MHz)	Transition Type	Relative Transition Strength
1_{01}	1_{11}	8,266	$\frac{1}{2}$	$\frac{3}{2}$	$\frac{3}{2}$	$\frac{5}{2}$	-98.62	c	0.00
			$\frac{1}{2}$	$\frac{3}{2}$	$\frac{3}{2}$	$\frac{3}{2}$	-74.65	c	0.00
			$\frac{3}{2}$	$\frac{3}{2}$	$\frac{1}{2}$	$\frac{3}{2}$	-66.59	c	0.00
			$\frac{1}{2}$	$\frac{1}{2}$	$\frac{3}{2}$	$\frac{1}{2}$	-56.59	c	0.00
			$\frac{3}{2}$	$\frac{1}{2}$	$\frac{1}{2}$	$\frac{1}{2}$	-48.53	c	0.00
			$\frac{3}{2}$	$\frac{3}{2}$	$\frac{3}{2}$	$\frac{5}{2}$	-18.84	c	0.00
			$\frac{1}{2}$	$\frac{3}{2}$	$\frac{1}{2}$	$\frac{3}{2}$	-14.58	c	0.00
			$\frac{3}{2}$	$\frac{3}{2}$	$\frac{5}{2}$	$\frac{5}{2}$	-11.96	c	0.00
			$\frac{1}{2}$	$\frac{3}{2}$	$\frac{3}{2}$	$\frac{1}{2}$	-11.33	c	0.00
			$\frac{3}{2}$	$\frac{3}{2}$	$\frac{1}{2}$	$\frac{1}{2}$	-3.27	c	0.00
			$\frac{1}{2}$	$\frac{1}{2}$	$\frac{1}{2}$	$\frac{1}{2}$	3.49	c	0.00
			$\frac{3}{2}$	$\frac{3}{2}$	$\frac{3}{2}$	$\frac{3}{2}$	5.13	c	0.00
			$\frac{3}{2}$	$\frac{3}{2}$	$\frac{5}{2}$	$\frac{3}{2}$	12.00	c	0.00
			$\frac{1}{2}$	$\frac{1}{2}$	$\frac{3}{2}$	$\frac{3}{2}$	12.55	c	0.00
			$\frac{3}{2}$	$\frac{1}{2}$	$\frac{1}{2}$	$\frac{3}{2}$	20.61	c	0.00
			$\frac{3}{2}$	$\frac{1}{2}$	$\frac{3}{2}$	$\frac{1}{2}$	23.19	c	0.00
			$\frac{1}{2}$	$\frac{3}{2}$	$\frac{1}{2}$	$\frac{1}{2}$	48.75	c	0.00
			$\frac{3}{2}$	$\frac{3}{2}$	$\frac{3}{2}$	$\frac{1}{2}$	68.45	c	0.00
			$\frac{1}{2}$	$\frac{1}{2}$	$\frac{1}{2}$	$\frac{3}{2}$	72.63	c	0.00
			$\frac{3}{2}$	$\frac{1}{2}$	$\frac{5}{2}$	$\frac{3}{2}$	99.21	c	0.00

$N''_{K_aK_c}$	$N'_{K_aK_c}$	Rotational Frequency (MHz)	J''	J'	F''	F'	Hyperfine Shift (MHz)	Transition Type	Relative Transition Strength
1_{01}	1_{10}	8,793	$\frac{1}{2}$	$\frac{3}{2}$	$\frac{3}{2}$	$\frac{5}{2}$	-102.17	*b*	0.00
			$\frac{1}{2}$	$\frac{3}{2}$	$\frac{3}{2}$	$\frac{3}{2}$	-76.09	*b*	0.00
			$\frac{3}{2}$	$\frac{3}{2}$	$\frac{1}{2}$	$\frac{3}{2}$	-68.02	*b*	0.00
			$\frac{1}{2}$	$\frac{3}{2}$	$\frac{3}{2}$	$\frac{1}{2}$	-55.26	*b*	0.00
			$\frac{3}{2}$	$\frac{3}{2}$	$\frac{1}{2}$	$\frac{1}{2}$	-47.19	*b*	0.00
			$\frac{3}{2}$	$\frac{3}{2}$	$\frac{3}{2}$	$\frac{5}{2}$	-22.39	*b*	0.01
			$\frac{1}{2}$	$\frac{3}{2}$	$\frac{1}{2}$	$\frac{3}{2}$	-16.01	*b*	0.01
			$\frac{3}{2}$	$\frac{3}{2}$	$\frac{5}{2}$	$\frac{5}{2}$	-15.52	*b*	0.03
			$\frac{1}{2}$	$\frac{1}{2}$	$\frac{3}{2}$	$\frac{1}{2}$	-9.07	*b*	0.01
			$\frac{3}{2}$	$\frac{1}{2}$	$\frac{1}{2}$	$\frac{1}{2}$	-1.01	*b*	0.01
			$\frac{3}{2}$	$\frac{3}{2}$	$\frac{3}{2}$	$\frac{3}{2}$	3.70	*b*	0.00
			$\frac{1}{2}$	$\frac{3}{2}$	$\frac{1}{2}$	$\frac{1}{2}$	4.82	*b*	0.00
			$\frac{3}{2}$	$\frac{3}{2}$	$\frac{5}{2}$	$\frac{3}{2}$	10.57	*b*	0.01
			$\frac{1}{2}$	$\frac{1}{2}$	$\frac{3}{2}$	$\frac{3}{2}$	17.56	*b*	0.02
			$\frac{3}{2}$	$\frac{3}{2}$	$\frac{3}{2}$	$\frac{1}{2}$	24.53	*b*	0.01
			$\frac{3}{2}$	$\frac{1}{2}$	$\frac{1}{2}$	$\frac{3}{2}$	25.62	*b*	0.01
			$\frac{1}{2}$	$\frac{1}{2}$	$\frac{1}{2}$	$\frac{1}{2}$	51.01	*b*	0.00
			$\frac{3}{2}$	$\frac{1}{2}$	$\frac{3}{2}$	$\frac{1}{2}$	70.71	*b*	0.00
			$\frac{1}{2}$	$\frac{1}{2}$	$\frac{1}{2}$	$\frac{3}{2}$	77.64	*b*	0.00
			$\frac{3}{2}$	$\frac{1}{2}$	$\frac{3}{2}$	$\frac{3}{2}$	97.35	*b*	0.00
			$\frac{3}{2}$	$\frac{1}{2}$	$\frac{5}{2}$	$\frac{3}{2}$	104.22	*b*	0.00

$N''_{K_aK_c}$	$N'_{K_aK_c}$	Rotational Frequency (MHz)	J''	J'	F''	F'	Hyperfine Shift (MHz)	Transition Type	Relative Transition Strength
1_{11}	2_{12}	9,144	$\frac{1}{2}$	$\frac{5}{2}$	$\frac{3}{2}$	$\frac{5}{2}$	-98.49	a	0.00
			$\frac{1}{2}$	$\frac{5}{2}$	$\frac{3}{2}$	$\frac{3}{2}$	-79.79	a	0.00
			$\frac{3}{2}$	$\frac{5}{2}$	$\frac{1}{2}$	$\frac{3}{2}$	-55.91	a	0.01
			$\frac{1}{2}$	$\frac{3}{2}$	$\frac{3}{2}$	$\frac{1}{2}$	-53.99	a	0.00
			$\frac{3}{2}$	$\frac{3}{2}$	$\frac{1}{2}$	$\frac{1}{2}$	-30.11	a	0.03
			$\frac{1}{2}$	$\frac{3}{2}$	$\frac{3}{2}$	$\frac{3}{2}$	-17.79	a	0.09
			$\frac{3}{2}$	$\frac{5}{2}$	$\frac{3}{2}$	$\frac{5}{2}$	-11.29	a	0.46
			$\frac{1}{2}$	$\frac{5}{2}$	$\frac{1}{2}$	$\frac{3}{2}$	-10.65	a	0.20
			$\frac{3}{2}$	$\frac{5}{2}$	$\frac{5}{2}$	$\frac{7}{2}$	-1.93	a	0.84
			$\frac{1}{2}$	$\frac{3}{2}$	$\frac{3}{2}$	$\frac{5}{2}$	-1.39	a	0.60
			$\frac{3}{2}$	$\frac{3}{2}$	$\frac{1}{2}$	$\frac{3}{2}$	6.09	a	0.32
			$\frac{3}{2}$	$\frac{5}{2}$	$\frac{3}{2}$	$\frac{3}{2}$	7.41	a	0.19
			$\frac{3}{2}$	$\frac{5}{2}$	$\frac{5}{2}$	$\frac{5}{2}$	12.68	a	0.17
			$\frac{1}{2}$	$\frac{3}{2}$	$\frac{1}{2}$	$\frac{1}{2}$	15.15	a	0.15
			$\frac{3}{2}$	$\frac{5}{2}$	$\frac{5}{2}$	$\frac{3}{2}$	31.38	a	0.02
			$\frac{3}{2}$	$\frac{3}{2}$	$\frac{3}{2}$	$\frac{1}{2}$	33.21	a	0.03
			$\frac{1}{2}$	$\frac{3}{2}$	$\frac{1}{2}$	$\frac{3}{2}$	51.35	a	0.00
			$\frac{3}{2}$	$\frac{3}{2}$	$\frac{3}{2}$	$\frac{3}{2}$	69.41	a	0.01
			$\frac{3}{2}$	$\frac{3}{2}$	$\frac{3}{2}$	$\frac{5}{2}$	85.81	a	0.01
			$\frac{3}{2}$	$\frac{3}{2}$	$\frac{5}{2}$	$\frac{3}{2}$	93.38	a	0.00
			$\frac{3}{2}$	$\frac{3}{2}$	$\frac{5}{2}$	$\frac{5}{2}$	109.78	a	0.02

$N''_{K_aK_c}$	$N'_{K_aK_c}$	Rotational Frequency (MHz)	J''	J'	F''	F'	Hyperfine Shift (MHz)	Transition Type	Relative Transition Strength
2_{02}	2_{11}	9,345	$\frac{3}{2}$	$\frac{5}{2}$	$\frac{5}{2}$	$\frac{7}{2}$	-113.91	*b*	0.00
			$\frac{3}{2}$	$\frac{5}{2}$	$\frac{5}{2}$	$\frac{5}{2}$	-96.28	*b*	0.00
			$\frac{3}{2}$	$\frac{5}{2}$	$\frac{3}{2}$	$\frac{5}{2}$	-83.87	*b*	0.00
			$\frac{3}{2}$	$\frac{5}{2}$	$\frac{5}{2}$	$\frac{3}{2}$	-75.20	*b*	0.00
			$\frac{3}{2}$	$\frac{5}{2}$	$\frac{3}{2}$	$\frac{3}{2}$	-62.78	*b*	0.00
			$\frac{3}{2}$	$\frac{3}{2}$	$\frac{3}{2}$	$\frac{1}{2}$	-24.52	*b*	0.00
			$\frac{3}{2}$	$\frac{5}{2}$	$\frac{1}{2}$	$\frac{3}{2}$	-24.05	*b*	0.01
			$\frac{5}{2}$	$\frac{5}{2}$	$\frac{5}{2}$	$\frac{7}{2}$	-22.11	*b*	0.01
			$\frac{5}{2}$	$\frac{5}{2}$	$\frac{3}{2}$	$\frac{5}{2}$	-21.52	*b*	0.01
			$\frac{5}{2}$	$\frac{5}{2}$	$\frac{7}{2}$	$\frac{7}{2}$	-12.55	*b*	0.05
			$\frac{3}{2}$	$\frac{3}{2}$	$\frac{5}{2}$	$\frac{3}{2}$	-6.16	*b*	0.00
			$\frac{5}{2}$	$\frac{5}{2}$	$\frac{5}{2}$	$\frac{5}{2}$	-4.48	*b*	0.03
			$\frac{5}{2}$	$\frac{5}{2}$	$\frac{3}{2}$	$\frac{3}{2}$	-0.43	*b*	0.01
			$\frac{5}{2}$	$\frac{5}{2}$	$\frac{7}{2}$	$\frac{5}{2}$	5.08	*b*	0.01
			$\frac{3}{2}$	$\frac{3}{2}$	$\frac{3}{2}$	$\frac{3}{2}$	6.26	*b*	0.02
			$\frac{3}{2}$	$\frac{3}{2}$	$\frac{5}{2}$	$\frac{5}{2}$	12.63	*b*	0.04
			$\frac{3}{2}$	$\frac{3}{2}$	$\frac{1}{2}$	$\frac{1}{2}$	14.22	*b*	0.01
			$\frac{5}{2}$	$\frac{5}{2}$	$\frac{5}{2}$	$\frac{3}{2}$	16.60	*b*	0.01
			$\frac{3}{2}$	$\frac{3}{2}$	$\frac{3}{2}$	$\frac{5}{2}$	25.05	*b*	0.00
			$\frac{5}{2}$	$\frac{3}{2}$	$\frac{3}{2}$	$\frac{1}{2}$	37.83	*b*	0.01
			$\frac{3}{2}$	$\frac{3}{2}$	$\frac{1}{2}$	$\frac{3}{2}$	44.99	*b*	0.00
			$\frac{5}{2}$	$\frac{3}{2}$	$\frac{3}{2}$	$\frac{3}{2}$	68.61	*b*	0.00
			$\frac{5}{2}$	$\frac{3}{2}$	$\frac{5}{2}$	$\frac{3}{2}$	85.64	*b*	0.00
			$\frac{5}{2}$	$\frac{3}{2}$	$\frac{3}{2}$	$\frac{5}{2}$	87.39	*b*	0.00
			$\frac{5}{2}$	$\frac{3}{2}$	$\frac{5}{2}$	$\frac{5}{2}$	104.43	*b*	0.00
			$\frac{5}{2}$	$\frac{3}{2}$	$\frac{7}{2}$	$\frac{5}{2}$	113.99	*b*	0.00

$N''_{K_aK_c}$	$N'_{K_aK_c}$	Rotational Frequency (MHz)	J''	J'	F''	F'	Hyperfine Shift (MHz)	Transition Type	Relative Transition Strength
1_{01}	2_{02}	9,647	$\frac{1}{2}$	$\frac{5}{2}$	$\frac{3}{2}$	$\frac{5}{2}$	-85.56	a	0.01
			$\frac{1}{2}$	$\frac{5}{2}$	$\frac{3}{2}$	$\frac{3}{2}$	-68.53	a	0.00
			$\frac{3}{2}$	$\frac{5}{2}$	$\frac{1}{2}$	$\frac{3}{2}$	-60.46	a	0.02
			$\frac{1}{2}$	$\frac{3}{2}$	$\frac{3}{2}$	$\frac{1}{2}$	-44.91	a	0.00
			$\frac{3}{2}$	$\frac{3}{2}$	$\frac{1}{2}$	$\frac{1}{2}$	-36.85	a	0.01
			$\frac{3}{2}$	$\frac{5}{2}$	$\frac{5}{2}$	$\frac{7}{2}$	-8.47	a	1.12
			$\frac{1}{2}$	$\frac{5}{2}$	$\frac{1}{2}$	$\frac{3}{2}$	-8.45	a	0.25
			$\frac{1}{2}$	$\frac{3}{2}$	$\frac{3}{2}$	$\frac{3}{2}$	-6.18	a	0.10
			$\frac{3}{2}$	$\frac{5}{2}$	$\frac{3}{2}$	$\frac{5}{2}$	-5.78	a	0.59
			$\frac{3}{2}$	$\frac{5}{2}$	$\frac{5}{2}$	$\frac{5}{2}$	1.09	a	0.24
			$\frac{3}{2}$	$\frac{3}{2}$	$\frac{1}{2}$	$\frac{3}{2}$	1.88	a	0.44
			$\frac{1}{2}$	$\frac{3}{2}$	$\frac{3}{2}$	$\frac{5}{2}$	6.24	a	0.82
			$\frac{3}{2}$	$\frac{5}{2}$	$\frac{3}{2}$	$\frac{3}{2}$	11.26	a	0.27
			$\frac{1}{2}$	$\frac{3}{2}$	$\frac{1}{2}$	$\frac{1}{2}$	15.17	a	0.22
			$\frac{3}{2}$	$\frac{5}{2}$	$\frac{5}{2}$	$\frac{3}{2}$	18.13	a	0.02
			$\frac{3}{2}$	$\frac{3}{2}$	$\frac{3}{2}$	$\frac{1}{2}$	34.87	a	0.05
			$\frac{1}{2}$	$\frac{3}{2}$	$\frac{1}{2}$	$\frac{3}{2}$	53.90	a	0.00
			$\frac{3}{2}$	$\frac{3}{2}$	$\frac{3}{2}$	$\frac{3}{2}$	73.60	a	0.02
			$\frac{3}{2}$	$\frac{3}{2}$	$\frac{5}{2}$	$\frac{3}{2}$	80.48	a	0.00
			$\frac{3}{2}$	$\frac{3}{2}$	$\frac{3}{2}$	$\frac{5}{2}$	86.02	a	0.00
			$\frac{3}{2}$	$\frac{3}{2}$	$\frac{5}{2}$	$\frac{5}{2}$	92.90	a	0.01

$N''_{K_aK_c}$	$N'_{K_aK_c}$	Rotational Frequency (MHz)	J''	J'	F''	F'	Hyperfine Shift (MHz)	Transition Type	Relative Transition Strength
1_{10}	2_{11}	10,199	$\frac{1}{2}$	$\frac{5}{2}$	$\frac{3}{2}$	$\frac{5}{2}$	-107.61	a	0.00
			$\frac{1}{2}$	$\frac{5}{2}$	$\frac{3}{2}$	$\frac{3}{2}$	-86.52	a	0.00
			$\frac{1}{2}$	$\frac{5}{2}$	$\frac{1}{2}$	$\frac{3}{2}$	-59.89	a	0.01
			$\frac{1}{2}$	$\frac{3}{2}$	$\frac{3}{2}$	$\frac{1}{2}$	-48.26	a	0.01
			$\frac{1}{2}$	$\frac{3}{2}$	$\frac{1}{2}$	$\frac{1}{2}$	-21.63	a	0.04
			$\frac{1}{2}$	$\frac{3}{2}$	$\frac{3}{2}$	$\frac{3}{2}$	-17.48	a	0.09
			$\frac{3}{2}$	$\frac{5}{2}$	$\frac{3}{2}$	$\frac{5}{2}$	-13.96	a	0.46
			$\frac{3}{2}$	$\frac{5}{2}$	$\frac{1}{2}$	$\frac{3}{2}$	-13.70	a	0.21
			$\frac{3}{2}$	$\frac{5}{2}$	$\frac{5}{2}$	$\frac{7}{2}$	-5.50	a	0.84
			$\frac{1}{2}$	$\frac{3}{2}$	$\frac{3}{2}$	$\frac{5}{2}$	1.31	a	0.60
			$\frac{3}{2}$	$\frac{5}{2}$	$\frac{3}{2}$	$\frac{3}{2}$	7.13	a	0.18
			$\frac{1}{2}$	$\frac{3}{2}$	$\frac{1}{2}$	$\frac{3}{2}$	9.15	a	0.30
			$\frac{3}{2}$	$\frac{5}{2}$	$\frac{5}{2}$	$\frac{5}{2}$	12.13	a	0.16
			$\frac{3}{2}$	$\frac{3}{2}$	$\frac{1}{2}$	$\frac{1}{2}$	24.56	a	0.13
			$\frac{3}{2}$	$\frac{5}{2}$	$\frac{5}{2}$	$\frac{3}{2}$	33.22	a	0.01
			$\frac{3}{2}$	$\frac{3}{2}$	$\frac{3}{2}$	$\frac{1}{2}$	45.39	a	0.03
			$\frac{3}{2}$	$\frac{3}{2}$	$\frac{1}{2}$	$\frac{3}{2}$	55.33	a	0.00
			$\frac{3}{2}$	$\frac{3}{2}$	$\frac{3}{2}$	$\frac{3}{2}$	76.17	a	0.02
			$\frac{3}{2}$	$\frac{3}{2}$	$\frac{3}{2}$	$\frac{5}{2}$	94.95	a	0.01
			$\frac{3}{2}$	$\frac{3}{2}$	$\frac{5}{2}$	$\frac{3}{2}$	102.25	a	0.01
			$\frac{3}{2}$	$\frac{3}{2}$	$\frac{5}{2}$	$\frac{5}{2}$	121.04	a	0.02

$N''_{K_aK_c}$	$N'_{K_aK_c}$	Rotational Frequency (MHz)	J''	J'	F''	F'	Hyperfine Shift (MHz)	Transition Type	Relative Transition Strength
3_{03}	3_{12}	10,218	$\frac{5}{2}$	$\frac{7}{2}$	$\frac{7}{2}$	$\frac{9}{2}$	-128.90	*b*	0.00
			$\frac{5}{2}$	$\frac{7}{2}$	$\frac{7}{2}$	$\frac{7}{2}$	-112.59	*b*	0.00
			$\frac{5}{2}$	$\frac{7}{2}$	$\frac{5}{2}$	$\frac{7}{2}$	-97.44	*b*	0.00
			$\frac{5}{2}$	$\frac{7}{2}$	$\frac{7}{2}$	$\frac{5}{2}$	-91.62	*b*	0.00
			$\frac{5}{2}$	$\frac{7}{2}$	$\frac{5}{2}$	$\frac{5}{2}$	-76.47	*b*	0.00
			$\frac{5}{2}$	$\frac{7}{2}$	$\frac{3}{2}$	$\frac{5}{2}$	-40.96	*b*	0.00
			$\frac{7}{2}$	$\frac{7}{2}$	$\frac{5}{2}$	$\frac{7}{2}$	-25.65	*b*	0.01
			$\frac{7}{2}$	$\frac{7}{2}$	$\frac{7}{2}$	$\frac{9}{2}$	-23.79	*b*	0.01
			$\frac{5}{2}$	$\frac{5}{2}$	$\frac{5}{2}$	$\frac{3}{2}$	-20.91	*b*	0.00
			$\frac{7}{2}$	$\frac{7}{2}$	$\frac{9}{2}$	$\frac{9}{2}$	-12.42	*b*	0.07
			$\frac{7}{2}$	$\frac{7}{2}$	$\frac{7}{2}$	$\frac{7}{2}$	-7.48	*b*	0.05
			$\frac{5}{2}$	$\frac{5}{2}$	$\frac{7}{2}$	$\frac{5}{2}$	-6.17	*b*	0.00
			$\frac{7}{2}$	$\frac{7}{2}$	$\frac{5}{2}$	$\frac{5}{2}$	-4.67	*b*	0.03
			$\frac{7}{2}$	$\frac{7}{2}$	$\frac{9}{2}$	$\frac{7}{2}$	3.89	*b*	0.01
			$\frac{5}{2}$	$\frac{5}{2}$	$\frac{5}{2}$	$\frac{5}{2}$	8.98	*b*	0.04
			$\frac{5}{2}$	$\frac{5}{2}$	$\frac{7}{2}$	$\frac{7}{2}$	12.54	*b*	0.06
			$\frac{7}{2}$	$\frac{7}{2}$	$\frac{7}{2}$	$\frac{5}{2}$	13.49	*b*	0.01
			$\frac{5}{2}$	$\frac{5}{2}$	$\frac{3}{2}$	$\frac{3}{2}$	14.60	*b*	0.02
			$\frac{5}{2}$	$\frac{5}{2}$	$\frac{5}{2}$	$\frac{7}{2}$	27.70	*b*	0.00
			$\frac{5}{2}$	$\frac{5}{2}$	$\frac{3}{2}$	$\frac{5}{2}$	44.49	*b*	0.00
			$\frac{7}{2}$	$\frac{5}{2}$	$\frac{5}{2}$	$\frac{3}{2}$	50.88	*b*	0.00
			$\frac{7}{2}$	$\frac{5}{2}$	$\frac{5}{2}$	$\frac{5}{2}$	80.78	*b*	0.00
			$\frac{7}{2}$	$\frac{5}{2}$	$\frac{7}{2}$	$\frac{5}{2}$	98.94	*b*	0.00
			$\frac{7}{2}$	$\frac{5}{2}$	$\frac{5}{2}$	$\frac{7}{2}$	99.49	*b*	0.00
			$\frac{7}{2}$	$\frac{5}{2}$	$\frac{7}{2}$	$\frac{7}{2}$	117.65	*b*	0.00
			$\frac{7}{2}$	$\frac{5}{2}$	$\frac{9}{2}$	$\frac{7}{2}$	129.02	*b*	0.00

$N''_{K_aK_c}$	$N'_{K_aK_c}$	Rotational Frequency (MHz)	J''	J'	F''	F'	Hyperfine Shift (MHz)	Transition Type	Relative Transition Strength
0_{00}	1_{11}	13,102	$\frac{1}{2}$	$\frac{3}{2}$	$\frac{1}{2}$	$\frac{3}{2}$	-69.56	*b*	0.00
			$\frac{1}{2}$	$\frac{1}{2}$	$\frac{1}{2}$	$\frac{1}{2}$	-51.49	*b*	0.00
			$\frac{1}{2}$	$\frac{3}{2}$	$\frac{3}{2}$	$\frac{5}{2}$	-19.89	*b*	0.03
			$\frac{1}{2}$	$\frac{3}{2}$	$\frac{1}{2}$	$\frac{1}{2}$	-6.23	*b*	0.01
			$\frac{1}{2}$	$\frac{3}{2}$	$\frac{3}{2}$	$\frac{3}{2}$	4.08	*b*	0.02
			$\frac{1}{2}$	$\frac{1}{2}$	$\frac{1}{2}$	$\frac{3}{2}$	17.65	*b*	0.02
			$\frac{1}{2}$	$\frac{1}{2}$	$\frac{3}{2}$	$\frac{1}{2}$	22.14	*b*	0.01
			$\frac{1}{2}$	$\frac{3}{2}$	$\frac{3}{2}$	$\frac{1}{2}$	67.40	*b*	0.00
			$\frac{1}{2}$	$\frac{1}{2}$	$\frac{3}{2}$	$\frac{3}{2}$	91.28	*b*	0.00
0_{00}	1_{10}	13,629	$\frac{1}{2}$	$\frac{3}{2}$	$\frac{1}{2}$	$\frac{3}{2}$	-70.99	*c*	0.00
			$\frac{1}{2}$	$\frac{3}{2}$	$\frac{1}{2}$	$\frac{1}{2}$	-50.16	*c*	0.00
			$\frac{1}{2}$	$\frac{3}{2}$	$\frac{3}{2}$	$\frac{5}{2}$	-23.44	*c*	0.00
			$\frac{1}{2}$	$\frac{1}{2}$	$\frac{1}{2}$	$\frac{1}{2}$	-3.97	*c*	0.00
			$\frac{1}{2}$	$\frac{3}{2}$	$\frac{3}{2}$	$\frac{3}{2}$	2.64	*c*	0.00
			$\frac{1}{2}$	$\frac{1}{2}$	$\frac{1}{2}$	$\frac{3}{2}$	22.66	*c*	0.00
			$\frac{1}{2}$	$\frac{3}{2}$	$\frac{3}{2}$	$\frac{1}{2}$	23.48	*c*	0.00
			$\frac{1}{2}$	$\frac{1}{2}$	$\frac{3}{2}$	$\frac{1}{2}$	69.66	*c*	0.00
			$\frac{1}{2}$	$\frac{1}{2}$	$\frac{3}{2}$	$\frac{3}{2}$	96.29	*c*	0.00

$N''_{K_aK_c}$	$N'_{K_aK_c}$	Rotational Frequency (MHz)	J''	J'	F''	F'	Hyperfine Shift (MHz)	Transition Type	Relative Transition Strength
2_{12}	3_{13}	13,701	$\frac{3}{2}$	$\frac{7}{2}$	$\frac{5}{2}$	$\frac{7}{2}$	-103.34	a	0.00
			$\frac{3}{2}$	$\frac{7}{2}$	$\frac{5}{2}$	$\frac{5}{2}$	-84.64	a	0.00
			$\frac{3}{2}$	$\frac{7}{2}$	$\frac{3}{2}$	$\frac{5}{2}$	-68.24	a	0.01
			$\frac{3}{2}$	$\frac{5}{2}$	$\frac{5}{2}$	$\frac{3}{2}$	-48.56	a	0.00
			$\frac{3}{2}$	$\frac{5}{2}$	$\frac{3}{2}$	$\frac{3}{2}$	-32.16	a	0.03
			$\frac{3}{2}$	$\frac{5}{2}$	$\frac{5}{2}$	$\frac{5}{2}$	-13.12	a	0.07
			$\frac{5}{2}$	$\frac{7}{2}$	$\frac{5}{2}$	$\frac{7}{2}$	-6.25	a	0.93
			$\frac{5}{2}$	$\frac{7}{2}$	$\frac{3}{2}$	$\frac{5}{2}$	-6.24	a	0.62
			$\frac{5}{2}$	$\frac{7}{2}$	$\frac{7}{2}$	$\frac{9}{2}$	-4.68	a	1.33
			$\frac{3}{2}$	$\frac{5}{2}$	$\frac{3}{2}$	$\frac{5}{2}$	3.28	a	0.71
			$\frac{3}{2}$	$\frac{5}{2}$	$\frac{5}{2}$	$\frac{7}{2}$	3.32	a	1.05
			$\frac{3}{2}$	$\frac{5}{2}$	$\frac{1}{2}$	$\frac{3}{2}$	4.04	a	0.37
			$\frac{5}{2}$	$\frac{7}{2}$	$\frac{7}{2}$	$\frac{7}{2}$	8.37	a	0.14
			$\frac{5}{2}$	$\frac{7}{2}$	$\frac{5}{2}$	$\frac{5}{2}$	12.46	a	0.16
			$\frac{5}{2}$	$\frac{7}{2}$	$\frac{7}{2}$	$\frac{5}{2}$	27.07	a	0.01
			$\frac{5}{2}$	$\frac{5}{2}$	$\frac{3}{2}$	$\frac{3}{2}$	29.84	a	0.12
			$\frac{5}{2}$	$\frac{5}{2}$	$\frac{5}{2}$	$\frac{3}{2}$	48.54	a	0.01
			$\frac{5}{2}$	$\frac{5}{2}$	$\frac{3}{2}$	$\frac{5}{2}$	65.28	a	0.00
			$\frac{5}{2}$	$\frac{5}{2}$	$\frac{5}{2}$	$\frac{5}{2}$	83.97	a	0.02
			$\frac{5}{2}$	$\frac{5}{2}$	$\frac{7}{2}$	$\frac{5}{2}$	98.59	a	0.00
			$\frac{5}{2}$	$\frac{5}{2}$	$\frac{5}{2}$	$\frac{7}{2}$	100.42	a	0.00
			$\frac{5}{2}$	$\frac{5}{2}$	$\frac{7}{2}$	$\frac{7}{2}$	115.04	a	0.01

$N''_{K_aK_c}$	$N'_{K_aK_c}$	Rotational Frequency (MHz)	J''	J'	F''	F'	Hyperfine Shift (MHz)	Transition Type	Relative Transition Strength
2_{02}	3_{03}	14,410	$\frac{3}{2}$	$\frac{7}{2}$	$\frac{5}{2}$	$\frac{7}{2}$	-98.37	a	0.01
			$\frac{3}{2}$	$\frac{7}{2}$	$\frac{5}{2}$	$\frac{5}{2}$	-80.21	a	0.00
			$\frac{3}{2}$	$\frac{7}{2}$	$\frac{3}{2}$	$\frac{5}{2}$	-67.79	a	0.02
			$\frac{3}{2}$	$\frac{5}{2}$	$\frac{5}{2}$	$\frac{3}{2}$	-43.92	a	0.00
			$\frac{3}{2}$	$\frac{5}{2}$	$\frac{3}{2}$	$\frac{3}{2}$	-31.51	a	0.02
			$\frac{3}{2}$	$\frac{5}{2}$	$\frac{5}{2}$	$\frac{5}{2}$	-8.42	a	0.07
			$\frac{5}{2}$	$\frac{7}{2}$	$\frac{7}{2}$	$\frac{9}{2}$	-8.38	a	1.49
			$\frac{5}{2}$	$\frac{7}{2}$	$\frac{5}{2}$	$\frac{7}{2}$	-6.57	a	1.03
			$\frac{5}{2}$	$\frac{7}{2}$	$\frac{3}{2}$	$\frac{5}{2}$	-5.44	a	0.69
			$\frac{5}{2}$	$\frac{7}{2}$	$\frac{7}{2}$	$\frac{7}{2}$	2.99	a	0.16
			$\frac{3}{2}$	$\frac{5}{2}$	$\frac{3}{2}$	$\frac{5}{2}$	4.00	a	0.80
			$\frac{3}{2}$	$\frac{5}{2}$	$\frac{5}{2}$	$\frac{7}{2}$	6.74	a	1.18
			$\frac{3}{2}$	$\frac{5}{2}$	$\frac{1}{2}$	$\frac{3}{2}$	7.23	a	0.42
			$\frac{5}{2}$	$\frac{7}{2}$	$\frac{5}{2}$	$\frac{5}{2}$	11.59	a	0.19
			$\frac{5}{2}$	$\frac{7}{2}$	$\frac{7}{2}$	$\frac{5}{2}$	21.16	a	0.01
			$\frac{5}{2}$	$\frac{5}{2}$	$\frac{3}{2}$	$\frac{3}{2}$	30.84	a	0.15
			$\frac{5}{2}$	$\frac{5}{2}$	$\frac{5}{2}$	$\frac{3}{2}$	47.88	a	0.01
			$\frac{5}{2}$	$\frac{5}{2}$	$\frac{3}{2}$	$\frac{5}{2}$	66.35	a	0.00
			$\frac{5}{2}$	$\frac{5}{2}$	$\frac{5}{2}$	$\frac{5}{2}$	83.38	a	0.02
			$\frac{5}{2}$	$\frac{5}{2}$	$\frac{7}{2}$	$\frac{5}{2}$	92.95	a	0.00
			$\frac{5}{2}$	$\frac{5}{2}$	$\frac{5}{2}$	$\frac{7}{2}$	98.54	a	0.00
			$\frac{5}{2}$	$\frac{5}{2}$	$\frac{7}{2}$	$\frac{7}{2}$	108.10	a	0.01

$N''_{K_aK_c}$	$N'_{K_aK_c}$	Rotational Frequency (MHz)	J''	J'	F''	F'	Hyperfine Shift (MHz)	Transition Type	Relative Transition Strength
2_{11}	3_{12}	15,283	$\frac{3}{2}$	$\frac{7}{2}$	$\frac{5}{2}$	$\frac{7}{2}$	-118.48	a	0.00
			$\frac{3}{2}$	$\frac{7}{2}$	$\frac{5}{2}$	$\frac{5}{2}$	-97.51	a	0.00
			$\frac{3}{2}$	$\frac{7}{2}$	$\frac{3}{2}$	$\frac{5}{2}$	-78.72	a	0.01
			$\frac{3}{2}$	$\frac{5}{2}$	$\frac{5}{2}$	$\frac{3}{2}$	-41.96	a	0.00
			$\frac{3}{2}$	$\frac{5}{2}$	$\frac{3}{2}$	$\frac{3}{2}$	-23.17	a	0.04
			$\frac{3}{2}$	$\frac{5}{2}$	$\frac{5}{2}$	$\frac{5}{2}$	-12.06	a	0.07
			$\frac{5}{2}$	$\frac{7}{2}$	$\frac{3}{2}$	$\frac{5}{2}$	-9.69	a	0.64
			$\frac{5}{2}$	$\frac{7}{2}$	$\frac{5}{2}$	$\frac{7}{2}$	-9.57	a	0.93
			$\frac{5}{2}$	$\frac{7}{2}$	$\frac{7}{2}$	$\frac{9}{2}$	-8.25	a	1.33
			$\frac{3}{2}$	$\frac{5}{2}$	$\frac{5}{2}$	$\frac{7}{2}$	6.65	a	1.04
			$\frac{3}{2}$	$\frac{5}{2}$	$\frac{3}{2}$	$\frac{5}{2}$	6.73	a	0.69
			$\frac{3}{2}$	$\frac{5}{2}$	$\frac{1}{2}$	$\frac{3}{2}$	7.61	a	0.37
			$\frac{5}{2}$	$\frac{7}{2}$	$\frac{7}{2}$	$\frac{7}{2}$	8.06	a	0.13
			$\frac{5}{2}$	$\frac{7}{2}$	$\frac{5}{2}$	$\frac{5}{2}$	11.40	a	0.15
			$\frac{5}{2}$	$\frac{7}{2}$	$\frac{7}{2}$	$\frac{5}{2}$	29.03	a	0.01
			$\frac{5}{2}$	$\frac{5}{2}$	$\frac{3}{2}$	$\frac{3}{2}$	45.87	a	0.11
			$\frac{5}{2}$	$\frac{5}{2}$	$\frac{5}{2}$	$\frac{3}{2}$	66.96	a	0.01
			$\frac{5}{2}$	$\frac{5}{2}$	$\frac{3}{2}$	$\frac{5}{2}$	75.76	a	0.00
			$\frac{5}{2}$	$\frac{5}{2}$	$\frac{5}{2}$	$\frac{5}{2}$	96.85	a	0.03
			$\frac{5}{2}$	$\frac{5}{2}$	$\frac{7}{2}$	$\frac{5}{2}$	114.48	a	0.00
			$\frac{5}{2}$	$\frac{5}{2}$	$\frac{5}{2}$	$\frac{7}{2}$	115.56	a	0.00
			$\frac{5}{2}$	$\frac{5}{2}$	$\frac{7}{2}$	$\frac{7}{2}$	133.20	a	0.02

$N''_{K_aK_c}$	$N'_{K_aK_c}$	Rotational Frequency (MHz)	J''	J'	F''	F'	Hyperfine Shift (MHz)	Transition Type	Relative Transition Strength
1_{01}	2_{12}	17,410	$\frac{1}{2}$	$\frac{5}{2}$	$\frac{3}{2}$	$\frac{5}{2}$	-85.94	*b*	0.00
			$\frac{1}{2}$	$\frac{5}{2}$	$\frac{3}{2}$	$\frac{3}{2}$	-67.24	*b*	0.00
			$\frac{3}{2}$	$\frac{5}{2}$	$\frac{1}{2}$	$\frac{3}{2}$	-59.18	*b*	0.00
			$\frac{1}{2}$	$\frac{3}{2}$	$\frac{3}{2}$	$\frac{1}{2}$	-41.44	*b*	0.00
			$\frac{3}{2}$	$\frac{3}{2}$	$\frac{1}{2}$	$\frac{1}{2}$	-33.38	*b*	0.00
			$\frac{3}{2}$	$\frac{5}{2}$	$\frac{5}{2}$	$\frac{7}{2}$	-13.90	*b*	0.04
			$\frac{1}{2}$	$\frac{5}{2}$	$\frac{1}{2}$	$\frac{3}{2}$	-7.17	*b*	0.01
			$\frac{3}{2}$	$\frac{5}{2}$	$\frac{3}{2}$	$\frac{5}{2}$	-6.15	*b*	0.02
			$\frac{1}{2}$	$\frac{3}{2}$	$\frac{3}{2}$	$\frac{3}{2}$	-5.24	*b*	0.00
			$\frac{3}{2}$	$\frac{5}{2}$	$\frac{5}{2}$	$\frac{5}{2}$	0.72	*b*	0.01
			$\frac{3}{2}$	$\frac{3}{2}$	$\frac{1}{2}$	$\frac{3}{2}$	2.82	*b*	0.01
			$\frac{1}{2}$	$\frac{3}{2}$	$\frac{3}{2}$	$\frac{5}{2}$	11.16	*b*	0.03
			$\frac{3}{2}$	$\frac{5}{2}$	$\frac{3}{2}$	$\frac{3}{2}$	12.54	*b*	0.01
			$\frac{1}{2}$	$\frac{3}{2}$	$\frac{1}{2}$	$\frac{1}{2}$	18.64	*b*	0.01
			$\frac{3}{2}$	$\frac{5}{2}$	$\frac{5}{2}$	$\frac{3}{2}$	19.41	*b*	0.00
			$\frac{3}{2}$	$\frac{3}{2}$	$\frac{3}{2}$	$\frac{1}{2}$	38.34	*b*	0.00
			$\frac{1}{2}$	$\frac{3}{2}$	$\frac{1}{2}$	$\frac{3}{2}$	54.84	*b*	0.00
			$\frac{3}{2}$	$\frac{3}{2}$	$\frac{3}{2}$	$\frac{3}{2}$	74.54	*b*	0.00
			$\frac{3}{2}$	$\frac{3}{2}$	$\frac{5}{2}$	$\frac{3}{2}$	81.42	*b*	0.00
			$\frac{3}{2}$	$\frac{3}{2}$	$\frac{3}{2}$	$\frac{5}{2}$	90.94	*b*	0.00
			$\frac{3}{2}$	$\frac{3}{2}$	$\frac{5}{2}$	$\frac{5}{2}$	97.82	*b*	0.00

$N''_{K_aK_c}$	$N'_{K_aK_c}$	Rotational Frequency (MHz)	J''	J'	F''	F'	Hyperfine Shift (MHz)	Transition Type	Relative Transition Strength
1_{01}	2_{11}	18,992	$\frac{1}{2}$	$\frac{5}{2}$	$\frac{3}{2}$	$\frac{5}{2}$	-90.05	c	0.00
			$\frac{1}{2}$	$\frac{5}{2}$	$\frac{3}{2}$	$\frac{3}{2}$	-68.96	c	0.00
			$\frac{3}{2}$	$\frac{5}{2}$	$\frac{1}{2}$	$\frac{3}{2}$	-60.89	c	0.00
			$\frac{1}{2}$	$\frac{3}{2}$	$\frac{3}{2}$	$\frac{1}{2}$	-30.70	c	0.00
			$\frac{3}{2}$	$\frac{3}{2}$	$\frac{1}{2}$	$\frac{1}{2}$	-22.63	c	0.00
			$\frac{3}{2}$	$\frac{5}{2}$	$\frac{5}{2}$	$\frac{7}{2}$	-21.02	c	0.00
			$\frac{3}{2}$	$\frac{5}{2}$	$\frac{3}{2}$	$\frac{5}{2}$	-10.26	c	0.00
			$\frac{1}{2}$	$\frac{5}{2}$	$\frac{1}{2}$	$\frac{3}{2}$	-8.88	c	0.00
			$\frac{3}{2}$	$\frac{5}{2}$	$\frac{5}{2}$	$\frac{5}{2}$	-3.39	c	0.00
			$\frac{1}{2}$	$\frac{3}{2}$	$\frac{3}{2}$	$\frac{3}{2}$	0.08	c	0.00
			$\frac{3}{2}$	$\frac{3}{2}$	$\frac{1}{2}$	$\frac{3}{2}$	8.14	c	0.00
			$\frac{3}{2}$	$\frac{5}{2}$	$\frac{3}{2}$	$\frac{3}{2}$	10.83	c	0.00
			$\frac{3}{2}$	$\frac{5}{2}$	$\frac{5}{2}$	$\frac{3}{2}$	17.70	c	0.00
			$\frac{1}{2}$	$\frac{3}{2}$	$\frac{3}{2}$	$\frac{5}{2}$	18.87	c	0.00
			$\frac{1}{2}$	$\frac{3}{2}$	$\frac{1}{2}$	$\frac{1}{2}$	29.38	c	0.00
			$\frac{3}{2}$	$\frac{3}{2}$	$\frac{3}{2}$	$\frac{1}{2}$	49.09	c	0.00
			$\frac{1}{2}$	$\frac{3}{2}$	$\frac{1}{2}$	$\frac{3}{2}$	60.16	c	0.00
			$\frac{3}{2}$	$\frac{3}{2}$	$\frac{3}{2}$	$\frac{3}{2}$	79.86	c	0.00
			$\frac{3}{2}$	$\frac{3}{2}$	$\frac{5}{2}$	$\frac{3}{2}$	86.74	c	0.00
			$\frac{3}{2}$	$\frac{3}{2}$	$\frac{3}{2}$	$\frac{5}{2}$	98.65	c	0.00
			$\frac{3}{2}$	$\frac{3}{2}$	$\frac{5}{2}$	$\frac{5}{2}$	105.52	c	0.00

References

[1] MOLPRO, Version 2002.6, H.-J. Werner, P. J. Knowles, R. Lindh, F. R. Manby, M. Schtz, P. Celani, T. Korona, G. Rauhut, R. D. Amos, A. Bernhardsson, A. Berning, D. L. Cooper, M. J. O. Deegan, A. J. Dobbyn, F. Eckert, C. Hampel, G. Hetzer, A. W. Lloyd, S. J. McNicholas, W. Meyer, M. E. Mura, A. Nickla, P. Palmieri, R. Pitzer, U. Schumann, H. Stoll, A. J. Stone, R. Tarroni, and T. Thorsteinsson, University College Cardiff Consultants Limited, 2004